CHEMICAL REVIEWS

pubs.acs.org/CR

Review

Electronic Structure Modeling of Metal−Organic Frameworks

Jenna L. Mancuso, Austin M. Mroz, Khoa N. Le, and Christopher H. Hendon*

Cite This: *Chem. Rev.* 2020, 120, 8641−8715

Read Online

ACCESS | Metrics & More | Article Recommendations

ABSTRACT: Owing to their molecular building blocks, yet highly crystalline nature, metal−organic frameworks (MOFs) sit at the interface between molecule and material. Their diverse structures and compositions enable them to be useful materials as catalysts in heterogeneous reactions, electrical conductors in energy storage and transfer applications, chromophores in photoenabled chemical transformations, and beyond. In all cases, density functional theory (DFT) and higher-level methods for electronic structure determination provide valuable quantitative information about the electronic properties that underpin the functions of these frameworks. However, there are only two general modeling approaches in conventional electronic structure software packages: those that treat materials as extended, periodic solids, and those that treat materials as discrete molecules. Each approach has features and benefits; both have been widely employed to understand the emergent chemistry that arises from the formation of the metal−organic interface. This Review canvases these approaches to date, with emphasis placed on the application of electronic structure theory to explore reactivity and electron transfer using periodic, molecular, and embedded models. This includes (i) computational chemistry considerations such as how functional, *k*-grid, and other model variables are selected to enable insights into MOF properties, (ii) extended solid models that treat MOFs as materials rather than molecules, (iii) the mechanics of cluster extraction and subsequent chemistry enabled by these molecular models, (iv) catalytic studies using both solids and clusters thereof, and (v) embedded, mixed-method approaches, which simulate a fraction of the material using one level of theory and the remainder of the material using another dissimilar theoretical implementation.

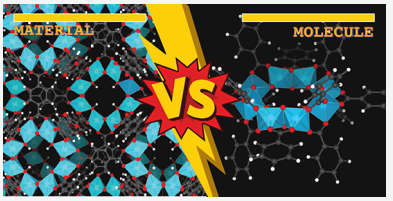

Downloaded via UNIV GENT on May 19, 2022 at 12:43:09 (UTC).
See https://pubs.acs.org/sharingguidelines for options on how to legitimately share published articles.

CONTENTS

Special Issue: Porous Framework Chemistry

Received: February 25, 2020
Published: July 16, 2020

© 2020 American Chemical Society

https://dx.doi.org/10.1021/acs.chemrev.0c00148
Chem. Rev. 2020, 120, 8641−8715

1. INTRODUCTION

Since their conception,[1] metal−organic frameworks (MOFs) have attracted practitioners from organic, inorganic, and materials disciplines,[2−4] each with a shared interest in physical properties afforded by mixing multitopic organic linkers and metal ions or clusters (secondary building units, SBUs, or nodes).[5,6] The combination of SBUs with the multitude of linkers has enabled a seemingly infinite landscape of materials with modular properties,[7] all featuring one commonality: crystallographically ordered void spaces.[8,9] Porosity in conjunction with functional MOF components catalyzed interest in these materials as atomically precise pores enable a series of heterogeneous gas storage[10−12] and separation technologies[13,14] as well as access to extremely high loadings of catalytically active centers.[15−18] In more recent embodiments, exotic electronic structures have been discovered,[19−21] providing a foundation for applications in high surface area electrodes in electrochemical devices[22−29] and as ordered arrays of qubits for MOF-mediated quantum computing.[30−32] Clearly, their diverse composition and structure enable a wealth of possible applications.

Many of these applications depend on the accessibility of the pores; pore topology is largely determined by the shape, size, and composition of the linkers.[33,34] Of course, the node composition and topology also play a determining role in the structure,[6,35,36] but there are far fewer synthetic handles available to modify and create novel inorganic clusters. Thus, the prediction of MOF properties is well-suited to computation,[37] as we can rapidly construct a large family of MOFs using only the geometry of the SBUs and a nearly endless selection of linkers.[38] Indeed, one of the most elegant aspects of MOF chemistry is the ability to transmetallate[39−43] and geometrically substitute one linker for another of similar geometry[44−46] enabling a broad gamut of structurally related materials.[47] Such isoreticularity[48−50] is a cornerstone of the field[51−53] and has been a key focus for several years with notable successes (e.g., efficient absorption of water,[54−57] and as site isolated catalysts[58−60]).

Focusing on the organic and inorganic components separately, there is a rich history of both molecular and solid-state chemistries from which to draw insight. The design principles that underpin these fields can also be applied to MOFs, enabling subtle electronic control of the bulk MOF properties; chemists can use pre- and postsynthetic design of organic linkers to augment the properties of the bulk material.[61] The power afforded by constructing materials from molecules should not be undersold; it is easier to modulate a molecular property than it is to postsynthetically modulate a material property. To illustrate this power, both the linker and the inorganic node have been used as hosts for molecular catalysts (an example is emphasized in the center of Figure 1).[62,63] The paradigm of appending known, active, catalysts to MOFs, via either linker functionalization[64,65] or node modifications,[66−70]

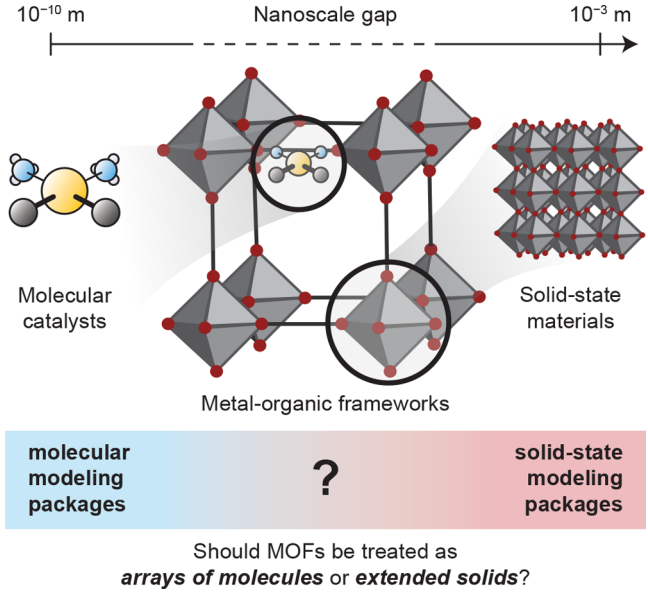

Figure 1. Metal−organic frameworks are uniquely positioned between the molecule, Å scale, and material, mm scale, and consequently behave as both molecules and extended solids.

often only serves the purpose of supporting an otherwise homogeneous catalyst.[71] The fact one is able to append a catalyst to the surface of a solid without grossly diminishing its function highlights a key design principle:[72] the electronic structure of most MOFs does not impact the local electronic structure of the catalytically active site, Figure 1. In other words, from this limited perspective, most MOFs are *not* greater than the sum of their parts, they are merely an array of ordered molecules.

However, there are certain instances where the assembly and composition of a MOF clearly does augment the electronic properties of its constituents; they are more complicated than an array of molecules. For example, the ionization potential of benzene dicarboxylic acid is 9.9 eV,[73] yet when it is used to construct Zn-MOF-5,[12] Ti-MIL-125 (Materials Institute Lavoisier),[74] and UiO-66 (Universitetet i Oslo),[75] three examples of frameworks whose frontier orbitals are centered on benzene dicarboxylate (BDC) ligand, BDC exhibits ionization potentials of 7.3, 7.7, and 7.0 eV, respectively.[76] Given the energetics of the linkers are hence susceptible to augmentation depending on the electrophilicity of the metal ions/clusters, the assembly of the MOF itself can have an impact on the electronics of the system, even if the states themselves are largely localized. This enables opportunities for MOFs in optical[77,78] and photocatalytic[79−81] applications, where the MOF structure and composition play a determining role in the chemistry of the localized states.

Thus, by making the assumption that all MOFs feature highly localized electronic states, we limit our ability to provide insight into some of their properties, particularly for materials with high levels of covalency at the metal−ligand interface[82] and for MOFs that feature extended inorganic connectivity (e.g., MOF-74[83]). Consider the family of champion electrically conductive 2D MOFs constructed from square planar metals and oxidized planar hexatopic linkers. The most studied scaffold, Ni_3(hexaiminotriphenylene)$_2$ (Ni_3(HITP)$_2$),[84,85] only assembles in the presence of chemical oxidants. Analyses of the electronic structure have revealed that the emergent properties

https://dx.doi.org/10.1021/acs.chemrev.0c00148
Chem. Rev. 2020, 120, 8641−8715

of the framework are difficult to rationalize from molecular design principles alone, as the linkers should feature unpaired electrons, but the MOF itself shows no EPR signal.[85−87] Indeed, it is more appropriate to consider these sorts of MOFs from a solid-state perspective, where the orbitals delocalize to form bands[88,89] and the symmetry of the crystal becomes important for correct descriptions of electron energetics.

1.1. Are MOFs an Array of Molecules or Extended Solids?

It is the molecule/material duality of MOFs that places them in the "nanoscale" gap, somewhere between molecule and material, Figure 1. Beyond a few simple design principles (e.g., presence of extended inorganic connectivity, stacking of conjugated linkers, magnetism, etc.[90−92]), which clearly depend on extended solid-state interactions, it is difficult to assess where the electronic structure and physical properties of new frameworks will lay on a spectrum between molecule and solid. This duality poses challenges for modeling MOFs, where computational chemists must make a decision to whether they model them as molecules or extended solids.

Within the theoretical framework, the primary difference between solid-state and molecular software packages is the application of periodic boundary conditions.[93] Practitioners are thus presented with a modeling paradox: should the material be treated as a bulk solid, in principle obtaining the correct electronic structure but with reduced capabilities to compute things like reaction transition states?[94] Or should one save computational time and model a truncated fraction using molecular software packages, enabling a broader array of computational tools and higher level of theory but perhaps sacrificing a proper description of the electronic structure?[95]

Of course, the ideal model would be one that treats the MOF as a periodic solid, but can readily apply high levels of theory (typically limited to molecular software packages) to important components in the material.[96] Ultimately, the purpose of a model is to help explain and predict experimental realities using the smallest possible computational system. Hence, it is not surprising that both molecular and solid-state modeling approaches have been fruitful in the MOF field, as the scaffolds may very well act more like one than the other. In this Review, we canvas the application of electronic structure methods applied to MOFs, examining both molecular and extended solid approaches. Emphasis is placed on the methods used in a series of landmark studies to outline a general approach to simulating these complex, beautiful materials. We will discuss general considerations for electronic structure theory (section 2), the broad methods invoked when modeling MOFs as truncated molecular clusters (section 3), and as extended solids (section 4), as well as specific calculation considerations in catalytic studies (section 5), and finally discuss the application of multiscale and embedded modeling procedures (section 6).

2. GENERAL CALCULATION CONSIDERATIONS

Electronic structure calculations provide insight into chemical systems at a fidelity that may be evasive with experimentation alone. The reliability and robustness of the calculations depend not only on the structure and identity of the chemical system but also on the functional and basis set. To judge the accuracy of a model, calculated results are compared with experimental or higher level computational data[97] (e.g., band gap for electronic properties, bond length/angles and lattice parameters for structure, or vibrations and formation enthalpies to investigate stability).[98,99] The interdependence of functional and structure poses a multifaceted challenge of functional selection to obtain both realistic physical parameters and electronic wave functions.

By far the most important factor in obtaining reliable computational data is using reliable atomic coordinates. As such, it is good practice to perform electronic calculations on structures equilibrated at that level of theory; small deviations in atomic positions can result in large electronic disparities.[100] Yet, it is routine to report high-level electronic structure calculations on geometries obtained using structures equilibrated at lower levels of theory;[101,102] we will later discuss the implications of doing so, and why it has been so successful. Still, there are reports of practitioners using experimental crystallographic positions in density functional theory (DFT) models for large and complex systems when computational equilibration exceeds the abilities of the computational resources available; this has proven useful in rationalizing experimental phenomena.[103,104] While none of these approaches provide the true ground state electronic density associated with the terminal functional used for the reported the electronic properties,[105] the models themselves are reproducible and consistently provide useful insights into the chemistry of both molecules and MOFs alike.[101,106,107]

Although one may become disenchanted with computational approaches because, at face value, it would appear one could "turn knobs" to recover essentially any desired result, responsible benchmarking and control studies curtail problematic model reductions and parametrizations. In reality, no DFT approach is perfect because the nature of the functional that recovers the exact density and energy is unknown and a vast array of functionals and corrective terms exist simply to account for deficiencies in the mathematical description of electron exchange and correlation. But it is worth remembering what modelers are trying to achieve; fundamentally, the primary objectives of an electronic structure model are 2-fold: (i) be reproducible, such that future studies invoking a published methodology may build from past results, and (ii) effectively describe the realistic chemical system in light of the various approximations and additions that were chosen during model construction. The many knobs thus exist because of the breadth of physics present in MOFs. For example, it may be necessary to add additional dispersion terms to recover computational lattice parameters in highly conjugated frameworks that more closely match experiment and spin−orbit coupling (SOC) may not be important for tetrahedral Zn(II), but will certainly be needed for tetrahedral Co(II).[108]

Of course, the basis set also plays a role in the accuracy of computed properties. Here we will only make a few general remarks but refer the interested reader to an excellent series of previous works.[109−113] For polar compounds, and MOFs in particular, it is important to describe the localization of electrons and their polarization and diffusivity. To do so requires a basis set of "sufficient size", which refers to the minimum number of functions necessary to accurately describe the shape of the electron density. Basis functions themselves come in many forms, the most intuitive being "atom-centered",[109,114−116] which construct molecular orbitals or bands from some linear combination of atomic orbitals. In addition to inclusion of valence orbitals, other functions can be added to describe diffuse electron density far from the nuclei (useful for noncovalent interactions and anions) and electronic polarization (arising from chemical interactions between atoms with different electronegativities). The most common basis in solid-state calculations is a series of plane-waves,[117,118] which simulta-

https://dx.doi.org/10.1021/acs.chemrev.0c00148
Chem. Rev. 2020, 120, 8641−8715

neously enable the description of the bonding interactions within the unit cell while also enabling sampling of long-range interactions beyond the periodic boundary condition. The basic assumption for the remainder of this Review is that a sufficiently large basis set has been used to properly account for diffuse and polarized electron density.[119]

One further assumption for charge analysis and other postprocessing techniques is a preconverged wave function generated from a self-consistent field (SCF) routine,[120] i.e., for a given geometry, the electronic component of the Hamiltonian has reached the minimum value within a certain tolerance. This section will serve to detail several general considerations when applying electronic structure theory to MOFs, including functional and basis set selection (section 2.1), correctional terms (section 2.2), and charge and spin analyses (section 2.3).

2.1. Functional Selection

DFT is founded on the theorems of Hohenberg and Kohn, which purport that the energy of a chemical system is a direct function of the ground-state electron density.[121] In practice, the Kohn−Sham[122] formalism is used to construct the ground-state electron density of interacting electrons in a static external potential from density functions describing individual, non-interacting electrons. The main shortcoming of DFT, however, is that there is no known functional that satisfies the Hohenberg and Kohn theorem, and hence we are unable to compute the exact energy or ground-state density of a system. Instead, a range of available functionals exist that vary in their approximate treatment of the exchange-correlation term of the Hamiltonian (where exchange and correlation are purely quantum mechanical effects that can be thought of as a repulsive and attractive term, respectively); the challenge lies in identifying which functional provides the best electron density or energy for a particular chemical system based on the parameters considered during functional construction and the dominant physics present in the MOF. There is ongoing dialogue about the relative advantages of employing a functional parametrized to better approximate the "real" electron density, or "real" energy; however, there is room in electronic structure modeling for both philosophies.[123]

Within the DFT construct, functionals are divided into broad classes based on their treatment of the electron density gradient; this hierarchy of electronic structure approaches is sometimes referred to as Jacob's ladder, Figure 2.[124,125] The bottom rung of the ladder begins with the local (spin) density approximation (LDA, LSDA), which assumes a homogeneous distribution of electrons throughout the material. LDA functionals therefore are readily applied to metals, i.e., materials with nonzero density of states (DOS) at the Fermi level (E_F), such as bulk platinum. Some common LDA functionals include VWN[126] and PZ81.[127] However, it would be misguided to apply any variation of LDA to the subset of metallic MOFs[19,128−130] (e.g., $Ni_3(HITP)_2$),[84,85] despite their nonzero DOS at E_F. The electron density is not homogeneously distributed throughout the scaffold; the electron density on the Ni and N are vastly different and the bond will be improperly described.

Instead, the generalized gradient approximation (GGA)[131,132] and related methods are applied to systems with varying electron density (e.g., molecules, MOFs, inorganic clusters, etc.). GGA considers both the electron density and the gradient of the electron density when recovering energetic values and hence enables better descriptions of systems with inhomogeneous charge density, such as metal−organic hybrids. Familiar "pure"

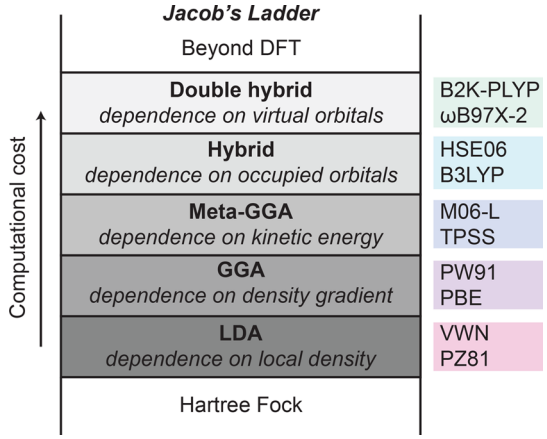

Figure 2. Jacob's ladder of functionals where accuracy increases with computational cost. Some common functionals corresponding with each rung are listed on the right.

GGA functionals include PBE[133] and PW91,[132] and these have been widely invoked in both the molecular and solid-state communities for both structure and derivative electronic property analysis.[134,135]

Still, the core shortcoming of all standard GGA approaches (and DFT approaches in general) is their inability to correctly describe both electron exchange and correlation;[136] a variety of more extravagant GGA methods combining progressively more complicated mathematics have been implemented in order to better describe these two key components of electronic structure theory. So-called meta-GGA functionals (such as M06-L[137] and TPSS[138]) historically invoke both the first and second derivative of the electron density to describe the system, while hybrid GGA functionals include some amount of exact electron exchange as computed with the Hartree−Fock exchange functional (HF). The GGA functional PBE, for example, becomes the hybrid functional PBE0[139] upon addition of 25% HF exchange. The same functional can have a screened potential added, becoming HSE06.[140] Conversely, the most ubiquitous hybrid GGA functional, B3LYP,[141] has components of exchange computed with HF, LDA/VWN, and GGA/B,[142] in addition to the exchange and correlation computed at the GGA/LYP[143] level.

Given the diverse library of functionals to choose from, it is unsurprising that both experimentalists and theorists can feel overwhelmed in the early stages of model construction. Indeed, the most common practice is to invoke a well-documented functional known to recover the appropriate electron density or energy for similar chemical systems. With this in mind, hybrid-GGA methods are widely viewed as the minimum level of theory necessary to describe the electronic structure of systems where exchange and correlation play a major role in the electronic structure. This is particularly pertinent in MOFs containing spin-polarized transition metals,[144] where exchange interactions not only play a leading role in the energy of the material, but also define the nature of the frontier orbitals/bands, as well as the band gap of semiconducting materials. In light of these considerations, by far the most common hybrid functionals used in MOF modeling are PBE0, HSE06, B3LYP, M06, and variations thereof,[145] despite their significant increase in computational demand.[146]

Rather than boldly sticking with one functional, systematic functional analyses may be performed to identify the optimal exchange-correlation treatment for each material or study. DFT

https://dx.doi.org/10.1021/acs.chemrev.0c00148
Chem. Rev. 2020, 120, 8641−8715

results can benchmarked to quantities derived from experiment or higher level ab initio calculations such as band gap energy,[147] ionization potential,[148] lattice parameters,[97] and formation enthalpies.[149] One study monitored the incorporation of bipyridine dicarboxylate (bipydc) linkers into UiO-67 (a MOF formally made from biphenyldicarboxylate, bpdc) by comparison of computed band gap and experimental lattice parameter contraction. There, they found excellent agreement between experimental lattice parameters and unit cells optimized with the PBE functional corrected for solids (PBEsol), Figure 3.[106] In the same study, the PBEsol[150] yielded

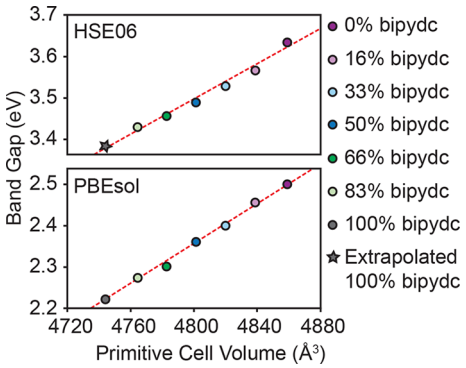

Figure 3. Linear correlation between computed electronic band gap and bipyridine dicarboxylate (bipydc) incorporation in Zr-UiO-67. The HSE06 (top) and PBEsol (bottom) functionals show qualitatively the same trend, but PBEsol consistently underestimates the band gap by ~1 eV. The gray star represents the extrapolated value derived from the best fit line to account for a computational limitation. Data obtained from ref 106.

consistently smaller band gaps than HSE06 (HSE06 was routinely greater by ~1 eV), but qualitatively comparable trends in electronic differences as a function of substitution are observed. A similar conclusion was reached in another study examining a larger selection of MOFs with an analogous metal and ligand chemistry, Figure 4.[149] The data in Figures 3 and 4 also highlight a common theme in the literature: GGA functionals tend to underestimate both the experimental and hybrid-computed band gap, and the addition of exact (HF) exchange is necessary to recover more realistic electronic band gaps.[151−153] In sum, assuming a sufficiently high-fidelity basis set, pure GGA functionals are the lowest level of theory required to provide a reasonable electronic description of most MOFs. However, the recovery of experimental semiconducting properties requires the incorporation of some exact exchange.

Sometimes, however, the disagreement between experiment and theory is more subtly hidden in poorly described interactions such as long-range dispersion; the addition of correctional terms can also help empirically tune a DFT output to match an experimental data set or simply add additional physics that may better describe the system. These additional Hamiltonian terms will be considered in the following subsections, as will eigenvalue alignment procedures that allow energetic comparisons between quantum mechanical simulations of chemically disparate MOFs.

2.2. Correctional Terms

Generally, computational chemists are more concerned with trends than quantitative relationships, but there are circumstances where it is nice to have both qualitative and quantitative predictive power such as obtaining both accurate lattice

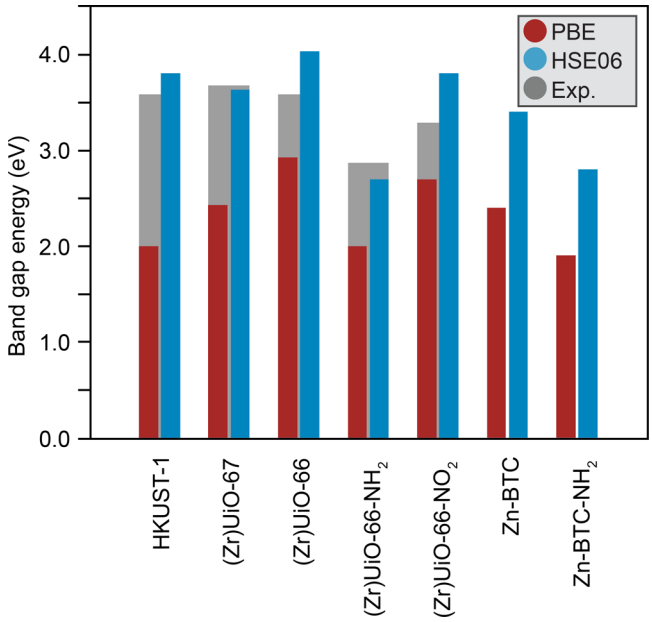

Figure 4. Computed electronic band gaps of HKUST-1, UiO-67, UiO-66, Zn-BTC, and linker functionalized derivatives. HSE06 systematically predicts larger band gap energies than PBE, more closely matching the experimental values. Data obtained from ref 149.

parameters and electronic band gaps. The exchange-correlation functionals discussed in section 2.1 are known to overdelocalize valence electrons and overstabilize metallic ground states, often resulting in differences between experiment and theory.[154] Correctional terms can mitigate this discrepancy, providing a route to accurately reproduce material properties.[97] However, correctional terms are somewhat empirical and invoke mixed opinions from theorists; they can help incorporate more accurate physics and interactions into a model, but this comes at the deficit of potentially overfitting parameters to a particular material. Here we discuss two of the common correction procedures, Grimme's dispersion corrections (section 2.2.1) and the Hubbard *U* model (section 2.2.2), which both feature tunable parameters.

2.2.1. Grimme's Dispersion Corrections. Both GGA and hybrid functionals tend to underestimate van der Waals forces that arise from long-range dispersive interactions.[155] Indeed, these forces play a critical role in the MOF field due to their significant impact on crystal packing and physisorption.[97] To mitigate this deficit, dispersion correctional terms may be incorporated with GGA and hybrid functionals. It should be noted that dispersion corrections may lead to "double-counting" correlation in strongly bound systems (i.e., unphysically high repulsion at short interatomic distances), therefore damping functions are included to counterbalance this effect.[156−160]

Grimme's dispersion methods, DFT-D2[161] and DFT-D3,[162] are commonly used to account for electronic dispersion; they provide an empirical correction to account for long-range Coulombic interactions otherwise unaccounted for in standard Kohn−Sham DFT.[163] DFT-D2 only accounts for interactions between all possible pairs of atoms in a material, while DFT-D3 also accounts for interactions across three atomic centers.[164] The various approaches to fitting the corrections parameters are well-documented,[165−167] and numerous methods are available to account for dispersion past the atom pairwise sum of

https://dx.doi.org/10.1021/acs.chemrev.0c00148
Chem. Rev. 2020, 120, 8641−8715

Coulombic potentials performed in DFT-D. Although these approaches are not common in MOF literature.[155]

There are countless examples of both D2 and D3 incorporation in MOF modeling; here we select a handful that are particularly pedagogical. Remembering that one primary reason for the inclusion of dispersion corrections is to more accurately recover *geometric structure* (which directly influences the subsequent electronic structure), the application of these corrections may be inspired by both structure and electronics. For example, drastic temperature-dependent phase transformations from narrow to large pore topologies in the "wine rack" MOFs (e.g., MIL-53)[168,169] are stabilized by dispersion at low temperatures and entropic effects at high temperatures.[170] One study theoretically examined dispersion interactions to identify methodologies that replicate pore volumes in flexible frameworks.[170] PBE-D3 with Becke−Johnson damping and Axilrod−Teller−Muto (a three-body damping term) corrections showed the best match with experimental structure data.[171,172] This computational methodology was also effective in generating adsorption isotherms of methane on Zr-based MOFs,[173] albeit at the cost of a significant increase in computational time due to inclusion of additional CH_4 molecules.[174,175]

From an electronic perspective, the structure determines the energies of the electrons. In a report by Zhao, Wang, and colleagues, a mixed-valent Cu(I)−Cu(II) MOF was presented for photocatalytic hydrogen evolution.[176] There, the PBEsol-D2 approach was used to recover an accurate geometric structure. The HSE06 functional was then used to obtain reliable MOF redox potentials, thus rationalizing their catalytic observations. Similarly, PBEsol-D3 was applied in a study focused on elucidating the effect of hydroxamate groups as alternative MOF connecting motifs on photocatalytic performance.[177] There, dispersion corrections were used to improve the description of the metal−ligand interfacial geometry.

These examples point to a more general theme, though; structure is paramount in determining electron energetics, and electron energetics are paramount for applications where objective comparisons of electron energies are used to understand reactivity and stability. As a result, dispersion corrections are advantageous because DFT may struggle to describe systems whose chemistry is dominated by weak secondary interactions.

2.2.2. Hubbard *U* Correction. There is an erroneous self-interaction of electrons in DFT that stems, in part, from constructing the energy functional using single-particle spin densities.[178,179] Resultantly, two-body Coulomb interactions between different electrons and self-interactions become indistinguishable, causing artificial stabilization of delocalized states.[180] This effect is most evident in strongly correlated systems such as those with unpaired electrons and localized *d*- and *f*-electrons.[154] The exchange-correlation components of functionals attempt to account for the self-interaction error themselves, yet the energy may still be poorly approximated.[181] One correction is to introduce a Hubbard *U* term on specific atomic components; the procedure is generally referred to as DFT+*U*.[182]

The *U* term accounts for possible repulsive forces between atomic centers, which become relevant when changes in oxidation and spin state, and reagent binding may be important.[183−187] In essence, the Hubbard *U* correction is an attempt to account for the localization of electrons from Columbic interactions,[188−193] which GGA and LDA functionals often fail to properly describe.[194] The Hubbard correction is typically associated with correlation, yet it can also explicitly account for onsite exchange, *J*.[195] Though generally, the effective Hubbard *U* correction, U_{eff}, is employed,

$$U_{eff} = U + J \tag{2.1}$$

such that U_{eff} is functional and basis set dependent, and these terms are not separated.[196] The value of U_{eff} can be recovered in several ways, including semiempirically tuning the value to fit an experimental observable such as band gap.[154] The use of *U* or U_{eff} is often ambiguous in literature, yet incorporation in the Hamiltonian is identical; the inclusion of *J* can be implicit; empirically tuned values would expectedly incorporate onsite exchange, while this value may not be explicitly cited or known.

The transferability of the *U* parameter depends on the similarity between chemical systems. *U* = 4 eV, for example, known to provide a realistic description for transition metals in oxygen environments,[197] was invoked to appropriately account for charge transfer when studying the oxidation of $Co_3(NDC)_3DMF_4$ (NDC = 2,6-naphthalendicarboxylic acid) by I_2.[198] However, the addition of a *U* term is largely empirical and hence may accurately recover one electronic property at the sacrifice of another.[199] More robustly, *U* may be resolved from self-consistent ab initio calculations[200] by the linear response approach. In doing so, *U* is effectively determined by the difference between the bare and screened second derivative of total energy as a function of atomic occupancies[201] and may even be computed using the self-consistent DFT + *U* procedure.[202]

The linear response method of recovering ab initio U_{eff} values was invoked to study CO_2 binding with M-MOF-74 (M = Mg, Ti, V, Cr, Mn, Fe, Co, Ni, Cu, and Zn) in order to obtain a reliable description of localized *d*-states in the transition metals.[186] The calculated values of U_{eff} ranged from 10.4 eV for Cu to 4.0 eV for V, effectively highlighting the importance of deriving individual values for systems of interest; these values were also consistently greater than empirically derived parameters for the inorganic metal oxides (likely due to differences in ligand field strength).[203] Yet, Co-MOF-74 can be used as a representative example of how large changes in U_{eff} may still correspond to small differences in small molecule binding energies. Over the range 0−5.4 eV, lattice parameters and CO_2 binding energies were found to monotonically increase, yet good agreement between theoretical and experimental lattice parameters was found between 2 and 5 eV and the overall increase in binding energy was only ∼1 kcal/mol. For reference, U_{eff} was found to be 5.3 eV with the linear response method. Still, the CO_2 binding energies computed with the ab initio U_{eff} corrections showed superior agreement with experimental binding energies over empirically determined parameters.

Similar to the inclusion of HF exchange, addition of a Hubbard *U* parameter to the electron−electron interaction energy can improve the agreement between theoretical and experimental band gap values.[204] However, rather than universally, the *U* correction is atomistically applied. The relative performance of *U* corrections and hybrid functionals compared across a host of semiconductors and metal oxides found that application of the *U* correction to *only* the metal valence *d*-orbitals yielded more realistic band gap energies than when the *U* correction was applied to both the metal and nonmetal atoms.[204] Band gaps of open shell metal oxides were always improved using such *U* corrections. Results were

https://dx.doi.org/10.1021/acs.chemrev.0c00148
Chem. Rev. 2020, 120, 8641−8715

comparable to hybrid functionals, suggesting U corrections may be an adequate alternative to the more computationally intensive hybrid counterparts for this system.

It is by no means gospel that the addition of a U term can replace the electronics obtained using hybrid functionals. The U parameter magnitude massively impacts the electronic band gap, as seen by increasing the value of the Hubbard U parameter from 0 to 4 eV, which causes massive perturbations to the band diagram of $Fe_3(HTB)_2$ (HTB = hexathiolbenzene, Figure 5).[205]

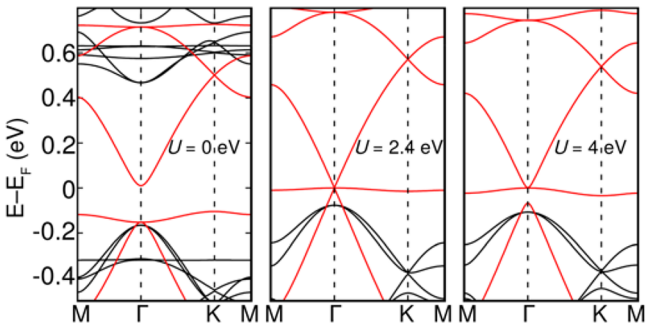

Figure 5. Fermi-aligned electronic band structures for $Fe_3(HTB)_2$ calculated with PBE + U. Increasing values for the Hubbard U parameter significantly perturb the frontier electronic states associated with the square planar Fe(II) atom. Reproduced with permission from ref 205. Copyright 2019 Springer Nature Limited under CC BY 4.0, https://creativecommons.org/licenses/by/4.0/.

In a separate study, band gaps computed with PBE+U and HSE06 were compared, Figure 6.[206] Spin polarized calculations were performed to account for the open shell character of the Cu(II)-3d^9 shells and antiferromagnetic coupling between

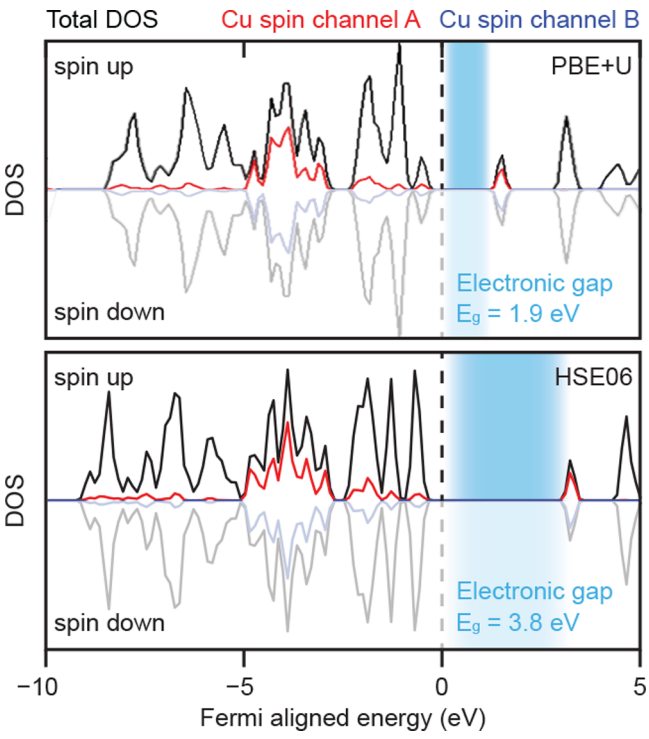

Figure 6. Comparison of density of states (DOS) of HKUST-1 obtained with DFT + U and HSE06. Both functionals produced similar DOS, however, hybrid/HSE06 yielded a larger band gap than DFT + U. Adapted with permission from ref 206. Copyright 2015 AIP Publishing.

geminal metals were described using the broken symmetry approach.[207] Although the DOS profiles constructed with each approach were very similar, the band gap at Γ estimated by PBE + U (U = 5 eV for the Cu 3d electrons) is approximately half of that estimated by the HSE06 functional.

With regards to band gap underestimation, systems whose band gaps are poorly recovered by functionals that exclude HF exchange may be subject to a mixed theory or postprocessing strategy sometimes referred to as the "scissor operation".[208] In effect, the procedure is a rigid shift of the computed conduction band energetics to either match experiment or higher levels of theory. The approach itself is predicated on the rigid band model; most bands in materials do not significantly change shape as a function of functional.[209,210] Thus, a rigid shift is applied to the conduction band minimum (CBM) computed using pure GGA such that it is aligned to the CBM obtained from a hybrid functional or experimental measurement.[211] This strategy was invoked for DOS plots constructed to study the locality of photogenerated electrons and holes in Fe substituted Al/Zn porphyrinic MOFs as a function of metal location, identity, and coordination sphere.[212] PBE + U was employed but HSE06 recovered a wider band gap; the band edges of the PBE + U band structure were thus aligned according to the hybrid band gap energy. Partial substitution of Al with Fe was found to provide the optimal band gap to encompass the appropriate electrode potentials for oxygen evolution and hydrogen evolution reactions.[212] Generally speaking, the scissor operation is less favorable than more involved corrections because it lacks any predictive capabilities and is instead invoked only to make band gaps appear to be quantitatively recovered.

In sum, dispersion corrections like the Grimme methodologies have been found to effectively recover both the structure of systems with weak long-range or secondary bonding interactions like redox coupling and π-interactions lost by the spatial restrictions necessarily applied to the complex functions and an enhanced electronic description of semiconducting properties. The Hubbard U correction offers a more targeted approach that has also demonstrated the capability to overcome DFT approximations.

2.3. Computational Ionization Potentials

Beyond the electronic band gap, another fundamental chemical property that provides insight into MOF utility is the ionization potential. Unlike energetics obtained using molecular models paired with Koopmans'[213] or Janak's[214] theorems (which essentially state that the eigenvalue associated with the highest energy electron is equal to the ionization potential, Figure 7a), the eigenvalues of the highest occupied band in solid-state calculations cannot be directly used as approximates for the ionization potential of the material. Eigenvalues recovered from molecular modeling software are intrinsically referenced to the electrostatic potential of 0 eV, i.e., vacuum, because no spatial limitation is applied to the decay of the electric field. On the other hand, solid-state models include a system-dependent uniform background potential that augments eigenvalues. Models that invoke periodic boundary conditions require the addition of a background potential in order to dampen the effects of propagating a unit cell with a nonzero electric field. The Vienna ab initio Software Package (VASP),[118,215−217] an example of a common solid-state software package, reports band energies with respect to the average potential of the unit cell, rigidly altering energetic eigenvalues based on system-dependent chemical potentials.

https://dx.doi.org/10.1021/acs.chemrev.0c00148
Chem. Rev. 2020, 120, 8641−8715

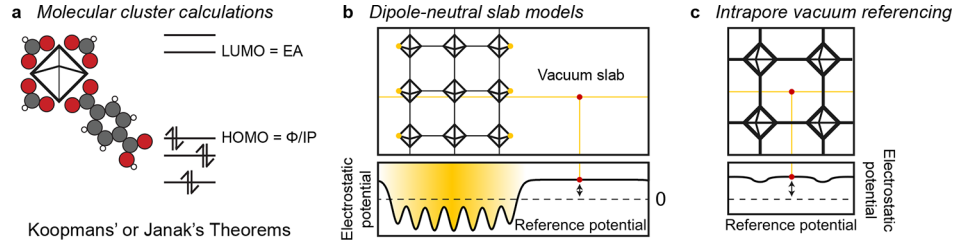

Figure 7. A comparison of vacuum alignment approaches to recover the ionization potential of materials. (a) A molecular subcomponent of the MOF is cleaved and the ionization potential of the bulk is estimated from the HOMO energy obtained in molecular modeling packages. (b) Using a "slab" model, a dipole neutral surface is cleaved and the reference potential is obtained in the vacuous space. (c) Using the internal vacuum within MOFs enables a dipole-free recovery of the work function.

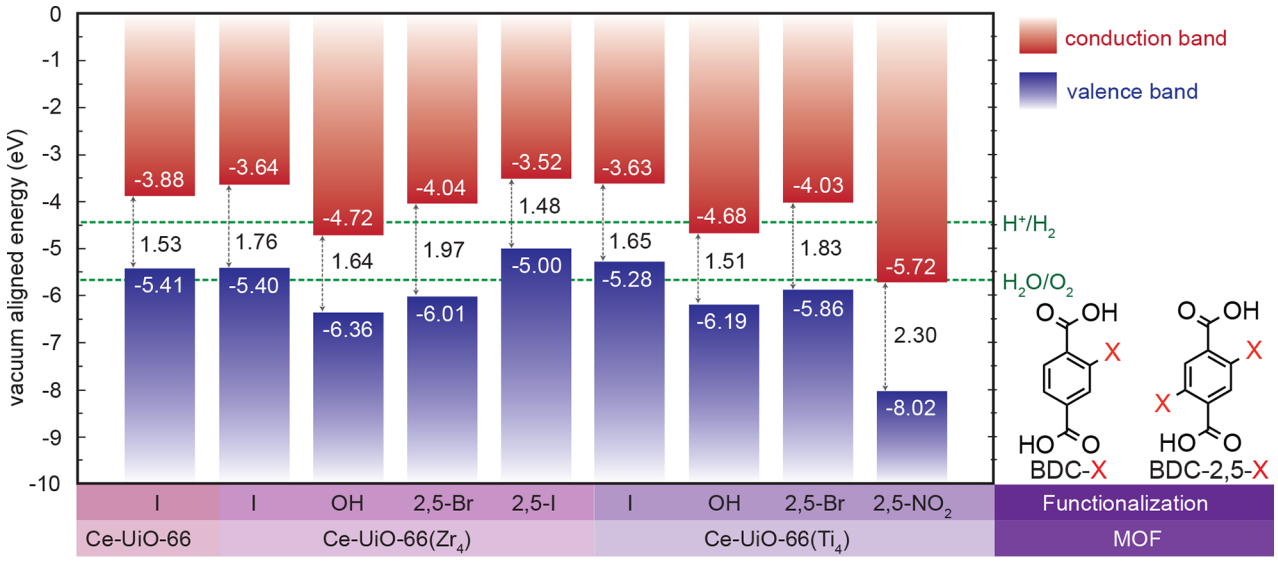

Figure 8. Linker functionalization in cerium containing variants of UiO-66 was shown to modulate the oxidative and reductive band-edge potentials giving access to a MOF that is capable of bother the hydrogen evolution and oxygen evolution reactions. Other redox potentials can then be coaligned. Adapted with permission from ref 222. Copyright 2018 American Chemical Society.

In principle, if every atom in a discrete MOF particle was modeled in molecular software packages, then the ionization potential could be recovered from a single SCF procedure. Unfortunately, the electron count would make the calculation impossible. Further, the chemistry of crystallite termination is often unknown. There are obvious advantages to simulating the bulk of a MOF by invoking periodic boundary conditions; however, the consequence of this approach is that the eigenvalues recovered from periodic DFT are not referenced to an internal standard of 0 eV. Quantitative comparison between DFT results obtained for systems with any difference in chemical potential (even something as simple as the addition of a H atom) must be referenced in some way, e.g., to the background potential or an empirical value such as an experimental potential or work function.[147] Alternatively, one could truncate the MOF to some representative molecule and perform a molecular calculation on the fragment (section 3), but thorough benchmarking is necessary to ensure the model is sufficient.

The simplest approach to compare differences in electron energetics of periodic systems is to align the energy axis to the Fermi level.[128,218−221] However, the Fermi-aligned approach is not overly helpful in most cases because it does not unequivocally separate whether the chemical perturbation affected the valence or conduction band energies. For example, it is not immediately clear whether the addition of an amino group added to a BDC will destabilize the valence, or stabilize the conductions bands, and Fermi level alignment does not conclusively answer that question.[222] This however can be answered if the scaffold is aligned to the vacuum level.

While there are countless alignments one could chose (e.g., the standard hydrogen electrode, the Ag/AgCl potential, etc.), by far the most convenient is alignment to the vacuum level via the background potential. In conventional solid-state modeling, i.e., purely inorganic crystalline materials, the typical approach for recovering the background potential energy is to define a crystallographic surface by including enough empty volume in the unit cell for the electrostatic potential to plateau to a constant value; the plateaued potential indicates the region of the unit cell where the potential is solely defined by the uniform background potential and therefore equal in value.[223] This potential can then be deducted from all eigenvalues to obtain their value with respect to a potential that represents vacuum, Figure 7.

Critically, the surface cleavage approach comes with three main challenges: (i) the surface must be dipole neutral to recover a nonvarying potential in the vacuum region of the cell,[223] Figure 7b, (ii) formation of crystallographic surface induces restructuring of the surface,[224] and (iii) the large requisite slab models make computational procedures quite time-consuming. Zhao and colleagues managed to account for all of these effects by resolving the surface of an unsaturated Ni/

https://dx.doi.org/10.1021/acs.chemrev.0c00148
Chem. Rev. 2020, 120, 8641−8715

Co bimetallic MOF nanosheet.[225] Crystal morphology was experimentally studied using both ex situ and in situ X-ray absorption spectroscopy (XAS) to determine the nature of the dominant exposed surface facet, and TEM measurements were matched to theoretical lattice parameters. Extended X-ray absorption fine structure (EXAFS) data was used to match model thickness and determine the nature of coordinatively unsaturated surface sites. K-edge X-ray absorption near edge spectroscopy (XANES) was performed for each heavy element to further corroborate the nature of coordinatively unsaturated surface sites. The surface model was then created by replicating the coordination number and oxidation states of surface sites deduced from this barrage of experimental methods and comparing the relative stabilities of each model. Clearly, this is an intensive and dedicated process but is also one that is somewhat misaligned with the general application and design of MOFs; synthetic groups, in particular those who examine catalysis in MOFs, invoke that catalysis is happening *within* the MOF at atomically precise sites in the bulk. Hence, it is *not* the surface of the crystal that is necessarily understood but rather the electronic structure of the material viewed from within the pores.

Conveniently, although it is difficult to describe the nature of a crystallite surface, the high symmetry of MOFs complimented by their large pores often yield a sufficient internal volume to identify the background potential, enabling a vacuum alignment from within, Figure 7c.[148] Indeed, this method is robust for pore diameters greater than 5 Å and enables powerful predictive capabilities for redox active catalytic MOFs[226] that will be discussed further in section 5. Illustratively, this alignment approach enabled the screening of linker functional groups in Ce-containing MOFs for the photocatalytic water-splitting reaction, Figure 8.[222,227] The solid-state application of Janak's theorem is achieved by subtracting the electrostatic potential of the pore from the valence band eigenvalues. In doing so, the valence band maximum (VBM) and CBM can be aligned to the vacuum level, granting access to direct comparison with other reaction potentials such as water oxidation and hydrogen reduction. Conduction band edges above the reduction potential of the acceptor and valence band edges below the oxidation potential of the donor indicate that, under the ideal model conditions, the desired electron transfer processes should be achieved upon irradiation. Indeed, many systemic DFT studies on MOFs center around the effect of metal identity on bulk properties such as the band gap and band edges.[212,228−230]

In sum, the confines of a unit cell coupled with the self-consistent nature of DFT yields arbitrary eigenvalues if the internal energy is not referenced to a known potential. Unreferenced energies limit energetic comparisons to MOFs with identical chemical potentials (i.e., compositions). At minimum, Fermi-aligned potentials enable comparison of relative internal energy gaps, however, vacuum-aligned electron energies enable the screening of materials for semiconducting applications.

2.4. Charge and Spin Densities

Previous sections were generally concerned with the computation of electron potentials, another critical outcome of electronic structure modeling is identifying where in the crystal these electrons are localized. Spin density, and more generally charge density, are useful parameters that enable quantitative analysis of electron density throughout chemical systems. While we will present a brief overview of this concept and its application to MOF modeling, we point the more interested reader to reviews that discuss the topic in-depth.[13,187] Here we examine the partitioning schemes employed to assign an identity and parentage to charge density in chemically interacting systems to highlight the utility of the familiar approaches (Mulliken, Bader, and Natural Bond Orbital (NBO) analyses, as well as Charge Model 5) and their application to MOFs.

2.4.1. Spin Polarization. In the simplest closed-shell (or restricted) implementation of DFT, electrons are assumed to be fully paired. Unless otherwise stipulated, electronic spins are forced to be collinear, i.e., either "up" or "down". Obviously this poses problems when modeling materials featuring components with uneven numbers of electrons.[231] Indeed, many MOFs contain unpaired electrons hosted on transition metals, and these systems require a spin-polarized approach that effectively doubles the size of the Slater determinant (and hence the computation time). All conventional modeling packages offer an input setting to enable spin-polarization, which can of course be applied to systems that inevitably converge to closed-shell structures.

Locally, transition metal nodes in MOFs exhibit *d*-orbital splitting analogous to that observed in small molecule chemistry. The extent of this splitting depends on the ligand field created by the linker, hence the linker is also responsible for determining the magnetic properties of the MOF. In principle, all spin states should be possible, assuming synthetic chemists can design linkers with sufficiently small fields. Electrons in *d*-orbitals are highly sensitive to ligand geometry, and there is at least one example of a temperature-induced spin-transition in an Fe-containing MOF,[232] Figure 9. Transitions from spin-paired to spin-polarized commonly cause modeler headaches, and it can be extremely helpful to have some prior estimate of the spin state from experiment (using techniques such as magnetometry, EPR or Mössbauer spectroscopy). In the absence of experimental characterization of the oxidation and spin state, it is important to examine all possible spin orientations for systems containing atoms other than d^0 and d^{10} metals or radical linkers. The simplest and most robust approach to elucidating the spin-state of a material with DFT is to rigorously sample all electronic orientations and compare the total energies; the lower energy structure corresponds to the ground state.[233,234]

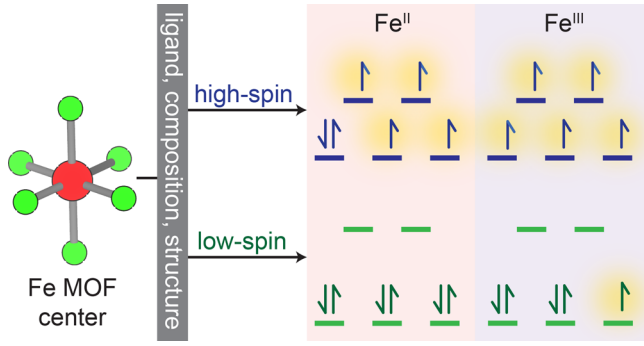

Figure 9. Transition metal *d*-orbitals split in the presence of ligand electric fields. The extent of splitting dictates the spin state of the metals and, owing to the diversity of ligands available, both high and low spin Fe(II)[235−237] and high spin Fe(III)[238,239] are known. Low spin Fe(III) is observed if a sufficiently large ligand field is used to construct the MOF.[240]

As a direct consequence of building materials from transition metals, unpaired metal-centered electrons may engage in weak magnetic coupling. While their ordered magnetic interactions

https://dx.doi.org/10.1021/acs.chemrev.0c00148
Chem. Rev. 2020, 120, 8641−8715

are temperature dependent, and almost all MOFs are disordered at room temperature,[241−245] the electronic configuration has a major impact on the computed DOS and band gap in static DFT. Spin-structure is extremely sensitive to chemical geometry (e.g., bond length), thus given static DFT is effectively temperature independent, the relative stability of magnetic ordering obtained through such models may not be indicative of the magnetic ground state at room temperature. Indeed, the weak magnetic coupling associated with MOFs yields low Curie temperatures (temperature of magnetic ordering <200 K).[218,241] Strongly coupled magnetic systems are attractive for power transfer applications, but direct magnetic exchange requires overlap between the electronic wave functions of two magnetic sites and MOFs are typically low-density materials. For example, while the Cu−Cu dimer in HKUST-1 is antiferromagnetically coupled, longer range paddlewheel-to-paddlewheel internode distances exceed 8 Å, far too long-range for any appreciable magnetic ordering.[246]

To assess the strength of interactions between spin-active centers, the coupling constant (J) between neighboring centers can be recovered either by invoking spin Hamiltonians such as the Ising and Heisenberg−Dirac-van Vleck models[247−250] or the broken symmetry approach, which invokes a spin-polarized formalism and constructs a broken symmetry solution for the low-spin state.[251] Broken symmetry states are not pure spin states but rather mixtures of the low- and high-spin states.[252] The broken symmetry approach recovers J by constructing a state of mixed spin symmetry (and reduced spatial symmetry) and a reference pure spin state to evaluate the extent and phase of interactions.[207,253−255] If $J > 0$, ferromagnetic pairing of spins is favorable, if $J < 0$ antiferromagnetic spin coupling is favorable, and if $J = 0$ neighboring spins are noninteracting.[256]

Truly disordered paramagnetic behavior is difficult to account for, Figure 10. Although modeling disordered spin provides little insight into chemical systems, there are certainly circumstances where unpaired electron spins align off-axis, i.e., noncollinear spins, a phenomenon induced by SOC.[257] While SOC effects may break the degeneracy of one-electron energy levels, they are typically eclipsed by the magnitude of other electronic interactions and therefore provide only a negligible contribution to the electronic structure.[258] Indeed, SOC greatly increases computational cost. Thus, SOC effects have largely been reserved to study exotic magnetic properties such as the quantum spin hall effects found in MOF-based Kagome lattices.[259,260] SOC should likely be applied to systems containing Co(II)[261] or heavy metals, however this is infrequently performed in literature.

Unless we know otherwise, spin-polarized MOFs are generally first modeled as ferromagnets. A comparison of fully geometrically equilibrated ferro- and antiferromagnetic structures are required to assign the ground-state spin structure. Furthermore, resources often limited modelers to one computational cell: this poses a challenge when modeling materials whose magnetic ordering permeates further than one cell or for cells containing an odd number of metal ions. In other words, it is *always possible* to model a spin-polarized system in a ferromagnetic form, but it is not always possible to model it either noncollinearly or antiferromagnetically. To be clear, the shortcoming in treating noncollinearity, and magnetism in general, is not related to the theory itself, but rather the system size; given unlimited resources SOC could (theoretically) be applied to MOF supercells as necessary to describe off-axis spin-disorder.

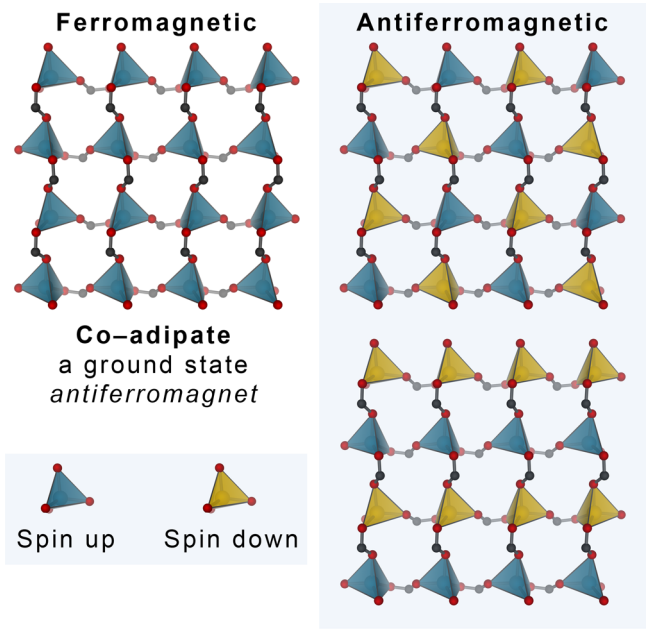

Figure 10. While there are a multitude of electronic configurations available in spin-polarized MOFs, generally the MOF is either modeled as a ground state antiferromagnet or ferromagnet. Shown is the 2D plane of carboxylate-bridged Co in Co(adipate), a ground-state antiferromagnet with magnetic ordering shown in the top right. Data obtained from ref 262.

In sum, MOFs featuring open-shell chemistry require spin-polarized computations to account for the unpaired electrons. The locality and concentration of spin and, more broadly, charge density throughout a MOF has implications for charge transport (where charge should be delocalized),[263] as well as catalytic and luminescent applications (where charge should be localized).[264] To deduce the magnitude and density of atomistic charges, partitioning schemes must be applied to assign electron density from bonding areas to distinct nuclei (section 2.4.2).

2.4.2. Charge and Spin Analysis. Spin analyses, which specifically examine the locality and energy of *unpaired* electrons, are made possible by the general methods that examine the charge density (i.e., electron density). Charge analyses reveal the spatial concentration of charges within chemical systems, providing critical insight into oxidation states, extent of charge delocalization across dissimilar components of a material, as well as charge transfer events, etc. Either spatial or relative electron density partitioning schemes are applied to charge densities extracted from standard self-consistent field procedures; however, considering charge density is a continuous function of position, its partitioning in a bonded material is an inherently qualitative task. Most methods based on rigid cutoffs for atomic radii fail in the presence of strongly ionic or highly covalent bonding where their approximations break down.[265,266] Nevertheless, the electronic insight afforded by charge analyses is continuously valuable for materials development, such as tuning interaction strengths between lattice components and adsorbates[267] or providing a measure of Lewis acidity to refine catalytic performance;[268] even with systematic errors, relative trends can be elucidated by comparing the change in charge density of different components in the material.

Mulliken Analysis: Mulliken charges arise from Mulliken population analysis; this orbital-based protocol deconstructs the electronic population surrounding a nucleus into atomic orbitals

https://dx.doi.org/10.1021/acs.chemrev.0c00148
Chem. Rev. 2020, 120, 8641−8715

and overlap populations.[269] Effectively, the charge associated with each atom, and the density shared between atoms, are found by projecting the wave function onto an atomic-centered basis set. Naturally, Mulliken charge analysis is very efficient for highly ionic species, where the electron density is highly localized in certain regions in the crystal.

Mulliken charges obtained using the CHelpG method have been shown to be reliable for determining electrostatic potential charges.[270] Li and colleagues applied this pairing to assess changes in charge density on the heteroatoms of the fluorescent ligands in BUT-12 and BUT-13 with and without methyl substituents.[271] The analysis revealed that the methyl groups increased electron density at the carboxyl oxygen atoms, thus increasing the strength of Zr−O bonds and presumably hydrolytic stability, necessary for the detection and removal of antibiotics and organic explosives from water.

In another example by Farha, Hupp, Gagliardi, Cramer, and colleagues, Mulliken densities were used to evaluate the extent of spin delocalization in cobalt species deposited on NU-1000 as a function of oxidation state.[272] The authors aimed to compare activation barriers for competing radical processes during the oxidative dehydrogenation of propane to propene. Exploring oxidation states from Co(IV) to Co(II), a quartet Co(III) center with an accompanying oxo-radical was identified as the lowest energy spin-state, consistent with experimental XANES spectra of the activated system, Figure 11. The rate-determining step

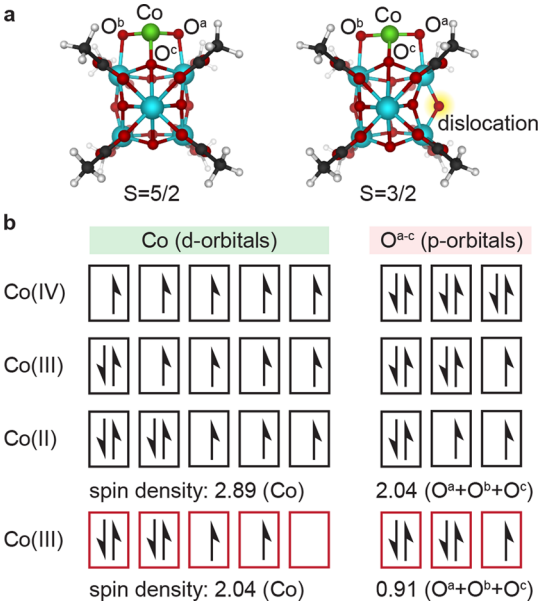

Figure 11. Spin density localization can be computed quantitatively with partitioning schemes such as Mullliken analysis to elucidate spin-configuration of delocalized systems. Here, various oxidation states of Co grafted to the node of NU-1000 were examined, the lowest energy configuration is presented in red. Adapted with permission from ref 272. Copyright 2016 American Chemical Society.

was found to be mediated by a radical base,[272] prompting a follow-up study that also invoked Mulliken spins but to assess how promoter ion Lewis acidity affects the nature and activity of Co active sites.[273]

Charge Model 5: Charge Model 5 (CM5)[274] derives partial atomic charges from Hirshfeld population analysis and is also capable of recovering both spin and charge density. Unlike Mulliken analysis, which recovers charges from partitioning with the basis set, Hirshfeld analysis relies on the separation of the electron density in real space.[275] Hirshfeld populations are derived through electron density perturbation by comparing (i) the ground state free atom, (ii) molecular electron density, and (iii) "pro-molecule" electron density, which is the electron density of free atom electron clouds centered at the DFT optimized atomic positions (i.e., the atomic electron density associated with, but unperturbed by, the crystallographic arrangement).

CM5 was applied to assess the effect of appending Ni(II) olefin oligomerization catalysts to the NU-1000 node decorated with electron-withdrawing chelating ligands.[276] To achieve higher resolution charge density gradients, a single point calculation was performed with a larger basis set. Experimentally, selectivity for C_4 products increased with chelate inclusion; mechanistic analysis showed increased activation barriers for C−C coupling and thermodynamic favorability of 1-butene release. The CM5 analysis revealed charge density reduction from both the linker oxygens and zirconium with a concomitant increase in charge associated with oxygen atoms that correlated with the electron withdrawing ability of the added node ligands ($(OH)_4(H_2O)_4$ < $(acac)_4$ < $(Facac)_4$, where acac = acetylacetone; Facac = hexafluoroacetylacetone); the authors rationalize that increased Lewis acidity as well as ligand reorganization modulates the catalytic cycle.

In a separate study, CM5 was implemented in the study of Fe(II) adsorption sites in MIL-100, −101, and −808 that catalyze the oxidation of alkanes to alcohols.[277] The reactivity of each framework toward oxygenation (formation of Fe(IV)═O from Fe(II) with N_2O as the oxidant) correlated with the partial charge on the central oxygen of the inorganic cluster, Figure 12. The spin densities of the Fe(IV)═O species in all frameworks were within tenths of an electron of each other and their differences were deemed neglibile, independent of the crystal connectivity and composition.

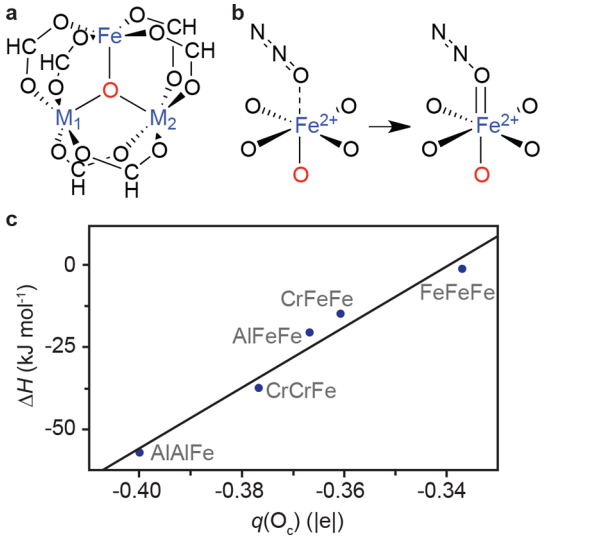

Figure 12. (a) Cluster model for the node of MIL-100 capped using six formate groups for the study of the hydroxylation of ethane to ethanol and methane to methanol. (b) The conversion of divalent Fe(II) species to Fe(IV)═O species by N_2O. (c) Reaction enthalpy (for b) vs the charge of the central oxygen of the cluster (Label in red in all structures. All metal ions are in blue, M1 and M2 can be Fe, Al, or Cr). Adapted with permission from ref 277. Copyright 2019 American Chemical Society.

https://dx.doi.org/10.1021/acs.chemrev.0c00148
Chem. Rev. 2020, 120, 8641−8715

Bader Charge Analysis: The Bader analysis is based on the quantum theory of atoms in molecules[278−281] and is one of the more popular methods because it does not apply a rigid radius for all atoms and therefore recovers system-dependent atomic volumes.[282−296] Its success is, in part, attributed to the availability of open-source postprocessing packages that read standard DFT outputs. The Bader volumes, i.e., the regions of density assigned to each atom are apportioned using zero flux surfaces in the electron density gradients.[280] The modern Bader method uses a grid-based numerical algorithm to track electron density gradients in DFT-generated charge densities.[297−300] A variety of different grid methods have been developed to identify the zero flux gradients;[299−301] the on-grid method is presented in Figure 13. Conveniently, postprocessing tools exist for the implementation of Bader charge analysis on both periodic[302] and molecular (cluster) systems.[301]

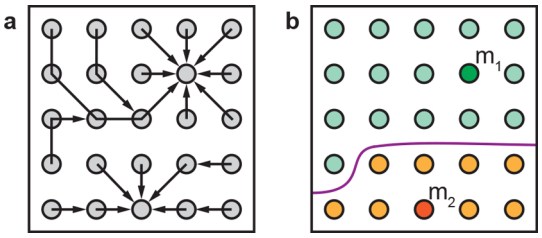

Figure 13. An illustration of the steepest ascent paths (a) on a charge density grid to find the Bader volumes using the on-grid analysis method. The ascent trajectories are constrained to the grid points, moving at each step to the neighboring grid points toward which the charge density gradient is maximized. Each trajectory either terminates at a new charge density maximum, or at a grid point which has already been assigned (b) the Bader volume is then created by collecting all grid points assigned to a corresponding maximum (m_1 and m_2) separated by Bader surfaces (purple curved line). Image created with the artistic guidance of G. Henkelman.[299]

Among the countless examples of Bader analysis applied to MOFs,[295,303−306] we highlight perhaps the most obvious case: monitoring the change in charge density with chemical functionalization. Bader analysis provided an electronic handle to monitor the change in charge density of pendant hydroxides in an $InO_4(OH)_2$ cluster in MIL-68(In). This MOF was reported to catalyze the conversion of CO_2 and epoxides. The reaction mechanism is known to proceed by CO_2 activation via adsorption at these basic sites and changes in the Lewis basicity of the −OH directly augment the rate and selectivity of the transformation. After NH_2 functionalization, Bader charge analysis of the OH indicated an increased O charge density, which was then used to rationalize the increase in rate of cyclic carbonate formation.[307]

The same Bader procedure was used to monitor O_2 reduction at coordinatively unsaturated metal sites in a family of structurally similar MOFs.[308] The relative redox activity of the open metal sites as a function of (i) linker functionalization, (ii) anion exchange of bridging ligands, and (iii) changes in the formal oxidation state of the metal center. The relative propensity for O_2 reduction was quantified by comparing the Bader charge on the oxygens of O_2 adsorbed to each MOF with that of the oxygen atoms in H_2O_2, H_2O, and free O_2. Selective binding of O_2 over N_2 was identified for all MOFs, except those containing V(II).

In essence, Bader charge analysis is a measure of relative orbital localization. It is therefore helpful in identifying the oxidation states of metal centers and may provide a better description of delocalized systems than the preceding methods.

Natural Bond Orbital (NBO) Analysis: Contrary to Mulliken (rigid radii) and Bader (system dependent radii) analyses, natural population analysis (NPA) considers the electron density distribution of a system by constructing its own orthonormal natural atomic orbitals (NAOs) directly from the density matrix.[309] Natural orbitals are required to be orthonormal and have maximum occupancy to acquire compact expressions for atomic and bond properties.[310] NAOs differ from standard atomic orbitals (AOs) because their spatial diffuseness is optimized for their electronic environment (e.g., orbitals are contracted in cationic regions and expanded if a region is more anionic). Local inhomogeneity in charge is thus accounted for without the use of multiple additional basis functions and eliminates the basis set dependence of Mulliken and Hirschfeld population analysis methods.[269]

Building off this approach, NAOs can be used to construct so-called natural bond orbitals (NBOs). NBOs are localized electron pair orbitals for bonding and lone pairs (as well as their corresponding antibonding states); as such, these orbitals lie between AOs, obviously localized on atoms, and molecular orbitals (MOs), delocalized over the whole molecule.[310] Thus, NBOs have the advantage of aligning with Lewis structure bonding patterns that are the typical qualitative understanding of bonding.[311] These orbital sets are constructed from a series of transformations from the input basis set; first to NAOs, then natural hybrid orbitals, which construct the NBOs.[311,312] This series of transformations can be helpful in understanding backbonding,[313] charge transfer,[314] H-bonding and van der Waals complexes,[310] hyperconjugation,[315] and other general intermolecular interactions. While originally employed for molecular systems, NBO analysis has been extended to plane-wave DFT for periodic systems.[316]

While NBO is a partitioning scheme generally used to examine bonding patterns, it is also a useful method to elucidate local charge effects. For instance, the Lewis acidity of open metal sites was investigated with NBO charge calculations on cluster models to develop an understanding of catalytic transformations in $Cu_2(BTC)_3$ and CuMIPT (MIPT = 5-methylisophthalate).[317] A larger reduction in NBO charge on copper upon CO binding was observed for $Cu_2(BTC)_3$, indicating that CuMIPT is not as Lewis acidic. Either the reduction in symmetry or loss of the weak activating group diminished the electron donating ability of carboxylates in CuMIPT. A separate study used atomic charges from NBO to understand the different catalytic reactivity of square planar Cu(II) centers in oxygen and nitrogen environments toward 1,3-dipolar cycloaddition or "click" reactions.[318] Each MOF showed nearly identical Cu charge densities yet MOFs with CuN_4 demonstrated superior activity to CuO_4-containing MOFs. The authors suggested that changes in reactivity could be attributed to the ligand field and the donor atoms' propensity to H-bond. CuO_4 has a stronger affinity for water and showed the longest catalytic induction period.

In summary, numerous charge partitioning procedures are available, and their pairing with high resolution quantum mechanical analyses enables the quantification of atomic charges in bonded systems that provide insight into a variety of chemical properties in MOFs. Still, charge analyses are most effective when monitoring changes in charge, rather than absolute charge. The subsequent sections of this review examine the application of these approaches through the exploration of two modeling

https://dx.doi.org/10.1021/acs.chemrev.0c00148
Chem. Rev. 2020, 120, 8641−8715

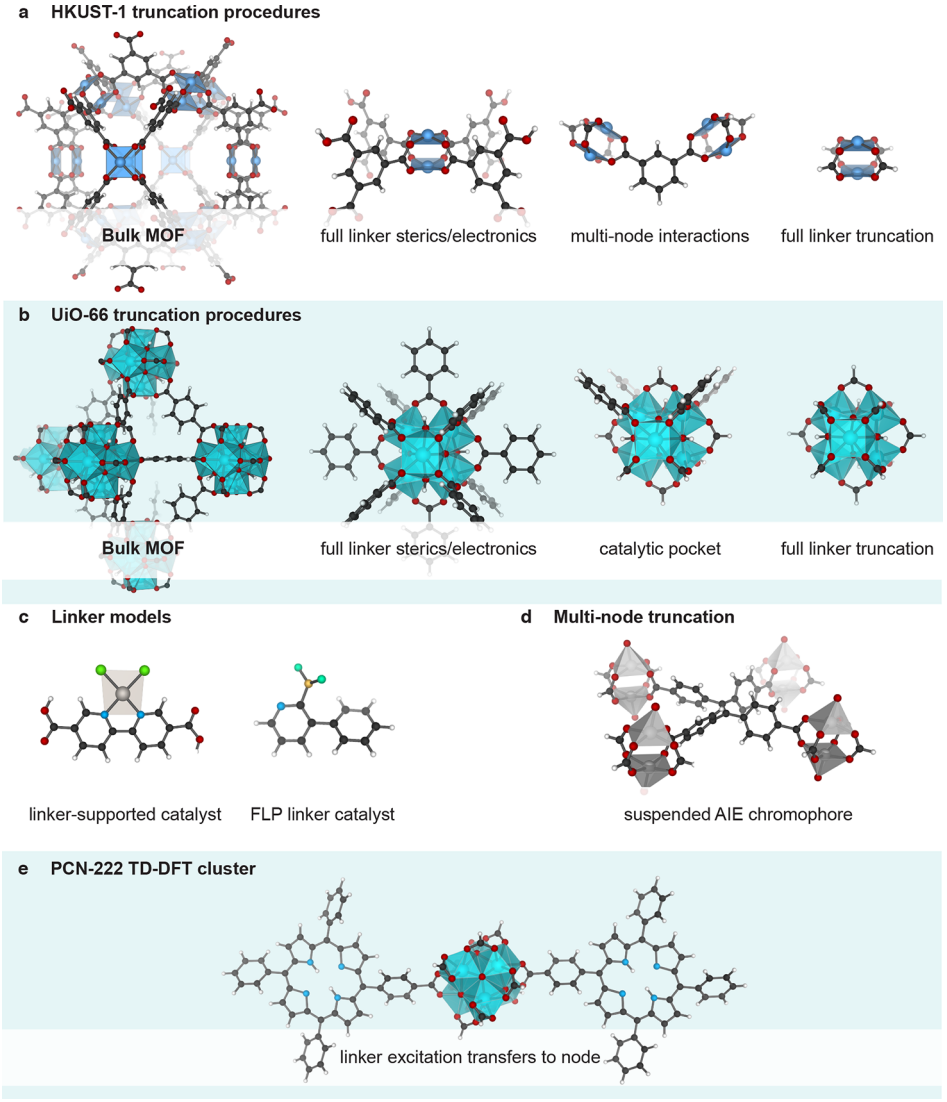

Figure 14. Various clusters used in computations of catalytic and photophysical transformations in MOFs. (a) HKUST-1 has been modeled using a single node passivated with protonated benzene tricarboxylic acid motifs, as well as formates. Furthermore, internode interactions have been captured by truncating to include two nodes. (b) UiO-66 is widely thought to be an ideal support for catalytically active metals by atomic layer deposition onto the nodes surface. There, the electronic structure of the ZrO motifs is relatively unperturbed by formate vs benzoate passivation, and models instead vary based on the extent in which they include the pseudopore created by the benzoate pocket. (c) Some models conjecture that the operative physics and chemistry of the MOF can be described entirely by a free ligand. The simplest cluster extraction is one that yields a free, protonated linker and its appendages. (d) Instances where the electronic structure of the linker is dependent on the chemistry of the nodes truncate to a full linker bound to all inorganic components. (e) Some studies include both complete nodes and linkers, in order to capture photophysical transformations that involve both the metal and ligand.

paradigms in the MOF community: the treatment of MOFs as molecules and, separately, as solids.

3. MOLECULAR MODELING OF MOF CLUSTERS

MOFs with localized electronic structures, i.e., those that are acting more like an array of molecules, are routinely modeled by extracting a fraction of the extended solid and treating it with a high level of theory as implemented in molecular modeling suites.[319] There is an advantage to modeling a MOF as a truncated molecule: computational complexity scales with the number of electrons, (e.g., $O(n^3)$ for GGA, $O(n^5)$ for hybrids). However, the process of extracting a fraction of atoms from a MOF reduces the periodicity of the system and mandates some form of passivation. The chemical decisions made in this approximation are hence a possible source of systematic error; careful benchmarking and vibrational analysis should complement truncation procedures. Furthermore, this approach is obviously less applicable to MOFs with delocalized electronic structure or scaffolds whose properties arise from extended symmetry (e.g., magnetism, conductivity, radical delocalization).[320] Still, reducing model size and eliminating periodic boundary conditions broadens the applicable methodologies for examining chemical properties. This procedure is utilized when subtle local changes that occur in electronically localized scaffolds are more important than bulk stabilization effects, such as changes in charge and bonding over the course of a reaction.

Even at the best of times, MOF nomenclature is problematic, and these issues are amplified when talking about molecular truncations of bulk structures, termed "cluster models". To

https://dx.doi.org/10.1021/acs.chemrev.0c00148
Chem. Rev. 2020, 120, 8641−8715

clarify, when discussing the size and types of models used for molecular modeling, the term "cluster" refers to *any* subsection of the MOF that contains at least one chemically complete motif (i.e., a fraction of the framework that, at minimum, contains a complete node, linker, etc.) rather than to the inorganic component of the material. For example, both a single metal node surrounded by truncated linkers and a free linker in its protonated form are examples of clusters.

Cluster models provide a unique opportunity to perform reactivity studies using levels of theory that are not afforded in solid-state approaches. This section discusses key considerations for extracting clusters from bulk MOFs (section 3.1), best practices in optimizing cluster geometries (section 3.2), and applications of post-DFT methods enabled by reducing model size (section 3.3). The final subsection will briefly discuss the methods and challenges associated with determining the geometric structure of poorly defined crystallographic systems in order to model their electronic structure (section 3.4).

3.1. Cluster Extraction

Cluster models may be extracted from either experimental or computationally equilibrated structures.[321] Equilibrating the latter structures in their periodic forms prior to cluster extraction significantly improves electronic convergence of the cluster:[212] this is particularly important for MOFs that contain strained metal geometries.[322−325] In both cases, it is then common practice to simulate the pseudorigidity of the MOF by fixing the coordinates of terminal atoms/groups of atoms. However, the process of cluster extraction unquestionably results in the loss of some information, either electronic or steric. The challenge, more broadly, is in the construction of a model that contains the dominant geometric and electronic properties of the system, and modelers are prepared to make some (major) approximations in order to do so. The value of benchmarking cluster models by comparison to extended solids and experimental geometries cannot be understated.[97,272]

One of the early challenges in cluster extraction is the emergence of negative vibrational modes that correspond to the molecular cluster wanting to relax into a geometry dissimilar to the solid-state. These models often then feature low frequency negative vibrational modes associated with the structure not being in a local minimum. The imaginary frequency may persist after geometric relaxation and can impact the calculation of thermodynamic properties, such as Gibbs free energy and formation enthalpies.[326] The same vibrations may also be found in protocols where a low level of theory is used to obtain an equilibrated structure, followed by applying a higher level of theory to obtain electronic properties.[327−330] Yet each of these are common practices in the modeling community, and while this propagates a small error, it should be systematic if the procedure is applied consistently throughout.[105,331]

One method to eliminate negative frequencies simply and artificially replaces their magnitude with a value that reduces the effect of unphysical modes on the equations of state built using the quasiharmonic approximation.[98,332,333] In other words, if we assign these modes to vibrations associated with the formation of the pseudolattice, then we can arbitrarily adjust their contribution. While this is a somewhat crude correction scheme, the energetic implications of large-scale structural distortions are expected to be of much greater magnitude. Persistent negative frequencies associated with modes artificially impacted by model parameters, such as boundary treatment, are often ignored.[334,335] In practice, however, these modes can potentially be eliminated by subsequent optimizations or refining convergence criteria.

Beyond the geometric constraints placed on a cluster model, the other major challenge arises due to bond cleavage from the bulk. Regardless of the size or composition of the cluster model, extraction of an isolated region from an infinite solid will require installation of extrinsic passivating groups, rigidly altering the electronic structure, and sometimes the symmetry of the chemical system.[336] A significant amount of attention is paid to this stage of model development; improper passivation can inadvertently augment the charge of the cluster, the oxidation states of metals and ligands or, in the worst case scenario, cause calculations to oscillate and never converge (wasting both time and resources).[337]

Generally, MOF cluster models are formed by cleaving the material at a remote metal−linker interface (often the weakest bond in the material) and simply passivating the valence through addition of hydrogen (formally $H^{\bullet}$ prior to the self-consistent field routine, Figure 14d).[338] Alternative passivation options include the use of fluorine to emulate the electron withdrawing nature of the Lewis acidic metal cluster[339] or more elaborate orbital capping methods.[340,341] The only real mandate is that if a σ bond is cleaved in the extraction process, then a σ bond must be made in the passivation process. The same is true for other bond types, however cleaving through conjugated networks is generally a bad idea (e.g., it would be ill-advised to approximate an aromatic ring as *cis*-1,3-butadiene). Intuitively, the fewer bonds one cleaves, the less perturbed the electronics will be.

In practice, there is no real universal approach to extracting clusters from MOFs; practitioners will cleave whatever they think best captures the chemistry of the system. However, we can broadly summarize the mentalities arriving at the representative clusters shown in Figure 14:

- Approach 1 (intact nodes, the most commonly invoked), includes an explicit node (i.e., the inorganic component in the MOF), and the associated inner-sphere donor atoms from the anions. This approach is widely used because it enables a reasonable description of the operative chemistry at the node, enabling computations of node-supported catalysis[342,343] and gas sorption properties at open metal sites[344,345] among others discussed below. In these models, the linkers must be neutrally terminated to some discrete approximate of the MOF linker (e.g., BDC approximated as formate, Figure 14a). There is some degree of creativity involved in this process because BDC, for example, can be approximated as a formate, a benzoate, or a protonated BDC (Figure 14a,b). To determine an appropriate degree of truncation a common practice is to begin with the smallest system (e.g., formate for BDC) and build outward toward inclusion of the full linker and beyond until the resultant analysis stops changing. The success of a given ligand truncation scheme depends on the purpose of the model (e.g., including aromatic motifs of linkers may be useful to simulate the pore environment). A mixed approach to linker truncation is commonly used for inorganic clusters with bulky ligands (such as the *catalytic pocket* model shown in Figure 14b) because the aromatics around the active site may play an allosteric role while remote ligands likely do not contribute to catalytic function, nor do they significantly alter the chemistry of the node.

https://dx.doi.org/10.1021/acs.chemrev.0c00148
Chem. Rev. 2020, 120, 8641−8715

- Approach 2 (intact linkers), a cluster of a MOF is created such that the complete linker is intact, and the node is accounted for in some creative way. In the simplest example, a linker can be extracted and passivated with protons, Figure 14c. Here, the Lewis acidity of the node is obviously poorly accounted for, but its effect may not be overly important (e.g., for studies relating to the geometry of a linker-supported catalytic metal). Full SBUs may be appended to linker termini where their influence controls the properties of interest (e.g., conformational restriction during optical transitions,[346] Figure 14e). Other exotic examples may include complete linkers passivated by approximate nodes (e.g., nodes that are geometrically related to the MOF but contain more simple metals such as switching Fe^{2+} for Mg^{2+}).[347]

Most models follow approach 1, and feature complete nodes passivated by some representative anions. As an illustrative example, the performance of UiO-66 and UiO-66-NH_2 for the cross-aldol condensation of propanal with benzaldehyde has been assessed using both cluster and periodic models.[348] The cluster model was composed of one Lewis acidic $[Zr_6(\mu_3\text{-}O)_4(\mu_3\text{-}OH)_4]^{12+}$ node, with pendant linkers modeled as formates on the remote portion of the node, and benzoates on the active half (Figure 15). The idea of a mixed ligand model can

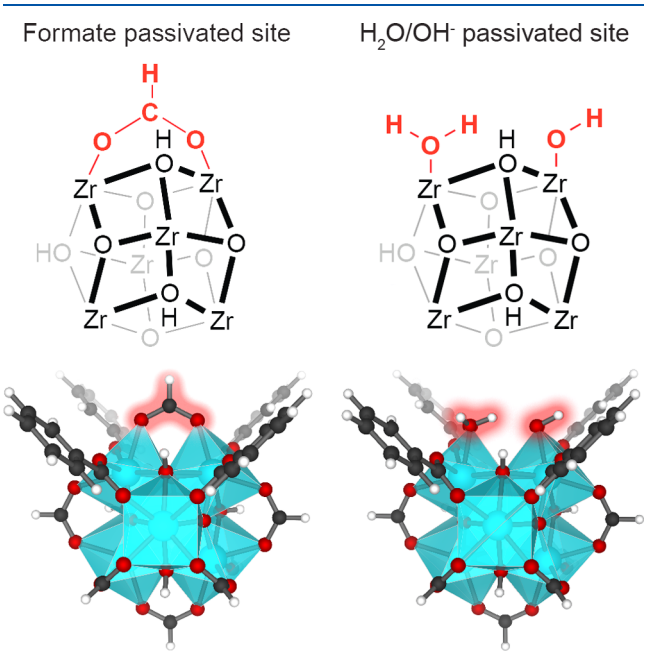

Figure 15. Cluster model of UiO-66 wherein one of the BDC linkers is passivated with a formate or the aqua/hydroxyl pair.[356]

be thought of as a method to locally simulate a pseudopore environment (i.e., approximating local steric interactions around the site of interest). In a related study, protonation of the active hydrate sites (Figure 15) was found to play a critical role in the reaction pathway of Fischer esterification due to the dual Brønsted acidity/basicity of water molecules coupled with the Lewis acid catalytic function of defective Zr(IV) centers.[349]

Naturally, the full linker must be present to study systems where the linker plays an operative role in the chemistry of the MOF (approach 2). In fact, there are both thermal and photocatalytic examples where a cluster model may be a single linker, Figure 14c, although inclusion of a complete linker and node are most common, particularly in photoapplications.[346,350,351] These "linker models" are familiar in inert MOF scaffolds that can support catalytically active linkers, as discussed in section 5. For example, biphenyl dicarboxylate (bipydc) linkers hosting catalytically active species that were incorporated in UiO-67 derivatives can be modeled as the free acid with catalytically interesting metals bound through the N-donor, Figure 14c. The simulated platinum XANES data of the cluster model matches that of the same catalytic linker incorporating into the MOF indicating that electronic behavior of the linker-metal interaction was not overly affected by framework incorporation.[352−354]

Cluster models can also be used to study photophysical properties if the photoactive motifs are intact. In other words, the frontier states of a MOF may be individually assessed using isolated cluster models, provided there is no charge transfer between the components, i.e., when the valence and conduction band edges of the solid are centered on either the linker, or separately, the node. However, many MOFs feature ligand-to-metal excitations, and models may even erroneously predict such excitations due to the truncation procedure. For example, a cluster model featuring a single Zr-oxo node suspended by hydrogen-passivated porphyrin linkers was generated to explore the nature of frontier orbitals responsible for photocatalytic oxidative amine couplings, Figure 14e.[355] From that model, the lowest unoccupied orbital is dominated by contributions from the Zr-oxo moiety, yet the experimental UV−vis response correlated with linker energetics suggests excited linkers may transfer charge to the inorganic node.

A linker-only model (approach 2) was also used to simulate modified UiO-67 hosting borane frustrated Lewis pairs (FLPs), Figure 14c.[357,358] Approximation of the MOF chemistry as a single proton-passivated linker was valid in this case because only the FLP centers were responsible for heterolytic dissociation of H_2 in the hydrogenation of CO_2 to methanol via formic acid.[357] However, the model apparently omitted critical interactions of reagents with the inorganic node; periodic calculations performed to assess the success of the cluster model identified strong interactions between H_2 and the node. As a result, the mechanistic analysis was performed with the climbing-image nudged elastic band (CI-NEB) method with the bulk structure modeled using periodic boundary conditions (section 4); however, inclusion of the node in the model may have been important.[358]

Beyond these examples, there have been more extreme cluster extractions designed to include the effects of pore encapsulation. The pore is thought to provide additional physical influence on properties such as site adsorptivity,[359] enantioselectivity,[360] and size selectivity[361,362] as functions of the pore volume, aperture, and composition. In such cases, a complete description of the pore aperture and/or cage created within may be necessary to explain intrapore reactivity. Such was the case for a borylation catalyst incorporated as the linker of a UiO-67-analogue.[363] The heterogenized system exhibited >99% chemoselectivity toward a monoborylated product, far exceeding the selectivity of its homogeneous counterpart.[362] Gibb's free energy profiles were first recovered from the isolated linker model (Figure 16d), but it took the implementation of a large UiO-67-analogue cluster model, containing both the tetrahedral and octahedral pores of the MOF, Figure 16a−c, to deduce that selectivity of their catalytic reaction resulted from pore confinement restricting access to the diborylated product rather than local sterics or electronic interactions.[363]

https://dx.doi.org/10.1021/acs.chemrev.0c00148
Chem. Rev. 2020, 120, 8641−8715

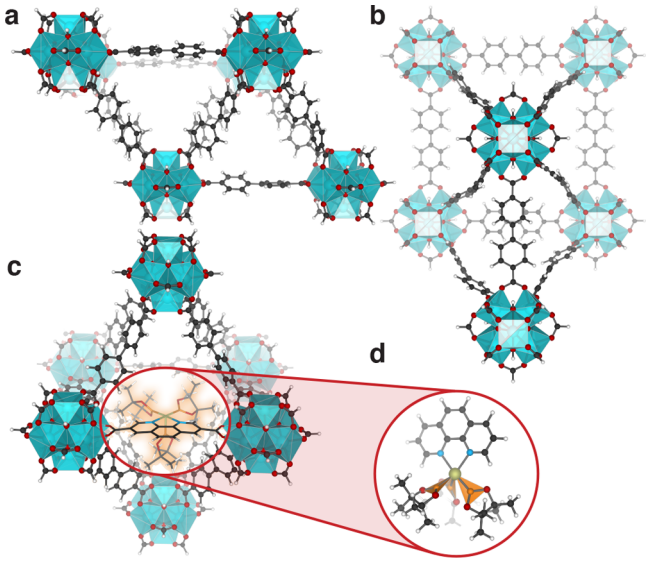

Figure 16. (a) Top and (b) side view of a modified UiO-67 scaffold. The model contained a complete description of both pores, enabling assessment of energetic barriers for product diffusion throughout, which seemingly enhanced selectivity for monoborylated products during catalytic methane borylation; the energetics of reaction pathways were compared with the pore cluster model (c) and linker cluster model (d) and similar reaction coordinated diagrams were recovered. Image adapted from data presented in ref 362.

Clearly, the size of a cluster model, i.e., the portion of the framework included in the model, will be different between MOFs of different chemical composition, but it can also vary when attempting to recover different information regarding the same scaffold. For instance, the Cu-dimer paddlewheel node found in Cu_3BTC_2 was approximated to cupric formate to study small molecule binding at its open metal site, Figure 14a, and similar binding energies of small gases were recovered using the cluster model, the periodic model, and experiment.[364] However, the same node required inclusion of complete BTC linkers (passivated with hydrogen) to account for their steric role while modeling a carbonyl-ene reaction.[365] In a different instance, the Knoevenagal reaction of malononitrile and benzaldehyde to 2-benzylidenemalonitrile was modeled at the Cu(II) site.[366] The authors noted the possibility of reagents binding to more than one node, thus two formate-passivated Cu-paddlewheels were included and linked together using a 1,3-benzene dicarboxylate model of BTC, Figure 14a. This cluster was validated by implementing periodic interpolation schemes between intermediates identified through cluster modeling (section 5). The cluster model predicted that deprotonation of malononitrile creates a Brønsted acid from one organic linker, and the adjacent Cu(II) Lewis acid facilitates subsequent reaction steps both electronically and through geometric prearrangement. The periodic model, however, showed that adjacent Cu(II) sites from a *third* Cu paddlewheel, not included in the cluster model, provided additional stabilization that reduced the highest activation barrier by ∼5 kcal/mol. One might conclude, then, that the cluster model should have included three SBUs for accurate electronic properties, although the mechanism itself was qualitatively constant.

Determining the appropriate extent of linker truncation for a model requires some chemical intuition, but the choice is aided by synthetic design. Modelers have learned a lot about their selection of both cluster models and defect passivating agents by simply examining the modulators used in experiment. Modulators are monotopic ligands with local geometry similar to the linker that primarily aid in prenucleation and organization of the inorganic clusters during MOF synthesis. The resulting crystals may host monotopic modulators that became trapped at the site of missing linkers. Formic acid is a common modulator added to metal-carboxylate mixtures to facilitate crystal growth. Hence, it should not be surprising that one of the most common truncation schemes is the simplification of aromatic carboxylate ligands to pendant formates.[367] The exclusion of phenyl motifs in BDC linkers might raise eyebrows, however formates are routinely found bound to Zr nodes in experiment due to the inherent defective nature of real materials.

However, as illustrated by the pairing BDC, tetrakis(*p*-benzoate)pyrene (TBAPy), and BTC with the same Zr_6-oxo node to yield three dissimilar MOFs with increasing node connectivity, metal sites that are not coordinatively saturated can be passivated by hydroxy- or aqua-ligands depending on the charge compensating requirements, Figure 17. Linker vacancies

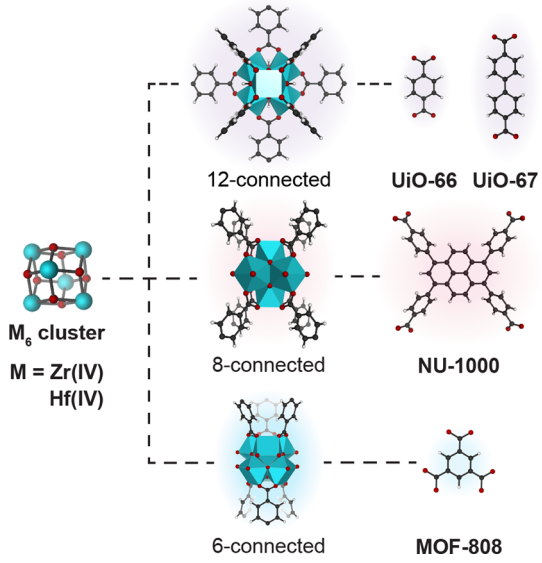

Figure 17. Connectivity of MOFs built from inorganic clusters can be varied by changing the directionality associated with the linker; ditopic BDC ligands create a 12-connected SBU, tetratopic TBAPy ligands form 8-connected SBUs, and triptoic BTC ligands for a 6-connected SBU.

are capable of hosting transition metal catalysts.[368−370] These have been widely studied in the UiO-66 and NU-1000 frameworks, which have periodic "defect sites",[371−374] while metal appendage to UiO-66 mandates the use of a linker-vacancy model (Figure 14b);[375] metals are thought to bind via two bonds formed with node-bound hydroxyls/hydrates.[376−378]

Even without appended metals, the nucleophilic node-bound hydrates/hydroxides are thought to be active sites for the hydrolysis of nerve agents. A tremendous amount of effort has been invested in the topic, and we will highlight a notable example: linker-vacant UiO-66 and MOF-808 models compared for the decomposition of Sarin (Figure 18).[379] The energetic pathway obtained from DFT was similar for both systems, yet the relative rates of detoxification experimentally are MOF-808 < UiO-66.[329,359] It was suggested that the mixed aqua and hydroxy coordination sphere in MOF-808 has the greatest capacity for thermal rearrangements to stabilize reaction species

https://dx.doi.org/10.1021/acs.chemrev.0c00148
Chem. Rev. 2020, 120, 8641−8715

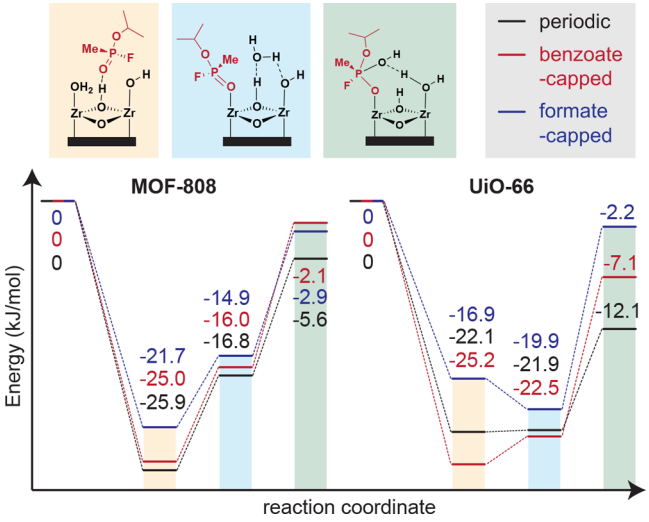

Figure 18. Decomposition of Sarin on Zr-oxo nodes in defective UiO-66 and MOF-808. Subtle differences in predicted reactivity are noted, and these depend on the capping agent used in the cluster model. Image produced from data presented in ref 379.

through hydrogen bonding.[379] The effect of linker truncation was assessed by comparing these results to a half formate−half benzoate capped model and the largest difference in energy along the reaction pathway was ∼1 kcal/mol, bolstering speculations that the openness of catalytic sites on these nodes reduces the significance of linker identity in small molecule transformations, Figure 18.

Even if the electronic properties of the cluster remain intact in the extraction procedure, the excluded chemistry may have had an unforeseen operative role in a catalytic cycle. To model reaction conditions, the explicit inclusion of small molecules such as solvent or water may become important.[380] In one case, four explicit water molecules were included in a mixed ligand formate/benzoate cluster model of UiO-66-NH_2 (in addition to an implicit solvation model) to study the hydrolysis of phosphonate ester bonds in chemical warfare agents catalyzed by UiO-66-NH_2.[381] An experimental investigation of zirconia cluster based MOFs showed the presence of amines either in the MOF (UiO-66-NH_2) or the agent VX (*O*-ethyl *S*-diisopropylaminoethyl methylphosphonothiolate) significantly enhances the rate of hydrolytic decomposition.[382] Multiple water molecules were included to assess whether the amino groups were behaving as Brønsted bases to catalyze hydrolysis or passively tuning the hydrogen bonding network to increase the nucleophilicity of water molecules around Zr(IV).[381,383] The *trans*-benzoate linkers across the active site were aminated, as adopted from the comparative study of UiO-66 and UiO-66-NH_2 for aldol condensation.[384] The transition state barrier for water addition was higher when the activated water molecule was coordinated to the aniline unit rather than the hydroxyl ligands of the node, suggesting the amino group does not electronically participate in the reaction, and is instead active in orienting the nucleophilic water molecules.

Indeed, the extent of hydration (e.g., number of linker defects in UiO-66 or coordinated water molecules) can play a determining role in the catalysis.[348,385] Water exhibits a dual role in the hydrolytic reactions with nerve agents, where it functions as a gate-keeper for adsorption by blocking the Lewis acid sites on Zr-oxo nodes, in addition to acting as a nucleophile.[348,349] The necessary and endergonic displacement of water to initiate nerve agent hydrolysis makes its explicit presence an important consideration in these models.[329] Explicit consideration of CO_2 was further shown to hinder nerve agent degradation by preferentially binding to Lewis acidic sites.[386] Further, in the presence of CO_2, H_2O, and dimethyl methylphosphonate (DMMP), carbonate formation is preferred to DMMP decomposition. Although CO_2 prevents the hydrolytic degradation of DMMP on Zr(IV) sites, it was found to facilitate the desorption of its degradation products to regenerate the catalyst. Thus, cluster models concerned with enhancing reactivity or selectivity may benefit from explicit inclusion of small molecules that may be advantageous.

In summary, the process of cleaving and extracting clusters for catalytic modeling is somewhat of a case-by-case process. Depending on the active component, the cluster model may focus on a complete node or linker and additional subunits (e.g., additional nodes or linker components) are included if they play an electronic or steric role. To verify the results from cluster models, values can be compared to calculations performed on the bulk or experimental parameters; transition states and intermediates found from cluster modeling can be confirmed through interpolative procedures described in section 5.1.2. The following sections detail the modeling protocols practitioners employ once they have a cluster model at hand.

3.2. Geometry Constraints for Cluster Optimization

While the primary challenge of cluster model extraction is related to the chemistry of the truncation (i.e., how to cut the solid appropriately and passivate the dangling bonds), there are further considerations that must be addressed in order to obtain reliable computational data. The most important of these is how to appropriately geometrically equilibrate the cluster once it has been extracted; omission of the repeating framework provides additional degrees of freedom that may permit the molecular cluster to access conformations unattainable in the constraints of the lattice. To mediate this, geometric constraints are applied to certain atoms or functional groups to mimic the rigidity of a crystalline MOF.[387]

The main objective of a geometric equilibration is to minimize forces on atoms and obtain a stable local minimum energy structure.[327] However, as we alluded to in section 2, occasionally systems are so large that certain atoms must be frozen/fixed in their experimental positions in order to simplify the model; the same protocol is mandated in cluster extraction. Common atomic freezing procedures described herein for subsequent optimizations include freezing the passivating motifs, terminal nodes/linkers, or the *para*-carbons in BDC-containing MOF-clusters, as this still allows the ring face to rotate without expanding the pseudolattice.

As an example, the frozen *para*-carbons in a metal-appended NU-1000 derivative were sufficient to maintain the ligand orientation while studying hydrolysis of the phosphonate ester bond present in nerve agents.[329] The authors employed acetate-capped cluster models to assess the reaction profile for VX and 3,3-dimethyl-2-butanyl methylphosphonofluoridate, assuming the openness of the catalytic site would prevent significant contributions between the reagent and the surrounding linkers. No constraints outside of frozen *para*-carbons were applied to this cluster yet the directionality of the framework appeared to be maintained, pointing to the geometric rigidity of the Zr-oxo nodes. In a different study, benzoate linkers were employed to study the degradation of methylparaxon on the NU-1000 node.[388,389] The hydrogen atoms *para* to the carboxylate were

https://dx.doi.org/10.1021/acs.chemrev.0c00148
Chem. Rev. 2020, 120, 8641−8715

again kept fixed, and reasonable quantitative agreement was found between theory and experiment. In sum, freezing a *para*-positioned atom does allow for ring rotation, while preventing distortion of the pseudolattice.

Maihom, Limtrakul, and colleagues examined CO oxidation of N_2O on HKUST-1 analogues (M_3BTC_2, M = Cr, Fe, Co, Ni, Cu, and Zn).[390] The model included four BTC linkers bound to one cupric paddlewheel, and the terminal carboxylic acid protons were kept fixed. In this case, the ligands were unlikely to deform throughout the reaction. However, this example serves as particularly pedagogical: one can imagine a circumstance where a reaction pathway involves major distortions to the active metal site that may be stabilized by improperly allowing the ligands to unbind throughout or artificially expanding/contracting the coordination bond lengths.

Finally, in perhaps the most extreme application of atom constraints, a study by Ryu, Kim, Choi, Kang, and colleagues featured a linker-bound catalyst, $ReI(CO)_3$(2,2′-bipyridine-5,5′-dicarboxylate), which performed CO_2 reduction. The photocatalytic response of the MOF was observed to increase with the concentration of aminated-bpy linkers,[391] and EXAFS revealed bonding interactions between the amine-functionalized linkers and catalytic linkers that indicated ligand cooperativity. A creative cluster model featuring the catalyst linker complexed with an amine-based linker in close proximity was taken from the experimentally refined crystallographic structure to explore the energetic reaction profile, Figure 19. To model framework

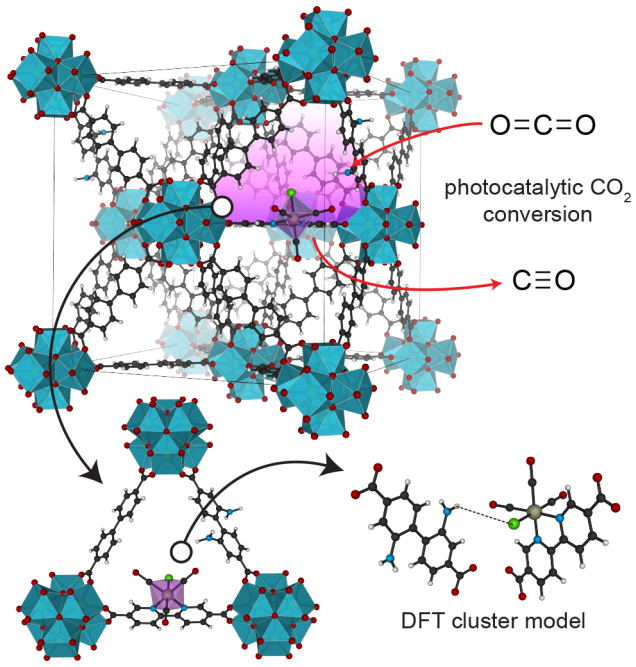

Figure 19. Isolation of the target clusters from a mixed-linker UiO-67 derivative bearing aminated and catalyst-loaded linkers; linker arrangement was maintained without directionality imposed by inorganic components by constraining carboxylate oxygens.[391]

rigidity, the carboxylates were constrained throughout the study. Indeed, this is an excellent example of a *model*: the operative chemistry was captured in their "cluster", even though its construction is somewhat esoteric.

In sum, there are numerous combinations of optimization and truncation protocols one could follow, and it is not immediately clear which yields the most reliable results. Indeed, the best solution depends on the chemistry of each framework, and the purpose of the model; it is thus difficult to be prescriptive, and once again benchmarking schemes comparing relative cluster model sizes, ab initio, or experimental data is strongly encouraged. Still, the breadth of modeling capabilities available to molecular models is worth the structural simplifications because the electronic insights gleaned from extensive and high-level studies build design principles that guide MOF developments in every field in which they are applied.

3.3. Post-DFT Methods

One of the most compelling benefits of cluster models is the ability to apply levels of theory that would otherwise be too cost prohibitive in periodic modeling. These higher levels of theory afford better electronic descriptions, which can be useful in cases where the electrons traverse a shallow potential energy surface.[392] Rather than construct the ground-state density using a single Slater determinant,[393] a multiconfigurational approach can be used to resolve energies of near-degenerate electrons, and those on a very shallow potential energy surface.[394] By sampling more than a single electronic configuration, these methods can provide more reliable information about nonground-state configurations.[395] Multiconfigurational self-consistent field (SCF) methods, e.g., complete active space SCF (CASSCF),[396,397] can be used to obtain reference functions for multireference approaches that account for dynamic correlation such as Møller−Plesset or coupled cluster approaches.[98] A CASSCF configuration interaction (CI) wave function is constructed from all possible Slater determinants generated within the active space (i.e., a finite number of frontier orbitals, Figure 20) thus providing an

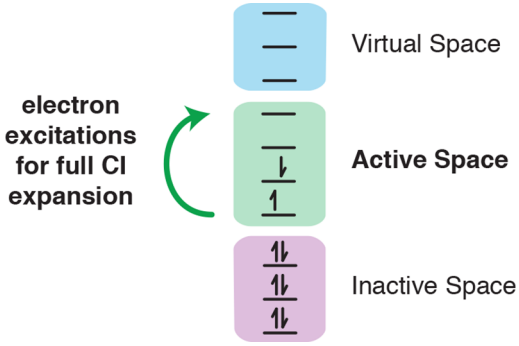

Figure 20. Schematic of energetic spaces partitioned with active-space approaches. The inactive space shown in purple is filled with paired electrons and the virtual space shown in blue is both empty and inaccessible to the sampled excitations, while all possible electronic configurations are explored in the active space based on the number of allowed transitions (e.g., singles, doubles, etc.) and available configurations.

even more thorough description of the electronic structure than possible with a single reference function.[398] Yet, the literature in this field, particularly applied to MOFs, is sparse due to the obvious hardware limitations.

A full CI analysis, which optimizes all the possible configuration state functions of all electrons, is presently impossible for systems larger than a handful of atoms.[399] To make CI and multireference calculations feasible, the number of transitions and orbitals explicitly included in the SCF procedure is reduced.[400,401] The electrons/orbitals and transitions that are explicitly accounted for in CI calculations are termed the "active

https://dx.doi.org/10.1021/acs.chemrev.0c00148
Chem. Rev. 2020, 120, 8641−8715

space". Determining an active space that captures both all orbitals relevant to each state and remains computationally tractable is quite challenging.[402] For example, complex magnetic behavior exhibited by a Dy(III)-based MOF ($\{[Dy_2(HCAM)_3(H_2O)_4]\cdot 2H_2O\}_n$, where H_3CAM = 4-hydroxypyridine-2,6-dicarboxylic acid)[403] was explored with an active space of the nine electrons in the seven f-orbitals, that determine the magnetic phases. Ultimately, the results were inconclusive on the magnetic orientation (i.e., ferromagnetic or antiferromagnetic) because the maximum limitations of the hardware were reached with this simplified model.

A similar approach was used to examine the spin state of Fe centers in the Fe(II)-based MOF, $Fe_2(DOBDC)$ (DOBDC = 2,5-dioxido-1,4-benzenedicarboxylate), which can activate the C−H bond of ethane for N_2O oxidation to ethanol.[327] Upon heating of N_2O bound $Fe_2(DOBDC)$, Figure 21, transient high-spin Fe(IV)-oxo sites were formed and served as mimics of enzymatic heme and nonheme motifs (known for facile activation of strong C−H bonds).[404,405] Single points of CASSCF and CASPT2 were again used to identify the oxidation and spin state of each of the metal atoms in trimetallic oxo-centered MOF clusters depending on the combination of Fe, Cr, and Al.[277]

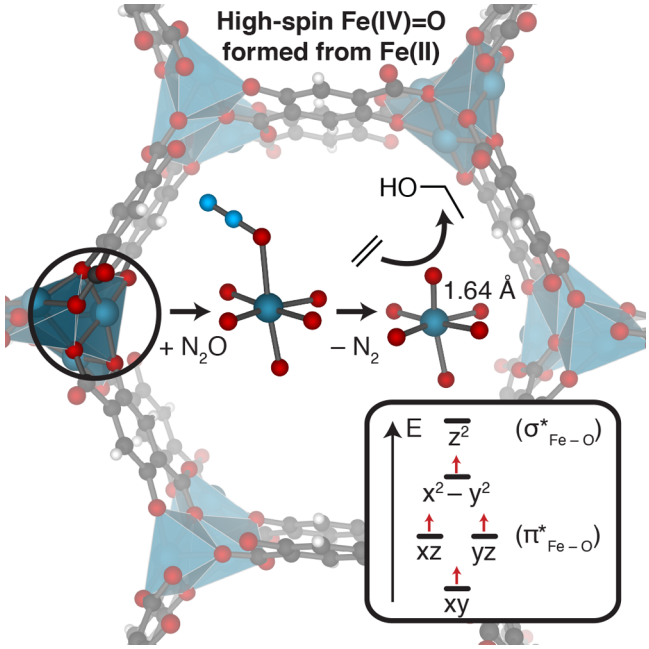

Figure 21. Multiconfigurational calculations can be used to determine the nature of the iron active site in FeDOBDC (dihydroxybenzenebicarboxylate). Formation of the high spin Fe(IV) species was facilitated through MOF incorporation by bulk stabilization of the reactive species and the weak carboxylate ligand field. Coordination of N_2O with a coordinatively unsaturated metal site of the activated framework forms Fe(IV)═O species capable of activating the C−H bonds of ethene toward oxidation. Image adapted from data presented in ref 327.

Multireference calculations have been employed in MOFs to study the relationship between concerted and stepwise low-energy transfers of both protons and electrons because of the shallow potential energy surfaces in question. Oxidative dehydrogenation, for example, requires the transfer of both electrons and protons, through either proton coupled electron transfer (PCET), which describes proton transfer with concomitant electron transfer, or hydrogen atom transfer, which describes the transfer of a proton to an existing radical, Figure 22a.[406] Multireference calculations are well suited to distinguishing PCET mechanistics because the potential energy surface is often shallow. Single point multireference calculations, both with complete and restricted active space methods, followed by second-order perturbation theory to include dynamic correlation, were performed on cluster models of heterobimetallic oxide clusters, (CoO)(MO)(OH_2) (M = Ti, Mn, Fe, Co, Ni, Cu, and Zn), appended to the NU-1000 zirconia node (Figure 22c). The cluster employed for geometry optimizations was further reduced to enable multireference calculations, Figure 22b. By analyzing the reaction energies and Hirshfeld spin populations to identify the metal oxidation states upon MOF incorporation, the authors determined that when transition metal oxides are partially substituted with low-valent transition metals the mechanism of proton transfer switches from stepwise proton and electron transfer, to hydrogen atom transfer.

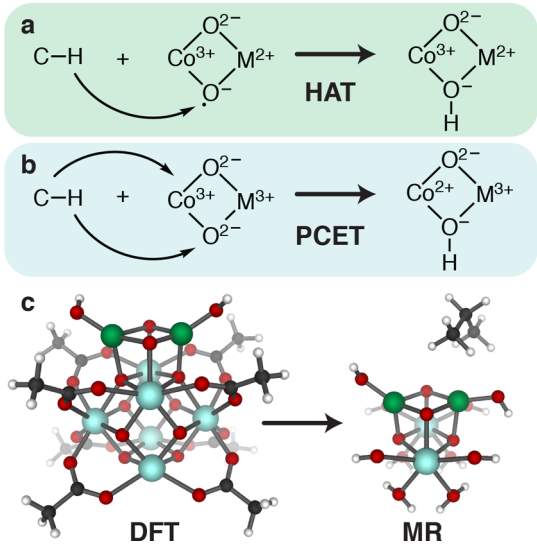

Figure 22. Radical processes, such as (a) hydrogen atom transfer, which involves the transfer of a proton to an existing radical, and (b) PCET, which involves the transfer of a proton and electron, are sensitive to level of theory and are well-suited to multireference (MR) calculations. Yet, MR calculations mandate a reduction in system size (c) to mitigate increased computational resources owing to the increase in electronic resolution.[406]

In another rare example of CI methods applied to MOFs, the difference in catalytic activity of Co(II) and Ni(II) species deposited onto the node of NU-1000 for ethylene oligomerization was studied.[407] Single-point CASSCF calculations followed by second-order perturbation theory (CASPT2) applied to key intermediates identified with DFT revealed an empty 3d-orbital on the low spin Ni, not present in high spin Co, which can hybridize with ethylene 2p-orbitals to stabilize the rate-determining ethylene insertion step, Figure 23. Activities calculated from cluster models with formate-truncated linkers deviated from experiment by 12 and 8 kcal/mol for Co and Ni, respectively. The authors suggest this may be the result of considering only mononuclear reactive sites in their model despite the possibility of binuclear or polynuclear active sites. Later it was determined that Ni atoms and Ni_4 groups have similar activity for the ethylene dimerization process, the origin of selectivity in this MOF is still under debate.[408] We further

https://dx.doi.org/10.1021/acs.chemrev.0c00148
Chem. Rev. 2020, 120, 8641−8715

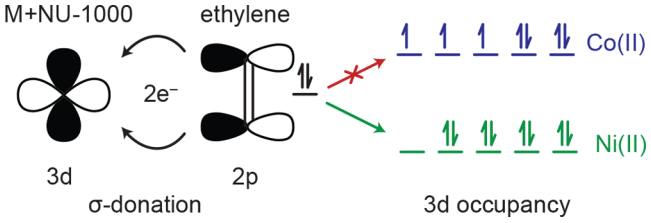

Figure 23. Multiconfigurational analysis on the rate-determining transition state for Co(II) and Ni(II) appended to NU-1000 revealed that the reacting molecular orbital is rehybridized during the bond forming step such that the transition state is stabilized by hybridization with the metal d-orbitals. The formally empty orbital on Ni(II) can more readily hybridize as evidenced by its 48% contribution to the MO versus the 15% contribution from Co 3d orbitals. Adapted with permission from ref 407. Copyright 2016 American Chemical Society.

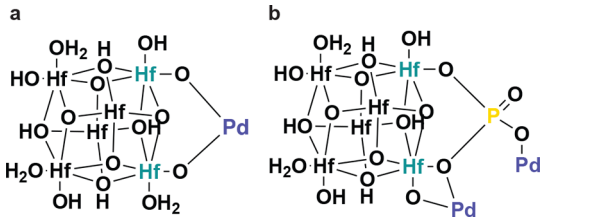

Figure 24. Node structures obtained from single crystal X-ray crystallography for palladium species deposited (a) on the pristine Hf-MOF-808 node and (b) on the phosphate acid-functionalized node. Addition of sulfate or phosphate groups to the node of Hf-MOF-808 was found to stabilize deposited Pd(II) species for catalysis of the oxidative Heck reaction. Reproduced with permission from ref 409. Copyright 2019 American Chemical Society.

note that conventional DFT modeling approaches would likely have been able to resolve the differences in the electronic structure of Co(II) and Ni(II). Regardless, post-DFT methods certainly offer additional electronic information, and their utility will become further valued as MOFs are investigated for other shallow PES transitions.

In summary, post-DFT methods offer the highest available quantum mechanical description, but are limited by the size of input geometries. The importance of functional and passivation procedures escalates with higher-order electronic procedures because of the interdependence between structure and electron configuration. Conveniently, however, cluster models have been able to replicate structural data obtained from crystalline samples further supporting the case for regions of bulk MOFs with a localized electronic nature functioning as isolated subunits.

3.4. Structural Elucidation

In the previous sections, all of the electronic structure models heavily relied on truncating the MOF in some predictable and rational way as to not augment the electronic structure of the cluster. However, until now, we have taken for granted the position of unrefinable atoms, such as pendant protons unless the crystal structures are solved with neutron diffraction, the proton topology is empirically added during the refinement process. Further, more modern MOF modification techniques such as postsynthetic transmetalation, ligand exchange, and atomic layer deposition (ALD) enable a broader gamut of MOF chemistry with progressively more ill-defined local geometry and composition. Indeed, node-appended metals are often assumed or inferred, but it is rarely possible to directly measure their location (Figure 24).[409] In these challenging cases, cluster DFT approaches have proven extremely useful in assigning various structural components of MOFs, and these investigations are often bolstered by complementary X-ray absorption spectroscopic data.

MOFs featuring group IV metal-oxo nodes, such as Hf_6- or Zr_6-based nodes (e.g., MOF-808, NU-1000, UiO-66, MOF-545, -535, -525,[410] BUT-12, -13,[271] ACM-10/11[411]), have been persistently interesting because of the strong, stable metal−carboxylate bonds formed at the interface of the node and linker.[271,412] The structural fortitude of these MOFs has inspired postsynthetic functionalization procedures to produce solid-state systems with chemically distinct active sites, yet (i) the effectively random nature of deposition techniques convolutes model determination and (ii) dynamic proton topology of the cluster support on which metallic species are deposited adds another level of complexity to structural elucidation and reactivity studies.[413,414] In the particular case of metal deposition onto zirconia (and similar) nodes, the first challenge is thus defining the proton topology; hydrogen bonding and the relative orientation of μ_3-OH, μ_3-O, −OH, and $-OH_2$ ligands will directly impact the deposition of extrinsic species as well as overall node reactivity (e.g., reagent−MOF interactions).[415,416]

In fact, despite being extensively studied by crystallography, the proton topology on the Zr_6-node of NU-1000 was resolved using a combination of cluster and periodic models, in conjunction with experimental data.[417] To achieve neutrality, 16 protons need to be added to the Zr_6O_8 cluster (excluding its eight pendant carboxylates); three distinct oxygen environments combine to give a complex series of protonation states, Figure 25.[417] By comparing the total energies of all of the possible orientations (six are shown in Figure 25), with the carbon atoms of the benzoate ligands frozen throughout the optimization, the −MIX tautomer that maximized hydrogen bonding between the −OH and $-OH_2$ ligands was found to be the most stable conformer by >100 kJ/mol in both solid-state and molecular models. The same proton topologies have been beneficial in characterizing the binding modes of metals to other Zr-oxo nodes, supporting several catalytic predictions discussed throughout this review. However, we do point out that the DFT minimum energy structure and the experimentally relevant structure may be different (i.e., the protons may be more labile than we conclude from models).

Unlike the example shown in Figure 24, the crystallographic ordering of postsynthetically added metals rarely results in periodically repeating arrangements. Instead, DFT paired with XAS can be used to help assign the metal coordination environment.[418] Two notable investigations spring to mind the challenging case of assigning the nuclearity of a copper-oxo species formed in situ on the Zr(IV)-node of NU-1000. In the original report, an argument is made for the formation of a Cu-hydroxide chain-like species that bridged two nodes. For the purpose of the paper, the identity of the catalyst was less important: the MOF performed selective oxidation of methane to methanol. Later, the identity of the Cu-oxo catalyst was refined from XAS and DFT data to a more plausible Cu-dimer (Figure 26).[419] Regardless of the catalysts true identity, these two papers serve the greater purpose of reminding us that models are simply that, models.

Throughout section 3, procedures were outlined that reduce the size of a quantum mechanical model either for efficiency or to access higher level theories without reducing the quality of extracted data. MOFs were shown to be effectively modeled by

https://dx.doi.org/10.1021/acs.chemrev.0c00148
Chem. Rev. 2020, 120, 8641−8715

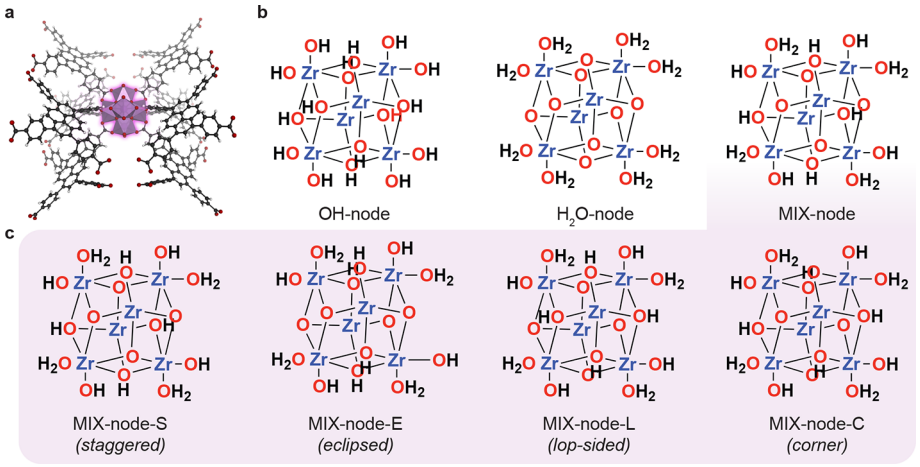

Figure 25. Proton topology of Zr_6-based MOF. (a) Zr_6 node with eight carboxylate linkers attached to NU-1000. (b) The three structural isomers (OH-node, H_2O-node, and MIX-node). (c) The four conformers that were considered for the MIX-node in the cluster model. Adapted with permission from ref 417. Copyright 2014 American Chemical Society.

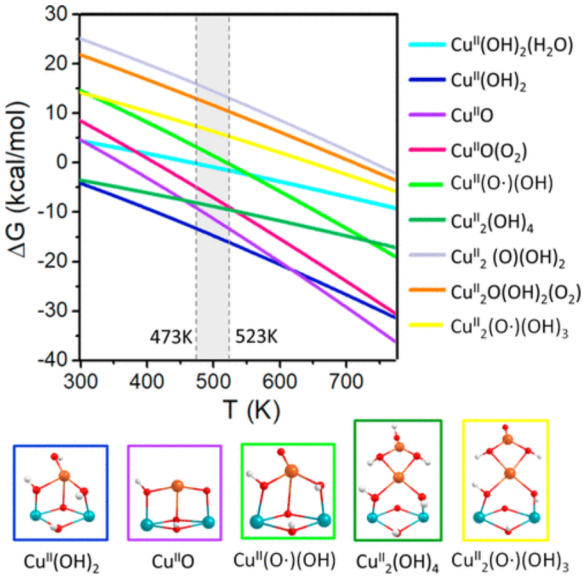

Figure 26. Phase diagram constructed for lowest energy configurations of Cu(II)-oxo species possibly formed under O_2 activation on NU-1000. The overlay of formation energies as a function of temperature reveal in the temperature region associated with the deposition technique (shown in the gray box) the $Cu^{II}(OH)_2$ species is thermodynamically preferred. Reproduced from ref 419. Copyright 2017 American Chemical Society.

extracting electronically independent subunits that include the relevant chemistry. Bonds cleaved in the extraction can then be passivated, most commonly by hydrogen atoms, and constrained optimizations can be performed such that rigidity imposed by the crystalline lattice is replicated. Given that cluster extraction and truncation procedure can play an operative role in the chemistry of the model, these approaches should be benchmarked, for example to a period model. Many of the shortcomings of cluster models are alleviated if resources permit the MOF to be modeled fully as an extended solid; the following section discusses models of periodically repeating systems and the successes and shortcomings thereof.

4. MOFS AS EXTENDED SOLIDS

While it is certainly convenient to approximate extended MOF structures as finite molecules using the procedures discussed in section 3, it is their crystallinity and ordered porosity that has stimulated many of the developments in the MOF field. Indeed, with the exception of rare amorphous variants,[336,420−425] MOFs are ordered solids. Thus, conventional solid-state modeling techniques can be applied where MOF crystals possess symmetry operations that enable the description of the extended material using a repeating unit. This section is intended to provide a background and some general calculation considerations when modeling periodic MOF properties (section 4.1), including their electronic band gaps (section 4.2), electronic band structures, and DOS (section 4.3, 4.4 and 4.5), as well as their lattice vibrations (section 4.6). Finally, we discuss MOFs with imperfections, those that host vacancies and interstitials (section 4.7).

4.1. Periodic Models and *k*-Points

Viewing MOFs as an extended array of molecules, each component (i.e., the linker and the prenucleated node) contains a family of molecular orbitals. Upon self-assembly of the MOF these electrons mix to form new molecular orbitals that expand over larger and larger regions of space. In principle, one could model a complete MOF crystallite (i.e., a *very* large chemical system as a molecule) and obtain the exact electron energetics and spatial distributions for all possible molecular orbitals in the material. Owing to symmetry, however, several of the molecular orbitals in the crystallite will be very similar in energy and centered on the same atoms. These geometric degeneracies enable a reduction in computational cost by modeling the associated electrons as interacting periodically in bands, Figure 27.

Electronic bands can be thought of as delocalized molecular orbitals whose energy depends on the extent of electronic interaction in crystallographic directions within the crystal. Indeed, Bloch's Theorem purports that for a nondefective material, the periodicity of the lattice describes the periodicity of the overall wave function.[426] Information on both the structural and electronic properties of a bulk sample can therefore be gleaned from a single unit cell (although the approach does not provide information about the surface chemistry at the grain boundaries of a crystallite). One way of thinking about the

https://dx.doi.org/10.1021/acs.chemrev.0c00148
Chem. Rev. 2020, 120, 8641−8715

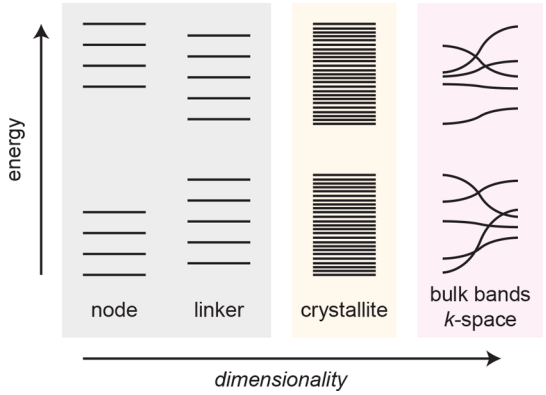

Figure 27. As size of a chemical system increases toward an infinite solid, the number of molecular orbitals becomes very large. For high symmetry materials, the crystallite can be described using a smaller, repeating unit, whose projection through reciprocal space generates electronic bands.

construction of bands in solids is to first create molecular orbitals for all atoms contained within the computational cell, then, using harmonics, the electronic interactions with neighboring cells are computed.[427] By doing so, both the electronic properties of the discrete unit cell are recovered, as well as the influence of longer ranged (de)localization and electrostatics, which can only be observed by sampling beyond one computational cell.[428]

While it is convenient to visualize bands as large delocalized molecular orbitals in real space, they are often computed in reciprocal space (i.e. *k*-space) using Bloch's theorem paired with a basis set constructed from interfering planewaves to determine the combinations and populations of electronics bands. *k*-space vectors can be loosely thought to sample long-range interactions in the crystallographic directions defined by the *k*-vector.

From experimental convention, a crystallographic unit cell (or conventional cell) contains the smallest chemical representation of a system that exhibits the same overall symmetry as the pristine lattice. Calculations using this geometry, composition, and associated lattice parameters will certainly be suitable for direct calculation of electronic properties, however, some space groups offer symmetry related primitive cells that contain a smaller repeating crystalline unit of lower symmetry.[429] Typically, calculations are run on the primitive cell unless the unit cell is required to capture magnetic ordering or structural deformations that cannot be described using the smallest repeating unit, some examples of which are shown in Figure 28.

Every ordered MOF crystallizes into one of 230 unique space groups,[432] each containing a series of high symmetry *k*-points.[433] The lowest crystal symmetry, *P*1, features no internal symmetry operations, all atoms in the cell are unique and must be explicitly computed, and hence there is only one high symmetry *k*-point in the first Brillouin zone, Γ.[433] Chemically, the Γ-point is the equivalent of projecting the molecular orbitals contained within the unit cell in three dimensions: the electronics of the material are governed by the interactions captured explicitly within the computational cell rather than their interactions with neighboring cells. MOFs typically crystallize in high symmetry space groups,[426] and often feature more than one symmetrically *unique* *k*-point that will contribute to the total energy of the system, and hence should be sampled during the SCF.

Within crystals that feature anisotropic bonding (for example, graphene, 2D MOFs, etc.) certain crystallographic directions contribute more significantly to the bonding and stabilization of

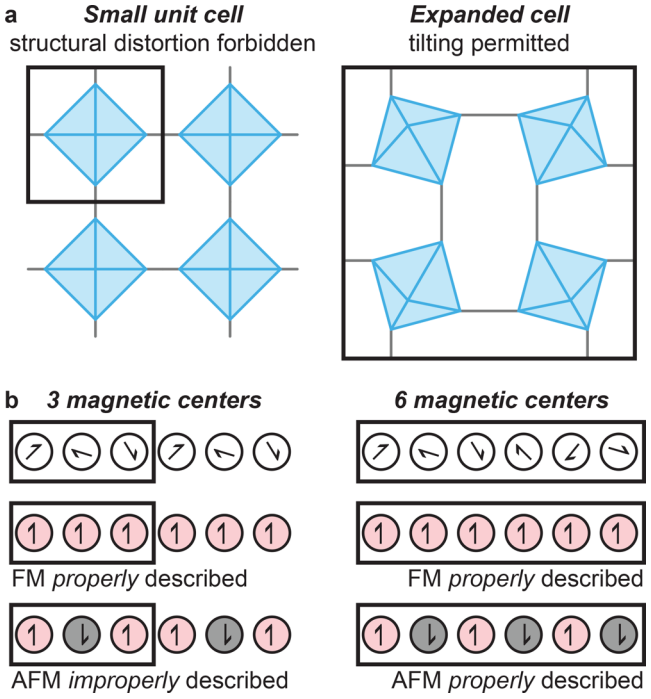

Figure 28. Although the smallest computational cell can save resources, an improper model may be recovered if a chemical interaction permeates beyond a single geometric cell. For example, (a) structural distortions are sometimes captured in temperature independent DFT (the ground state may feature titling of nodes);[430] and (b) magnetic ordering can be challenging if the unit cell contains an odd number of coupling metals (for example, the unit cell of Co_2Cl_2bis(1*H*-1,2,3-triazolo[4,5-*b*],[4,5-*i*])dibenzo[1,4]dioxin), (BTDD), contains 3 Co-(II), which do prefer to order antiferromagnetically[431]).

the system than others. In the 2D examples, the in-plane and out-of-plane interactions will contribute differently and sometimes seemingly unpredictably to the total energy of the system. It is hence good practice to sample as many *k*-points as possible to ensure a more tightly converged total electronic energy.

The selection of *k*-points depends on the crystal symmetry, and these *k*-points traverse the first Brillouin zone.[434] In practice, the contribution of each sampled *k*-point is taken as a weighted average (determined by symmetry) to recover the total system energy. The position of sampled *k*-points through the first Brillouin zone is computed with one of two philosophically dissimilar approaches: a Γ-centered Monkhorst−Pack, or a non-Γ-centered Monkhorst−Pack *k*-grid. The main difference is that the former forces sampling of the Γ, while the latter does not guarantee that any high symmetry points are sampled.[435] Crystal symmetry thus helps inform two key computational considerations: (i) the feasibility of using a computational primitive cell, and (ii) the *k*-path to explicitly examine how electron energies changed in the extended solid. Almost all of these considerations are enabled in freely available software, and high symmetry points of the first Brillouin zone can be found in online databases like the Bilbao Crystallographic Server.[433]

In principle, one would compute the total energy of a system by integrating over the entire first Brillouin zone or approximating the integration with the summation of a very large number of *k*-points. In practice, the total energy is asymptotically related to the number of *k*-points and a convergence test is required to elucidate when a sufficiently dense grid has been invoked. We can distill the key

https://dx.doi.org/10.1021/acs.chemrev.0c00148
Chem. Rev. 2020, 120, 8641−8715

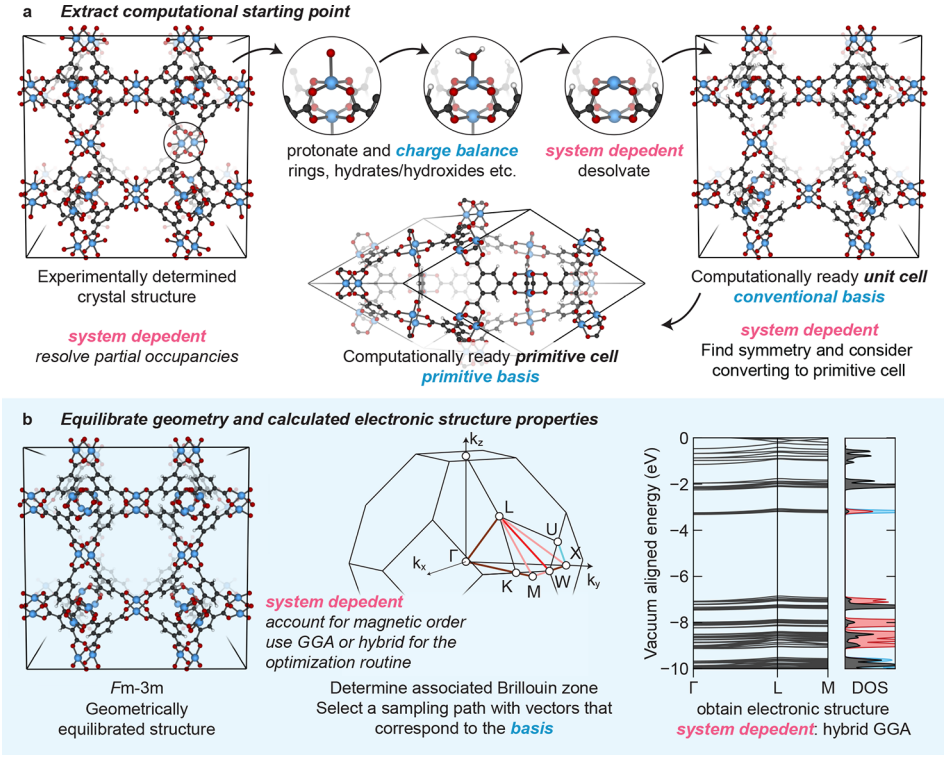

Figure 29. General computational approach used to obtain electronic structure properties from solid-state structures. (a) Beginning with an experimentally obtained crystal structure, partial occupancies must be resolved. Then, where applicable, protons must be added to charge balance the cell, in effect establishing the oxidation state of the metals. Extrinsic solvent may be removed to simulate the activated MOF. Symmetry can then be enforced and a computational primitive cell may be available. (b) The structure can then be equilibrated, and higher level electronic structure properties can be obtained by sampling the first Brillouin zone, including electronic band structures and corresponding density of states.

considerations for *k*-grid generation and their impact on the material properties down to the following:

- In Bloch's theorem, planewave cutoff (i.e., the basis set) and the *k*-points are independent. Yet both affect the total energy of the system. Hence, to obtain converged results, it is good practice to benchmark the *k*-grid and basis set separately.
- Generally, sampling additional *k*-points provides better descriptions of long-range orbital interactions within a crystal system. Increasing *k*-grid density does not always reduce the total energy of the system that depends on the nature of the bonding and antibonding orbitals.[436] It is therefore difficult to predict the impact on total energy without first running the calculation.
- Empirically, a *k*-grid with a density of 25× (lattice parameter)$^{-1}$ provides an estimate of the *k*-point density required for a reasonable sampling of electronic interactions within the crystal.[429] Computational feasibility of the resultant grids relies on large lattice parameters, which typically infer large numbers of explicitly defined chemical interactions within the unit cell, the extent of electronic interactions rapidly diminishes in real space, hence why large crystals often show little dependence on increased *k*-point density. There is a trade-off between modeling large systems with many explicit electrons, versus small systems with many explicit *k*-points. Moreover, while a reduction to the primitive cell vastly reduces the Slater determinant's size, it comes at the penalty of requiring several additional *k*-points (which contribute significantly to the computational time).
- In MOF chemistry, it is common to perform geometric optimizations with a sufficient *k*-grid at a lower level of theory, then refine the electronic structure with a single-point energy calculation at a higher level of theory; the size of the *k*-grid in either case is determined by MOF symmetry and resource availability.
- Importantly, there is no formal relationship between lattice parameter and *k*-point density; rather, large unit cells often contain sufficient descriptions of strong interactions, and hence long-range sampling does not overly alter the energetics of the system. Regardless of whether this is true for all MOFs, this procedure produces a highly reproducible systematic error in the total energy of the system that is acceptable in many cases.
- Most MOFs crystallize in high symmetry space groups, and it is good practice to include all high symmetry *k*-points in the computation of the total energy of the system, and ideally during the optimization routine.

Regardless of how many *k*-points are selected for the optimization routine, the material must be geometrically equilibrated (and the SCF must be converged) to ensure that the energetics are computed without spurious numerical fluctuation. A schematic of the general computational approach for solid-state materials is shown in Figure 29. Assuming that a structure has been optimized, the following sections discuss the computable properties and utility of using a solid-state model for MOF systems.

https://dx.doi.org/10.1021/acs.chemrev.0c00148
Chem. Rev. 2020, 120, 8641−8715

4.2. Electronic Band Gap

The ionic lattices of most MOFs feature a discrete electronic band gap, while some can be described as metallic (classified as having nonzero DOS at the Fermi level).[437] Within the subgroup of materials that feature electronic band gaps, their conductive properties depend on numerous other properties (e.g., the material's defect chemistry, the mobility of the charges, the electronic band gap, etc.). Because standard solid-state computations omit temperature, and without an exhaustive defect analysis, we are unable to assign the position of the Fermi level. In light of this, MOFs are largely insulating materials, but we note that they are interchangeably referred to as semiconductors in the literature.[438−441]

The fundamental energy gap, E_g, is defined by the lowest energy occupied-to-unoccupied transition in a system (independent of whether it is symmetry allowed);[442] its magnitude is the difference in energy between the VBM and CBM. Because of a derivative discontinuity and other localization errors associated with the exchange potential in semiconducting systems, GGA functionals systematically underestimate MOF band gaps.[443−445] Empirically, this systematic underestimation can be improved by incorporating a component of exact HF exchange into the Hamiltonian.[446,447] However, the computational expense associated with hybrid functionals[448] prompts the recovery of semiconducting properties from single-point calculations at this level of theory on a structure obtained using GGA.[57]

MOFs with bands that exhibit different energies as a function of *k*-space (i.e., band dispersion) may exhibit an indirect band gap, schematically presented in Figure 30, where the VBM and CBM occur at different points in reciprocal space. In such cases, Γ-point sampling is insufficient to capture the dominant electronic influences. The lowest energy transition in an indirect band gap material requires the coupling of photon absorption/emission to a phonon mode in order to conserve energy and momentum because the wave vector at the top of the valence band does not match the wave vector at the bottom of the conduction band.[449] Indirect band gaps thus diminish the intensity but extend the lifetime of formed excitons by preventing recombination; indirect band gaps are desirable in photoactive solids for the enhancement of quantum efficiency.[450] Although there are almost no reported indirect-band MOFs,[451,452] the changing band gap energy in reciprocal space is a phenomenon ripe for exploration.

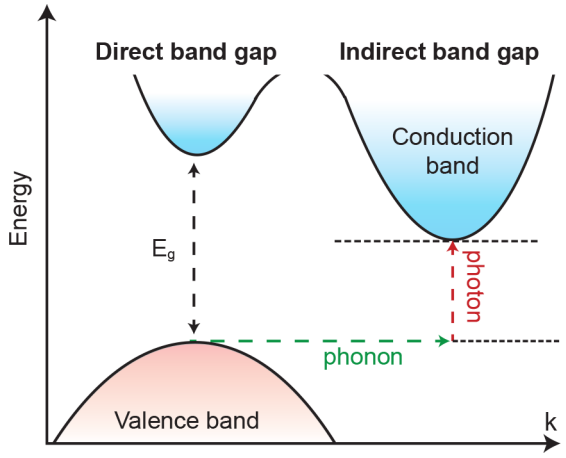

Figure 30. An illustration of the band gap in a semiconductor as a function of reciprocal space when the CBM and VBM are at the same point in reciprocal space providing a direct band gap and when they are at different points in reciprocal space creating an indirect minimum absorption energy.

Certainly, most MOFs feature wide band gaps and highly localized electronic structures that give rise to flat bands with well-defined orbital contributions to the frontier states and direct gaps. The localization of electrons makes MOFs intriguing for photocatalytic applications,[80,453−457] as it affords one route toward accessing dense populations of high energy electrons localized on transiently reduced motifs,[458,459] discussed further in section 5. Moreover, electronic structure may be tuned to desirable bulk properties, facilitated by the inherent modularity of MOFs.

Although the nature of band edges is material/composition dependent, the electronic band gap of a MOF can be modified by metathesis and functionalization of the linker and/or inorganic node. There are four possible frontier orbital orientations in MOFs, wherein the band edges are defined by (i) ligand-to-ligand, (ii) ligand-to-metal, (iii) metal-to-ligand, or (iv) metal-to-metal excitations, ultimately dictated by the material composition. Countless examples of DFT screenings are reported for band gap modulation via metal[212,221,228,460−463] and linker exchange[79,220,464−471] across the gamut of MOFs. MOF-5, for example, has been subject to numerous theoretical studies systematically exchanging components of the inorganic node[230,460,463,472−474] or the linker.[475−478] In one study, the authors made isovalent substitutions for both the inorganic oxo, as well as the transition metals, and from PBE (which systematically underestimates the band gap), these modifications shifted bulk MOF-5 (E_g = 3.6 eV) into the visible region, Figure 31.[479]

In a complementary study, both GGA and hybrid functionals showed tetrahedral Co(II) transmetalation in MOF-5 resulted in band gap reduction, and an eventual transition from semiconducting to metallic with two cobalt per node.[463] Experimental efforts revealed that up to ∼3 Co(II) per cluster could be incorporated in the presence of solvent, forming blue

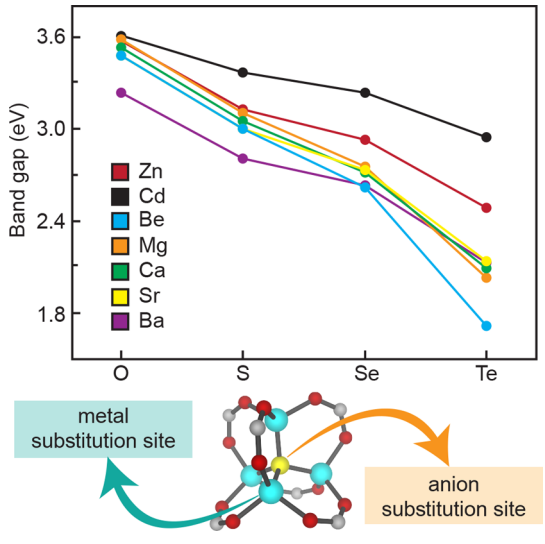

Figure 31. Evolution of the calculated PBE band gap (top) for X_4Y-MOF-5, where X is the substituted metal (X = Zn, Cd, Be, Mg, Ca, Sr, Ba) and Y is the substituted anion at the center of the metal node depicted in yellow (Y = O, S, Se, Te), Adapted with permission from ref 479. Copyright 2014 American Chemical Society.

https://dx.doi.org/10.1021/acs.chemrev.0c00148
Chem. Rev. 2020, 120, 8641−8715

crystallites with octahedral Co(II).[473,480,481] Together, this indicates that in models assuming isogeometric substitution of tetrahedral Co(II), the resulting metallicity is likely an indication of material instability, Co(II) prefers to be octahedral in MOF-5.

Still, transmetalation is a fruitful route to control the nature of band edges in an otherwise wide gap MOF. Several practitioners have examined the substitution of transition metals in place of Zr(IV) in UiO-66,[229,482,483] however, it is inconclusive whether incorporation proceeds via transmetalation or node grafting.[484] The application of DFT has shown that certain metal ions seemingly reduce the band gap from the addition of states below or above the native conduction or valence band. For example, both Ce-[485,486] and Ti-substituted[487] UiO-66 install empty *f*- and *d*-orbitals, respectively, at the conduction band edge, reducing the requisite excitation wavelength. The installation of empty metal states at the conduction band edge of MOFs with ligand-centered excitations is indeed one strategy for engendering linker-to-metal charge transfer[461] and has applications in photocatalysis discussed further in section 5.

A more popular strategy, particularly in the realm of photocatalysis, is organic linker functionalization. For example, one study showed that the band gap of MIL-125, a MOF with an organic valence band and inorganic conduction band,[74,79] depends the electron donating or withdrawing ability of functional groups on the BDC linkers, Figure 32.[464] In most

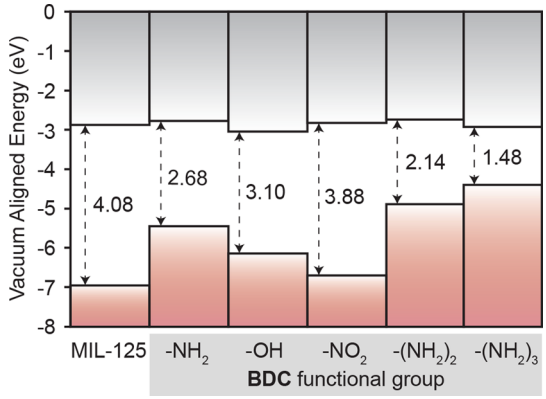

Figure 32. Fermi-aligned band edges of MIL-125 derivatives reveal the addition of states from organic functionalization raise E_F closer to the conduction band edge providing facile band gap modulation. Data obtained from ref 464. Copyright 2018 AIP Publishing.

cases, the linkers can be installed presynthetically, however, linker exchange and postsynthetic functionalization[45,46,52,488] have proven effective to access structures that are otherwise in phase competition or would simply not self-assemble.[489]

Beyond electronic modulation of the band gap via linker and node functionalization, structural perturbation is also a route to alter the electronics of deformable MOFs; the physical structure is another variable parameter in MOFs that may exhibit flexibility or polymorphism. Perhaps the best example is conveyed through the breathing behavior of "wine rack" MOFs.[490−492] The open- and closed-pore structures of several monometallic forms of MIL-53 was computed using the HSE06 functional with Grimme's D3 dispersion correction.[493] The degree to which energy levels (e.g., valence band, conduction band, and band gaps) were perturbed by the strain was quantified with the deformation potential,[102] and the band gap was shown to depend on both the metal composition[493] and framework density Figure 33.[102] This pressure-induced band gap control was further demonstrated with the breathable MIL-47 framework, Figure 33.[102,494]

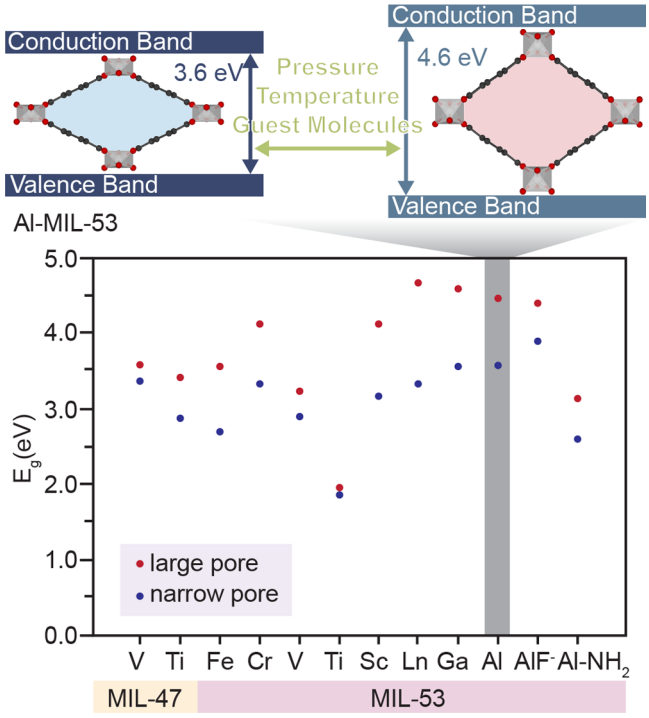

Figure 33. (a) MIL-53 is a prototypical example of the dynamic, ionic construction of MOFs instilling the framework with flexural freedom that alters its macroscopic properties, in this case, band gap energy. (b) the scatter plot shows through calculated band gaps of the narrow pore and large pore forms of several MIL-53 (with M(III) metal cations) and MIL-47 (with M(IV) metal cations) inorganic derivatives that the band gap of more condensed systems (i.e., the narrow pore form) is lower. Adapted with permission from ref 493. Copyright 2015 American Chemical Society.

Because most MOFs feature large discrete band gaps, a tremendous amount of effort has been invested in understanding the electronic structure of a family of 2D MOFs that feature a narrow or zero electronic gap.[19,129,130,218,241,243,495−501] Many of these materials arrange to form hexagonal pores and feature characteristic "Kagome" electronic bands arising from 3-fold degeneracy at certain *k*-points (usually denoted as the K point in hexagonal crystal systems, although strictly speaking the direction of the K vector does depend on the space group).[502,503] As shown in Figure 34, the Kagome bands occur in the conduction band at the K point as seen by the "Dirac cone". If appropriately modeled using SOC,[504] the bands themselves do not cross in *k*-space (the physics underpinning this effect are concisely presented in previously published work).[505,506] While this gap is often very small (10s of meV), the nondegeneracy of these states permits unusual physics.[100,507]

Many of these exotic electronic properties are found in the most well-studied 2D MOF, $Ni_3(HITP)_2$.[19,128,508−510] For example, while both $Ni_3(HITP)_2$ and the Cu(II) analogue are predicted to be bulk metals due to delocalized π-electrons in the out-of-plane direction,[19] $Ni_3(HITP)_2$ features a narrow in-plane gap, and a Dirac cone in the conduction band, Figure 34.[85,511] The out-of-plane stacking orientations have posed problems for modelers, because the anisotropic bonding leads to shallow potential energy surfaces, which provokes long computations

https://dx.doi.org/10.1021/acs.chemrev.0c00148
Chem. Rev. 2020, 120, 8641−8715

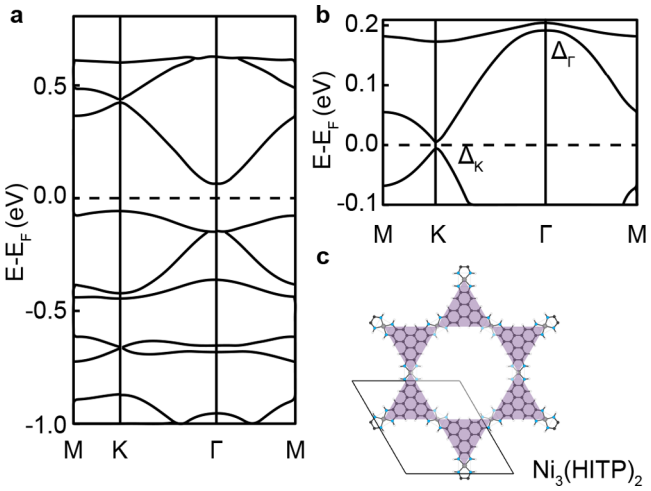

Figure 34. Electronic band structure of monolayer $Ni_3(HITP)_2$ (c) exhibits (a) closed-gap Dirac cones when spin−orbit coupling is ignored. These Dirac cones open upon spin−orbit coupling inclusion, (b), as seen by the enlarged view. Adapted with permission from ref 502. Copyright 2014 American Physical Society.

and dissimilar electronic properties depending on stacking orientation, Figure 35.[512] Interestingly, the hexa-substituted benzene analogue features in-plane metallicity.[128]

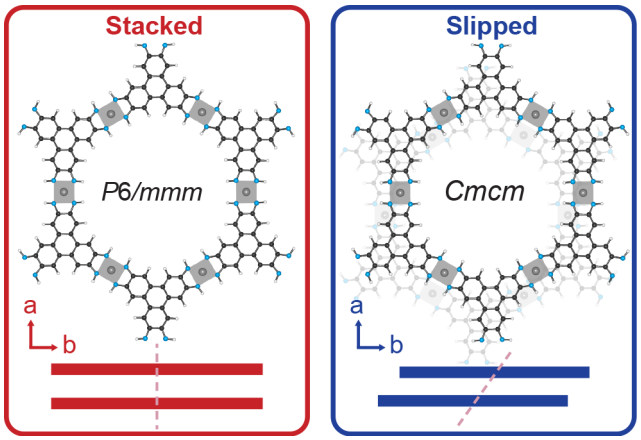

Figure 35. Both eclipsed and slipped stacking modes of $Ni_3(HITP)_2$. The out-of-plane stacking impacts both the π-delocalization of the aromatic systems in the van der Waals direction, as well the crystal symmetry.

While bulk models of $Ni_3(HITP)_2$ are metallic, a band gap is observed in monolayer models. The band gap observed in the monolayer models of $Ni_3(HITP)_2$ (Figure 34) can also be recovered by artificially elongating the intersheet distance. A band gap emerges at approximately 5 Å,[509] and the open metal-sites of square planar Ni(II) are exposed. Foster and colleagues proposed a retrofitting procedure to create a 3D connected version of the catecholate-based MOF based on this exposure.[509,513−515] The influence of metal identity on band gap has of course been assessed (Cu(II), Ni(II), Pt(II), Pd(II), as well as less common Ta(II), Rh(II), and Ir(II));[516] these studies reveal that the metal plays a role in balancing strong electron correlation effects and SOC, while linker redox state seemed to be one avenue to modulate the Fermi level.[517−519521]

Interesting electronic phenomena are also observed in quantum mechanical simulations of isostructural frameworks where the linker motifs bond through sulfur atoms rather than nitrogen. $Fe_3(HTTP)_2$ (HTTP = hexathioltriphenylene), for example, transitions from a bulk metal to having a discrete gap at low temperatures (130 K).[130] PBE-D3 calculations found an intersheet offset of ∼1.25 Å to be the most stable stacking conformation by <100 meV per Fe(II) ion, indicating a shallow potential energy surface.[130] In that study, the material was predicted to be a metal in some sheet orientations, while in others, both the magnetism and geometric structure gave rise to the emergence of a band gap. Indeed, shallow PESs will continue to pose problems for computational chemists; the best effort with this family of 2D materials has been to use the experimental c-parameter and equilibrate within that restriction. Importantly, the slipped orientation perturbs the structure out of a hexagonal space group *P6/mmm* to orthorhombic Cmcm.

In sum, MOF band gap energies can be effectively modified by altering the components on which frontier bands are localized, or adding new states within the existing band gap of a parent MOF through metathesis procedures. Both of these procedures enable predictive power in targeting material properties through systematic DFT studies. Although the band gap energy and frontier band identity play a role in determining the utility of a MOF in both light absorption and electrical applications, the lifetime of the charge carriers depends not only on the gap (or lack thereof) but rather on the charge. The following sections will discuss how the electronic band structure and DOS of a material can be used to predict electronic behaviors, among them charge mobility.

4.3. Electronic Band Structures

Electronic band structures are a plot of electronic energy as a function of *k*-space (i.e., electron momentum). The shape of the bands provides tremendous amounts of information about material properties, including the potential to transport charges, overall material stability and, to the trained eye, even the composition. Given MOFs are made from discrete molecules, it is somewhat unsurprising most feature localized (i.e., flat) electronic bands that facilitate the use of cluster models (section 3). However, through development with a complement of experiment and theory, there are increasing examples of MOFs featuring curved (i.e., dispersive) bands and interesting MOF applications that rely on the description of bulk electronic structure. Thus, this section will discuss the calculation and implications of MOF electronic band structures.

The electronic band structure is simply constructed by sampling the energy of electrons at various *k*-points. The difference in energy between the bottom and top of the band at two dissimilar *k*-points is referred to as the bandwidth, or band dispersion, and is essentially a measure of the "curviness" of the bands. Higher band dispersion means more mobile charge carriers and also indicates something about the extent of orbital overlap and long-range interactions in that crystallographic vector. Because these plots ultimately depict electron momentum, the second derivative of a band near a high symmetry *k*-point (sometimes called special points) yields the effective mass of a charge carrier in that band.

Perhaps it is somewhat intuitive that a highly symmetric crystal would feature a large degree of electronic degeneracy within the unit cell; it is less intuitive to imagine how crystal symmetry affects the bulk electronic properties, i.e., those that extend beyond a single computational cell. As mentioned in the previous section, the material should be properly equilibrated using all of the high symmetry *k*-points in addition to a dense

https://dx.doi.org/10.1021/acs.chemrev.0c00148
Chem. Rev. 2020, 120, 8641−8715

grid between them. Practically, however, this is often impossible, but also unnecessary; generally flat-banded materials (like MOFs) can be described with Γ-only sampling because the insulating interface between the metal and ligand is sufficiently accounted for by explicit orbital interactions within the computational unit cell.[21,522,523] It is, however, typically good practice to sample all labeled high symmetry *k*-points for the given space group,[432,524,525] as presented in the *Bilbao Crystallographic Server*,[433] ensuring that the total energy has included all important long-range interactions.[526]

Although the chemical connectivity in MOFs is usually highly symmetric, MOFs themselves have highly anisotropic electron density through the crystallographic unit cell: there are pores! Thus, it is expected that the electronic band structures should contain some interesting information, albeit subtle, arising from the periodic absences of electron density. Indeed, one paradigm in the conductive MOF literature is whether the charge carriers are more delocalized through-space or through-bonds.[527,528] The band structure sheds light on this. Consider two similar scaffolds made from π-stacked triphenylene-based linkers: in the case of Ln(hexahydroxytriphenylene), the inorganic nodes form continuous ionic bonds throughout the material,[258] whereas in $Ni_3(HITP)_2$ the sheets are nonbonded. In both cases, the greatest band curvature is found to be centered on the linker, but associated with the out-of-plane direction. In other words, the conductivity mode is "through space".[527,528] The delineation of "through-bond" or "through space" should not be confused with that between band or hopping conduction, which are separate mechanisms that can be distinguished by the presence of an activation energy associated with the conduction.[527,529,530]

Electronic band structure calculations primarily serve to graphically identify crystallographic directions in which electrons are highly delocalized and strongly interacting. Such plots contain a significant amount of information when paired with the crystal structure and a map of the high symmetry *k*-points for the MOFs parent space group. The analysis can be further complimented by quantitative analysis of the electronic band dispersion (a concept we have already introduced), and most importantly, the density of states.

4.4. Electronic Band Dispersion

Band dispersion is the difference in energy of a band between two high symmetry points in reciprocal space. Greater dispersion is thought to indicate the material may be a better electrical conductor in that direction.[531] Perhaps a more apt description is to think of dispersion (or curvature) as an indicator of electron and hole delocalization. In this mindset, the "effective mass" of a charge carrier can be computed to quantify the extent of delocalization associated with a band. In doing so, the mass of a free charge carrier in vacuum, m_0, is renormalized to describe its behavior in the periodic potential of the MOF. The second derivative of a band near a special point or crossing the Fermi-level yields the effective mass, m^*, of the electron or hole that would populate that band via

$$\frac{1}{m^*} = \frac{1}{\hbar}\frac{\partial^2 E(k)}{\partial k^2} \tag{4.1}$$

where $\hbar$ is the reduced Planck's constant.[532] In practice, this is readily solved by fitting a parabola to a series of *k*-points very near the point of interest. Often, practitioners will present both "heavy" and "light" effective masses, corresponding to the bands with the least and most curvature, respectively.

As an example of the utility of quantifying band dispersion, we highlight the electronic band structures of sheet-slipped $Co_3(HTTP)_2$ computed with PBE-D3.[129] In this case, $Co_3(HTTP)_2$ is thought to conduct through-space (the authors also conjecture a band transport mechanism from their experimental data).[129] While the transport mechanism remains open to debate, computations suggest that the direction of conduction (i.e., in- vs out-of-plane) in $Co_3(HTTP)_2$ is likely to be out-of-plane with effective masses of $1.29m_0$ (M−Γ and A−H) and $0.29m_0$ (Γ−A), respectively, Figure 36. A similar study was performed for the Fe-based analogue and the average effective mass (m^*_{avg}/m_0) was determined to be $0.88m_0$.[130,533]

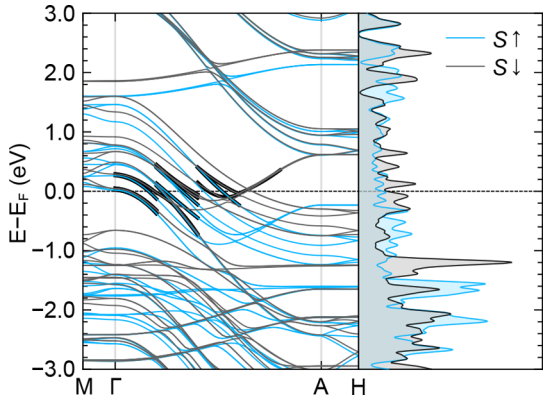

Figure 36. Electronic band structure of $Co_3(HTTP)_2$ and the associated spin-separated density of states. The Fermi level crosses bands in the Γ−A vector, indicating this material is metallic. Reproduced with permission from ref 129. Copyright 2017 American Chemical Society.

Beyond elucidating intrinsic conduction pathways, monitoring changes to the effective mass in the presence of small molecules has been applied to develop MOFs as chemiresistive sensors.[534,535] Chemiresistive sensors operate by measuring changes in conductivity from charge localizing at binding sites, a property that is indicated by the flattening of bands, i.e., changes in the effective mass of the charge carriers. Electronic band structures of desolvated MOF-74 suggested that the heavy charge carriers exist perpendicular to the direction of extended inorganic connectivity (~$200m_0$) while the electron effective mass was ~$2m_0$ along this pathway.[534] Binding of small gas molecules (and likely solvent) changes the electron effective mass; upon binding of CH_4 the electron effective mass increases to $250m_0$, yet binding of CO_2 reduces the electron effective mass to $56m_0$ and H_2 to $160m_0$. While this study shows that MOF-74 does feature a notable change in charge carrier effective mass, the effective masses were too low to be used in a practical application.

A final consideration in the computation of the electronic band structure is that while the computed band dispersion is recovered from temperature-independent DFT, the experimental observation of the band dispersion itself does depend on temperature. Thus, dispersion energies less than kT (i.e., the Boltzmann distribution at the operating temperature) are lost by the thermal smearing of states and can be considered essentially flat; the precision enabled by DFT may cause the appearance of subtle electronic phenomena, such as an indirect band gap, that are inconsequential under realistic thermal conditions. This particular issue was highlighted in a recent publication, where the authors predict band dispersion on the order of kT (<30

https://dx.doi.org/10.1021/acs.chemrev.0c00148
Chem. Rev. 2020, 120, 8641−8715

meV) and attributed the observable bulk properties of Zn-SURMOF-2[536] to this dispersion and its indirect band gap. While it is difficult to imagine a dispersion of this magnitude being a factor at room temperature, it does highlight that periodic DFT is precise and does enable high fidelity studies of dissimilar electronic states in materials with subtly changing energetics.

4.5. Density of States

DOS plots are critical to assessing electronic band parentage, providing information about the type of charge transport that may exist, be it ligand-to-ligand, metal-to-ligand, ligand-to-metal, or metal-to-metal fundamental gap. Hence, together with the electronic band structure and analysis of band dispersion, the DOS paints a comprehensive picture of the MOF's anticipated function.

The integral of the DOS indicates how many electrons occupy that energy level, and its parentage informs which atoms/orbitals are contributing to that energy level. Often, DOS plots are partitioned into atomic specific contributions (atom-projected DOS, pDOS) or orbital specific contributions (orbital-projected DOS), providing tremendous amount of insight into the nature of the bands in a material, as well as a lens through which the effects of linker functionalization, compositional substitutions, and interstitial influences may be assessed.[537−540] The DOS is computed for all sampled *k*-points, enabling practitioners to examine the DOS at a single *k*-point, or the sum of them. The former can be helpful when MOF bands cross one another in *k*-space and has been used fruitfully in MOF calculations for systems with large unit cells.[541]

In spin polarized materials, the DOS representation may be further partitioned by spin; the spin-refined DOS plot of a $Mn_3(HTB)_2$ (HTB = hexathiobenzene) monolayer reveals that the material is a "half-metal" with a band gap of 1.54 eV in one spin channel with metallic bands in the other, Figure 37.[542] Similar behavior was identified for Mn(II)-PBP (PBP = 5,5′-bis(4-pyridyl)(2,2′-bipirimidine)).[543] This knowledge is valuable because the spin bias afforded by the high degree of spin-splitting is advantageous for spintronic devices that require precise control over electron dipole orientation.[544]

DOS plots have also been helpful in determining the directionality of charge transport in conductive MOFs. Charge hopping is likely the mechanism of electron transport in most MOFs, commonly promoted accessing mixed valency through either partial redox of the metal/linker or via photoexcitation.[545−549] Of the relatively conductive MOFs, those with the largest electrical conductivities typically contain an accessible iron redox couple.[550,551] One of the most conductive 3D MOFs, $Fe(tri)_2$ (tri = 1,2,3-triazolate), undergoes facile oxidation to yield an electrical conductivity enhancement from 10^{-9} to 10^{-1} S/cm.[236,552] From a hybrid GGA calculation, the pristine divalent material is predicted to have a band gap of 4.4 eV; partial oxidation of the framework creates midgap Fe(III) *d*-states seen in the DOS although (the density of these states is proportional to the extent of oxidation), decreasing the band gap to 1.5 eV, Figure 38.[550] The same design principle was used in a variety of other Fe containing MOFs, including $Fe_2(BDT)_3$,[541] $(NBu_4)_2Fe^{III}(dhbq^{-2/-3})_3$ (dhbq = 2,5-dioxidobenzoquinone/1,2-dioxido-4,5-semiquinone),[553] and $Fe_2(DSBDC)$ (DSBDC = 2,5-disulfidobenzene-1,4-dicarboxylate).[554] In all cases, the authors attribute the increase in electrical conductivity to a loosely bound β-spin electron of Fe(II), which acts as the source of the enhanced rate of charge hopping.[555]

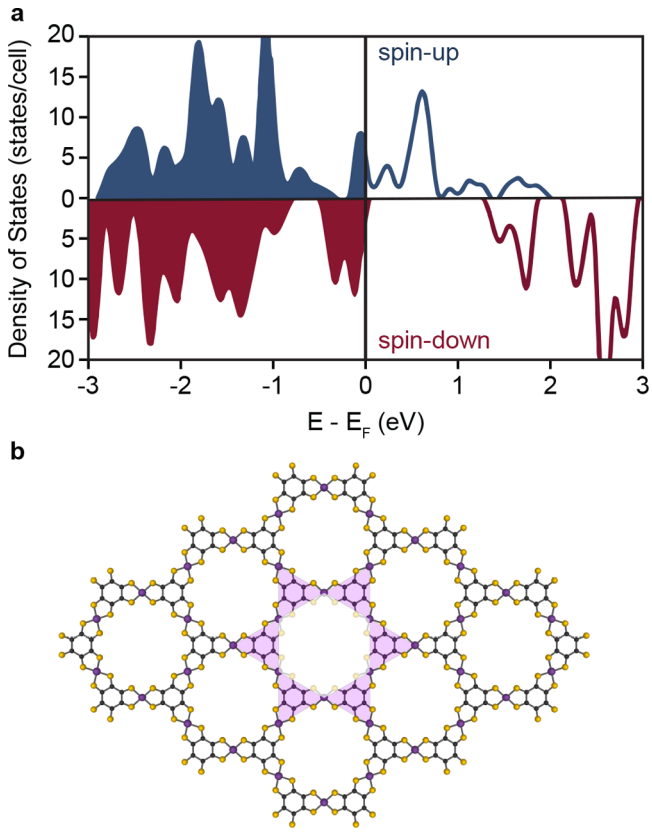

Figure 37. Spin-separated DOS (a) of the $Mn_3(HTB)_2$ Kagome lattice illustrated as the purple shading of the 2D planar $Mn_3(HTB)_2$ supercell (b) show the unique half-metallic property of being a metal in one spin-channel but a semiconductor in the other. Adapted with permission from ref 542. Copyright 2014 American Physical Society.

There are also fleeting reports of Fe(III) reduction as a route to installing electron charge carriers (i.e., *n*-type doping). In a landmark publication, $Fe_2(BDP)_3$ (BDP = 1,4-benzenedipyrazolate)[557] was reduced, enabling Fe(II) charge delocalization that mimics classic $d^{5/6}$ bimetallic molecular complexes.[558] Fractional reduction of $Fe_2(BDP)_3$ with potassium naphthalenide to yield $K_xFe_2(BDP)_3$ $(0 \leq x \leq 2)$ accessed nearly a 10 000-fold conductivity enhancement experimentally.[557] Here, the authors performed their calculations on an approximate solid-state system, with the linkers being truncated to their inner-sphere pyrazolates, likely to reduce computational cost (Figure 39). Chemical reduction of the framework was modeled with periodic boundary conditions by adding a single electron to a six-iron super cell ($[Fe(pz)_3]_6$), in the absence of a potassium counterion.[557] The concept of ligand n-doping was also demonstrated using reduction of the organic linker in a naphthalene diimide-containing MOF.[546]

Similar computational procedures have been applied to probe the oxidation of organic linkages. The family of M_2TTFTB (TTFTB = tetrathiafulvalene tetrabenzoate) MOFs[559] have a valence band that is highly delocalized along the π-stacked TTFTB chain, Figure 40.[560] The directionality of charge transport was exploited such that only the out-of-plane lattice vector was sampled to assess band dispersion. Upon oxidation, the hole was free to hop along the extended π-stacked pathway. MOFs that feature the same linker but do not crystallize with extended π-overlap, feature much lower electrical conductivity.[411]

https://dx.doi.org/10.1021/acs.chemrev.0c00148
Chem. Rev. 2020, 120, 8641−8715

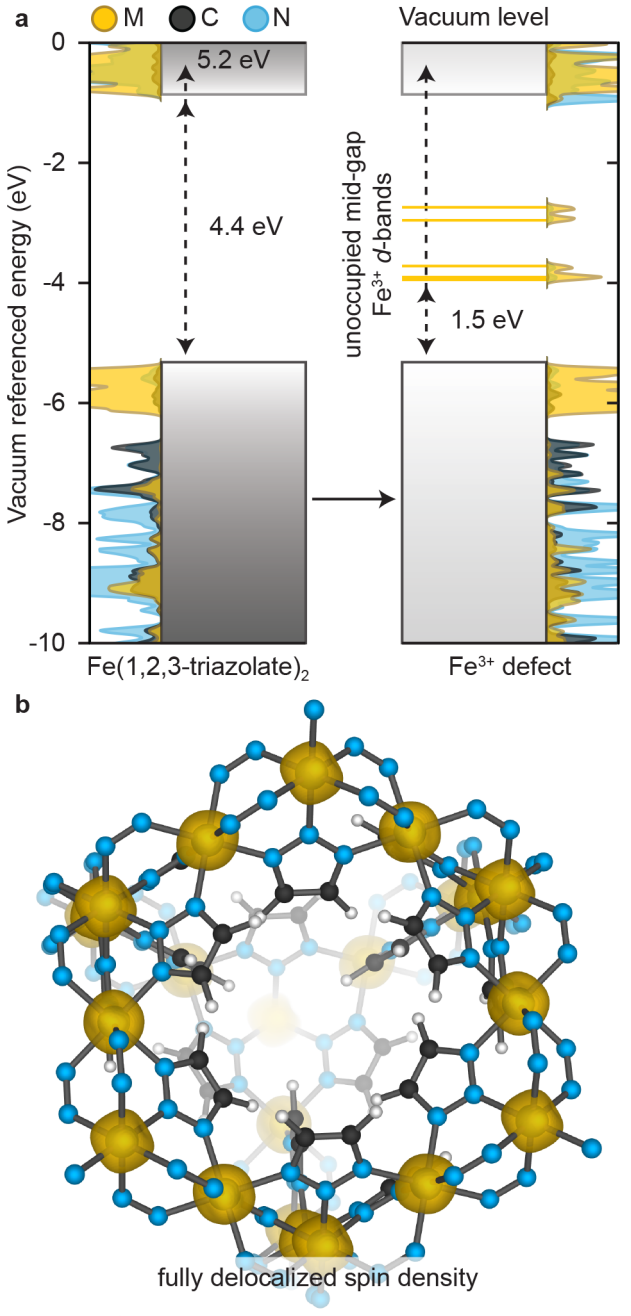

Figure 38. (a) The density of states for the Fe^{2+}-containing MOF, $Fe(1,2,3\text{-triazolate})_2$ features the emergence of midgap Fe^{3+} *d*-bands. (b) The spin-density of the high spin Fe^{3+} defect is fully delocalized over all Fe atoms in the system. Image reproduced with permission from ref 556. Copyright 2017 Royal Society of Chemistry

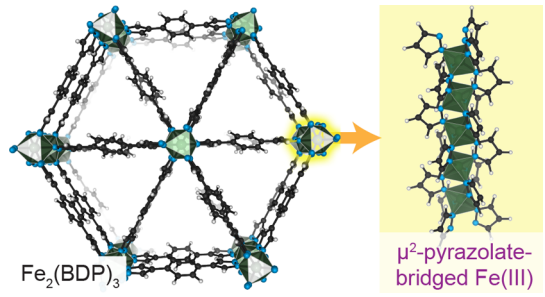

Figure 39. Directionality of charge motion in $Fe_2(BDP)_3$ was exploited in order to generate the electronic band structure and projected density of states for $Fe_2(BDP)_3$ upon elimination of the extended structure in two-dimensions to generate the 2-pyrazolate-bridged Fe(III) so that the 1D interactions that drive electron transport could be examined. Data obtained from ref 557.

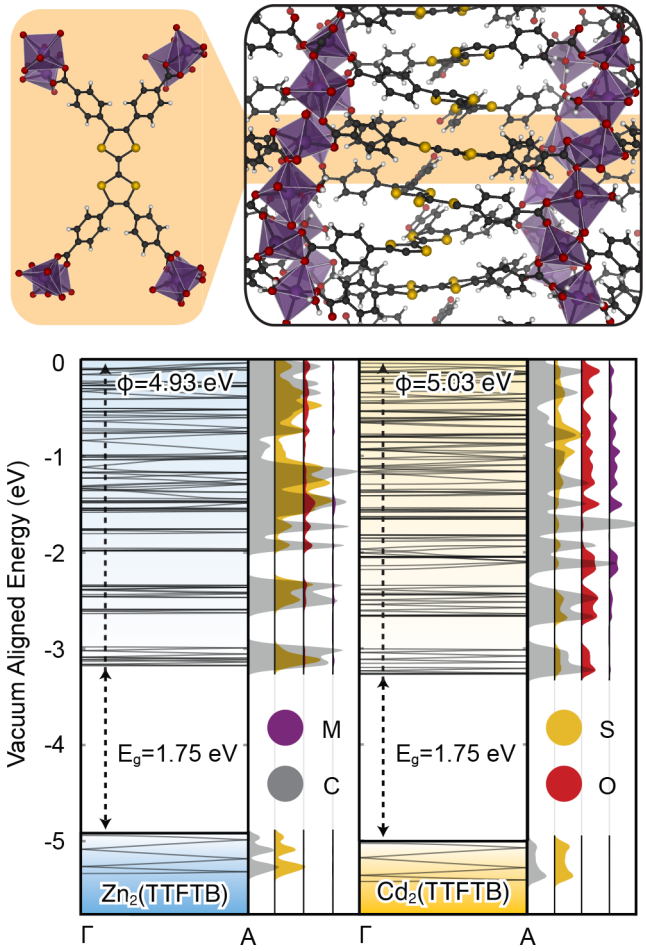

Figure 40. Electronic band structure and correlating density of states for $M_2(TTFTB)$ where M = Zn or Cd shown as gray polyhedral, >300 meV band dispersion of a 6-fold degenerate valence band is observed.

Obviously, DOS plots are instructive beyond the paradigm of visualizing possible charge transport pathways. A more subtle invocation of pDOS plots was applied to a Ni/Co bimetallic ultrathin MOF nanosheet to indicate electronic coupling between metals.[225] Charge transfer between the metals was deduced visually by comparing the pDOS plots for mono-metallic Co- and Ni-MOFs and the mixed Co/Ni-MOF. The authors report that electronic coupling across metal centers results in an increase and decrease in the density of unoccupied e_g states for Ni and Co, respectively, due to a balance between electron−electron repulsion and π-donating abilities, Figure 41.

In sum, the electronic DOS provides a detailed view of the atomistic contributions to energy levels, which can be quite complex for large chemical systems. Information gleaned from these analyses gives modelers the ability to predict the locality and direction of electron transfer, which are important in catalytic applications. The DOS also helps classify a material as a metal or semiconductor/insulator based on the absence or presence of density at the Fermi level. However, this section only focused on the utility and application of *electronic* DOS, which

https://dx.doi.org/10.1021/acs.chemrev.0c00148
Chem. Rev. 2020, 120, 8641−8715

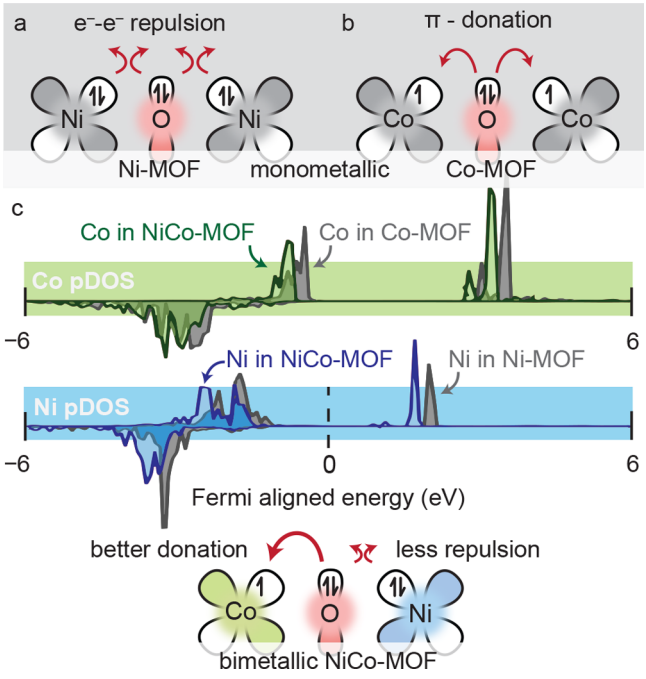

Figure 41. Fermi-aligned DOS of monometallic MOF nanosheets built with (a) Ni and (b) Co revealed the resultant alteration of *d*-state density associated with bimetallic species (c). Ni(II) species experience electron repulsion from inorganic oxo ligands, while Co(II) species experience π-donation from the inorganic oxo ligands. These individual effects behave cooperatively in the bimetallic species; the donation of electron density from oxygen to Co(II) diminishes electronic repulsion from Ni(II). Data obtained from ref 225.

can be identified at a single *k*-point or summed over the entire *k*-grid. A similar sampling and DOS analysis can be performed on vibrational band structures (i.e., phonon bands), where the DOS then describes the population of oscillators, a dynamic phenomenon.

4.6. Lattice Vibrations: Phonons

While the focus of this review is on static modeling rather than structural dynamic events, thermal properties and electronic structure are fundamentally interdependent, e.g., conduction bands in a semiconductor become populated with increasing temperature and increased conductivity is observed in a metal at lower temperatures. The phonon discussion will thus be limited to the general theory and utility in unison with electronic structure methods. Exciton behavior in semiconductors, for example, has intrinsic dependence on electron−phonon coupling such that electronic excitations, exciton recombination, and charge transport processes may be mediated by the active phonon modes.[561] Identifying the lattice vibrations and structural components that enhance or hinder the desired electronic events enables refinement of the chemical system.[562]

The ground-state electron density obtained through self-consistent DFT procedures yields first derivatives of the total energy such as the forces acting on nuclei; phonon frequencies are a second-order derivative and require additional perturbative analysis of the electron density.[563,564] Phonon frequencies are therefore obtained by measuring the lattice response to ionic perturbations through either direct or linear-response approaches.[565] The direct approach calculates the force constants in a supercell built from translations of the primitive cell in response to explicit lattice distortions to construct the dynamical matrix,[566] while the linear response approach invokes a relationship between harmonic force constants and perturbation to electron density in order to reduce computational expense.[567]

The frozen-phonon technique is the simplest of the direct approaches wherein the quadratic dependence of total energy on ionic displacements is exploited to extract the frequency of the phonon mode acting normal to a displacement (typically 0.01 Å);[170,534,568,569] the force constant matrix is constructed by displacing each atom in the cell and calculating the resulting forces on every other atom.[570] Only phonon-modes with wave vectors smaller than the unit cell can be computed with this approach, commonly mandating supercells. Using the Hellman−Feynman theorem, force constants can be obtained from Fourier transformation of the dynamical matrix constructed through density functional perturbation theory (DFPT). DFPT involves the direct computation of second derivatives as the system response to application of an external potential, giving access to the dynamical matrix regardless of wave vector without the need for supercell construction.[122,571,572] Force constants obtained through either finite displacement methods or DFPT can be used to further compute phonon band structures and DOS as well as other thermal properties.[573]

The simplest applications of phonon calculations in MOFs have aimed to identify the active vibrational modes that contribute to structural transitions such as negative thermal expansion,[574−576] adsorbate induced distortions,[577] or thermal transport abilities.[568,569] First, the presence of an imaginary (negative) vibrational frequency indicates either dynamic instabilities (if the negative modes occur anywhere besides Γ), or absolute instability (if the negative modes occur at Γ).[578] Phonon DOS and band structures constructed with MOF-5 supercells were used to assess structural dynamics.[579] These studies, performed at the Γ-point, invoked the finite distance method with displacements of 0.01−0.03 Å. The origin of negative thermal expansion observed with this system was found to originate from the trampoline mode associated with BDC linkers, Figure 42.[579,580] Vibrational modes further give access to

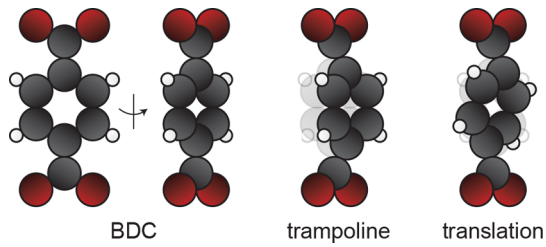

Figure 42. Linker-derived low frequency phonon modes are linked to the negative thermal expansion of MOF-5, presented in ref 579.

experimental data such as experimental IR and Raman spectra, which aids both in benchmarking theoretical models and interpreting experimental spectra. Studying the hydrolytic degradation of MOF-74, the growth of a new peak in time-resolved IR spectra was identified as the O−D stretch of a deuterated carboxylate terminus by invoking phonon mode analysis; from this structure and vibrational mode, a pathway and the associated kinetic barriers were able to be derived for the overall reaction.[581]

Indeed, of greater interest to electronic structure modeling is the impact of phonon interactions on electronic transitions and other energetic pathways. DFT calculations are temperature-independent, often approximated as 0 K, which neglects the

https://dx.doi.org/10.1021/acs.chemrev.0c00148
Chem. Rev. 2020, 120, 8641−8715

impact of molecular vibrations on properties of interest. To account for thermal contributions, phonon frequencies must be inserted into the vibrational partition function to obtain thermodynamic quantities such as the zero-point energy (ZPE) correction and vibrational finite-temperature corrections to internal energy, entropy, and free energy as performed to determine the mechanical and catalytic properties of V-MIL-47.[583] The thermal analysis employed to recover the zero-point energy typically involves obtaining the SCF harmonic frequencies for the system in question using the rigid rotor/harmonic oscillator approximation.[582,585] Finite temperature contributions[584] may be considered to complete the contribution of nonpotential energy terms. Theoretical frequencies are typically larger than experimentally observed values due to the neglect of anharmonicity in the theoretical treatment.[586−591]

Electron−phonon coupling plays a key role in nonradiative recombination processes, Figure 43. First-principle phonon

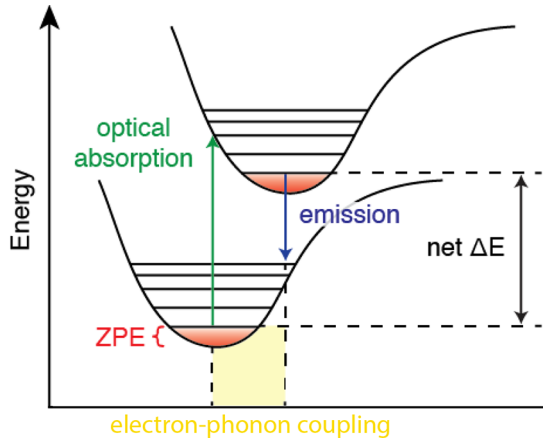

Figure 43. Contribution of phonon modes to electronic properties is a function of changing ionic positions altering the available energetic states and symmetry allowed transitions.

calculations cannot directly provide the rate of electron−hole recombination, however, nonadiabatic ab initio molecular dynamics simulations (AIMD) have been implemented to predict exciton decay and recombination rates.[592,593] As a demonstration of this, Syzgantzeva and colleagues showed that phonon modes for Zr-UiO-66-NH_2 recovered with the finite displacement method were correlated to the frequencies of optical transitions in order to identify which modes were associated with phonon-assisted nonradiative decay.[594] Vibrations contributing to electron−hole recombination process were found to be low frequency soft modes comprised of both ligand and node displacements. Design strategies targeting the suppression of soft phonon modes to extend charge carrier lifetime may therefore be developed via either metal or ligand exchange.

The utility of phonon calculations further extends to the prediction of electronic conductivity. Charge mobility, for example, is encumbered by phonon-scattering events. Predicting the motion of an electron through solid-state materials requires a multifaceted analysis accounting for not only the intrinsic electronic structure but also the nature of the charge carrier and its interaction with other lattice properties. To elucidate the effect of linker functionalization on the electrical conductivity of Zr-UiO-66, the conductivities of a pristine model and two substituted derivatives were calculated via the expression $\sigma = q\mu n$, where σ is the electrical conductivity, μ is the charge mobility, n is the charge carrier density, and q is the charge of the carrier.[595] Charge mobility was calculated using the Boltzmann equation with a relaxation time approximation derived by Bardeen and Shockley for nonpolar semiconductors[596]

$$\mu = \left(\frac{C_1 \hbar^4 q}{E_1 q}\right)^2 (m_e m^*)^{5/2} (T k_B)^{3/2} \tag{3.1}$$

where C_1 is the elastic constant, E_1 is the 3D deformation potential, m^* is the parabolic effective mass, and m_0 is the mass of an electron at rest (a constant). Generally, the Boltzmann expression of Bardeen and Shockley is applicable to materials with low moduli where acoustic phonon scattering is likely to be the dominant electron scattering mechanism.[596] As discussed in section 3, the effective mass along a specified k-path can be estimated from the electronic band structure via

$$E = \frac{\hbar k^2}{2m^*} \tag{3.2}$$

The 3D deformation potential descriptor, which offers a relationship between the phonon mode and an electric scattering potential to account for the probability of interband scattering, can be found by fitting a linear equation to the energy of the LUMO as a function of strain

$$E_{LUMO} = E_1 \times \varepsilon + E_0 \tag{3.3}$$

The elastic constant quantifies material resistance to deformation and can be estimated by relating the volumetric strain energy applied through finite displacements to the total energy, E

$$E = \frac{1}{2} V \cdot C_1 (1 + \varepsilon)\varepsilon^2 + E_0 \tag{3.4}$$

where V is the volume of the cell and ε is the strain. Lastly, the charge carrier density can be estimated by integrating over the DOS, $g(E)$, and the Fermi−Dirac distribution, $f_D(E)$,[597]

$$n = \int_{LUMO} g(E) f_D(E)\, dE = \int_{LUMO} \frac{g(E)\, dE}{1 + \exp[(E - E_f)/k_B T]} \tag{3.5}$$

where E is the total energy, E_F is the Fermi energy, k_B is the Boltzmann constant, and T is the temperature. Ultimately, functionalization of UiO-66 BDC with both NH_2 and NO_2 resulted in decreased conductivity due to a reduction in charge mobility. However, linker functionalization increases the number of occupied states near the LUMO in MOFs; functionalization of linkers may thus be viewed as a route to enhancing carrier concentrations in MOFs with ligand-centered frontier bands.

Charge mobility of the UiO-66, UiO-66-NH_2, and UiO-66-NO_2 Zr(IV) family was further assessed as a function of inorganic substitution with Ti(IV) and Hf(IV) using the same relaxation time approximation.[598] Because of the small band gap from titanium d-states at the CBM, Ti(IV)-UiO-66-NH_2 yielded the highest conductivity value (1.0×10^{-7} S/cm), despite having the smallest intrinsic mobility, because the charge carrier concentration compensates for the localization of frontier conduction band on titanium.[598] Together, these UiO-66 investigations isolated the impact of linker functionalization and metal identity on the various contributions to electronic

https://dx.doi.org/10.1021/acs.chemrev.0c00148
Chem. Rev. 2020, 120, 8641−8715

conductivity. Charge mobility was thus found to be dependent on metal identity due to its impact on electron−phonon scattering, while charge carrier density could be augmented with both organic and inorganic substitution.

Phonon calculations have clear utility in unifying the static DFT approach with thermal contributions to electronic properties in the absence of molecular dynamics simulations. The simulation of vibrational spectra including Raman and IR are further enabled by recovering the phonon modes: the ability to assign discrete spectroscopic handles with a material motion is helpful both for structural determination and overall characterization. However, phonon analysis is typically resource limited to highly ordered materials, where the phonon band structure may show interesting dispersion at high symmetry *q*-points. Yet, a burgeoning area of interest in the MOF community is the study of materials with reduced symmetry, either due to melting or defects.

4.7. Defects

In the previous sections, MOFs have largely been treated as pristine, defect-free extended solids. Indeed, periodic boundary conditions demand crystallinity. This approximation is deeply rooted in the characterization of MOFs, as evidenced by the procedures for obtaining the crystal structure, pore volume, and gas uptake properties, which typically assume a pristine architecture.[599] However, defect formation is entropically favorable,[600] thus all materials contain defects. Indeed, significant effort has been invested in *minimizing* experimental defect concentrations,[601] but defects can also give rise to highly desirable properties (including the formation of charge carriers via doping pathways, open metal sites for catalysis, creating chromophores,[602] etc.),[603] and as such are an emerging area of interest to the MOF field.[604]

In conventional crystalline materials (e.g., Si) there are three general types of defects: (i) vacancies, where an atom is missing from the lattice, (ii) substitutions, where a lattice atom is exchanged for one that does not normally occupy that lattice site, and (iii) interstitials, where an additional atom is in a typically unfilled lattice site.[605,606] MOFs regularly exhibit vacancies in the form of missing nodes or linkers,[375] and substitutions through isoreticular chemistry or postsynthetic metathesis, Figure 44.[607] Further, MOFs can play host to a variety of species within their pores, which can be considered interstitials.[608] Each of these defect types may spawn additional functionality and modularity to the parent framework, the most catalogued of which is the liberation of active sites for catalysis via linker vacancies.[609]

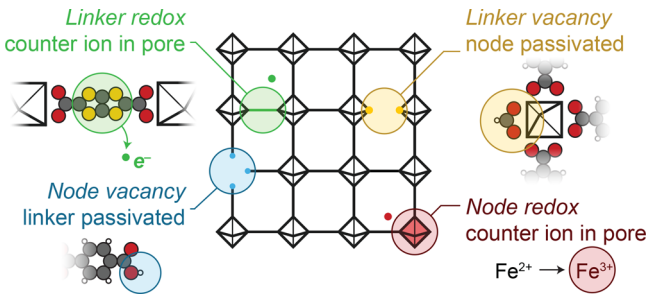

Figure 44. Node or linker vacancies result in charge balancing ions bound to the vacant sites (e.g., a proton or formate). Both nodes and linkers can also be redox active forming structurally bound charge carriers.

Pairs or groups of these lattice point defects yield further terminology: Frenkel and Schottky defects. A Frenkel defect is essentially a vacancy and compensatory interstitial that yield a charge neutral material, while Schottky defects are defined by multiple vacancies that sum to zero charge. Because MOFs are ionic, both Frenkel and Schottky defects are common. For example, a combined node and linker vacancy may be considered a Schottky defect and a linker omission passivated by an additional formate may be considered a Frenkel defect. Moreover, exotic Frenkel defects may be installed by including a charge balancing ion within the pore after the redox of a MOF component (Figure 44); this is uniquely enabled in MOFs considering they contain large amounts of vacuous space to support the ions.[765−769]

Because defects are often enthalpically disfavored, and installation is driven by entropy, there is a concentration limit at which the free energy of the formation of additional defects becomes positive. The defect concentration limit depends on the host material, but conventional semiconductors are limited to only a few percent.[610] Because of their low lattice density and limited electronic delocalization, MOFs can uniquely exceed these concentrations by at least an order of magnitude, sustaining very high vacancy populations.[226] For example, MUF-32, can reversibly reach linker vacancy defect concentrations of 80%.[611] These high defect concentrations come as a mixed blessing because on one hand we are able to model them in a crystallographic unit cell and not have to worry about their effective concentration, but we must worry about the impact of artificial defect periodicity. Hence, one challenge with pristine models is that they neglect the electronic impact of defects present in real systems. For example, experimental measurements on $Ni_3(HITP)_2$ thin films indicate semiconducting behavior in contrast to theoretical predictions.[85,612] Critical analysis of the available experimental characterization of $Ni_3(HITP)_2$ deduced structural defects must be governing electron mobility; computational models depicting internal interfaces demonstrated that polycrystallinity hinders electron flow.[511]

The following subsections will serve to revisit methodologies that relate to electronic properties of MOFs in which vacancies (section 4.7.1), substitutions (section 4.7.2), and interstitials (section 4.7.3) have been shown to alter bulk behavior through QM methods, largely through discussion of UiO derivatives.

4.7.1. Vacancies. Vacancies occur as either missing linkers or metal clusters, as well as single atom omissions from the inorganic clusters.[613] The elucidation of experimental vacancies is extremely challenging in MOFs and other solids, often requiring a potpourri of experimental methods (PXRD, EXAFS, NMR, IR, etc.) to extract even an average defect concentration per node.[376,614,615] As a result, we are still learning about their formation in extremely well-studied materials and only have a rudimentary understanding of their formation.[616−619]

To completely characterize a defect in MOFs, a combined theory and experimental approach is often required. For example, the identity of anionic species coordinated to the node at a linker vacancy in UiO-66 and -67 was obtained by IR and NMR experiments; the catalytic mechanism occurring at active sites defined by these defects was then studied with an appropriate cluster model to assess reagent adsorption in the presence and absence of linkers.[620] More advanced experimental methods, such as diffuse scattering, electron microscopy, transmission electron microscopy, and electron crystallography,

https://dx.doi.org/10.1021/acs.chemrev.0c00148
Chem. Rev. 2020, 120, 8641−8715

have also been paired with theory to refine structural motifs of defects.[621,622]

Periodic models, however, still face challenges for defective systems because of the cost associated with forming a unit cell sufficiently large enough to mitigate artificial defect ordering.[623] Furthermore, vacancies are realistically either anionic or cationic and often compensated by an adventitious counterion, mandating some charge passivation routine.[624] In experiment, these ions originate from the salts or solvents used in the synthesis, and these salts can be used to inform model construction.[625]

Modulators can be used to deliberately install linker vacancies as they compete with the multitopic linker to bind to the metal node either during synthesis or postsynthetic modification.[607,608,614] Cluster vacancies may be targeted by achieving multiple linker vacancies; this causes either an absence of a linker for the cluster to bind to or the stability of an already bound cluster to be compromised.[377] Linker vacancy concentration may be tuned using a variety of synthetic conditions ranging from modulator concentration and acidity[626] to solvent selection.[627,628] Selectively altering linker vacancy concentration not only enables cluster vacancy formation but also affords defect engineering, which can be used to intentionally alter macroscopic properties. For example, increased modulator concentration during synthesis correlated to increased gas uptake in defective UiO-66 due to additional missing linkers, as experimentally demonstrated by Wu et al. with N_2 uptake isotherms.[629]

Most computational defect studies have been performed on the UiO-series of materials, as they are known to feature high concentrations of defects. Both linker and node vacancies have been extensively explored: a recent study showed that linker vacancies capped with trifluoroacetate are more resistant to hydrolytic and acidic degradation, Figure 45.[630] By systematic construction of periodic models with differing defective forms, vacuum-aligned DOS spectra demonstrated only slight changes to frontier bands and band gap with linker vacancies, but larger perturbations in the case of missing clusters.[369]

Kinetic insights into defect formations can help bridge the gap between pristine ground states and observed materials. To address this, one could employ ab initio molecular dynamics to identify intermediate species formed during linker removal, followed by nudged elastic band (NEB, section 5.1.2) to refine the energetic path between intermediates of interest.[631] As an example, the role of dehydroxylation in the kinetic formation of linker vacancies has also been explored.[632] From NEB, dangling hydroxyl bonds were found to match unassigned IR stretches from experimental characterization of UiO-66 samples; decoordination of BDC and an associated hydroxyl is followed by protonation of the dangling hydroxyl and water desorption. The activation barriers were found to decrease in energy with increasing linker defects, suggesting the formation of linker vacancies might be correlated. This finding is further consistent with experimental work on linker vacancies in UiO-66(Hf).[621] Indeed, vacancy defects can be used to anchor adatoms and interstitials enabling catalysis. The challenge then becomes deliberate installation of such defects—an area we expect DFT will prove useful toward guiding experiments in the future.

4.7.2. Substitutions. A substitution involves removing a chemical component from its lattice site and replacing it with a different species;[605,606] in MOFs, this takes the form of a linker[79,149,220,464,475,627,633−638] or metal[19,221,460,479,484,560,634,636,639−646] substitution. Considering

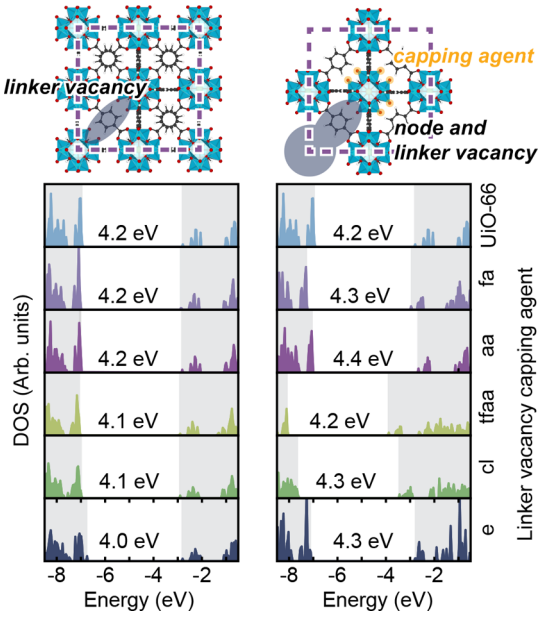

Figure 45. Band gap and DOS were compared for two defective UiO-66 models, with one featuring a linker vacancy (left) and one featuring a node and four linker vacancies (right), as a function of capping agents (fa = formic acid, aa = acetic acid, tfaa = trifluoroacetic acid, cl = Cl^-/H_2O, e = dehydroxylated metal cluster). The band gap and DOS for pristine UiO-66 is pictured for reference at the top. Data obtained from ref 630.

the parent MOF as the "pristine" lattice, linker functionalization (e.g., BDC to amino-BDC) can also be considered a linker substitution, where the undecorated linker is entirely replaced by a new, functionalized linker. Substitution defects can be intentionally created at the former site of a vacancy (the most extreme example can be thought of as retrofitting[513]) or through postsynthetic ligand and metal exchanges.

Computational explorations of linker functionalization and metal substitution have demonstrated the utility of these defects in modulating both bulk material properties[79,149,220,221,460,464,472,475,479,484,634,645] and local electronics.[635,636,642,646] The simplicity of interchanging MOF components both experimentally and theoretically makes the investigation of material augmentations through substitutional defects particularly powerful. The number of substitutions included per unit cell or cluster model reflects the concentration of the defect; substitutions may vary from a single or few linker/metal lattice points[79,634,635,641] to complete substitution of all linkers/metals in the model.[79,149,460,639,644] The change in MOF properties upon inclusion of an extrinsic component is dependent on the extent of substitution.[647−649]

Linker substitutions and metal substitutions also offer a route to tuning the local interactions between MOFs and small molecular guests.[650−654] The conformation and selectivity of binding, approximated in DFT methodologies by the relative exothermicity, influence the performance of MOFs for functions like catalysis or separations.[635,636,642,646] Linker substitutions may be introduced postsynthetically by introducing new molecules of the appropriate size and symmetry into a defective MOF system. UiO-66, for example, features high quantities of linker vacancies,[607,655] which can be saturated by the introduction of functional ligands; monodentate 3-mercaptoisobutyric acid was introduced into defective UiO-66 to incorporate a thiol functionality for cation trapping.[635] To

https://dx.doi.org/10.1021/acs.chemrev.0c00148
Chem. Rev. 2020, 120, 8641−8715

examine the competition of Hg^{2+} binding with Ba^{2+}, Zn^{2+}, and Pb^{2+} to the newly introduced thiol moieties, a benzoate cluster model of UiO-66 with two linkers substituted for 3-mercaptoisobutyric acetate ligands was used. UiO-66-SH showed preferential binding for Hg(II) over Ba(II), but Zn(II) and Pb(II) are expected to bind competitively. Binding energies of 33 and 49 kcal/mol were calculated for Hg^{2+} bound to a single thiol (SH−Hg, although this is unphysical in reality) and in a bridging fashion between two SH groups (HS−Hg—SH), respectively. This study thus demonstrated that to increase Hg^{2+} binding energies (and therefore selectivity) higher densities of linker vacancies (and therefore substitutions) are desired. Such studies demonstrate the utility of monitoring defect-related properties as a function of concentration.

When constructing hypothetical materials, it is important to consider the feasibility of MOF synthesis. Metal metathesis may cause material instabilities due to resultant strain from differences in atomic radii and related electronic properties.[641,643,644] The ramifications of making Ni(II) and Cd(II) substitutions to Mg-MOF-74 were studied by comparing the total energy of the periodic models for Mg−Ni and Mg−Cd mixed species to the pristine, monometallic M-MOF-74 species.[641] Hypothetical mixed MOFs were constructed as an average of the lattice parameters from the contributing monometallic species, and systems with variable dispersions and concentrations were compared. Importantly, disperse arrangements of substituted metals showed lower overall energies than when metal types segregated into rich domains. Additionally, smaller mismatch between the lattice parameters of the single metal systems (Mg-MOF-74 and Ni-MOF-74) produced the most stable bimetallic structures (Mg-Ni-MOF-74), Figure 46. In a similar vein, a study invoking the statistical distributions of symmetry related bimetallic systems with variable composition generated the same qualitative statement: less lattice mismatch resulted in more stable structures.[643]

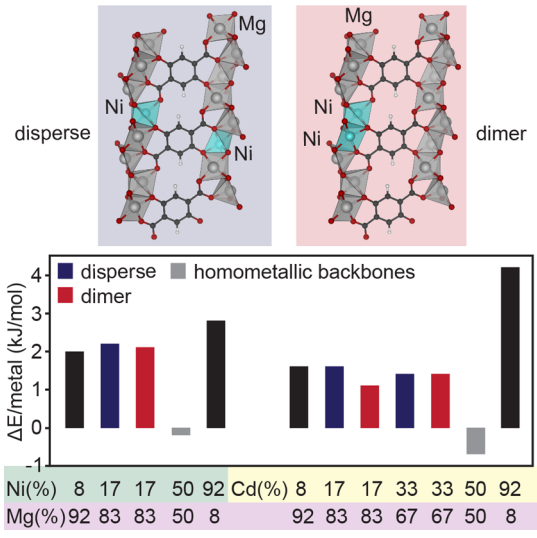

Figure 46. Mixing is more favorable in the Mg-Ni-MOF-74 due to the lack of strain from ion size mismatch. ΔE/metal is the energy of various MM-MOF-74 compositions relative to a linear interpolation of the appropriate compositions of the respective homometallic MOFs, positive value corresponds with a favored composition. The metal percentage corresponds to the appropriate amount of metal substitution in a 12-metal-ions-containing supercell. Adapted from ref 641.

One strategy to compute defect formation energies in MOFs is to reference their formation energetics to their element components. In a study by Han and colleagues, they sought to engineer the band gap of MOF-5 to collect lower energy photons through metal and central anion substitution, Figure 31.[479] In this case, their interest in defect formation was from a bottom-up synthetic approach; the concentration of a substitution can increase until it, itself, is a pristine new material, or the substituted system may be an independent synthesis. For the purposes of material development, it can aid in intuition to think of new isoreticular materials as a perturbation from the parent framework. This study thus highlights the importance of reference states: elemental references are certainly transferrable, but any number of other references could have been chosen, directly affecting the computed formation energies.

In summary, substitutional defects have been a cornerstone of experimental MOF chemistry, enabling new chemical properties in otherwise benign scaffolds. However, exploration of their formation energetics has been largely limited to only a handful of MOFs, but the number of reports continues to grow as the importance of defects is realized.

4.7.3. Interstitials. Interstitial defects differ from substitutional defects in that they occupy a point in the lattice that would otherwise be unoccupied. Whereas a transmetalated system features a defect in place of an original atom (substitution), metal species deposited atop/appended to nodes are extraneous (interstitials). Interstitials in MOFs are difficult to define given the inherent porosity and high surface area of this class of materials, which offers more sites for interstitial introduction than are intrinsic to the framework. Hence, in some sense, all guests introduced to the MOF can be considered interstitial.

Perhaps the most intriguing example is the inclusion of guests that create novel charge transport pathways between otherwise noninteracting nodes. Bridging motifs may be introduced by incorporating a new coordinating species or covalent functionalization of existing linkers to bridge pore space. For instance, tetracyanoquinodimethane (TCNQ) is a tetratopic redox active molecule that fortuitously can bridge adjacent Cu-paddlewheels in $Cu_3(BTC)_2$. The extent of bridging was shown to cause an increase in electrical conductivity (6 orders of magnitude, up to 0.07 S/cm).[656] Comparing periodic models of the pristine framework and with the TCNQ interstitial showed strong binding (84 kJ/mol) and cluster models consisting of two benzoate-capped paddlewheels saturated with water molecules and bridged by TCNQ, showed new conduction band states localized on the TCNQ molecule.[656,657] It was thus reasoned that thermally promoted charge transfer between the framework and guest molecule enhanced charge mobility. Later, scanning electron microscopy and porosimetry supported the bridging arrangement of TCNQ proposed by theory.[658]

Nonnative organic linkers bridging metal sites also impacted charge mobility in $Ni_3(HITP)_2$.[659] Band structures, calculated using the B3LYP hybrid functional and the triple-ζ basis set, pob-TZVP, were constructed for different forms of $Ni_3(HITP)_2$ including a variant with layers separated by 4,4′-bipyridine bridging the nickel sites and pristine $Ni_3(HITP)_2$ with the same interlayer spacing as the bridged derivative. Bulk $Ni_3(HITP)_2$ is found to be metallic, but the band gap widens with increasing interlayer separation, and upon inclusion of the bipyridine interstitial band dispersion is seen to decrease, effective mass values increase, and the band gap widens; $Ni_3(HITP)_2$ is rendered a semiconductor. The authors note that square-planar Ni(II) bound to four nitrogen atoms results in filled d_z^2 orbitals,

https://dx.doi.org/10.1021/acs.chemrev.0c00148
Chem. Rev. 2020, 120, 8641−8715

which do not readily bond to additional out of plane organic linkers. Potential energy curves for pyridine coordination to this square planar motif showed the hypothetical semiconducting structure was unlikely to form, however $Cr_3(HITP)_2$ with bridging 4,4′-bipyridine may be an alternative, stable structure.

MIL-125 serves as our final example to frame the contention of defects in MOFs. In the original report,[74] Dan-Hardi and colleagues noted that MIL-125 became black upon exposure to UV light in the presence of an alcohol. The authors offered a hypothesis that this occurred due to a proton-and-electron transfer onto the MOF, yielding a Ti^{3+} and a narrow resultant band gap. In a follow-up study, Walsh and Catlow demonstrated that a similar outcome could be achieved by the photoelimination of an inorganic oxo, Figure 47.[613] There, they

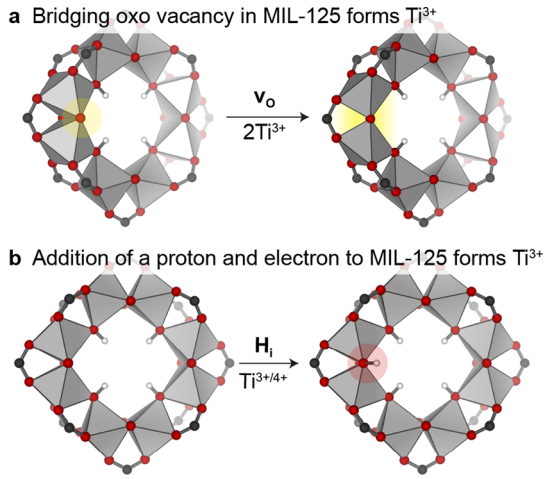

Figure 47. MIL-125 is known to turn black upon photoexcitation in the presence of alcohols. (a) Walsh and Catlow suggested that the color change could have been attributed to the formation of O_2 via photoelimination.[613] In contrast, (b) Mayer and colleagues revisited this problem and demonstrated that the color changes was likely due to an inorganic hydrogen atom transfer to the inorganic oxo.[660]

modeled the defect using O_2 as the reference. However, the outstanding issue with this photoelimination mechanism was that, if operable, this process should occur in the absence of an alcohol (there are no reports to support this claim). Recently, Mayer and colleagues revisited this discussion and demonstrated that the original hypothesis of Dan-Hardi was likely correct; MIL-125 turned black due to PCET, Figure 47.[660] Regardless, both of these studies demonstrated a powerful concept that reaches beyond MIL-125; inorganic defects are a prevalent and relatively unexplored aspect of MOF chemistry.

While the computations of defects have been historically challenging due to size limitations[623,625,630,632,645] this is an area that is primed for rapid development because it is the defects that enable the charges to flow in conductors and act as the grafting sites for catalysts. Computational chemistry is well-suited to perform systematic studies and will undoubtedly enable a broader gamut of materials with desired properties. We expect that the prevalence of computational defect studies will extended to frameworks beyond the Zr-oxo based reports,[629−632,661−668] to MOFs with more complex topologies and connectivity.[669,670] The first 20 years of MOF chemistry was spent demonstrating they are crystallographically ordered materials. The next 20 years will likely focus on their imperfections.

5. CATALYSIS

With a few notable exceptions,[528,671−676] the application of MOFs in heterogeneous catalysis draws on concepts deeply rooted in molecular chemistry.[268] The modular nature of the node and linker enables access to molecularly precise, site-isolated reactive sites[677] while also affording different local chemistry to molecular analogues.[60,678,679] Yet, MOFs are uniquely dissimilar to molecular analogues: their porosity engenders an additional modular parameter, and subtle differences in coordination environment of node-incorporated metals compared to conventional homogeneous catalysts make MOFs ideal for accessing novel reactivity, and for performing fundamental mechanistic studies.

Generally, design strategies targeting specific reactions have included incorporation of catalytically active linkers,[680] the formation of SBUs that are intrinsically catalytic,[72,681] and using encapsulation of catalytic species in the pores (examples are shown in Figure 48).[682,683] Post synthetic modification methods[684] such as cationic metal exchange,[685] linker exchange,[686,687] linker functionalization,[688−690] and atomic layer deposition (ALD)[66,691] have been further utilized to tune existing scaffolds and provide access to materials that are otherwise inaccessible through direct synthesis.

Computational analysis of catalytic mechanisms and active site geometries requires the identification of key intermediates and transition states that determine the overall efficiency of the catalytic cycle. Such studies are more sophisticated than simple geometry optimizations of ground state materials as they include computationally intensive transition state search methods based on saddle point searching or interpolative schemes.[695] However, once these structures are identified; screening various chemical modulations becomes relatively simple.

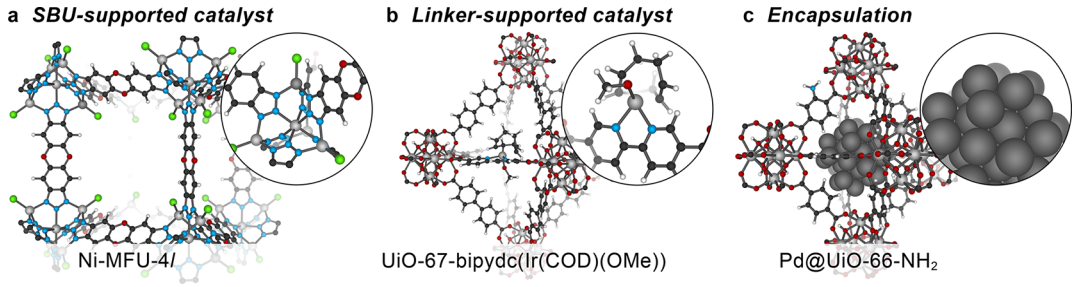

Figure 48. Some avenues for appending molecular catalysts. (a) Ni transmetalation in MFU-4*l* yields a catalyst capable of selective olefin oligomerization.[72] (b) Ligand exchange in UiO-67 enables the support of Ir(COD)(OMe) (COD = cyclooctadiene), a catalyst for C−H borylation of arenes.[692] (c) Encapsulation of Pd in amino-functionalized UiO-66 catalyzes the hydrogenation reactions.[693,694]

https://dx.doi.org/10.1021/acs.chemrev.0c00148
Chem. Rev. 2020, 120, 8641−8715

Unfortunately, transition-state searching can sometimes feel like finding a needle in a haystack; if the chemical system has more than four atoms, the potential energy surface (PES) has more than three dimensions and from there the PES becomes very complicated, very quickly. To simplify the challenge of determining the appropriate gradients to follow (both transition state searches and generally in modeling), it is helpful to extract clusters using the procedures discussed in section 3. Molecular modeling in catalytic studies of MOFs is seemingly requisite to accomplish the exhaustive analyses necessary to determine both reaction pathways and their driving force.[696] This section discusses the use of cluster models (and a handful of solid-state examples) for computational kinetic studies (section 5.1) including transition state searches (section 5.1.1) and saddle point search methods (section 5.1.2, section 5.1.3), ending with the strategies to compute activation barriers and predict charge transfer phenomena in photoactive scaffolds (section 5.2).

5.1. Kinetics and Transition State Searches

Conventional ground-state DFT methods provide very precise estimates of geometries at intermediate points along a reaction pathway. Transition states are geometries that correspond to saddle points on the PES, and are the highest energy configuration that exists along the lowest energy pathway between two intermediates. This section proceeds with the assumption that the intermediate structures, either solid-state or cluster, have been initially equilibrated.

5.1.1. Transition-State Search Algorithms. The transition state is a saddle point on the PES that lies along the minimum energy path between intermediates, i.e., the dominant reaction pathway, and accordingly has exactly one negative (i.e., imaginary) frequency corresponding to a single direction of molecular motion with no restoring force. Analogous to ground-state equilibrations that converge to a minimum point on the PES, transition-state optimizations self-consistently converge to a saddle-point. Saddle point search methods generally take one of two forms: (i) interpolation methods, which step through a series of geometric configurations obtained by interpolating between the coordinates of "known" reactants and products, and (ii) surface walking algorithms, which are based on assessing the local gradients or Hessian matrices.[697] Ultimately, the various saddle point finding methods differ only in the manner with which they traverse the PES, but should in principle yield the same result.

5.1.2. Interpolation Algorithms. *Interpolation Algorithms*: One intuitive approach to find the transition state between intermediates is to construct a "chain-of-states" along the MEP by interpolating coordinates between the known reaction intermediates.[698] Interpolative schemes optimize a series of static chemical configurations referred to as images along the PES between the reactants and products to create a 2D energy profile; the resolution (and expense) of interpolation schemes is a function of the number of images as well as the chemical system, and their convergence relies on having a well-converged description of the starting materials and products.[699] Still, constructing a chain-of-states both reduces computational cost by limiting the degrees of freedom to sample, and ensures extracted geometries belong to the appropriate reaction coordinate.

The most common interpolation methods are the string[700−702] or NEB approaches,[703−706] which have been widely applied in inorganic surface catalysis[707,708] and ion diffusion,[709−711] and more recently to MOFs.[712−714] The various incarnations differ both in their convergence scheme and the reaction coordinate spacing kept between images. Importantly, the images obtained from interpolation algorithms that define the MEP may not necessarily contain the true transition state structure, and the results are often improved by the addition of a surface-walking algorithm to locate the true transition state using the highest energy structure, Figure 49.[702]

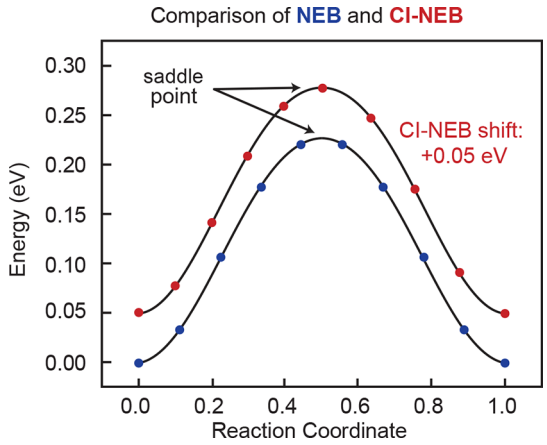

Figure 49. An illustrative representation of how pure interpolative schemes (e.g., NEB, blue) may overlook the true saddle point, but refinement schemes that employ gradient searching methods in addition to interpolative ones, such as CI-NEB (red) or subsequent transition state searches with surface-walking methodologies identify the saddle point. Image adapted from ref 702.

String Methods: The string method gets its name from the equal spacing kept between its connected "string" of images, achieved through a repositioning step after each SCF iteration.[700] Various embodiments of the string method have been developed: the simplified method[701] seeks to increase accuracy of the highest energy structure and computational efficiency, while the growing string method[702] adds more images until a complete reaction path and transition stare are identified.[702] Other alternatives exist (e.g., climbing image string, which is analogous to CI-NEB[715]) but are highly uncommon in MOF literature because the cluster modeling alternative generally provides higher fidelity data from smaller model sizes. In fact, string methods have only recently been applied to MOFs and are limited to the diffusion of gas throughout the pores.[716−718]

Nudged Elastic Band: Analogous to the string method, the NEB approach initializes a "chain-of-states" or "band" between the reactant and product configurations with images at fixed distances along the reaction path (n.b.: here, band does not refer to an electronic band, and to avoid ambiguity we will be explicit in our discussion of NEB). However, in NEB, the geometric perturbations between images along the PES is governed by spring forces applied along the band, hence the "elastic" band.[706,719] This chain-of-states converges to the MEP by optimization of each individual image and minimization of the spring force acting parallel to the band, as well as the true forces acting perpendicular to the reaction path. The result is a scan of the potential energy surface between reactants and products that traverses a saddle point; if the exact transition state is of interest, the highest energy structure obtained using NEB should be further refined.[705,720]

The climbing-image variant of NEB, CI-NEB, is the most widely used interpolation-based algorithm in MOF model-

https://dx.doi.org/10.1021/acs.chemrev.0c00148
Chem. Rev. 2020, 120, 8641−8715

ing,[704,721] and has also found success in solid-state transition state searches along simple reaction coordinates.[704,722,723] The climbing image, or the highest energy conformation, obtains a high resolution convergence to the saddle point without increasing the number of images by moving up the PES along the band, and down the PES perpendicular to the band, by way of the energy gradient without considering the spring forces.[704] CI-NEB was employed with PBEsol-D3 to assess the activation of hydrogen gas by UiO-66 with one linker per primitive cell functionalized with 1-(difluoroboranyl)-4-methyl-1*H*-pyrazole ($UiO\text{-}66\text{-}P\text{-}BF_2$).[357] The MEP and saddle point energy provided by CI-NEB demonstrated that activating H_2 via dissociative adsorption is a lower energy pathway than a reaction of H_2 with adsorbed CO_2.

In a related system, the transfer of hydrogen from palladium nanoparticles encapsulated in NH_2-UiO-66 ($Pd@NH_2\text{-}UiO\text{-}66$) to 2,3,5-trimethylbenzoquinone (TMBQ) was studied.[682] Thermodynamically stable configurations of palladium nanoparticles up to 32 atoms large encapsulated in the NH_2-UiO-66 pore were first determined with AIMD and refined at the Γ-point using DFT optimization with the PBE-D2 method.[724,725] Subsequent CI-NEB calculations with the Pd_{28} cluster revealed that increased catalytic activity likely stems from enhanced TMBQ binding due to cooperativity between the palladium nanoclusters and the NH_2 linker moieties.[682] This study benefited from an interpolative method because surface-walking algorithms would struggle to navigate the multitude of low-frequency modes in the PES of H_2 adsorption and desorption on a palladium surface.

In both cases, however, the dissociation and reaction of H_2 or H* (i.e., surface adsorbed $H^{\bullet}$) are readily performed via linear interpolation: at the time of writing, we are unaware of any examples of more complicated molecular transformations modeled using this approach. In short, it is easy to interpolate the trajectory of a proton; it is more difficult to interpolate the complicated trajectory of multiple atoms moving in 3D space.

5.1.3. Surface-Walking Algorithms. Surface-walking algorithms (e.g., quasi-Newtonian methods)[726−729] are often employed to refine transition state guesses from other methods such as NEB.[730] Occasionally called eigenvector following, these techniques proceed self-consistently by maximizing the energy along one local eigenmode of the Hessian while minimizing the energy along all other modes.[731] A good initial guess is critical because the transition state found as a result of these algorithms may follow an incorrect gradient, neglecting to connect the reactant to the desired product geometries (this occurrence is illuminated by intrinsic reaction coordinate calculations, section 5.1.5).[732]

Minimum mode finding algorithms, such as the dimer method,[733] calculate only the lowest eigenvalue and corresponding eigenvector. The "dimer" consists of two configurations of the system close together on the PES that are displaced by a fixed geometric distance.[734] As an example, the dimer method was employed to study the kinetics of hydrogen migration in cluster models of single metal atoms deposited on the node of MIL-125-NH_2.[735] The activity of MIL-125-NH_2 for the photoreduction of CO_2 to formate depends on the photogeneration of a Ti(III) active site via LMCT stabilized by hydrogenation of bridging oxo atoms. Here, the mechanistic differences between deposited Au and Pt were compared, and differences in H* binding energies were used to rationalize differences in reactivity. The diffusion barrier for hydrogen migration from the metal atoms to the bridging oxo units that facilitate Ti(IV) reduction, determined using the dimer method, showed the spillover mechanism was facile in the case of Pt loading and inhibited by the different preferential binding of Au to the lattice.

The most widely used embodiment, the "improved" dimer method, proceeds with fewer gradient calculations than the string or NEB methods.[736] However, the dimer method still suffers from difficulties with systems containing many low-frequency modes and with identifying a transition state along the targeted reaction coordinates. Again, this method works particularly well for protonic transition states and other one- or low-dimensional chemical events.

5.1.4. Combining Interpolative and Surface-Walking Methods. The most efficient way to locate transition states is through a combined interpolative and local saddle point search approach.[703] In this way, the interpolative scheme generates a reasonable initial guess for the transition state structure along the MEP, and a local surface-walking (saddle point searching) algorithm is then used to equilibrate the transient geometry. In the molecular software package Gaussian,[737] for example, both interpolation and surface-walking methods are used in the synchronous transit-guided quasi-Newton (STQN) approach to elucidate the structures of activated complexes.[738] If only a transition-state structure guess is provided, the Berny algorithm is used to converge to the saddle point.[739] When structures are provided on either side of the activated complex, a quadratic synchronous transit approach gets close to the quadratic region of the MEP, and the saddle-point is refined using a quasi-Newton or eigenvector following approach (QST2).[740] The uphill search direction for optimizing transition states is chosen based on the tangent of the synchronous transit path, and the eigenvector for this ascent direction is then fed into the quasi-Newton or eigenvector following algorithm to refine the saddle point.[741] QST3 additionally employs a transition state guess between the intermediates, which may increase the accuracy of the interpolated path mitigating the risk of calculation failure yet comes at a computational deficit.[742]

The STQN procedure was adopted to compare the catalytic efficiency of NTU-180, a Cu-paddlewheel-based MOF, for propylene carbonate formation from CO_2 and propylene oxide, in the presence of tetrabutylammonium bromide (TBAB).[743] To isolate the effects of pore confinement and node construction on the overall efficiency, the reaction energetics were compared across four models: (i) gas phase calculations without the presence of catalysts (e.g., without TBAB or NTU-180), (ii) in the presence of TBAB alone, (iii) on a hydrogen passivated Cu_2 paddle-wheel/TBAB cluster model, and (iv) a large NTU-180/TBAB model featuring six Cu_2 paddle-wheel units and 24 ligands. The lowest activation barrier for cycloaddition was exhibited by the NTU-180/TBAB model highlighting the importance of both confinement and Lewis acid Cu(II) sites in stabilizing the epoxide ring-opening step.

The catalytic activity of Fe_2M (Fe^{3+}, M = Ti^{2+}, V^{2+}, Cr^{2+}, Mn^{2+}, Fe^{2+}, Co^{2+}, Cu^{2+}, and Ni^{2+}) mixed valent nodes found in PCN-250 were investigated for the oxidative dehydrogenation of propane using N_2O as the oxidant.[744] Cluster models containing formate-passivated Fe_2M mixed valent nodes showed that oxygen-binding energy is strongly correlated with the N_2O and C−H activation barriers; we highlight the C−H activation barrier descriptor, Figure 50. Identifying the transition states played an operative role in determining the optimal metal identity for oxidative dehydrogenation of propane using N_2O. Moreover, increasing HOMO energy of the cluster model, facilitated by varying metal identity in Fe_2M, increases the

https://dx.doi.org/10.1021/acs.chemrev.0c00148
Chem. Rev. 2020, 120, 8641−8715

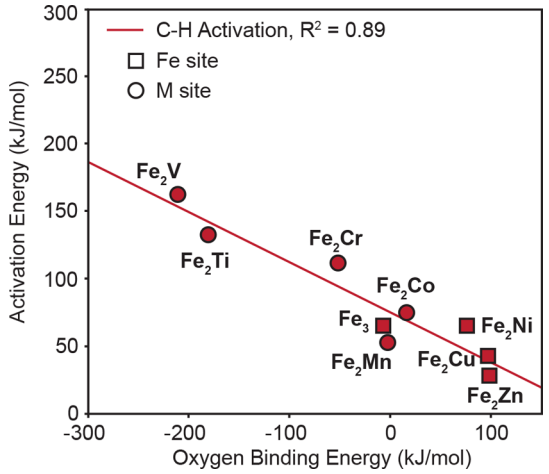

Figure 50. Lowest free energy M = O bond (M = Ti, V, Fe, Mn, Co, Ni, Cu, Zn) and the activation energies for C−H dehydrogenation are correlated. The shape of the data point indicates whether the reaction occurs on the Fe (square) or M (circle) site of the cluster. Reproduced with permission from ref 744. Copyright 2019 American Chemical Society.

oxygen bond strength due to the increased ability to donate electrons ultimately resulting in a decreased N_2O activation. Four materials were synthesized (M = Mn, Fe, Co, and Ni), and the calculated trend agrees with experiment, revealing, PCN-250(Fe_2Mn) ∼ PCN-250(Fe_3) > PCN-250(Fe_2Co) > PCN-250(Fe_2Ni); this is unsurprising considering the increasing electronegativity of the transition metals.

In periodic systems, NEB can be used to find an approximate saddle point in the potential energy surface, which can be further refined by applying CI-NEB with or without subsequent invocation of the dimer method. The images for CI-NEB may still straddle the true saddle point, thus surface-walking algorithms are preferred. Open metal sites in PCN-250 were screened for C−H activation with N_2O using the PBE-D3(BJ) level of theory; the rate limiting step was found to be metal oxidation using the CI-NEB+dimer method.[745] A similar procedure also used the CI-NEB+dimer method combined with high-throughput screening of adsorption studies in derivatives of HKUST-1[746] as well as the development of an apparent universal descriptor for C−H activation (discussed in more detail later in this section).[747] This balance of procedures provided by interpolation and gradient analysis is effective because CI-NEB is a high accuracy interpolative scheme that ensures a structure between the provided intermediate minima.

5.1.5. Confirming the Reaction Pathway. Typically, transitions states are "confirmed" through examination of computed vibrational modes. By definition, geometrically equilibrated structures have zero imaginary vibrational modes, while activated complexes should have exactly one, corresponding to the direction of the bond making/breaking process.[748] Vibrational analysis indeed confirms a geometric configuration is a saddlepoint on the PES, however, there is no guarantee that it is the saddlepoint along the MEP, i.e., the lowest energy transition state.

After confirmation that the identified saddle point corresponds to a first-order saddle point with one negative frequency via vibrational analysis, an intrinsic reaction coordinate (IRC) calculation can be performed to confirm the transition-state configuration actually connects the reactants and products.[749] The IRC is the path of steepest descent from the lowest energy saddle point to minima in both the forward (product) and backward (reactants) direction on the PES.[750] This mass-weighted steepest descent algorithm should be performed both in the forward and backward directions. The path defined by this calculation has no dynamic significance but is a convenient trajectory on the PES to reactant and product minima.[751] IRC calculations require initial force constants, which can either be computed at the beginning of the IRC calculation or fed into the calculation from the output of the transition state optimization.[752] We note that, during the revision of this Review, an excellent example of the use of IRC was published by Snurr and colleagues.[744] Following the reaction path may also adventitiously reveal unidentified intermediate states between the defined reactants and products.

5.1.6. Bridging Experiment and Theory. Transition states are of particular interest in kinetics studies. For example, it is helpful to convert computational geometries and corresponding energies into key metrics, such as reaction rates and turnover frequencies (TOFs), to enable comparison with experiment. Computational kinetics yields quantitative activation energies that can be used to predict a rate constant, k, via Eyring's transition state theory,[695]

$$k = \frac{k_b T}{h} e^{-\Delta G^{TS}/RT} \tag{5.1}$$

k is the reaction rate, k_b is Boltzmann's constant, h is Planck's constant, T is the absolute temperature, R is the universal gas constant, and ΔG^{TS} is the free energy change from the initial to transition states.

Motivated by a desire to optimize catalytic cycles, efforts are usually placed on identifying the rate-determining step, the slowest step of the reaction. Typically, because the rate of the forward and reverse reactions become constant at equilibrium, practitioners deduce the rate-determining step as the highest energy transition state. While this simplification is acceptable for a single reaction path, catalytic cycles turnover and are thus offset in energy by the difference between reactants and products.[753] A universally general formalism is instead based on two rate-determining-*states*.[753−755] These are defined as the transition state and intermediate (not necessarily corresponding to the same reaction step) with the highest degree of rate control, i.e., the strongest influence on the overall rate upon an infinitesimal change in Gibb's free energy.[754] Within the context of catalysis, such states are referred to as the TOF-determining transition state (TDTS) and the TOF-determining intermediate (TDI), Figure 51.[753]

The TDTS and TDI can be found by maximizing the energetic span[756] (δE), which is defined by Kozuch and Shaik[753] as

$$\delta E = \begin{cases} E_{TDTS} - E_{TDI}, & \text{if TDTS after TDI} \\ E_{TDTS} - E_{TDI} + \Delta G_r & \text{if TDT before TDI} \end{cases} \tag{5.2}$$

from which the TOF, in its simplest form, can be approximated for a spontaneous reaction

$$\text{TOF} = \frac{k_b T}{h} e^{-\delta E/RT} \tag{5.3}$$

A thorough review of the energetic span model, including its full expression, is provided by Kozuch.[757]

While approximate reaction rates can be obtained from DFT energies using TST, there may be other variables at play that cause the model to diverge from experiment. For example, the

https://dx.doi.org/10.1021/acs.chemrev.0c00148
Chem. Rev. 2020, 120, 8641−8715

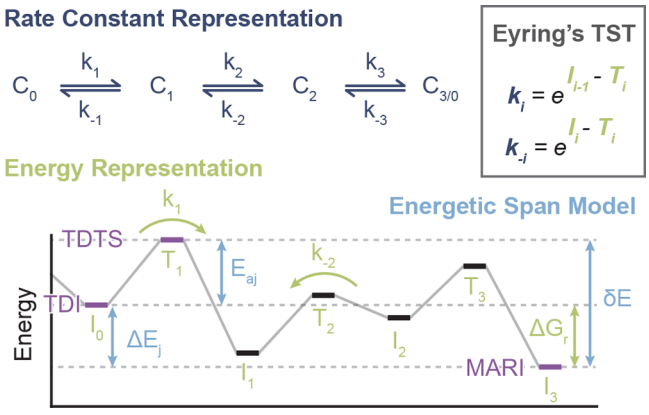

Figure 51. Rate constant representation of the TOF is often obtained from experimentation, yet computational chemistry operates out of the energy representation by producing an energy landscape. Eyring's transition state theory (TST) offers a mathematical translation between the energy and rate constant representations. The energy representation features the several transition states (T_x), including the TOF determining transition state (TDTS, rate limiting transition state), and several intermediates (I_x), including the TOF determining intermediate (TDI, most populated intermediate), and the most abundant reaction intermediate (MARI). The energetic span (δE) is the energy difference between the MARI and TDTS. The activation energy (E_{aj}) is the energy difference between the TDI and TDTS.

diffusion and adsorption behavior of reactants affects local concentrations at active sites.[758] The rate of diffusion to these active sites has been used to create what the authors claim to be a more realistic simulation of reaction conditions.[759]

Rate constants obtained from traditional TST are considered to be an upper limit because it is assumed that any species with sufficient energy will directly proceed to products.[760] A more accurate rate constant is recovered from variational transition state theory (VTST), which uses the minimum-flux criteria to determine the transition state.[761] Instead of invoking the rate constant obtained from the highest potential energy point, the transition state position is adjusted to minimize the rate constant.[761,762] Several flavors of VTST exist which help recover different material properties.[763]

Most often, DFT models provide electronic explanations for observable phenomena. On occasion, a more direct comparison of simulated reactions to experiment is desired. The interconversion between energies recovered from QM models and kinetic parameters can thus be valuable. While there is benefit to generating high resolution renderings of each structure along a mechanistic route because of the subtleties in product selectivity, the inexhaustible variations of MOF structure and chemistry needs to be narrowed toward the chemical space comprising interesting MOF properties and electronics.

5.1.7. Descriptors. Descriptors are transferable approximations built from correlations between atomic level properties obtained through simple implementations of static DFT and macroscopic experimental kinetics. The role of descriptors is to enable high-throughput catalyst screening without the need for involved kinetic investigations of methodically selected material derivatives.[764] Although not a MOF example, one of the finest demonstrations of this concept was presented by Nørskov and colleagues, who showed that the energetics of CH_3*-binding to the surfaces of metals correlated with their selectivity for hydrogenation of acetylene, even though CH_3* itself was not a reaction intermediate or transient species but rather a good barometer for sigma donation to the metal surface.[765,766] Thorough mechanistic investigation of individual systems for even single reactions requires a tremendous amount of computational resources and human effort. Descriptors are thus indispensable tools for the acceleration of materials discovery and development.

In conventional heterogeneous surface catalysis (e.g., surface of bulk Pt, Ir_2O_3, etc.), activity is commonly a function of adsorption and dissociation energies. These energies result from the coupling of transition metal *d*-states to the valence states of adsorbates.[764,767,768] In these instances, it may be useful to divide the metal electronic states into the *s*−*p* bands and the *d*-bands because adsorption energy is composed of bond energy contributions from coupling between the metal *sp* states when the adsorbate approaches the surface and between the renormalized adsorbate states (after *sp* coupling) with the metal *d*-states. Accordingly, the adsorption bond strength depends on the filling of the *d*-bands. The simplest model describes the *d*-band using only the *d*-band center (i.e., the difference in energy between the average energy of the *d*-band in the DOS, and the Fermi level), and it has been successfully applied as an adsorption energy descriptor.[769,770]

MOFs indeed have extremely large amounts of surface, an advantage for adsorption applications, however, most of it is catalytically benign. The *d*-band center descriptor has been employed to identify MOF catalysts for bifunctional oxygen evolution/reduction reactions (OER/ORR),[771] focusing on the 2D MOF, $(H_2NMe_2)_2M(Cl_2dhbq^{n-})_3$ (M = Ti, V, Cr, Mn, Fe, Co, and Cl_2dhbq = 2,5-dichloro-3,6-dihydroxybenzoquinone, M-DBQ-CP). The *d*-band center was shown to positively correlate with the Gibb's free energy change of the OER and ORR reaction intermediates, Figure 52. This led the authors to identify Ti-DBQ-CP as the most promising bifunctional catalyst of the studied series of MOFs, in addition to providing a pedagogical example of descriptors being useful in speeding up materials discovery.

Descriptors can be built by examining the correlation of a computable property such as activation energy in the case of catalysis.[772] For example, chemical descriptors were developed to identify $M_3(BTC)_2$ candidates for CO oxidation with N_2O, Figure 53.[390] To develop the descriptor, calculations were performed using a cluster model truncated to one M−M paddlewheel unit with four coordinated BTC linkers and the M06-L functional. N_2O decomposition, the first and rate-determining step in the catalytic cycle, is enhanced by charge transfer from the MOF to N_2O via π back-bonding. A linear relationship was found between activation energy and (i) the values of charge transfer, taken as the charge difference between the transition state and adsorption complexes ($q_{TS} - q_{ads}$), (ii) spin density (ρ), taken as the sum of the value over the node dimer transition metals, and (iii) the HOMO−LUMO gap composed of the MOF cluster model and N_2O, Figure 53.

In a different approach, chemical descriptors for the oxidative C−H bond activation of methane to methanol by a series of chemically diverse MOFs were identified using a high-throughput computational screening approach predicated on periodic DFT.[773] The authors show the active site formation energy, ΔE_O (forming the "active" metal-oxo via oxidation of the open-metal site), is a predictive metric for the reactivity of MOF active sites toward C−H activation. These correlations enable prediction of the active site stability and the methane C−H activation barrier from ΔE_O, halving the number of requisite

https://dx.doi.org/10.1021/acs.chemrev.0c00148
Chem. Rev. 2020, 120, 8641−8715

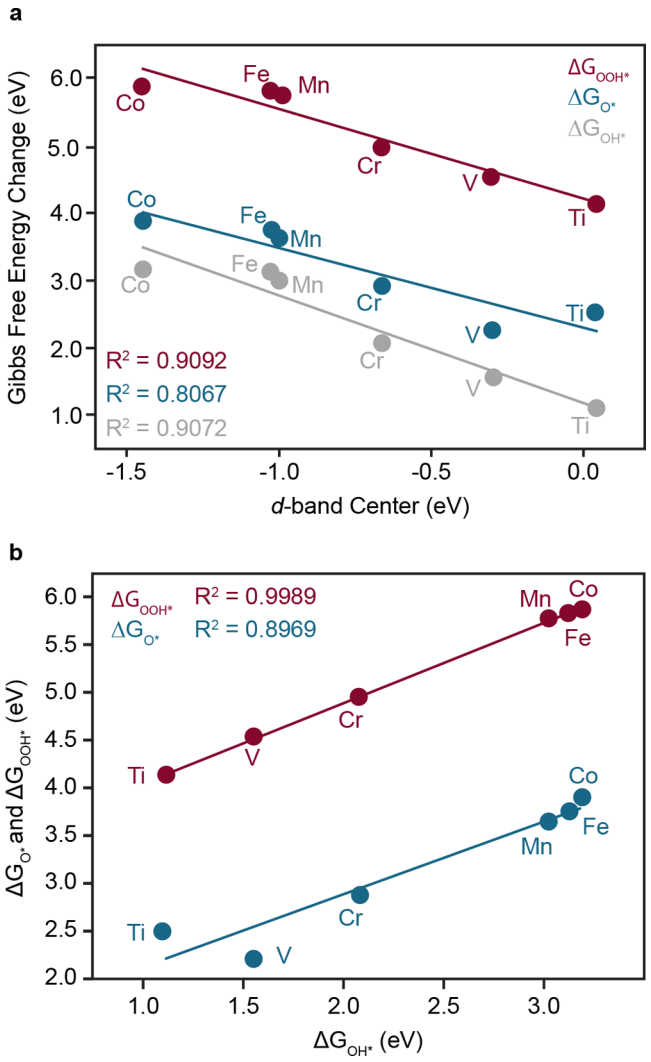

Figure 52. (a) The *d*-band center descriptor (*x*-axis) applied to $(H_2NMe_2)_2M$ $(Cl_2dhbq^{n-})_3$ (M = Ti^{2+}, V^{2+}, Cr^{2+}, Mn^{2+}, Fe^{2+}, Co^{2+}) showed excellent correlation with the Gibb's free energy change (*y*-axis) of adsorption for OER/ORR intermediates; the relationship with OOH* (burgundy), O* (teal), and OH* (gray) all scaled well with the d-band center as well as with each other as shown in (b), where the Gibb's free energy change of OOH* and O* are plotted as a function of OH*. Reproduced with permission from ref 771. Copyright 2018 Elsevier.

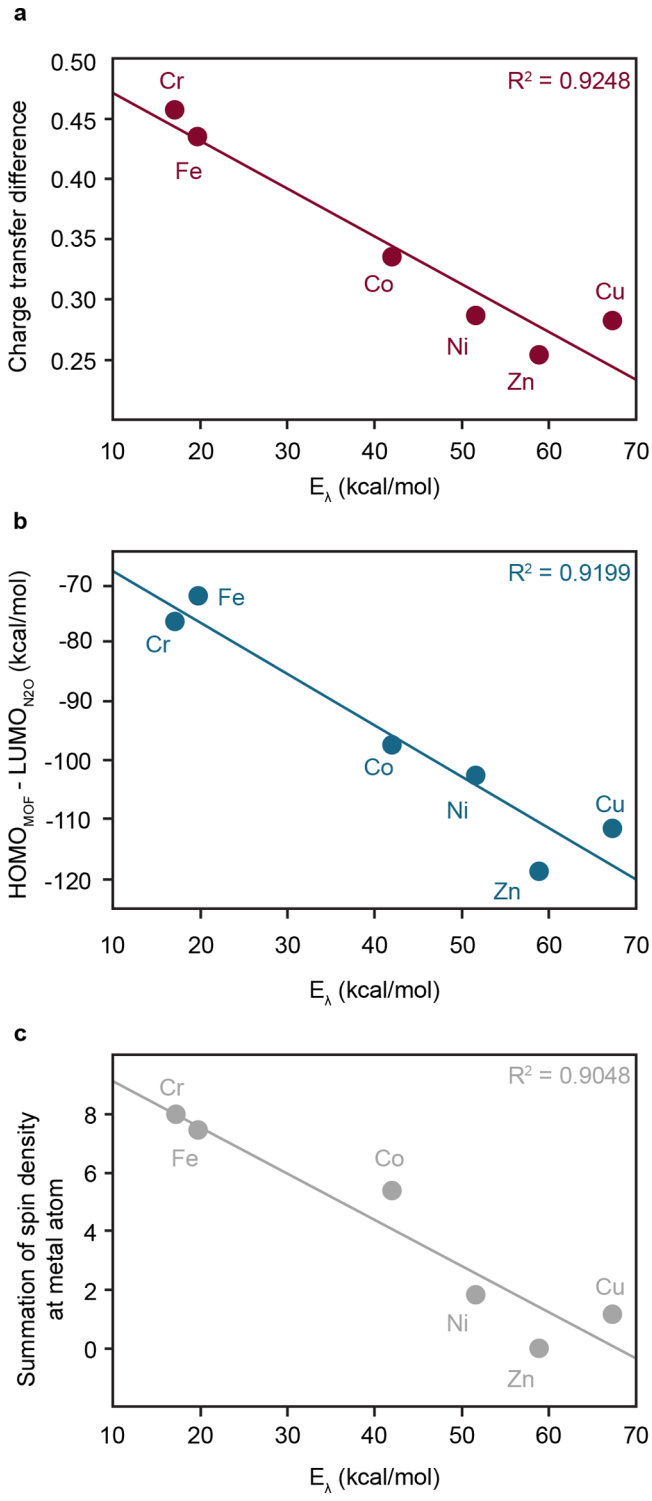

Figure 53. Activation energy (E_λ) of the rate-determining step in the oxidation of CO by N_2O over $M_3(BTC)_2$ (M = Fe, Cr, Co, Ni, Cu, and Zn) is correlated with the (a) charge transfer difference between the adsorption and transition states, (b) $HOMO_{MOF}$–$LUMO_{N2O}$ gap, and (c) summation of spin density at the metal atom. Reproduced with permission from ref 390. Copyright 2017 American Chemical Society.

DFT calculations to simply model the M═O formation, and MeOH desorption to return to the open-metal site catalyst.

Despite their obvious upside, descriptors have played less of a role in the development of novel MOF catalysts than, for example, borrowing principles from molecular chemistry.[677,774−776] Owing to the diverse chemical space, MOFs are well-suited to high-throughput studies employing descriptors for bulk property prediction. Because the scaffolds are largely assembled using the geometries of building blocks,[38] their likelihood of forming, their properties, etc. are all optimization targets rather than inputs.[777]

One of the motivating factors behind descriptors is the ability to accurately predict desirable material properties with easily calculated values. Yet, this process is highly manual, involving an intensive series of calculations to prove a generalizable correlation. Machine learning (ML), however, offers a more efficient route toward identifying the subtle electronic or structural changes that drive reactivity or instill certain electronic behavior.[778] Indeed, the predictive and generative power of ML algorithms is becoming increasingly popular in the chemical community[779−789] and MOF field;[219,777,790−792] for example, ML algorithms are being used to generate chemical

https://dx.doi.org/10.1021/acs.chemrev.0c00148
Chem. Rev. 2020, 120, 8641−8715

descriptors for improved target material and molecule generation.[793]

While seemingly unrelated, ML may be considered an extension of descriptors,[778] the main difference being that while ML algorithms accommodate multidimensional descriptions of the input data, descriptors rely on the theorist to screen relationships between chemically intuited system properties. In this way, ML affords an efficient route toward large-scale relationship screening to identify subtle trends in big data sets, which is often necessary for materials property predictions for complex systems. Multidimensional descriptions (typically referred to as features or labels) offer more complex analysis because they are often comprised of a mix of chemical and structural characteristics and properties; one study demonstrated both chemical and structural characteristics were necessary to maximize prediction of methane adsorption in a data set of ∼130 000 MOFs.[794]

Indeed, the power of both ML initiatives and descriptors lies in their generalizability, which is directly related to the chemical diversity of the data set used to construct the predictive tool.[795] Building this data set, however, is nontrivial; the robustness, generalizability, and accuracy of the result is dictated by the efficacy of the data with which the model is trained and strongly correlated to the data set size.[796] Throughout this Review, we have highlighted the computational resources necessary to pursue electronic structure theory level descriptions of MOFs, offering procedures to increase tractability and electronic resolution by truncating to cluster models, etc. In light of this, it is unsurprising that the majority of the current literature relies on Monte Carlo and molecular dynamics simulations to calculate features necessary to label data sets intended for ML studies; material properties like pore volume and surfaces areas are easily obtained from GCMC simulations. Understandably, ML models designed to predict electronic structure theory results have thus far largely focused on predicting wave functions or chemical properties for small-molecule data sets,[779,797] or specific properties such as refractive index,[798] save several recent materials discovery examples.[799,800] Electronic structure theory is primarily implemented in conjunction with GCMC simulations in materials-based ML studies,[219,801,802] or to serve as reference calculations for larger data sets in the MOF field.[803] Yet, with the advent of high-powered computing and improved algorithm development, we expect the MOF field to move toward both property and structure prediction, as it is already emerging in current literature.[804,805]

5.2. Photocatalysis

The localization of charge (i.e., flat bands) of most scaffolds and the ability to tune the size and parentage of the electronic band gap[806] makes MOFs interesting candidates for photoredox catalysis. Photoexcitation provides one route to accessing transient, exotic redox states,[456,807,808] and can further be used to promote an electron from the MOF to pore interstitials (e.g., absorbed polyoxometalates[809] or nanoparticles[810]).

Photocatalysis is predicated on the photocatalyst forming high energy, transient holes, and/or electrons, a process which is governed by (i) the photopromotion (e.g., band gap), (ii) relative alignment of vacant and occupied states in the catalyst and reactants (e.g., electron affinity and ionization potential/workfunction), and (iii) exciton lifetime.[59] Furthermore, there are four possible excitations in MOF materials, and they depend on the composition of the material: (i) ligand-to-ligand, (ii) ligand-to-metal, (iii) metal-to-ligand, and (iv) metal-to-metal excitations. In all cases, photoexcitation yields a hole in the valence band and an electron in the conduction band, which are then primed to do work, Figure 54.[811] Here, we discuss the utility of DFT in quantifying activation barriers, and identifying the modes and direction of charge transfer in photoactive MOFs.

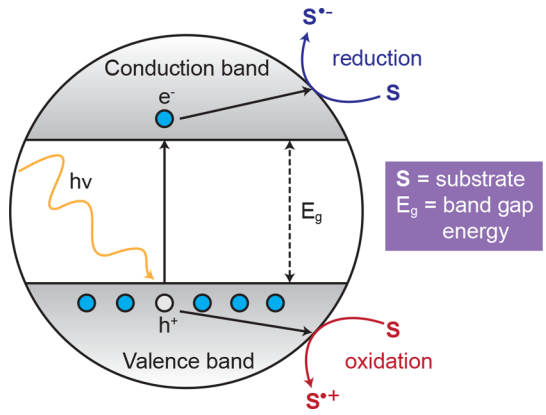

Figure 54. Photoexcitation of a valence electron to the conduction band minimum enables redox catalysis. Upon light absorption and excitation, electrons that populate the conduction band travel to the lower energy vacant states of an acceptor, while holes formed in the valence band exchange with electrons from higher energy occupied states of a donor.

5.2.1. Quantifying Activation Barriers. Experimentally, the energy of activation is quantified as the optical gap of a material, defined by the lowest energy dipole-allowed transition.[442] The fundamental gap, which is the difference in energy between the highest occupied and lowest unoccupied states in the material, is either close or identical in energy to the optical band gap.[442] Therefore, in theory, the fundamental electronic band gap is adopted as an approximation of the excitation wavelength.[812]

The computation of band gaps for solid systems is discussed in section 4, however, an accurate description of both the band gap and the valence band ionization potential are paramount for the prediction of photocatalytically relevant properties (i.e., hybrid functionals are necessary).[447] Again, the contribution of electron exchange is of particular importance when studying electronic transitions in metal ions.[445] Yet, the computational expense associated with hybrid functionals[448] prompts the recovery of optical and redox properties of MOFs from a single point hybrid functional calculation on a structure obtained using GGA theory.[57] This technique is prominent in MOF literature and was applied to study the impact of metalation on the photocatalytic properties of a porphyrinic MOF for water splitting and CO_2 reduction;[221] geometry optimizations were performed using PBEsol, followed by HSE06 to recover electronic properties. In all cases, the porphyrin alone was a chromophore; only the addition of Fe introduced new low-laying states. These midgap orbitals were used to justify the improved catalytic ability of the Fe porphyrin compared to other metals.

Static DFT recovers ground-state electron densities and may provide a poor description of the unoccupied orbitals populated upon photoexcitation. Methods like TD-DFT permit calculation of excited state electron configurations, i.e., the energy of a system is recovered when electrons are not placed in the lowest possible orbitals/higher-level Kohn−Sham orbitals are occu-

https://dx.doi.org/10.1021/acs.chemrev.0c00148
Chem. Rev. 2020, 120, 8641−8715

pied.[813] The optical gap can be found by identifying the first excited state; a simple task in molecular modeling packages, but rarely attempted in the solid-state.[814] When invoking periodic boundary conditions, the fundamental gap is thus taken as an approximate activation energy, however, the optical gap is narrower than the fundamental gap because of the exciton binding energy. This disparity between experiment and theoretical approximations can be observed in computations of HKUST-1. The electronic band gap is ∼3.5 eV using HSE06, but the material is strongly blue colored.[657,815] Conveniently, the localized electronic states in highly ionic MOFs again grants the opportunity to sensibly model local electronic structure with high levels of theory like TD-DFT by reducing the computational system to a cluster model.[21] Linker-to-linker transitions specifically offer increased control over band edge positions via molecular chemistry and functionalization.[536,816] In one study, amino- and nitro-functionalized UiO-66 showed band gap reduction using HSE03.[543] The same study also examined hydroxylated and dehydroxylated metal centers of UiO-66, revealing that hydroxylation increased the band gap of the bulk material, likely owing to the increased ionicity at the node/linker interface.

Indeed, the implementation of TD-DFT for MOF cluster structures has generally been successful in the case of linker-centered excitations. TD-DFT was also effectively applied to a series of UiO-66 derivatives when studying the origin of band gap perturbations as a result of varying linker identity.[817] Calculations were performed on cluster models of the hydrogen-passivated linkers, and HOMO−LUMO energies showed excellent agreement with values obtained from periodic calculations. Experimental adjustments to the optical response were found to be the result of additional linker states corresponding to the added functional groups.

The impact of framework rigidification and the chemical environment on the optoelectronic properties of light adsorbing molecules upon MOF inclusion is of interest to dampen unproductive photodecay.[818] TD-DFT simulations of 4′,4‴,4⁗,4⁗′-(ethene-1,1,2,2-tetrayl)tetrakis(([1,1′-biphenyl]-4-carboxylic acid)), a luminescent linker incorporated into MOF-5, were performed in the free and lattice-constrained cluster geometries.[819] Consistent with experimental results on the bulk MOF, TD-DFT showed the HOMO−LUMO gap was blue-shifted by ∼400 meV upon MOF inclusion due to a resultant conformational change and differences in terminal Lewis acidity; these data were in qualitative agreement with experiment.

While linker-to-linker transitions are more prevalent in MOFs than metal-to-ligand, ligand-to-metal, and metal-to-metal, the latter three transitions offer additional routes toward band gap modulation beyond organic functionalization. Band gap modulation of MOFs featuring metal-to-metal transitions can typically be accessed by substitution of transition metals into and onto nodes in otherwise wide gap scaffolds.[480,820] These materials then show standard crystal field splitting patterns related to their local ligand environment. Perhaps more interesting are linker-to-metal and metal-to-linker transitions; the electron and hole become spatially separated within MOFs featuring these transitions, giving rise to prolonged exciton lifetime.[821]

Perhaps the most exciting photophysical avenue in MOF chemistry is the control of ligand-to-metal excitations, as they are analogous to redox noninnocent molecules[822] while boasting potentially very large populations of photoaccessed reduced, site-isolated metals. Indeed, MOFs are able to stabilize excited-state radicals (e.g., with metals or linkers that yield a reasonable reduced product upon photoexcitation). The propensity of MOFs for electron storage was demonstrated in a series of landmark studies where the authors showed that MIL-125 could support photoaccessed Ti(III) in the presence of a sacrificial reductant.[660,823] The general approach invokes stabilization of the excited state by a cation (i.e., either proton or sodium) coupled electron transfer into the valence band hole of the photoexcited MOF. The generality of this approach is yet to be determined.

There are several methods outside of conventional DFT that may be invoked to assess the optical gap on relatively small cluster models with higher fidelity than ground-state, static implementations.[731] For example, single-reference configuration interaction calculations (CI) consider the contribution from higher energy states when computing the ground-state wave function; the range of configurations sampled is restricted for practicality. The "active space" is the number of orbitals included when considering (i) all excitations in the active space (CASSCF, section 3.3) or (ii) select excitations into select orbitals (singles, doubles, restricted active space, section 3.3), as recently reviewed.[319] CI methods provide a more accurate description of the frontier states and total energy in cases where low-lying excited states make a significant contribution at the operating temperature of the material and elsewhere that correlation effects are significant.[824,825] In brief, the presence and relationship between multiple low-energy excited-state configurations are accounted for thus improving the description of unoccupied orbitals/bands. CI wave functions can further be used in multireference calculations. Naturally, in addition to an astounding increase in computational expense, the success and accuracy of CI and MR calculations is dependent on the selection of an appropriate active space, a challenging procedure.[826]

In sum, the activation energy recovered from static DFT is most often reported as the fundamental band gap. Recovering experimental semiconductor band gaps in the solid-state empirically requires the inclusion of exact exchange in the Hamiltonian, however, molecular cluster models can be employed when frontier bands are localized on isolated components and are minimally perturbed by MOF incorporation. To obtain more accurate descriptions of the orbital interactions involved in excitation processes, post-DFT methods can be applied. However, the higher resolution quantum mechanical insights may mandate geometric or active space restrictions that diminish their ability to provide a realistic MOF model.

5.2.2. Predicting Charge Transfer Phenomena. Because most MOFs have flat bands, an exhaustive electronic band structure calculation is often a waste of computational resources. Instead, photocatalytic MOF chemistry can be explained using conventional DOS plots, which illustrate the orbitals contributing to each band.[827] In a photocatalytic reaction, from the ground state, absorption of a photon may promote an electron into the conduction band: the excited electron and hole are in kinetic competition between exciton recombination and the desired electron transfer.[828] The exciton binding energy, which drives recombination, is the attractive Coulombic force that must be overcome to separate a hole and electron[829] and thus decreases exponentially as a function of distance.[830] Photocatalyst design for systems with flat bands benefits from

https://dx.doi.org/10.1021/acs.chemrev.0c00148
Chem. Rev. 2020, 120, 8641−8715

localization of the excited electron on a separate component from its ground state.[226]

Many MOFs have wide band gaps stemming from valence and conduction bands centered on the organic linker, which are commonly conjugated systems dominated by $\pi-\pi^*$ transitions (e.g., MOF-5 and Zr^{IV}-UiO-66).[369,831−834] Wide gap materials, particularly, can host chromophores that sit mid gap relative to the bulk material. For example, a chromophore similar to the green fluorescent protein was appended to the biphenyl linker of a zinc-based MOF to inhibit low energy vibrational modes that deplete its signaling response.[835] Similarly, UiO-67 has been employed as an immobilization platform for a rhodium-based photocatalyst through postsynthetic linker exchange.[836] $[Cp^*Rh(bpydc)_3]Cl_2$ (bpydc = 2,2′-bipyridine-5,5′-dicarboxylic acid) performs the photoreduction of CO_2 to formate. DOS of the hybrid material revealed that the frontier states were defined by the new d−d transitions of rhodium, indicating the framework played a passive support role.

MOFs composed of late transition metals or metals with high quantum numbers will typically feature ligand-to-ligand transitions because the organic components have lower ionization potentials and higher electron affinities than the Lewis acidic metals.[837] Early experimental work presumed that the zinc-oxo clusters in MOF-5 operate as ZnO quantum dots via a ligand-to-metal charge transfer.[838,839] There, the GGA functional PBE, known for overstabilizing strongly bonded states, places the zinc orbitals closer to the conduction band edge. However, this was later debunked using a higher level of theory (HSEsol06)[840] paired with experiment: MOF-5 features primarily ligand centered excitations, Figure 55.[841] Higher

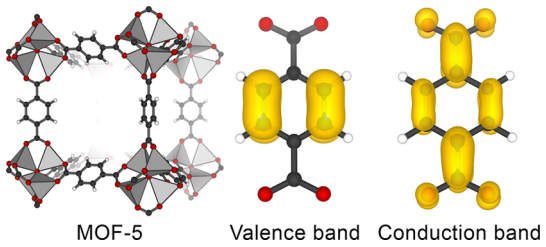

Figure 55. Valence and conduction band extrema projected at the Γ-point. The linkers are shown in isolation for clarity. Data obtained from ref 76.

energy conduction bands may also be populated via a multiphoton absorption process, although the prediction of the explicit energetics will depend heavily on the functional used.[842]

Unlike d^{10} MOFs, those constructed with Ti(IV) have reported photoaccessible Ti(III) states as evidenced by EPR and transient absorption spectroscopies, in addition to theory.[226,613,843−845] Vacuum level alignment of several Ti(IV)-based MOFs showed not only that the unoccupied titanium *d*-orbitals consistently dominate the conduction band but also that the CBM occurred at roughly the same eigenvalue for different linkers and node architectures, Figure 56.[461] Nodes built from the other d^0 ions (Zr(IV) and Hf(IV)) do not exhibit metal-based states near band edges, although Ce(IV)-UiO-66, which has empty *f*-orbitals, exhibits a conduction band dominated by metal orbitals.[227]

The DOS for MOFs known to undergo cation exchange, e.g., MOF-74 and MFU-4*l*, before and after transmetalation with Ti(IV) further revealed the generality of invoking the first row d^0-transition metal to generate low-lying metal-based acceptor states.[461] The substituted MOFs mimicked the electronic structure of pristine models but for the addition of unoccupied states from titanium *d*-orbitals below the native CBM. Comparatively, the energetic position of new metal d-states exhibited a greater dependence on the metal coordination sphere when incorporated through appendage rather than directly into the bulk lattice.[846]

Powerfully, in addition to modulating the chemical identity and energy of the conduction band through metal substitution without affecting organic valence bands, ligand-centered valence bands can be modulated by changing the organic motif with negligible perturbation to the conduction band if it is metal-based.[177] A renowned example of band gap modulation through organic linker functionalization is reduction of the MIL-125 band gap from the UV to visible light region through amino-functionalization,[847] and the same principles have been applied to other MOFs.[848−851] DOS plots show that electron donation from the amino group formed shallow midgap states at the valence band. Subsequent analysis with DFT established that the band gap could be further tuned by adjusting linker functional groups and the concentration of functionalized linkers.[79] Experimentally, it was observed that MIL-125-NH_2 indeed exhibited an optical gap in the visible range and, interestingly, the minimum band gap was reach at >50% linker substitution.[852] This observation leaves us wondering whether their observation was catalysis enabled by surface sites, or rather that the material became limited in quantum efficiency. Either way, this example highlights the symbiosis of theory and experiment by showing that visualization of the DOS is an indispensable tool for analyzing the band edges of photoactive system, especially for the fruitful modulation of exciton separating MOF species that can be selectively tuned from both band edges.

6. MULTISCALE, EMBEDDED, AND MIXED-METHOD MODELING

In the previous sections, the electronic structure was computed using quantum chemical descriptions of both the extended solid, and clusters cut therefrom. One of the main contributors to model size in methodologies invoking a molecular approximation is the size of the passivating ligands. Numerous examples were presented where their inclusion primarily serves to simulate the electrostatic potential and sterics of the pore. Yet, such van der Waals and weak dispersion interactions are readily captured at lower levels of theory (e.g., molecular mechanics, semiempirical, and HF approaches).[853] Rather than isolating a chemically relevant cluster for full quantum mechanical analysis that includes compositionally complex components responsible for simple electrostatic contributions, methodologies have been developed to embed a quantum mechanical model within another level of theory. Thus, the description of remote chemistry is maintained, while a higher level theory is applied at the active site.[854−856]

Generally, practitioners refer to these mixed methods as "embedded" systems, where one level of theory is surrounded by another. To make matters confusing, this approach is sometimes called "hybrid theory",[857] posing obvious problems for the DFT community. Further, they are also sometimes referred to as "multiscale models", specifically when the higher level of theory traverses one length-scale, while the lower level of theory traverses another. Such multiscale approaches are widely used in engineering,[858−860] geographical science,[861,862] and chemistry,[863−866] but here we will not delineate between it and

https://dx.doi.org/10.1021/acs.chemrev.0c00148
Chem. Rev. 2020, 120, 8641−8715

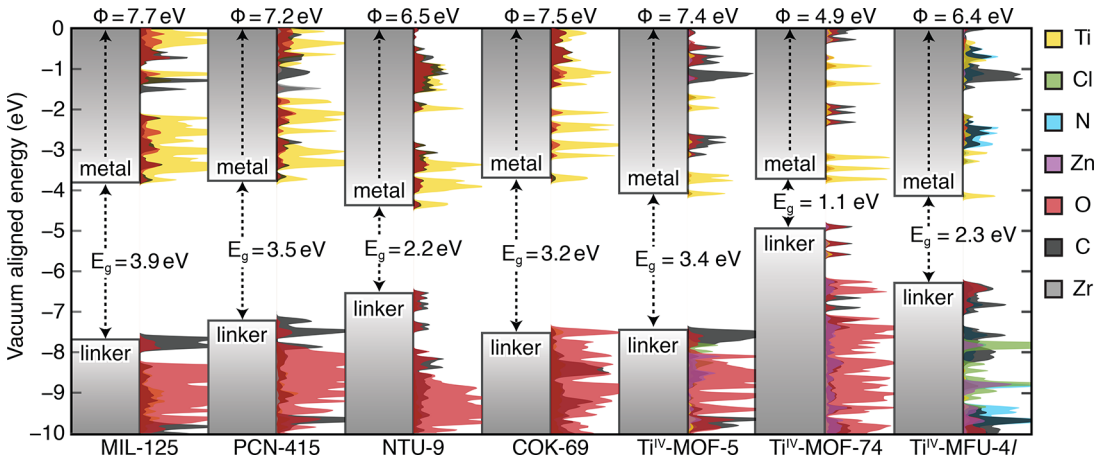

Figure 56. Atomic pDOS of MOFs containing titanium(IV) either natively (MIL-125, PCN-415, NTU-9, COK-9) or through synthetically accessible transmetalation (MOF-5, MOF-74, MFU-4*l*) reveals unoccupied titanium orbitals at the conduction band edge, with roughly the same electron affinity, and orbital-based states at the valence band edge, consistent with band gap reduction through addition of functional groups on linkers. Data obtained from ref 461.

embedding. Rather, this section specifically relates to the use of a high level of theory within a bath of a lower level. Regardless of the name, the utility of these approaches has enabled calculations of the chemistry of active sites in extremely large systems, and its development and application to biological systems warranted the 2013 Nobel Prize.[867−871]

In principle, a successful embedded model should feature essentially all of the chemistry that an all-electron calculation would provide and can be implemented in both molecular and solid-state configurations.[872] Generally, a two-layer (QM/MM) approach is invoked, where one region of the chemical system is described quantum mechanically, and the remaining regions are described using MM methods. Additional intermediate layers may be added, resulting in an *N*-layer approach; however, methods exceeding three layers have not been implemented in common software packages. The largest shortcoming of these models arises from the interfacial descriptions at the QM/QM, QM/SE, or QM/MM boundaries, but this is also an excellent platform to provide insights about the metal−organic interface. In this section, we highlight the basic components of typical multiscale modeling procedures applied to MOFs, with a particular focus on the two-layer QM/MM scheme, a convenient approach to maintaining a description of the pore without performing more expensive all-electron DFT.

6.1. Two-Layer QM/MM Schemes

QM/MM enables a description of steric interactions from a much cheaper Newtonian parametrized force field (FF) while maintaining an electronic description of key chemistry. A tremendous amount of work has been dedicated to the development of FFs,[873−878] and although they will not be discussed here, they do play a major role in determining the success of the embedded model. MM itself does not explicitly include descriptions of electrons[879] despite being parametrized from higher level DFT data and experiment. Several "general" FFs commonly used in MOF literature include, UFF,[880] AMBER,[881] AM1,[882] DREIDING,[883] and MNDO.[884] Recently, MOF-specific FFs have been developed such as BTW-FF[885] and MOF-FF,[886] however the confident utility of the force field only applies if it is used for systems in which it has been parametrized. Thinking back to an example presented in section 1, even the same linker (BDC) paired with different metals (forming MIL-125, MOF-5, and UiO-66) form materials with vastly different work functions, and therefore bonding properties. A single FF for BDC will likely fail if liberally applied to all BDC-containing MOFs; the nodes impact the electronics, geometry, and properties of the linker. Yet while MOF FFs lack generality and transferability, their implementation drastically reduces the time to solution, making their development a highly worthwhile endeavor.

The interfacial energy at the QM/MM must be accounted for in the self-consistent procedure of an embedded QM model. Two general schemes have been developed to account for the interaction at the QM/MM boundary, either additive or subtractive/extrapolative.[887] The total system energy of the additive scheme, E_{additive}, is recovered by summing the energy of the high-level/QM model region, $E_{\text{high, model}}$, the energy of its environment recovered by a lower-level of theory/MM, and an additional energy term, $E_{\text{interaction}}$, which includes mechanical and electronic embedding of the model region in its environment,

$$E_{\text{additive}} = E_{\text{high.model.}} + E_{\text{low,environment.}} + E_{\text{interaction}} \quad (6.1)$$

where

$$E_{\text{interaction}} = E_{\text{mech.embed.}} + E_{\text{el.embed.}} \quad (6.2)$$

Mechanical embedding ($E_{\text{mech.embed.}}$) is evaluated using the FF to describe physical interactions between the two layers of theory, while electronic embedding ($E_{\text{el.embed.}}$) accounts for the electronic effects created by atoms outside of the QM region. In practice, electronic embedding is often accomplished by treating the atoms in the MM region as point charges in the QM calculation; this procedure allows redistribution of the point charges to provide a more accurate electronic environment for the QM region.[887]

Contrarily, the subtractive scheme, otherwise known as the extrapolative scheme, inherently accounts for mechanical embedding; the interactions between the QM model and the MM environment are treated in the MM description of the entire system by subtracting the MM description of the QM model from the MM total energy.

$$E_{\text{subtractive}} = E_{\text{high.model.}} + E_{\text{low.system.}} - E_{\text{low.model.}} \quad (6.3)$$

This treatment of the boundary between layers of theory corrects error introduced by the interface between system

https://dx.doi.org/10.1021/acs.chemrev.0c00148
Chem. Rev. 2020, 120, 8641−8715

components.[888] Notice, the subtractive scheme does not include electrostatic embedding; this can be remedied by introducing electronic embedding models of varying sophistication.[857,889,890]

Like all applications of theory, multiscale models require a certain level of benchmarking and forethought in the model construction. The substituent test was developed to determine whether different levels of theory would combine to provide a reasonable description of a system by producing substituent values (*S*-values), which are meant to be minimized.[891−893] In a two-layer subtractive scheme, the *S*-values are derived from the overall error between the energy obtained through multiscale modeling, $E_{subtractive}$, and the energy of the complete system computed at the higher/QM level of theory, $E_{high,system}$,

$$E_{error} = E_{subtractive} - E_{high.system.} \quad (6.4)$$

From substitution of eq 6.3 into eq 6.4, we obtain

$$E_{error} = (E_{high.model.} + E_{low.model.} - E_{low.model.}) - E_{high.system.} \quad (6.5)$$

Rearrangement of this equation provides

$$E_{error} = (E_{low.sys.} - E_{low.model.}) - (E_{high.sys.} - E_{high,model.}) \quad (6.6)$$

where the parenthetical terms represent the *S*-value for the low ($S_{low} = E_{low.system.} - E_{low.model.}$) and high ($S_{high} = E_{high.system.} - E_{high.model.}$) levels of theory, yielding

$$E_{error} = S_{low} - S_{high} \quad (6.7)$$

Therefore, the minimum error occurs when S_{low} and S_{high} are equivalent.

The most popular incarnation of the subtractive embedded scheme is Our Own N-layered Integrated Molecular Orbitals and Molecular Mechanics (ONIOM),[868,893,894] which has been implemented in several popular software packages.[737] While ONIOM was developed from two-layer hybrid approaches,[891,895−899] its theory is not limited to two layers or restricted by level of theory.[867,900] In fact, there are several instances of ONIOM applied to cluster models of MOFs;[637,901,902] here, we highlight a representative example of elucidating the adsorption sites of CO_2 and CH_4 on MOF-5 cluster using a MP2/HF approach.[903] There, the authors systematically examined three cluster model sizes (Figure 57) with three unique binding orientations of the small gas molecules. Both the cluster model size and the ONIOM boundary location were important in the final system energy; a cluster model containing three linkers (Figure 57) was required to effectively describe the pore corner binding site, which was revealed to preferentially bind CO_2 and CH_4 over the other examined sites. This study further emphasizes the careful consideration required when developing a multiscale model to determine which portions can be reasonably excluded from the higher-level layer.

The ONIOM approach is not limited to molecular cluster calculations. In a representative study, O_2 binding to an open metal site in periodic M-MOF-74 (M = Mg, Ni, Zn, Co, Mn, and Fe) was studied using high level functionals.[904] A QM region was required because Fe undergoes oxidation upon binding of O_2, and the energetics also depend on neighboring cations. For this study, the 10 Å radius around the active site was treated with the hybrid functional B3LYP that included a line of three metal atoms and the associated DOBDC linkers with their non-

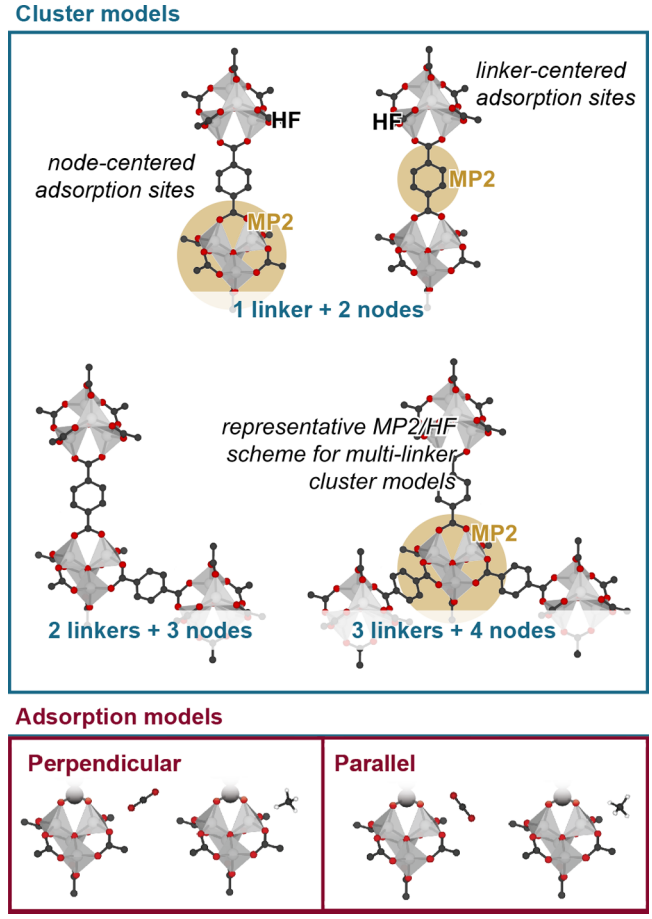

Figure 57. Partitioning employed for the ONIOM study (MP2/HF level) to elucidate CO_2 and CH_4 adsorptive sites on MOF-5. Three cluster models were examined, (i) 1 linker and 2 nodes, (ii) 2 linkers and 3 nodes, and (iii) 3 linkers and 4 nodes. Each of these models were partitioned for the ONIOM study, where either the node or linker were described at the higher level MP2 depending on which adsorptive site was being examined. Two gas molecule orientations to the node and linker, perpendicular and parallel, were considered. Hydrogen atoms are omitted for clarity. Data obtained from ref 903.

coordinating carboxylate and oxygen substituents separated into the MM layer. After testing several FFs for the MM layer, MOF-FF parametrized to both ferric and ferrous forms of a Fe-MOF-74 cluster model of the QM region was found to best reproduce structural elements and full QM values. The energy of binding was computed with QM/MM methods, where the two terminal metals of the QM region were exchanged; all M(II) ions in the MM sections were treated with Fe(II) parameters to avoid reparameterization of MOF-FF for each substitutional derivative.

In a related study with the same material, alkane hydroxylation was examined, Figure 58.[905] There, B3LYP was again employed in the same QM region, but UFF was applied to the periodic environment. All Fe(II) ions but the active site were replaced with nonmagnetic Mg(II) ions to simplify the spin-state effects across the extended lattice. This substitution of Mg(II) for Fe(II) is somewhat common, but is an obvious area for improvement. Spin natural orbitals were used to explain that the high spin state aids in C−H activation of alkanes, and encourages $H^{\bullet}$ abstraction.

A more precise description of framework contributions to the region of interest can be obtained by employing a QM/SE

https://dx.doi.org/10.1021/acs.chemrev.0c00148
Chem. Rev. 2020, 120, 8641−8715

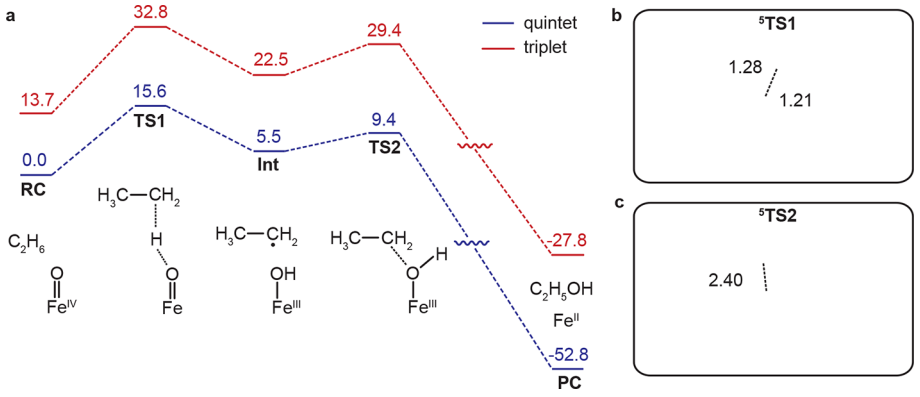

Figure 58. Partitioning employed for the ONIOM study (B3LYP/UFF level) and the relative potential energy profiles of the quintet and triplet iron states. Reproduced with permissions from ref 905. Copyright 2015 American Chemical Society.

model. SE methods provide information about the electronic structure, neglected in MM approaches, which can improve recovery of electronic perturbations of the bulk framework from changes in the QM region. Although the advantages of QM/SE schemes over QM/MM schemes have been discussed,[906] and such schemes have been implemented for biological systems,[907] there are sparing examples of its application in MOF modeling. Given the success of applying SE methods to MOFs, the scarcity of both QM/SE and QM/MM studies in MOF literature[908] may be a symptom of the field's youth.[909,910] While SE methods are not guaranteed to perform better than MM methods,[911] in some cases explicit electronic interactions with cavity walls, e.g., $\pi-\pi$ interactions, need to be considered.

The QM/SE ONIOM approach was employed to study the difference in stereocontrol exerted by the $R\bar{3}$,3′-diphenyl-1,1′-binaphthyl phosphate chiral catalyst when coordinated to Cu-dimer paddlewheels in a MOF.[912] The enantioselective Brønsted acid-catalyzed Friedel–Crafts reaction between indoles and imines yielded products of opposite chirality to the homogeneous system; because the electronic pore environment provided secondary interactions leading to selectivity, an explicit electronic description of the pore was included by treating the lower-level of theory region with PM6. A conductor-like polarizable continuum model (CPCM) was included for solvation effects.[913] Indeed, interactions between aromatic functionalities on the MOF and reactants were found to drive the difference in enantioselectivity due to electronic stabilization that could be better reproduced with explicit considerations of the electrons.

In an analogous comparison between a homogeneous and MOF-bound catalyst, ONIOM was applied to IRMOF-3 where structural parameters were elucidated from pure QM calculations and neutron-diffraction results obtained at 3.5 K were best reproduced when the lower-level of theory region was described by the PM3 functional.[914] The aniline catalyzed Knoevenagel condensation of benzaldehyde and ethyl-cyanoacetate was found to occur faster in IRMOF-3 than with molecular aniline. By considering several plausible reaction pathways and deactivation pathways as enabled by multiscale modeling, it was found that catalytic activity was improved within the MOF framework due to water adsorption; the Zn(II) sites adsorb water that would otherwise poison the catalytically active amine moieties.

6.2. Boundary Treatment

The greatest challenge in multiscale methods is not necessarily the combination of theories, but the treatment of the interface between layers.[915] Within any embodiment, the interface between levels of theory inevitably disrupts the description of direct interactions between components. Conceptually analogous to the cluster extraction procedure, the QM region must be "cleaved" from an extended solid. Thus, severed bonds must be saturated with hybrid orbitals,[340,916–920] pseudoatoms,[921–923] or, more commonly, link atoms like hydrogen, Figure 59.[903]

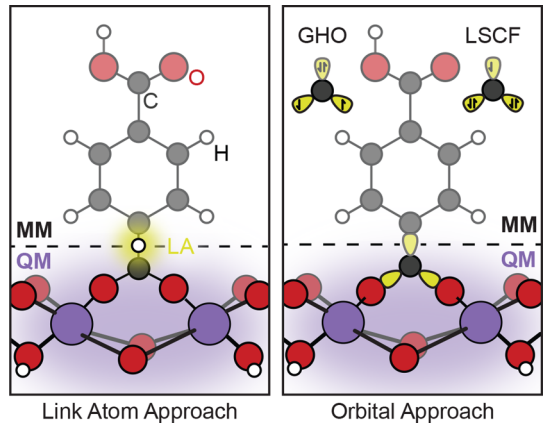

Figure 59. General approaches to boundary treatment. The link atom approach, wherein bonds divided between levels of theory, are capped by extrinsic atoms to saturate the valence shell of each atom on either side of the boundary. The orbital approach, which employs auxiliary orbitals in the MM region and active (SCF optimized) orbitals in the QM region through either a general hybridized approach[341] or a local-self-consistent approach[340,926], where localized orbitals are determined through parametrization of a related system.

Hydrogenation of dangling bonds is effective in removing spurious formal charges from the cluster environment, however, the saturating motif can further be tuned to reproduce the polarization of the truncated bonds.[339,924,925]

As an example, a QM/MM approach was used to study the proton topology in NU-1000.[927] Here, the objective was to simply reproduce electronic trends observed in full QM analysis of the same cluster model.[417] Unsurprisingly, the inclusion of electronic embedding in the multiscale model was necessary to reproduce full QM values. The boundary between layers of theory separated the anionic carboxyl groups from the phenyl ring and models were optimized using both hydrogen and tuned fluorine link atom approaches;[339] the energies and geometries recovered from full QM models were more accurately reproduced by models invoking hydrogen link atoms (a

https://dx.doi.org/10.1021/acs.chemrev.0c00148
Chem. Rev. 2020, 120, 8641–8715

somewhat intuitive result as the hydrogen link atom works reasonably well for cluster modeling, section 3).

Advantageously, the QM/MM study of proton topology in NU-1000 also explored the impact of linker presence in both QM and hybrid QM/MM procedures by comparing the relative energy of benzoate-, acetate-, and formate-capped cluster models with both procedures.[927] Energies and structures extracted from the full QM model of the benzoate capped cluster were consistent with its QM/MM model as well as both the full QM and QM/MM models of the acetate-capped cluster, however, full truncation of the linker to a formate resulted in an energetic difference for proton topology by up to 11 kcal/mol. It was noted that in the case of metal deposition or guest inclusion both formate and acetate models would likely be insufficient to incorporate linker effects, consistent with findings from its preceding literature.[417]

Like in cluster extraction, ongoing effort is placed on developing protocols for determining which bonds are the best interfacial regions in QM/MM models in MOFs. One study directly addressed this using a bond-tuned approach where the impact of the system-tuned fluorine link atoms in which the generality of a parameter set would be extended to the type of bond cleavage, e.g., C−C or C−O, was assessed.[928] The success and generality of this approach, however, will be revealed as more papers are published using the same protocol. The study does point to a larger issue: link atoms can result in overpolarization due to their proximity to point charges implemented in the MM layer. Localized orbitals correct this to some degree because the charge density is inherently distributed into the pseudo-orbital; these methods have more complex implementations.[929]

Charge redistribution techniques that adjust the position of point charges along the cross-boundary bond vector have been successful in eliminating negative modes in the QM/MM Hessian that correspond to inadequate boundary treatment. To assess the different electronic influence of varying the 5,5′-substituents of salen(Mn) catalysts when incorporated as MOF linkers, a redistributed charge and dipole method was applied.[335] The redistributed charge and dipole method adjusts the point charge on the first atom in the MM layer and distributes it evenly across the number of bonds it shares with the QM region and shifts the divided charges along the bond vector away from the link atom.[930]

The same scaffold, salen(Mn), is a catalyst known to perform enantioselective epoxidation of nonfunctionalized olefins was heterogenized into a mixed-linker MOF with biphenyl dicarboxylates and experienced increased enantioselectivity.[931] Full QM analysis of the homogeneous salen(Mn) catalyst developed modified Hammett parameters to describe the enantioselectivity of the catalyst with 5,5′-substitution.[932] The authors validated their QM/MM methodology where the changing substituents were treated at the MM level.[335] A DREIDING[56] FF was parametrized to a cluster model of the unsubstituted salen(Mn) linker extracted from the bulk MOF structure.[931] All other electronic embedding schemes resulted in overpolarization that returned imaginary modes at the QM/MM boundary; negative frequencies associated with interactions between the link atom and the MM point charges were ignored; it is unsurprising that the link atom bond length is not equilibrated. Refining treatment of dangling bonds at the truncated boundary continues to be integral to reproducing the electronic environment of the boundary region and, therefore, the general applicability of multiscale approaches to theoretical MOF studies.[933,934]

The periodic and ionic nature of MOFs enables both their simulation through solid-state techniques, molecular modeling approaches, and partitioning schemes. While modeling the bulk system provides the most holistic description of the electronic structure, molecular clusters provide access to higher levels of theory. These theories enable potentially excellent predictive power, albeit at the sacrifice of a description of the pore. Hence, while there are only a handful of examples of successful multiscale models being applied to MOFs, there is a real opportunity to reduce computational load (even if the implementation mandates serious consideration of the interface treatment, model size, and FF parametrization). In the advent of high-powered computing and continued advancement in hardware, we expect full quantum mechanical descriptions of larger systems will negate multiscale and full molecular mechanical approaches unless the multiscale approaches venture toward device length scales. Yet in the interim, these unique methods may be used to study diffusion properties,[935,936] nucleation,[937] encapsulation,[938,939] prenucleation events during self-assembly, and potentially for polymer growth in MOF pores.[940]

7. OUTLOOK AND CONCLUSIONS

Owing to their ionic construction, MOFs are positioned at the interface of molecular and materials studies, affording both periodic and molecular modeling approaches. Descriptive models that, through the efficient use of computer resources, may be used to recover precise quantitative quantum mechanical information about MOFs fuel the budding partnership between experiment and theory. Yet, as in any computational endeavor, there are several major considerations. Here, we aimed to broadly survey the current applications of electronic structure theory to MOF-centric research questions to date. In doing so, we draw a few solid conclusions:

- Despite the terminal goal of gaining predictive power through modeling, the development and success of a model can only truly be realized through comparison to a known, reproducible experiment, or higher level of theory; benchmarking in this fashion will help to inform the appropriate level of theory and potentially necessary correctional terms.
- The functional does play a major role in determining the properties of the MOF. Hybrid GGA functionals offer increased accuracy over pure GGA functionals yet augment the computational expense. The most common hybrid functionals used in MOF modeling are PBE0, HSE06, B3LYP, M06, and variations thereof. Often, structures are geometrically optimized to the GGA level, followed by a single point hybrid calculation to return the electronic structure. This minimizes computational expense, while affording a higher degree of electronic structure information, even if it is technically from a nonequilibrated structure.
- Correctional terms offer an empirically tuned route toward improved agreement between experimental observables and theoretical results. Dispersion correctional methods account for long-range Coulombic interactions otherwise neglected by the standard Kohn−Sham DFT formalism. Because of the impact of van der Waals forces in crystal packing and host−guest systems,

https://dx.doi.org/10.1021/acs.chemrev.0c00148
Chem. Rev. 2020, 120, 8641−8715

long-range electron correlations are a necessary consideration in MOF modeling. The Hubbard *U* correction term works to counteract the ubiquitous self-interaction error in DFT, accounting for the localization of electrons from Coulombic interactions. Both of these correctional terms may be employed to improve agreement between experiment and theory.

- Owing to the localized electronic structure of many MOFs, they may be modeled as molecular clusters, affording calculations at higher levels of theory. There exist two general approaches to extracting cluster models from MOFs, (i) preserved node, where an entire inorganic node is described while surrounding it with some form of linker approximate, and (ii) preserved linker, where at least one linker remains in its full form and crystallographic connectivity. Importantly, the specific composition and truncation points of a cluster model depends solely on the purpose of the model; thus, cluster size will differ, not only across MOF species but between models of the same MOF composition intended to recover different aspects of electronic structure. Regardless, extraction approaches generate dangling bonds that must be passivated to maintain charge neutrality; often, these are passivated with hydrogen or a truncated version of the original linker, for example truncating BDC to formates.
- The loss of framework rigidity in cluster models poses obvious computational challenges, considering many of interesting electronic properties arise from the specific orientation of inorganic and organic components. Thus, cluster optimization necessitates inclusion of geometric constraints, often accomplished by freezing judiciously selected terminal atoms to minimize unphysical framework distortions that may significantly augment resulting electronic descriptions.
- Reduced cluster model sizes can afford higher levels of theory, and subsequently higher electron resolution, otherwise prohibited by large chemical systems. Post-DFT methods, such as multiconfigurational approaches, are made tractable with cluster models, facilitating the assessment of metal oxidation and spin state, as well as explicit charge transfer mechanisms, etc.
- The crystallinity of MOFs facilitates periodic calculations, which enable bulk electronic and transport properties to be assessed. Taking advantage of the high symmetry points in MOFs enables accurate recovery of the electronic properties within the crystal. The manifestation of these electronic properties can be seen in the electronic band structures, which feature the band gap, and density of states (DOS) plots; both of these theoretical tools display the highly localized electronic structure of most MOFs, which gives rise to wide electronic band gaps with well-defined orbital contributions to the frontier states.
- The entropic favorability of defect formation motivates computational models that can accommodate and replicate their presence. While experimental efforts are often focused on *minimizing* defect concentration, their utility is coming into focus. Their presence can give rise to highly desirable bulk material properties, such as increased electrical conductivity and catalytically active open metal sites. Periodic models suffer from artificial modeling periodic defects, which may result in unrealistically high defect concentrations; thus, a supercell is typically required to obtain energies in better agreement with experiment. The advent of high-performance computing has allowed models to be constructed in which realistic defect concentrations are attainable, however, computational studies exploring reactivity of known defect sites have also found success employing cluster models of defective nodes.
- Owing to the complex crystallinity of MOFs, five types of defects must be considered: (i) vacancies, there is a missing linker or node in the lattice, (ii) substitutions, linkers, or nodes are postsynthetically modified or additional chemical motifs are introduced, (iii) interstitials, guest molecules within MOF pores (which have been shown to alter the electronic structure of the host MOF), (iv) Frenkel defects, a vacancy and compensatory interstitial to charge balance, and (v) Schottky defects, multiple vacancies that sum to zero charge.
- The molecular level of control over the bulk MOF afforded by the modular nature of the node and linker construction promotes targeted formulation of characterizable, site-isolated reaction sites, which are important in catalysis. Computational analysis of catalytic mechanisms and active site geometries facilitates the identification of key reaction intermediates and transition state geometries that would otherwise be indiscernible via experimentation alone. Interpolation and surface-walking algorithms offer computational pathways toward elucidation of the minimum energy pathway and transition-state structure. These may be coupled with computational kinetics via Eyring's transition state theory to quantify key experimental metrics, such as reaction rates and turnover frequency.
- The localization of charge in most MOFs positions them as potential candidates for redox catalysis, and electronic structure theory offers a powerful pathway toward quantifying key properties related to this application, including (i) energy of activation (e.g., band gap), (ii) relative alignment of vacant and occupied states in the catalyst and reactants (e.g., electron affinity and ionization potential/work function), and (iii) exciton lifetime. Moreover, band structures and DOS work to illuminate the specific charge transfer and metal/ligand redox noninnocence mechanisms at play.
- Embedded model systems, in which an area of interest is modeled at a higher level of theory and the surrounding is modeled at a lower level of theory, afford an improved level of steric description, while maintaining computational efficiency. Multiscale models, a specific embedding case, refer to systems where the area of interest is described at a high level of QM theory, while the rest of the system is treated with molecular mechanics, although semi-empirical or another level of QM can be employed as well. The main advantage of multiscale methods over cluster models is the inclusion of important effects from physical/steric interactions or the electrostatic field emanating from the surrounding framework, which is inherent in any cluster extraction scheme. Thus, these methods maintain a QM level description of the area of interest, while still accounting for the steric and electronic effects of the bulk system.
- The emergence of machine learning (ML) property prediction and material generation initiatives will play an

https://dx.doi.org/10.1021/acs.chemrev.0c00148
Chem. Rev. 2020, 120, 8641−8715

increasingly important role in the targeted design of novel frameworks.

In summary, this Review detailed the tension of considering MOFs as either molecules or as extended solids. While in reality the chemical properties of MOFs lay somewhere in between these two extremes, modeling approaches do not: one can either use molecular or solid-state software packages. Ultimately, the success of any model is predicated on the type of chemical interactions it is trying to include, as well as the resolution of the target properties. Hence, the same MOF can be modeled in several different ways, placing computational chemistry in a unique position to provide quantitative, predictive insights into MOF structure/function relationships.

Returning to our original conjecture: MOFs are truly a unique class of molecular materials, masquerading as either molecules or extended solids. It is this duality that invites contributions from the molecular, solid-state, and condensed matter physics communities, and continues to make this neoteric field rapidly evolve.

AUTHOR INFORMATION

Corresponding Author

Christopher H. Hendon − *Department of Chemistry and Biochemistry, University of Oregon, Eugene, Oregon 97405, United States;* orcid.org/0000-0002-7132-768X; Email: chendon@uoregon.edu

Authors

Jenna L. Mancuso − *Department of Chemistry and Biochemistry, University of Oregon, Eugene, Oregon 97405, United States*

Austin M. Mroz − *Department of Chemistry and Biochemistry, University of Oregon, Eugene, Oregon 97405, United States;* orcid.org/0000-0003-4166-8093

Khoa N. Le − *Department of Chemistry and Biochemistry, University of Oregon, Eugene, Oregon 97405, United States*

Complete contact information is available at: https://pubs.acs.org/10.1021/acs.chemrev.0c00148

Author Contributions

J.L.M., A.M.M., and K.N.L. wrote the first draft of the manuscript under the supervision of C.H.H.. All authors contributed to making the figures and editing the final version.

Notes

The authors declare no competing financial interest.

Biographies

Jenna L. Mancuso is a Ph.D. candidate in the Hendon Materials Simulation Group at the University of Oregon, where she employs density functional theory to predict electron transport pathways in metal−organic frameworks and resolve reaction mechanisms both in MOFs and between small molecules. She received her B.Sc. in Polymer Science and Engineering from Case Western Reserve University in Cleveland, OH, (2017) where she was inspired to pursue chemistry by Dr. John D. Protasiewicz. She then moved to Eugene, OR, and obtained her M.S. in Chemistry at UO (2018), where she continues to pursue her Ph.D.

Austin M. Mroz hails from Chicago, where her interest in science and engineering was developed at a young age. After her formative years, Austin traveled to Terre Haute, IN, where she attended Rose-Hulman Institute of Technology. There, she earned her B.Sc. in Mechanical Engineering (2016). Austin then divagated, completing her M.Sc. in Chemistry (2017) at the same university, where she examined the effect of selenomethionine on oxidative DNA damage. Austin is currently a Physical Chemistry Ph.D. candidate at the University of Oregon, working under the mentorship of Dr. Christopher H. Hendon in the Hendon Materials Simulation lab. Austin is primarily focused on developing open source postprocessing software to enhance data analysis of solid-state and molecular calculations, and modeling defects in MOFs.

Khoa N. Le is an NSF GRFP recipient and is currently pursuing his Ph.D. degree under the guidance of Dr. Hendon at the University of Oregon. He received his B.Sc. degree with focus on Chemistry in 2016 at Western Washington University with Mathematics and Biology minors. He worked a pharmaceutical company for a year and then attended the University of Oregon in 2018. His study focuses on the electronic properties and vibrational energy of materials (especially MOF) using computational methods. In Dr. Hendon's lab, Khoa is interested in utilizing computational methods to aid and guide experimentalists on the development and the microscopic understanding of conductive MOFs.

Dr. Christopher H. Hendon obtained his B.Sc. Adv. HONS from Monash University (2011) and Ph.D, from the University of Bath (2015). After a two-year postdoc at Massachusetts Institute of Technology, he joined the University of Oregon as a tenure track Assistant Professor of Chemistry, where his research group focuses the chemistry of porous materials, unusual electronic structure of small organic molecules, and coffee. He enjoys non-Zn-based MOFs, washed Ethiopian coffees, unoaked chardonnay, and east coast oysters.

ACKNOWLEDGMENTS

We are grateful to Prof. L. Gagliardi and Dr. T. W. Kasel for insightful discussions and to Prof. J. R. Long and Prof. M. Dincă for their invitation to submit this Review. We are also grateful to our colleague Prof. C. K. Brozek, who helped us frame the introduction and coined the term "the nanoscale gap". We are also extremely grateful to our colleagues whose willingness to promote open science was exemplified by providing us with their original data and imagery to include throughout the manuscript. This material is based upon work supported by the National Science Foundation through the Division of Materials Research under grant no. DMR-1956403. We also acknowledge the continued support from the Extreme Science and Engineering Discovery Environment (XSEDE), which is supported by the National Science Foundation [ACI-1548562], the PICS Coeus High Performance Computer, which is supported by the National Science Foundation [1624776], and the University of Oregon High Performance Computer, Talapas.

ABBREVIATIONS

acac = acetylacetone
AIMD = ab initio molecular dynamics simulations
AO = atomic orbital
BDC = benzene dicarboxylate
bipydc = bipyridine dicarboxylate
bpdc = biphenyldicarboxylate
BTC = benzene tricarboxylate
BTDD = 1*H*-1,2,3-triazolo[4,5-*b*],[4,5-*i*])dibenzo[1,4]-dioxin
CASPT2 = complete active space second-order perturbation theory
CASSCF = complete active space SCF
CBM = conduction band minimum
CDC = *trans*-1,4-cyclohexane-dicarboxylate

https://dx.doi.org/10.1021/acs.chemrev.0c00148
Chem. Rev. 2020, 120, 8641−8715

CI = configuration interaction
COD = cyclooctadiene
DFPT = density functional perturbation theory
DFT = density functional theory
dhbq = 2,5-dioxidobenzoquinone/1,2-dioxido-4,5-semiquinone
DMMP = dimethyl methlphosphonate
DOBDC = dihydroxybenzenebicarboxylate
DOS = density of states
DSBDC = 2,5-disulfidobenzene-1,4-dicarboxylate
E_F = Fermi level
E_g = fundamental energy gap
EXAFS = extended X-ray absorption fine structure
Facac = hexafluoroacetylacetone
FF = force field
FLP = frustrated Lewis pair
GGA = generalized gradient approximation
HF = Hartree−Fock
HITP = hexaiminotriphenylene
HKUST = Hong Kong University of Science and Technology
HTB = hexathiobenzene
HTB = hexathiolbenzene
HTTP = hexathioltriphenylene
LDA = local density approximation
LSDA = local spin density approximation
MIL = Materials Institute Lavoisier
MIPT = 5-methylisophthalate
MO = molecular orbital
MOF = metal−organic framework
NAO = natural atomic orbital
NBO = natural bond orbital
NDC = 2,6-naphthalendicarboxylic acid
NEB = nudged elastic band
NPA = natural population analysis
PBP = 5,5′-bis(4-pyridyl)(2,2′-bipirimidine
PCET = proton coupled electron transfer
SBU = secondary building unit
SCF = self-consistent field
SOC = spin−orbit coupling
TBAPy = tetrakis(*p*-benzoate)pyrene
tri = 1,2,3-triazolate
TTFTB = tetrathiafulvalene tetrabenzoate
UiO = Universitetet i Oslo
VBM = valence band maximum
XANES = X-ray absorption near edge spectroscopy
XAS = X-ray absorption spectroscopy
ALD = atomic layer deposition
MEP = minimum energy path
CI-NEB = climbing image nudged elastic band
TMBQ = 2,3,5-trimethylbenzoquinone
LMCT = ligand-to-metal charge transfer
STQN = synchronous transit-guided quasi-Newton
TBAB = tetrabytylammonium bromide
IRC = intrinsic reaction coordinate
TOF = turnover frequency
TDTS = TOF-determining transition state
TDI = TOF-determining intermediate
VTST = variational transition state theory
Cl_2dhbq = 2,5-dichloro-3,6-dihydroxybenzoquinone

REFERENCES

(1) Yaghi, O. M.; Li, G.; Li, H. Selective Binding and Removal of Guests in a Microporous Metal−Organic Framework. *Nature* **1995**, *378*, 703−706.
(2) Furukawa, H.; Cordova, K. E.; O'Keeffe, M.; Yaghi, O. M. The Chemistry and Applications of Metal-Organic Frameworks. *Science* **2013**, *341*, 1230444−1230444.
(3) Kitagawa, S.; Kitaura, R.; Noro, S. Functional Porous Coordination Polymers. *Angew. Chem., Int. Ed.* **2004**, *43*, 2334−2375.
(4) Li, H.; Eddaoudi, M.; O'Keeffe, M.; Yaghi, O. M. Design and Synthesis of an Exceptionally Stable and Highly Porous Metal-Organic Framework. *Nature* **1999**, *402*, 276−279.
(5) Eddaoudi, M.; Moler, D. B.; Li, H.; Chen, B.; Reineke, T. M.; O'Keeffe, M.; Yaghi, O. M. Modular Chemistry: Secondary Building Units as a Basis for the Design of Highly Porous and Robust Metal−Organic Carboxylate Frameworks. *Acc. Chem. Res.* **2001**, *34*, 319−330.
(6) Tranchemontagne, D. J.; Mendoza-Cortés, J. L.; O'Keeffe, M.; Yaghi, O. M. Secondary Building Units, Nets and Bonding in the Chemistry of Metal−Organic Frameworks. *Chem. Soc. Rev.* **2009**, *38*, 1257.
(7) Kawano, M.; Kawamichi, T.; Haneda, T.; Kojima, T.; Fujita, M. The Modular Synthesis of Functional Porous Coordination Networks. *J. Am. Chem. Soc.* **2007**, *129*, 15418−15419.
(8) Furukawa, H.; Ko, N.; Go, Y. B.; Aratani, N.; Choi, S. B.; Choi, E.; Yazaydin, A. O.; Snurr, R. Q.; O'Keeffe, M.; Kim, J.; Yaghi, O. M. Ultrahigh Porosity in Metal-Organic Frameworks. *Science* **2010**, *329*, 424−428.
(9) Eddaoudi, M.; Li, H.; Yaghi, O. M. Highly Porous and Stable Metal−Organic Frameworks: Structure Design and Sorption Properties. *J. Am. Chem. Soc.* **2000**, *122*, 1391−1397.
(10) Farha, O. K.; Özgür Yazaydın, A.; Eryazici, I.; Malliakas, C. D.; Hauser, B. G.; Kanatzidis, M. G.; Nguyen, S. T.; Snurr, R. Q.; Hupp, J. T. Novo Synthesis of a Metal−Organic Framework Material Featuring Ultrahigh Surface Area and Gas Storage Capacities. *Nat. Chem.* **2010**, *2*, 944−948.
(11) Mason, J. A.; Veenstra, M.; Long, J. R. Evaluating Metal−Organic Frameworks for Natural Gas Storage. *Chem. Sci.* **2014**, *5*, 32−51.
(12) Rosi, N. L. Hydrogen Storage in Microporous Metal-Organic Frameworks. *Science* **2003**, *300*, 1127−1129.
(13) Li, J.-R.; Kuppler, R. J.; Zhou, H.-C. Selective Gas Adsorption and Separation in Metal−Organic Frameworks. *Chem. Soc. Rev.* **2009**, *38*, 1477−1504.
(14) Li, J.-R.; Sculley, J.; Zhou, H.-C. Metal−Organic Frameworks for Separations. *Chem. Rev.* **2012**, *112*, 869−932.
(15) Chughtai, A. H.; Ahmad, N.; Younus, H. A.; Laypkov, A.; Verpoort, F. Metal−Organic Frameworks: Versatile Heterogeneous Catalysts for Efficient Catalytic Organic Transformations. *Chem. Soc. Rev.* **2015**, *44*, 6804−6849.
(16) Corma, A.; García, H.; Llabrés i Xamena, F. X. Engineering Metal Organic Frameworks for Heterogeneous Catalysis. *Chem. Rev.* **2010**, *110*, 4606−4655.
(17) Farrusseng, D.; Aguado, S.; Pinel, C. Metal-Organic Frameworks: Opportunities for Catalysis. *Angew. Chem., Int. Ed.* **2009**, *48*, 7502−7513.
(18) Gascon, J.; Corma, A.; Kapteijn, F.; Llabrés i Xamena, F. X. Metal Organic Framework Catalysis: *Quo Vadis* ? *ACS Catal.* **2014**, *4*, 361−378.
(19) Chen, S.; Dai, J.; Zeng, X. C. Metal−Organic Kagome Lattices M3(2,3,6,7,10,11-Hexaiminotriphenylene)2 (M = Ni and Cu): From Semiconducting to Metallic by Metal Substitution. *Phys. Chem. Chem. Phys.* **2015**, *17*, 5954−5958.
(20) Stassen, I.; Burtch, N.; Talin, A.; Falcaro, P.; Allendorf, M.; Ameloot, R. An Updated Roadmap for the Integration of Metal−Organic Frameworks with Electronic Devices and Chemical Sensors. *Chem. Soc. Rev.* **2017**, *46*, 3185−3241.
(21) Hendon, C. H.; Rieth, A. J.; Korzyński, M. D.; Dincă, M. Grand Challenges and Future Opportunities for Metal−Organic Frameworks. *ACS Cent. Sci.* **2017**, *3*, 554−563.

https://dx.doi.org/10.1021/acs.chemrev.0c00148
Chem. Rev. 2020, 120, 8641−8715

(22) Liu, L.; Zhou, Y.; Liu, S.; Xu, M. The Applications of Metal−Organic Frameworks in Electrochemical Sensors. *ChemElectroChem* **2018**, *5*, 6−19.
(23) Choi, K. M.; Jeong, H. M.; Park, J. H.; Zhang, Y.-B.; Kang, J. K.; Yaghi, O. M. Supercapacitors of Nanocrystalline Metal−Organic Frameworks. *ACS Nano* **2014**, *8*, 7451−7457.
(24) Morozan, A.; Jaouen, F. Metal Organic Frameworks for Electrochemical Applications. *Energy Environ. Sci.* **2012**, *5*, 9269−9290.
(25) Sheberla, D.; Bachman, J. C.; Elias, J. S.; Sun, C.-J.; Shao-Horn, Y.; Dincă, M. Conductive MOF Electrodes for Stable Supercapacitors with High Areal Capacitance. *Nat. Mater.* **2017**, *16*, 220−224.
(26) Wang, L.; Han, Y.; Feng, X.; Zhou, J.; Qi, P.; Wang, B. Metal−Organic Frameworks for Energy Storage: Batteries and Supercapacitors. *Coord. Chem. Rev.* **2016**, *307*, 361−381.
(27) Xia, W.; Mahmood, A.; Zou, R.; Xu, Q. Metal−Organic Frameworks and Their Derived Nanostructures for Electrochemical Energy Storage and Conversion. *Energy Environ. Sci.* **2015**, *8*, 1837−1866.
(28) Xu, Y.; Li, Q.; Xue, H.; Pang, H. Metal-Organic Frameworks for Direct Electrochemical Applications. *Coord. Chem. Rev.* **2018**, *376*, 292−318.
(29) Zheng, S.; Li, X.; Yan, B.; Hu, Q.; Xu, Y.; Xiao, X.; Xue, H.; Pang, H. Transition-Metal (Fe, Co, Ni) Based Metal-Organic Frameworks for Electrochemical Energy Storage. *Adv. Energy Mater.* **2017**, *7*, 1602733.
(30) Yamabayashi, T.; Atzori, M.; Tesi, L.; Cosquer, G.; Santanni, F.; Boulon, M.-E.; Morra, E.; Benci, S.; Torre, R.; Chiesa, M.; Sorace, L.; Sessoli, R.; Yamashita, M. Scaling Up Electronic Spin Qubits into a Three-Dimensional Metal−Organic Framework. *J. Am. Chem. Soc.* **2018**, *140*, 12090−12101.
(31) Zadrozny, J. M.; Gallagher, A. T.; Harris, T. D.; Freedman, D. E. A Porous Array of Clock Qubits. *J. Am. Chem. Soc.* **2017**, *139*, 7089−7094.
(32) Mezenov, Y. A.; Krasilin, A. A.; Dzyuba, V. P.; Nominé, A.; Milichko, V. A. Metal−Organic Frameworks in Modern Physics: Highlights and Perspectives. *Adv. Sci.* **2019**, *6*, 1900506.
(33) Lu, W.; Wei, Z.; Gu, Z.-Y.; Liu, T.-F.; Park, J.; Park, J.; Tian, J.; Zhang, M.; Zhang, Q.; Gentle, T., III; Bosch, M.; Zhou, H.-C. Tuning the Structure and Function of Metal−Organic Frameworks via Linker Design. *Chem. Soc. Rev.* **2014**, *43*, 5561−5593.
(34) Burnett, B. J.; Barron, P. M.; Hu, C.; Choe, W. Stepwise Synthesis of Metal−Organic Frameworks: Replacement of Structural Organic Linkers. *J. Am. Chem. Soc.* **2011**, *133*, 9984−9987.
(35) Schoedel, A.; Li, M.; Li, D.; O'Keeffe, M.; Yaghi, O. M. Structures of Metal−Organic Frameworks with Rod Secondary Building Units. *Chem. Rev.* **2016**, *116*, 12466−12535.
(36) Vodak, D. T.; Braun, M. E.; Kim, J.; Eddaoudi, M.; Yaghi, O. M. Metal-Organic Frameworks Constructed from Pentagonal Antiprismatic and Cuboctahedral Secondary Building Units. *Chem. Commun.* **2001**, 2534−2535.
(37) Colón, Y. J.; Snurr, R. Q. High-Throughput Computational Screening of Metal−Organic Frameworks. *Chem. Soc. Rev.* **2014**, *43*, 5735−5749.
(38) Wilmer, C. E.; Leaf, M.; Lee, C. Y.; Farha, O. K.; Hauser, B. G.; Hupp, J. T.; Snurr, R. Q. Large-Scale Screening of Hypothetical Metal−Organic Frameworks. *Nat. Chem.* **2012**, *4*, 83−89.
(39) Lalonde, M.; Bury, W.; Karagiaridi, O.; Brown, Z.; Hupp, J. T.; Farha, O. K. Transmetalation: Routes to Metal Exchange within Metal−Organic Frameworks. *J. Mater. Chem. A* **2013**, *1*, 5453−5468.
(40) Grancha, T.; Ferrando-Soria, J.; Zhou, H.-C.; Gascon, J.; Seoane, B.; Pasán, J.; Fabelo, O.; Julve, M.; Pardo, E. Postsynthetic Improvement of the Physical Properties in a Metal-Organic Framework through a Single Crystal to Single Crystal Transmetallation. *Angew. Chem., Int. Ed.* **2015**, *54*, 6521−6525.
(41) Asha, K. S.; Bhattacharjee, R.; Mandal, S. Complete Transmetalation in a Metal-Organic Framework by Metal Ion Metathesis in a Single Crystal for Selective Sensing of Phosphate Ions in Aqueous Media. *Angew. Chem., Int. Ed.* **2016**, *55*, 11528−11532.
(42) Das, S.; Kim, H.; Kim, K. Metathesis in Single Crystal: Complete and Reversible Exchange of Metal Ions Constituting the Frameworks of Metal−Organic Frameworks. *J. Am. Chem. Soc.* **2009**, *131*, 3814−3815.
(43) Song, X.; Kim, T. K.; Kim, H.; Kim, D.; Jeong, S.; Moon, H. R.; Lah, M. S. Post-Synthetic Modifications of Framework Metal Ions in Isostructural Metal−Organic Frameworks: Core−Shell Heterostructures via Selective Transmetalations. *Chem. Mater.* **2012**, *24*, 3065−3073.
(44) Islamoglu, T.; Goswami, S.; Li, Z.; Howarth, A. J.; Farha, O. K.; Hupp, J. T. Postsynthetic Tuning of Metal−Organic Frameworks for Targeted Applications. *Acc. Chem. Res.* **2017**, *50*, 805−813.
(45) Kim, M.; Cahill, J. F.; Su, Y.; Prather, K. A.; Cohen, S. M. Postsynthetic Ligand Exchange as a Route to Functionalization of 'Inert' Metal−Organic Frameworks. *Chem. Sci.* **2012**, *3*, 126−130.
(46) Kim, M.; Cahill, J. F.; Fei, H.; Prather, K. A.; Cohen, S. M. Postsynthetic Ligand and Cation Exchange in Robust Metal−Organic Frameworks. *J. Am. Chem. Soc.* **2012**, *134*, 18082−18088.
(47) Doonan, C. J.; Morris, W.; Furukawa, H.; Yaghi, O. M. Isoreticular Metalation of Metal−Organic Frameworks. *J. Am. Chem. Soc.* **2009**, *131*, 9492−9493.
(48) Ma, L.; Falkowski, J. M.; Abney, C.; Lin, W. A Series of Isoreticular Chiral Metal−Organic Frameworks as a Tunable Platform for Asymmetric Catalysis. *Nat. Chem.* **2010**, *2*, 838−846.
(49) Bellarosa, L.; Castillo, J. M.; Vlugt, T.; Calero, S.; López, N. On the Mechanism Behind the Instability of Isoreticular Metal-Organic Frameworks (IRMOFs) in Humid Environments. *Chem. - Eur. J.* **2012**, *18*, 12260−12266.
(50) Colombo, V.; Montoro, C.; Maspero, A.; Palmisano, G.; Masciocchi, N.; Galli, S.; Barea, E.; Navarro, J. A. R. Tuning the Adsorption Properties of Isoreticular Pyrazolate-Based Metal−Organic Frameworks through Ligand Modification. *J. Am. Chem. Soc.* **2012**, *134*, 12830−12843.
(51) Eddaoudi, M. Systematic Design of Pore Size and Functionality in Isoreticular MOFs and Their Application in Methane Storage. *Science* **2002**, *295*, 469−472.
(52) Garibay, S. J.; Cohen, S. M. Isoreticular Synthesis and Modification of Frameworks with the UiO-66 Topology. *Chem. Commun.* **2010**, *46*, 7700−7702.
(53) Sagara, T.; Klassen, J.; Ortony, J.; Ganz, E. Binding Energies of Hydrogen Molecules to Isoreticular Metal-Organic Framework Materials. *J. Chem. Phys.* **2005**, *123*, No. 014701.
(54) Burtch, N. C.; Jasuja, H.; Walton, K. S. Water Stability and Adsorption in Metal−Organic Frameworks. *Chem. Rev.* **2014**, *114*, 10575−10612.
(55) Furukawa, H.; Gándara, F.; Zhang, Y.-B.; Jiang, J.; Queen, W. L.; Hudson, M. R.; Yaghi, O. M. Water Adsorption in Porous Metal−Organic Frameworks and Related Materials. *J. Am. Chem. Soc.* **2014**, *136*, 4369−4381.
(56) Hanikel, N.; Prévot, M. S.; Fathieh, F.; Kapustin, E. A.; Lyu, H.; Wang, H.; Diercks, N. J.; Glover, T. G.; Yaghi, O. M. Rapid Cycling and Exceptional Yield in a Metal-Organic Framework Water Harvester. *ACS Cent. Sci.* **2019**, *5*, 1699−1706.
(57) Rieth, A. J.; Wright, A. M.; Skorupskii, G.; Mancuso, J. L.; Hendon, C. H.; Dincă, M. Record-Setting Sorbents for Reversible Water Uptake by Systematic Anion Exchanges in Metal−Organic Frameworks. *J. Am. Chem. Soc.* **2019**, *141*, 13858−13866.
(58) Ma, L.; Abney, C.; Lin, W. Enantioselective Catalysis with Homochiral Metal−Organic Frameworks. *Chem. Soc. Rev.* **2009**, *38*, 1248−1256.
(59) Zhang, T.; Lin, W. Metal−Organic Frameworks for Artificial Photosynthesis and Photocatalysis. *Chem. Soc. Rev.* **2014**, *43*, 5982−5993.
(60) Zhu, L.; Liu, X.-Q.; Jiang, H.-L.; Sun, L.-B. Metal−Organic Frameworks for Heterogeneous Basic Catalysis. *Chem. Rev.* **2017**, *117*, 8129−8176.
(61) Howarth, A. J.; Liu, Y.; Li, P.; Li, Z.; Wang, T. C.; Hupp, J. T.; Farha, O. K. Chemical, Thermal and Mechanical Stabilities of Metal−Organic Frameworks. *Nat. Rev. Mater.* **2016**, *1*, 15018.

https://dx.doi.org/10.1021/acs.chemrev.0c00148
Chem. Rev. 2020, 120, 8641−8715

(62) Valvekens, P.; Vermoortele, F.; De Vos, D. Metal−Organic Frameworks as Catalysts: The Role of Metal Active Sites. *Catal. Sci. Technol.* **2013**, *3*, 1435−1445.
(63) Jiao, L.; Wang, Y.; Jiang, H.-L.; Xu, Q. Metal-Organic Frameworks as Platforms for Catalytic Applications. *Adv. Mater.* **2018**, *30*, 1703663.
(64) Manna, K.; Zhang, T.; Greene, F. X.; Lin, W. Bipyridine- and Phenanthroline-Based Metal−Organic Frameworks for Highly Efficient and Tandem Catalytic Organic Transformations via Directed C−H Activation. *J. Am. Chem. Soc.* **2015**, *137*, 2665−2673.
(65) Feng, D.; Chung, W.-C.; Wei, Z.; Gu, Z.-Y.; Jiang, H.-L.; Chen, Y.-P.; Darensbourg, D. J.; Zhou, H.-C. Construction of Ultrastable Porphyrin Zr Metal−Organic Frameworks through Linker Elimination. *J. Am. Chem. Soc.* **2013**, *135*, 17105−17110.
(66) Klet, R. C.; Wang, T. C.; Fernandez, L. E.; Truhlar, D. G.; Hupp, J. T.; Farha, O. K. Synthetic Access to Atomically Dispersed Metals in Metal−Organic Frameworks via a Combined Atomic-Layer-Deposition-in-MOF and Metal-Exchange Approach. *Chem. Mater.* **2016**, *28*, 1213−1219.
(67) Mondloch, J. E.; Bury, W.; Fairen-Jimenez, D.; Kwon, S.; DeMarco, E. J.; Weston, M. H.; Sarjeant, A. A.; Nguyen, S. T.; Stair, P. C.; Snurr, R. Q.; Farha, O. K.; Hupp, J. T. Vapor-Phase Metalation by Atomic Layer Deposition in a Metal−Organic Framework. *J. Am. Chem. Soc.* **2013**, *135*, 10294−10297.
(68) Pal, T. K.; De, D.; Neogi, S.; Pachfule, P.; Senthilkumar, S.; Xu, Q.; Bharadwaj, P. K. Significant Gas Adsorption and Catalytic Performance by a Robust Cu^{II} -MOF Derived through Single-Crystal to Single-Crystal Transmetalation of a Thermally Less-Stable Zn^{II} -MOF. *Chem. - Eur. J.* **2015**, *21*, 19064−19070.
(69) Xu, Y.; Howarth, A. J.; Islamoglu, T.; da Silva, C. T.; Hupp, J. T.; Farha, O. K. Combining Solvent-Assisted Linker Exchange and Transmetallation Strategies to Obtain a New Non-Catenated Nickel (II) Pillared-Paddlewheel MOF. *Inorg. Chem. Commun.* **2016**, *67*, 60−63.
(70) Pal, T. K.; De, D.; Senthilkumar, S.; Neogi, S.; Bharadwaj, P. K. A Partially Fluorinated, Water-Stable Cu(II)−MOF Derived via Transmetalation: Significant Gas Adsorption with High CO_2 Selectivity and Catalysis of Biginelli Reactions. *Inorg. Chem.* **2016**, *55*, 7835−7842.
(71) Lee, C. Y.; Farha, O. K.; Hong, B. J.; Sarjeant, A. A.; Nguyen, S. T.; Hupp, J. T. Light-Harvesting Metal−Organic Frameworks (MOFs): Efficient Strut-to-Strut Energy Transfer in Bodipy and Porphyrin-Based MOFs. *J. Am. Chem. Soc.* **2011**, *133*, 15858−15861.
(72) Metzger, E. D.; Brozek, C. K.; Comito, R. J.; Dincă, M. Selective Dimerization of Ethylene to 1-Butene with a Porous Catalyst. *ACS Cent. Sci.* **2016**, *2*, 148−153.
(73) Benoit, F. Substituent Effects in Mass Spectrometry—III: Substituent Effects in the Dissociation of the Molecular Ions Ofpara Andmeta Substituted Benzoic Acids. *Org. Mass Spectrom.* **1973**, *7*, 295−303.
(74) Dan-Hardi, M.; Serre, C.; Frot, T.; Rozes, L.; Maurin, G.; Sanchez, C.; Férey, G. A New Photoactive Crystalline Highly Porous Titanium(IV) Dicarboxylate. *J. Am. Chem. Soc.* **2009**, *131*, 10857−10859.
(75) Cavka, J. H.; Jakobsen, S.; Olsbye, U.; Guillou, N.; Lamberti, C.; Bordiga, S.; Lillerud, K. P. A New Zirconium Inorganic Building Brick Forming Metal Organic Frameworks with Exceptional Stability. *J. Am. Chem. Soc.* **2008**, *130*, 13850−13851.
(76) Walsh, A.; Butler, K. T.; Hendon, C. H. Chemical Principles for Electroactive Metal−Organic Frameworks. *MRS Bull.* **2016**, *41*, 870−876.
(77) Chen, B.; Wang, L.; Zapata, F.; Qian, G.; Lobkovsky, E. B. A Luminescent Microporous Metal−Organic Framework for the Recognition and Sensing of Anions. *J. Am. Chem. Soc.* **2008**, *130*, 6718−6719.
(78) Allendorf, M. D.; Bauer, C. A.; Bhakta, R. K.; Houk, R. J. T. Luminescent Metal−Organic Frameworks. *Chem. Soc. Rev.* **2009**, *38*, 1330−1352.
(79) Hendon, C. H.; Tiana, D.; Fontecave, M.; Sanchez, C.; D'arras, L.; Sassoye, C.; Rozes, L.; Mellot-Draznieks, C.; Walsh, A. Engineering the Optical Response of the Titanium-MIL-125 Metal−Organic Framework through Ligand Functionalization. *J. Am. Chem. Soc.* **2013**, *135*, 10942−10945.
(80) Li, Y.; Xu, H.; Ouyang, S.; Ye, J. Metal−Organic Frameworks for Photocatalysis. *Phys. Chem. Chem. Phys.* **2016**, *18*, 7563−7572.
(81) Xiao, J.-D.; Jiang, H.-L. Metal−Organic Frameworks for Photocatalysis and Photothermal Catalysis. *Acc. Chem. Res.* **2019**, *52*, 356−366.
(82) Ziebel, M. E.; Gaggioli, C. A.; Turkiewicz, A. B.; Ryu, W.; Gagliardi, L.; Long, J. R. Effects of Covalency on Anionic Redox Chemistry in Semiquinoid-Based Metal−Organic Frameworks. *J. Am. Chem. Soc.* **2020**, *142*, 2653−2664.
(83) Tranchemontagne, D. J.; Hunt, J. R.; Yaghi, O. M. Room Temperature Synthesis of Metal-Organic Frameworks: MOF-5, MOF-74, MOF-177, MOF-199, and IRMOF-0. *Tetrahedron* **2008**, *64*, 8553−8557.
(84) Hmadeh, M.; Lu, Z.; Liu, Z.; Gándara, F.; Furukawa, H.; Wan, S.; Augustyn, V.; Chang, R.; Liao, L.; Zhou, F.; Perre, E.; Ozolins, V.; Suenaga, K.; Duan, X.; Dunn, B.; Yamamto, Y.; Terasaki, O.; Yaghi, O. M. New Porous Crystals of Extended Metal-Catecholates. *Chem. Mater.* **2012**, *24*, 3511−3513.
(85) Sheberla, D.; Sun, L.; Blood-Forsythe, M. A.; Er, S.; Wade, C. R.; Brozek, C. K.; Aspuru-Guzik, A.; Dinca, M. High Electrical Conductivity in Ni_3(2,3,6,7,10,11-Hexaiminotriphenylene)$_2$, a Semiconducting Metal−Organic Graphene Analogue. *J. Am. Chem. Soc.* **2014**, *136*, 8859−8862.
(86) Herebian, D.; Bothe, E.; Neese, F.; Weyhermüller, T.; Wieghardt, K. Molecular and Electronic Structures of Bis-(*o*-Diiminobenzosemiquinonato)Metal(II) Complexes (Ni, Pd, Pt), Their Monocations and -Anions, and of Dimeric Dications Containing Weak Metal−Metal Bonds. *J. Am. Chem. Soc.* **2003**, *125*, 9116−9128.
(87) Stiefel, E. I.; Waters, J. H.; Billig, E.; Gray, H. B. The Myth of Nickel(III) and Nickel(IV) in Planar Complexes. *J. Am. Chem. Soc.* **1965**, *87*, 3016−3017.
(88) Hendon, C. H.; Tiana, D.; Walsh, A. Conductive Metal−Organic Frameworks and Networks: Fact or Fantasy? *Phys. Chem. Chem. Phys.* **2012**, *14*, 13120−13132.
(89) Lin, C.-K.; Zhao, D.; Gao, W.-Y.; Yang, Z.; Ye, J.; Xu, T.; Ge, Q.; Ma, S.; Liu, D.-J. Tunability of Band Gaps in Metal−Organic Frameworks. *Inorg. Chem.* **2012**, *51*, 9039−9044.
(90) Farha, O. K.; Hupp, J. T. Rational Design, Synthesis, Purification, and Activation of Metal−Organic Framework Materials. *Acc. Chem. Res.* **2010**, *43*, 1166−1175.
(91) Canepa, P.; Chabal, Y. J.; Thonhauser, T. When Metal Organic Frameworks Turn into Linear Magnets. *Phys. Rev. B: Condens. Matter Mater. Phys.* **2013**, *87*, No. 094407.
(92) Tian, Y.; Wang, W.; Chai, Y.; Cong, J.; Shen, S.; Yan, L.; Wang, S.; Han, X.; Sun, Y. Quantum Tunneling of Magnetization in a Metal-Organic Framework. *Phys. Rev. Lett.* **2014**, *112*, No. 017202.
(93) Makov, G.; Payne, M. C. Periodic Boundary Conditions in *Ab Initio* Calculations. *Phys. Rev. B: Condens. Matter Mater. Phys.* **1995**, *51*, 4014−4022.
(94) *Computer Modeling of Microporous Materials*, 1st ed.; Catlow, C. R. A., van Santen, R. A., Smit, B. J., Eds.; Elsevier: Academic Press: Amsterdam, Boston, 2004.
(95) Hinchliffe, A. *Molecular Modeling for Beginners*; Wiley: Chichester, UK, Hoboken, NJ, 2003.
(96) Truhlar, D. G.; Garrett, B. C.; Klippenstein, S. J. Current Status of Transition-State Theory. *J. Phys. Chem.* **1996**, *100*, 12771−12800.
(97) Nazarian, D.; Ganesh, P.; Sholl, D. S. Benchmarking Density Functional Theory Predictions of Framework Structures and Properties in a Chemically Diverse Test Set of Metal−Organic Frameworks. *J. Mater. Chem. A* **2015**, *3*, 22432−22440.
(98) Odoh, S. O.; Cramer, C. J.; Truhlar, D. G.; Gagliardi, L. Quantum-Chemical Characterization of the Properties and Reactivities of Metal−Organic Frameworks. *Chem. Rev.* **2015**, *115*, 6051−6111.
(99) O'boyle, N. M.; Tenderholt, A. L.; Langner, K. M. Cclib: A Library for Package-Independent Computational Chemistry Algorithms. *J. Comput. Chem.* **2008**, *29*, 839−845.

https://dx.doi.org/10.1021/acs.chemrev.0c00148
Chem. Rev. 2020, 120, 8641−8715

(100) Lejaeghere, K.; Van Speybroeck, V.; Van Oost, G.; Cottenier, S. Error Estimates for Solid-State Density-Functional Theory Predictions: An Overview by Means of the Ground-State Elemental Crystals. *Crit. Rev. Solid State Mater. Sci.* **2014**, *39*, 1−24.
(101) Hamad, S.; Hernandez, N. C.; Aziz, A.; Ruiz-Salvador, A. R.; Calero, S.; Grau-Crespo, R. Electronic Structure of Porphyrin-Based Metal−Organic Frameworks and Their Suitability for Solar Fuel Production Photocatalysis. *J. Mater. Chem. A* **2015**, *3*, 23458−23465.
(102) Butler, K. T.; Hendon, C. H.; Walsh, A. Electronic Structure Modulation of Metal−Organic Frameworks for Hybrid Devices. *ACS Appl. Mater. Interfaces* **2014**, *6*, 22044−22050.
(103) Tayfuroglu, O.; Kocak, A.; Zorlu, Y. In Silico Investigation into H_2 Uptake in MOFs: Combined Text/Data Mining and Structural Calculations. *Langmuir* **2020**, *36*, 119−129.
(104) Park, S. S.; Hendon, C. H.; Fielding, A. J.; Walsh, A.; O'Keeffe, M.; Dincă, M. The Organic Secondary Building Unit: Strong Intermolecular π Interactions Define Topology in MIT-25, a Mesoporous MOF with Proton-Replete Channels. *J. Am. Chem. Soc.* **2017**, *139*, 3619−3622.
(105) Jackson, A. J.; Skelton, J. M.; Hendon, C. H.; Butler, K. T.; Walsh, A. Crystal Structure Optimisation Using an Auxiliary Equation of State. *J. Chem. Phys.* **2015**, *143*, 184101.
(106) Hendon, C. H.; Bonnefoy, J.; Quadrelli, E. A.; Canivet, J.; Chambers, M. B.; Rousse, G.; Walsh, A.; Fontecave, M.; Mellot-Draznieks, C. A Simple and Non-Destructive Method for Assessing the Incorporation of Bipyridine Dicarboxylates as Linkers within Metal−Organic Frameworks. *Chem. - Eur. J.* **2016**, *22*, 3713−3718.
(107) Hendrickx, K.; Vanpoucke, D. E. P.; Leus, K.; Lejaeghere, K.; Van Yperen-De Deyne, A.; Van Speybroeck, V.; Van Der Voort, P.; Hemelsoet, K. Understanding Intrinsic Light Absorption Properties of UiO-66 Frameworks: A Combined Theoretical and Experimental Study. *Inorg. Chem.* **2015**, *54*, 10701−10710.
(108) Goodenough, J. B. Spin-Orbit-Coupling Effects in Transition-Metal Compounds. *Phys. Rev.* **1968**, *171*, 466−479.
(109) Davidson, E. R.; Feller, D. Basis Set Selection for Molecular Calculations. *Chem. Rev.* **1986**, *86*, 681−696.
(110) Huzinaga, S. Basis Sets for Molecular Calculations. *Comput. Phys. Rep.* **1985**, *2*, 281−339.
(111) Schuchardt, K. L.; Didier, B. T.; Elsethagen, T.; Sun, L.; Gurumoorthi, V.; Chase, J.; Li, J.; Windus, T. L. Basis Set Exchange: A Community Database for Computational Sciences. *J. Chem. Inf. Model.* **2007**, *47*, 1045−1052.
(112) Kenny, S.; Horsfield, A.; Fujitani, H. Transferable Atomic-Type Orbital Basis Sets for Solids. *Phys. Rev. B: Condens. Matter Mater. Phys.* **2000**, *62*, 4899−4905.
(113) Bultinck, P.; Ayers, P. W.; Fias, S.; Tiels, K.; Van Alsenoy, C. Uniqueness and Basis Set Dependence of Iterative Hirshfeld Charges. *Chem. Phys. Lett.* **2007**, *444*, 205−208.
(114) Daga, L. E.; Civalleri, B.; Maschio, L. Gaussian Basis Sets for Crystalline Solids: All-Purpose Basis Set Libraries vs System-Specific Optimizations. *J. Chem. Theory Comput.* **2020**, *16*, 2192−2201.
(115) Helgaker, T.; Klopper, W.; Tew, D. P. Quantitative Quantum Chemistry. *Mol. Phys.* **2008**, *106*, 2107−2143.
(116) Hill, J. G. Gaussian Basis Sets for Molecular Applications. *Int. J. Quantum Chem.* **2013**, *113*, 21−34.
(117) Booth, G. H.; Tsatsoulis, T.; Chan, G. K.-L.; Grüneis, A. From Plane Waves to Local Gaussians for the Simulation of Correlated Periodic Systems. *J. Chem. Phys.* **2016**, *145*, No. 084111.
(118) Kresse, G.; Furthmüller, J. Efficient Iterative Schemes for Ab Initio Total-Energy Calculations Using a Plane-Wave Basis Set. *Phys. Rev. B: Condens. Matter Mater. Phys.* **1996**, *54*, 11169−11186.
(119) Frisch, M. J.; Pople, J. A.; Binkley, J. S. Self-consistent Molecular Orbital Methods 25. Supplementary Functions for Gaussian Basis Sets. *J. Chem. Phys.* **1984**, *80*, 3265−3269.
(120) Ehrenreich, H.; Cohen, M. H. Self-Consistent Field Approach to the Many-Electron Problem. *Phys. Rev.* **1959**, *115*, 786−790.
(121) Hohenberg, P.; Kohn, W. Inhomogeneous Electron Gas. *Phys. Rev.* **1964**, *136*, B864−B871.
(122) Kohn, W.; Sham, L. J. Self-Consistent Equations Including Exchange and Correlation Effects. *Phys. Rev.* **1965**, *140*, A1133−A1138.
(123) Medvedev, M. G.; Bushmarinov, I. S.; Sun, J.; Perdew, J. P.; Lyssenko, K. A. Density Functional Theory Is Straying from the Path toward the Exact Functional. *Science* **2017**, *355*, 49−52.
(124) Jäger, M.; Freitag, L.; González, L. Using Computational Chemistry to Design Ru Photosensitizers with Directional Charge Transfer. *Coord. Chem. Rev.* **2015**, *304*−*305*, 146−165.
(125) Mattsson, A. E. Density Functional Theory: In Pursuit of the "Divine" Functional. *Science* **2002**, *298*, 759−760.
(126) Vosko, S. H.; Wilk, L.; Nusair, M. Accurate Spin-Dependent Electron Liquid Correlation Energies for Local Spin Density Calculations: A Critical Analysis. *Can. J. Phys.* **1980**, *58*, 1200−1211.
(127) Perdew, J. P.; Zunger, A. Self-Interaction Correction to Density-Functional Approximations for Many-Electron Systems. *Phys. Rev. B: Condens. Matter Mater. Phys.* **1981**, *23*, 5048−5079.
(128) Dou, J.-H.; Sun, L.; Ge, Y.; Li, W.; Hendon, C. H.; Li, J.; Gul, S.; Yano, J.; Stach, E. A.; Dincă, M. Signature of Metallic Behavior in the Metal−Organic Frameworks M_3(Hexaiminobenzene)$_2$ (M = Ni, Cu). *J. Am. Chem. Soc.* **2017**, *139*, 13608−13611.
(129) Clough, A. J.; Skelton, J. M.; Downes, C. A.; de la Rosa, A. A.; Yoo, J. W.; Walsh, A.; Melot, B. C.; Marinescu, S. C. Metallic Conductivity in a Two-Dimensional Cobalt Dithiolene Metal−Organic Framework. *J. Am. Chem. Soc.* **2017**, *139*, 10863−10867.
(130) Clough, A. J.; Orchanian, N. M.; Skelton, J. M.; Neer, A. J.; Howard, S. A.; Downes, C. A.; Piper, L. F. J.; Walsh, A.; Melot, B. C.; Marinescu, S. C. Room Temperature Metallic Conductivity in a Metal−Organic Framework Induced by Oxidation. *J. Am. Chem. Soc.* **2019**, *141*, 16323−16330.
(131) Langreth, D. C.; Mehl, M. J. Beyond the Local-Density Approximation in Calculations of Ground-State Electronic Properties. *Phys. Rev. B: Condens. Matter Mater. Phys.* **1983**, *28*, 1809−1834.
(132) Perdew, J. P.; Chevary, J. A.; Vosko, S. H.; Jackson, K. A.; Pederson, M. R.; Singh, D. J.; Fiolhais, C. Atoms, Molecules, Solids, and Surfaces: Applications of the Generalized Gradient Approximation for Exchange and Correlation. *Phys. Rev. B: Condens. Matter Mater. Phys.* **1992**, *46*, 6671−6687.
(133) Perdew, J. P.; Burke, K.; Ernzerhof, M. Generalized Gradient Approximation Made Simple. *Phys. Rev. Lett.* **1996**, *77*, 3865−3868.
(134) Wang, J.; Zhou, Y. Dependence of Elastic Stiffness on Electronic Band Structure of Nanolaminate M_2AlC (M = Ti, V, Nb, and Cr) Ceramics. *Phys. Rev. B: Condens. Matter Mater. Phys.* **2004**, *69*, 214111.
(135) Riley, J. M.; Mazzola, F.; Dendzik, M.; Michiardi, M.; Takayama, T.; Bawden, L.; Granerød, C.; Leandersson, M.; Balasubramanian, T.; Hoesch, M.; Kim, T. K.; Takagi, H.; Meevasana, W.; Hofmann, Ph.; Bahramy, M. S.; Wells, J. W.; King, P. D. C. Direct Observation of Spin-Polarized Bulk Bands in an Inversion-Symmetric Semiconductor. *Nat. Phys.* **2014**, *10*, 835−839.
(136) Ciofini, I.; Adamo, C.; Chermette, H. Self-Interaction Error in Density Functional Theory: A Mean-Field Correction for Molecules and Large Systems. *Chem. Phys.* **2005**, *309*, 67−76.
(137) Zhao, Y.; Truhlar, D. G. A New Local Density Functional for Main-Group Thermochemistry, Transition Metal Bonding, Thermochemical Kinetics, and Noncovalent Interactions. *J. Chem. Phys.* **2006**, *125*, 194101.
(138) Tao, J.; Perdew, J. P.; Staroverov, V. N.; Scuseria, G. E. Climbing the Density Functional Ladder: Nonempirical Meta−Generalized Gradient Approximation Designed for Molecules and Solids. *Phys. Rev. Lett.* **2003**, *91*, 146401.
(139) Adamo, C.; Barone, V. Toward Reliable Density Functional Methods without Adjustable Parameters: The PBE0Model. *J. Chem. Phys.* **1999**, *110*, 6158−6169.
(140) Heyd, J.; Scuseria, G. E.; Ernzerhof, M. Erratum: "Hybrid Functionals Based on a Screened Coulomb Potential" [J. Chem. Phys. 118, 8207 (2003)]. *J. Chem. Phys.* **2006**, *124*, 219906.
(141) Yanai, T.; Tew, D.; Handy, N. A New Hybrid Exchange-Correlation Functional Using the Coulomb-Attenuating Method. *Chem. Phys. Lett.* **2004**, *393*, 51−57.

https://dx.doi.org/10.1021/acs.chemrev.0c00148
Chem. Rev. 2020, 120, 8641−8715

(142) Becke, A. D. Density-Functional Exchange-Energy Approximation with Correct Asymptotic Behavior. *Phys. Rev. A: At., Mol., Opt. Phys.* **1988**, *38*, 3098−3100.
(143) Lee, C.; Yang, W.; Parr, R. G. Development of the Colle-Salvetti Correlation-Energy Formula into a Functional of the Electron Density. *Phys. Rev. B: Condens. Matter Mater. Phys.* **1988**, *37*, 785−789.
(144) Janthon, P.; Luo, S. A.; Kozlov, S. M.; Viñes, F.; Limtrakul, J.; Truhlar, D. G.; Illas, F. Bulk Properties of Transition Metals: A Challenge for the Design of Universal Density Functionals. *J. Chem. Theory Comput.* **2014**, *10*, 3832−3839.
(145) Zhao, Y.; Truhlar, D. G. The M06 Suite of Density Functionals for Main Group Thermochemistry, Thermochemical Kinetics, Noncovalent Interactions, Excited States, and Transition Elements: Two New Functionals and Systematic Testing of Four M06-Class Functionals and 12 Other Functionals. *Theor. Chem. Acc.* **2008**, *120*, 215−241.
(146) Heyd, J.; Scuseria, G. E.; Ernzerhof, M. Hybrid Functionals Based on a Screened Coulomb Potential. *J. Chem. Phys.* **2003**, *118*, 8207−8215.
(147) Musho, T.; Li, J.; Wu, N. Thermodynamics of the Oxygen Evolution Electrocatalysis in a Functionalized UiO-66 Metal-Organic Frameworks. *Int. J. Quantum Chem.* **2016**, *116*, 1153−1159.
(148) Butler, K. T.; Hendon, C. H.; Walsh, A. Electronic Chemical Potentials of Porous Metal−Organic Frameworks. *J. Am. Chem. Soc.* **2014**, *136*, 2703−2706.
(149) Degaga, G. D.; Pandey, R.; Gupta, C.; Bharadwaj, L. Tailoring of the Electronic Property of Zn-BTC Metal−Organic Framework via Ligand Functionalization: An Ab Initio Investigation. *RSC Adv.* **2019**, *9*, 14260−14267.
(150) Perdew, J. P.; Ruzsinszky, A.; Csonka, G. I.; Vydrov, O. A.; Scuseria, G. E.; Constantin, L. A.; Zhou, X.; Burke, K. Restoring the Density-Gradient Expansion for Exchange in Solids and Surfaces. *Phys. Rev. Lett.* **2008**, *100*, 136406.
(151) Vrubel, I. I.; Senkevich, N. Y.; Khramenkova, E. V.; Polozkov, R. G.; Shelykh, I. A. Electronic Structure and Optical Response of Zn-Based Metal−Organic Frameworks. *Adv. Theory Simul.* **2018**, *1*, 1800049.
(152) Zhang, F.-M.; Sheng, J.-L.; Yang, Z.-D.; Sun, X.-J.; Tang, H.-L.; Lu, M.; Dong, H.; Shen, F.-C.; Liu, J.; Lan, Y.-Q. Rational Design of MOF/COF Hybrid Materials for Photocatalytic H_2 Evolution in the Presence of Sacrificial Electron Donors. *Angew. Chem., Int. Ed.* **2018**, *57*, 12106−12110.
(153) Dong, H. C.; Nguyen, H. L.; Le, H. M.; Thoai, N.; Kawazoe, Y.; Nguyen-Manh, D. Monitoring Mechanical, Electronic, and Catalytic Trends in a Titanium Metal Organic Framework Under the Influence of Guest-Molecule Encapsulation Using Density Functional Theory. *Sci. Rep.* **2018**, *8*, 16651.
(154) Himmetoglu, B.; Floris, A.; de Gironcoli, S.; Cococcioni, M. Hubbard-Corrected DFT Energy Functionals: The LDA+U Description of Correlated Systems. *Int. J. Quantum Chem.* **2014**, *114*, 14−49.
(155) Grimme, S. Density Functional Theory with London Dispersion Corrections: Density Functional Theory with London Dispersion Corrections. *Wiley Interdiscip. Rev.: Comput. Mol. Sci.* **2011**, *1*, 211−228.
(156) Grimme, S.; Ehrlich, S.; Goerigk, L. Effect of the Damping Function in Dispersion Corrected Density Functional Theory. *J. Comput. Chem.* **2011**, *32*, 1456−1465.
(157) Grimme, S. Accurate Description of van Der Waals Complexes by Density Functional Theory Including Empirical Corrections. *J. Comput. Chem.* **2004**, *25*, 1463−1473.
(158) Johnson, E. R.; Becke, A. D. A Post-Hartree-Fock Model of Intermolecular Interactions: Inclusion of Higher-Order Corrections. *J. Chem. Phys.* **2006**, *124*, 174104.
(159) Johnson, E. R.; Becke, A. D. A Post-Hartree−Fock Model of Intermolecular Interactions. *J. Chem. Phys.* **2005**, *123*, No. 024101.
(160) Attard, P. Statistical Mechanical Theory for Steady State Systems. *J. Chem. Phys.* **2005**, *122*, 154101.
(161) Grimme, S. Semiempirical GGA-Type Density Functional Constructed with a Long-Range Dispersion Correction. *J. Comput. Chem.* **2006**, *27*, 1787−1799.
(162) Grimme, S.; Antony, J.; Ehrlich, S.; Krieg, H. A Consistent and Accurate *Ab Initio* Parametrization of Density Functional Dispersion Correction (DFT-D) for the 94 Elements H-Pu. *J. Chem. Phys.* **2010**, *132*, 154104.
(163) Grimme, S.; Steinmetz, M. Effects of London Dispersion Correction in Density Functional Theory on the Structures of Organic Molecules in the Gas Phase. *Phys. Chem. Chem. Phys.* **2013**, *15*, 16031.
(164) Witte, J.; Mardirossian, N.; Neaton, J. B.; Head-Gordon, M. Assessing DFT-D3 Damping Functions Across Widely Used Density Functionals: Can We Do Better? *J. Chem. Theory Comput.* **2017**, *13*, 2043−2052.
(165) Smith, D. G. A.; Burns, L. A.; Patkowski, K.; Sherrill, C. D. Revised Damping Parameters for the D3 Dispersion Correction to Density Functional Theory. *J. Phys. Chem. Lett.* **2016**, *7*, 2197−2203.
(166) Goerigk, L. A Comprehensive Overview of the DFT-D3 London-Dispersion Correction. In *Non-Covalent Interactions in Quantum Chemistry and Physics*; Elsevier, 2017; pp 195−219.
(167) Schröder, H.; Creon, A.; Schwabe, T. Reformulation of the D3(Becke−Johnson) Dispersion Correction without Resorting to Higher than C_6 Dispersion Coefficients. *J. Chem. Theory Comput.* **2015**, *11*, 3163−3170.
(168) Liu, Y.; Her, J.-H.; Dailly, A.; Ramirez-Cuesta, A. J.; Neumann, D. A.; Brown, C. M. Reversible Structural Transition in MIL-53 with Large Temperature Hysteresis. *J. Am. Chem. Soc.* **2008**, *130*, 11813−11818.
(169) Loiseau, T.; Serre, C.; Huguenard, C.; Fink, G.; Taulelle, F.; Henry, M.; Bataille, T.; Férey, G. A Rationale for the Large Breathing of the Porous Aluminum Terephthalate (MIL-53) Upon Hydration. *Chem. - Eur. J.* **2004**, *10*, 1373−1382.
(170) Wieme, J.; Lejaeghere, K.; Kresse, G.; Van Speybroeck, V. Tuning the Balance between Dispersion and Entropy to Design Temperature-Responsive Flexible Metal-Organic Frameworks. *Nat. Commun.* **2018**, *9*, 4899.
(171) Axilrod, B. M.; Teller, E. Interaction of the van Der Waals Type Between Three Atoms. *J. Chem. Phys.* **1943**, *11*, 299−300.
(172) Muto, Y. Force between Nonpolar Molecules. *Proc. Phys. Math. Soc. Jpn.* **1943**, *17*, 629−631.
(173) Vandenbrande, S.; Verstraelen, T.; Gutiérrez-Sevillano, J. J.; Waroquier, M.; Van Speybroeck, V. Methane Adsorption in Zr-Based MOFs: Comparison and Critical Evaluation of Force Fields. *J. Phys. Chem. C* **2017**, *121*, 25309−25322.
(174) Moellmann, J.; Grimme, S. DFT-D3 Study of Some Molecular Crystals. *J. Phys. Chem. C* **2014**, *118*, 7615−7621.
(175) Lee, K.; Murray, É. D.; Kong, L.; Lundqvist, B. I.; Langreth, D. C. Higher-Accuracy van Der Waals Density Functional. *Phys. Rev. B: Condens. Matter Mater. Phys.* **2010**, *82*, No. 081101.
(176) Wu, Z.-L.; Wang, C.-H.; Zhao, B.; Dong, J.; Lu, F.; Wang, W.-H.; Wang, W.-C.; Wu, G.-J.; Cui, J.-Z.; Cheng, P. A Semi-Conductive Copper-Organic Framework with Two Types of Photocatalytic Activity. *Angew. Chem., Int. Ed.* **2016**, *55*, 4938−4942.
(177) Padial, N. M.; Castells-Gil, J.; Almora-Barrios, N.; Romero-Angel, M.; da Silva, I.; Barawi, M.; García-Sánchez, A.; de la Peña O'Shea, V. A.; Martí-Gastaldo, C. Hydroxamate Titanium−Organic Frameworks and the Effect of Siderophore-Type Linkers over Their Photocatalytic Activity. *J. Am. Chem. Soc.* **2019**, *141*, 13124−13133.
(178) Zhang, Y.; Yang, W. A Challenge for Density Functionals: Self-Interaction Error Increases for Systems with a Noninteger Number of Electrons. *J. Chem. Phys.* **1998**, *109*, 2604−2608.
(179) Mori-Sánchez, P.; Cohen, A. J.; Yang, W. Many-Electron Self-Interaction Error in Approximate Density Functionals. *J. Chem. Phys.* **2006**, *125*, 201102.
(180) Bao, J. L.; Gagliardi, L.; Truhlar, D. G. Self-Interaction Error in Density Functional Theory: An Appraisal. *J. Phys. Chem. Lett.* **2018**, *9*, 2353−2358.

https://dx.doi.org/10.1021/acs.chemrev.0c00148
Chem. Rev. 2020, 120, 8641−8715

(181) Tsuneda, T.; Kamiya, M.; Hirao, K. Regional Self-Interaction Correction of Density Functional Theory. *J. Comput. Chem.* **2003**, *24*, 1592−1598.
(182) Tolba, S. A.; Gameel, K. M.; Ali, B. A.; Almossalami, H. A.; Allam, N. K. The DFT+U: Approaches, Accuracy, and Applications. In *Density Functional Calculations—Recent Progresses of Theory and Application*; Yang, G., Ed.; InTech, 2018.
(183) Combelles, C.; Ben Yahia, M.; Pedesseau, L.; Doublet, M.-L. FeII/FeIII Mixed-Valence State Induced by Li-Insertion into the Metal-Organic-Framework Mil53(Fe): A DFT+U Study. *J. Power Sources* **2011**, *196*, 3426−3432.
(184) Combelles, C.; Yahia, M. B.; Pedesseau, L.; Doublet, M.-L. Design of Electrode Materials for Lithium-Ion Batteries: The Example of Metal−Organic Frameworks. *J. Phys. Chem. C* **2010**, *114*, 9518−9527.
(185) Combelles, C.; Doublet, M.-L. Structural, Magnetic and Redox Properties of a New Cathode Material for Li-Ion Batteries: The Iron-Based Metal Organic Framework. *Ionics* **2008**, *14*, 279−283.
(186) Mann, G. W.; Lee, K.; Cococcioni, M.; Smit, B.; Neaton, J. B. First-Principles Hubbard *U* Approach for Small Molecule Binding in Metal-Organic Frameworks. *J. Chem. Phys.* **2016**, *144*, 174104.
(187) Lee, K.; Howe, J. D.; Lin, L.-C.; Smit, B.; Neaton, J. B. Small-Molecule Adsorption in Open-Site Metal−Organic Frameworks: A Systematic Density Functional Theory Study for Rational Design. *Chem. Mater.* **2015**, *27*, 668−678.
(188) Hubbard, J. Electron Correlations in Narrow Energy Bands. *Proc. R. Soc. London A* **1963**, *276*, 238−257.
(189) Hubbard, J. Electron Correlations in Narrow Energy Bands. II. The Degenerate Band Case. *Proc. R. Soc. London A* **1964**, *277*, 237−259.
(190) Hubbard, J. Electron Correlations in Narrow Energy Bands III. An Improved Solution. *Proc. R. Soc. London A* **1964**, *281*, 401−419.
(191) Hubbard, J. Electron Correlations in Narrow Energy Bands IV. The Atomic Representation. *Proc. R. Soc. London A* **1965**, *285*, 542−560.
(192) Hubbard, J. Electron Correlations in Narrow Energy Bands V. A Perturbation Expansion about the Atomic Limit. *Proc. R. Soc. London A* **1967**, *296*, 82−99.
(193) Hubbard, J. Electron Correlations in Narrow Energy Bands VI. The Connexion with Many-Body Perturbation Theory. *Proc. R. Soc. London A* **1967**, *296*, 100−112.
(194) Wong-Ng, W.; Williamson, I.; Lawson, M.; Siderus, D. W.; Culp, J. T.; Chen, Y.-S.; Li, L. Electronic Structure, Pore Size Distribution, and Sorption Characterization of an Unusual MOF, {[Ni(Dpbz)][Ni(CN)4]}n, Dpbz = 1,4-Bis(4-Pyridyl)Benzene. *J. Appl. Phys.* **2018**, *123*, 245105.
(195) Liechtenstein, A. I.; Anisimov, V. I.; Zaanen, J. Density-Functional Theory and Strong Interactions: Orbital Ordering in Mott-Hubbard Insulators. *Phys. Rev. B: Condens. Matter Mater. Phys.* **1995**, *52*, R5467−R5470.
(196) Dudarev, S. L.; Botton, G. A.; Savrasov, S. Y.; Humphreys, C. J.; Sutton, A. P. Electron-Energy-Loss Spectra and the Structural Stability of Nickel Oxide: An LSDA+U Study. *Phys. Rev. B: Condens. Matter Mater. Phys.* **1998**, *57*, 1505−1509.
(197) Boukhvalov, D. W.; Dobrovitski, V. V.; Kögerler, P.; Al-Saqer, M.; Katsnelson, M. I.; Lichtenstein, A. I.; Harmon, B. N. Effect of Ligand Substitution on the Exchange Interactions in $\{Mn_{12}\}$-Type Single-Molecule Magnets. *Inorg. Chem.* **2010**, *49*, 10902−10906.
(198) Lee, D. Y.; Kim, E.-K.; Shrestha, N. K.; Boukhvalov, D. W.; Lee, J. K.; Han, S.-H. Charge Transfer-Induced Molecular Hole Doping into Thin Film of Metal−Organic Frameworks. *ACS Appl. Mater. Interfaces* **2015**, *7*, 18501−18507.
(199) Loschen, C.; Carrasco, J.; Neyman, K. M.; Illas, F. First-Principles LDA + U and GGA + U Study of Cerium Oxides: Dependence on the Effective U Parameter. *Phys. Rev. B: Condens. Matter Mater. Phys.* **2007**, *75*, No. 035115.
(200) Aryasetiawan, F.; Karlsson, K.; Jepsen, O.; Schönberger, U. Calculations of Hubbard U from First-Principles. *Phys. Rev. B: Condens. Matter Mater. Phys.* **2006**, *74*, 125106.
(201) Cococcioni, M.; de Gironcoli, S. Linear Response Approach to the Calculation of the Effective Interaction Parameters in the LDA + U Method. *Phys. Rev. B: Condens. Matter Mater. Phys.* **2005**, *71*, No. 035105.
(202) Kulik, H. J.; Cococcioni, M.; Scherlis, D. A.; Marzari, N. Density Functional Theory in Transition-Metal Chemistry: A Self-Consistent Hubbard U Approach. *Phys. Rev. Lett.* **2006**, *97*, 103001.
(203) Wang, L.; Maxisch, T.; Ceder, G. Oxidation Energies of Transition Metal Oxides within the GGA + U Framework. *Phys. Rev. B: Condens. Matter Mater. Phys.* **2006**, *73*, 195107.
(204) Verma, P.; Truhlar, D. G. Does DFT+U Mimic Hybrid Density Functionals? *Theor. Chem. Acc.* **2016**, *135*, 182.
(205) Baidya, S.; Kang, S.; Kim, C. H.; Yu, J. Chern Insulator with a Nearly Flat Band in the Metal-Organic-Framework-Based Kagome Lattice. *Sci. Rep.* **2019**, *9*, 13807.
(206) Gu, Z.-G.; Heinke, L.; Wöll, C.; Neumann, T.; Wenzel, W.; Li, Q.; Fink, K.; Gordan, O. D.; Zahn, D. R. T. Experimental and Theoretical Investigations of the Electronic Band Structure of Metal-Organic Frameworks of HKUST-1 Type. *Appl. Phys. Lett.* **2015**, *107*, 183301.
(207) Noodleman, L. Valence Bond Description of Antiferromagnetic Coupling in Transition Metal Dimers. *J. Chem. Phys.* **1981**, *74*, 5737−5743.
(208) Levine, Z. H.; Allan, D. C. Quasiparticle Calculation of the Dielectric Response of Silicon and Germanium. *Phys. Rev. B: Condens. Matter Mater. Phys.* **1991**, *43*, 4187−4207.
(209) Stern, E. A. Rigid-Band Model of Alloys. *Phys. Rev.* **1967**, *157*, 544−551.
(210) Lee, M.-S.; Mahanti, S. D. Validity of the Rigid Band Approximation in the Study of the Thermopower of Narrow Band Gap Semiconductors. *Phys. Rev. B: Condens. Matter Mater. Phys.* **2012**, *85*, 165149.
(211) Walsh, A.; Da Silva, J. L. F.; Wei, S.-H.; Körber, C.; Klein, A.; Piper, L. F. J.; DeMasi, A.; Smith, K. E.; Panaccione, G.; Torelli, P.; Payne, D. J.; Bourlange, A.; Egdell, R. G. Nature of the Band Gap of In2O3 Revealed by First-Principles Calculations and X-Ray Spectroscopy. *Phys. Rev. Lett.* **2008**, *100*, 167402.
(212) Aziz, A.; Ruiz-Salvador, A. R.; Hernández, N. C.; Calero, S.; Hamad, S.; Grau-Crespo, R. Porphyrin-Based Metal-Organic Frameworks for Solar Fuel Synthesis Photocatalysis: Band Gap Tuning via Iron Substitutions. *J. Mater. Chem. A* **2017**, *5*, 11894−11904.
(213) Koopmans, T. Über die Zuordnung von Wellenfunktionen und Eigenwerten zu den Einzelnen Elektronen Eines Atoms. *Physica* **1934**, *1*, 104−113.
(214) Janak, J. F. Proof That ∂ E ∂ n i = ε in Density-Functional Theory. *Phys. Rev. B: Condens. Matter Mater. Phys.* **1978**, *18*, 7165−7168.
(215) Kresse, G.; Joubert, D. From Ultrasoft Pseudopotentials to the Projector Augmented-Wave Method. *Phys. Rev. B: Condens. Matter Mater. Phys.* **1999**, *59*, 1758−1775.
(216) Kresse, G.; Hafner, J. Ab Initio Molecular Dynamics for Liquid Metals. *Phys. Rev. B: Condens. Matter Mater. Phys.* **1993**, *47*, 558−561.
(217) Kresse, G.; Hafner, J. Ab Initio Molecular-Dynamics Simulation of the Liquid-Metal–Amorphous-Semiconductor Transition in Germanium. *Phys. Rev. B: Condens. Matter Mater. Phys.* **1994**, *49*, 14251−14269.
(218) Li, W.; Sun, L.; Qi, J.; Jarillo-Herrero, P.; Dincă, M.; Li, J. High Temperature Ferromagnetism in π-Conjugated Two-Dimensional Metal−Organic Frameworks. *Chem. Sci.* **2017**, *8*, 2859−2867.
(219) He, Y.; Cubuk, E. D.; Allendorf, M. D.; Reed, E. J. Metallic Metal−Organic Frameworks Predicted by the Combination of Machine Learning Methods and Ab Initio Calculations. *J. Phys. Chem. Lett.* **2018**, *9*, 4562−4569.
(220) Li, J.; Musho, T.; Bright, J.; Wu, N. Functionalization of a Metal-Organic Framework Semiconductor for Tuned Band Structure and Catalytic Activity. *J. Electrochem. Soc.* **2019**, *166*, H3029−H3034.
(221) Hamad, S.; Hernandez, N. C.; Aziz, A.; Ruiz-Salvador, A. R.; Calero, S.; Grau-Crespo, R. Electronic Structure of Porphyrin-Based

https://dx.doi.org/10.1021/acs.chemrev.0c00148
Chem. Rev. 2020, 120, 8641−8715

Metal−Organic Frameworks and Their Suitability for Solar Fuel Production Photocatalysis. *J. Mater. Chem. A* **2015**, *3*, 23458−23465.
(222) Wu, X.-P.; Gagliardi, L.; Truhlar, D. G. Metal Doping in Cerium Metal-Organic Frameworks for Visible-Response Water Splitting Photocatalysts. *J. Chem. Phys.* **2019**, *150*, No. 041701.
(223) Logsdail, A. J.; Scanlon, D. O.; Catlow, C. R. A.; Sokol, A. A. Bulk Ionization Potentials and Band Alignments from Three-Dimensional Periodic Calculations as Demonstrated on Rocksalt Oxides. *Phys. Rev. B: Condens. Matter Mater. Phys.* **2014**, *90*, 155106.
(224) Tasker, P. W. The Stability of Ionic Crystal Surfaces. *J. Phys. C: Solid State Phys.* **1979**, *12*, 4977−4984.
(225) Zhao, S.; Wang, Y.; Dong, J.; He, C.-T.; Yin, H.; An, P.; Zhao, K.; Zhang, X.; Gao, C.; Zhang, L.; Lv, J.; Wang, J.; Zhang, J.; Khattak, A. M.; Khan, N. A.; Wei, Z.; Zhang, J.; Liu, S.; Zhao, H.; Tang, Z. Ultrathin Metal−Organic Framework Nanosheets for Electrocatalytic Oxygen Evolution. *Nat. Energy* **2016**, *1*, 16184.
(226) Nasalevich, M. A.; Hendon, C. H.; Santaclara, J. G.; Svane, K.; van der Linden, B.; Veber, S. L.; Fedin, M. V.; Houtepen, A. J.; van der Veen, M. A.; Kapteijn, F.; Walsh, A.; Gascon, J. Electronic Origins of Photocatalytic Activity in D0Metal Organic Frameworks. *Sci. Rep.* **2016**, *6*, 23676.
(227) Wu, X.-P.; Gagliardi, L.; Truhlar, D. G. Cerium Metal−Organic Framework for Photocatalysis. *J. Am. Chem. Soc.* **2018**, *140*, 7904−7912.
(228) Syzgantseva, M. A.; Ireland, C. P.; Ebrahim, F. M.; Smit, B.; Syzgantseva, O. A. Metal Substitution as the Method of Modifying Electronic Structure of Metal−Organic Frameworks. *J. Am. Chem. Soc.* **2019**, *141*, 6271−6278.
(229) Yasin, A. S.; Li, J.; Wu, N.; Musho, T. Study of the Inorganic Substitution in a Functionalized UiO-66 Metal−Organic Framework. *Phys. Chem. Chem. Phys.* **2016**, *18*, 12748−12754.
(230) Fuentes-Cabrera, M.; Nicholson, D. M.; Sumpter, B. G.; Widom, M. Electronic Structure and Properties of Isoreticular Metal-Organic Frameworks: The Case of M-IRMOF1 (M = Zn, Cd, Be, Mg, and Ca). *J. Chem. Phys.* **2005**, *123*, 124713.
(231) Illas, F.; de P R Moreira, I.; Bofill, J. M.; Filatov, M. Spin Symmetry Requirements in Density Functional Theory: The Proper Way to Predict Magnetic Coupling Constants in Molecules and Solids. *Theor. Chem. Acc.* **2006**, *116*, 587−597.
(232) Cirera, J.; Babin, V.; Paesani, F. Theoretical Modeling of Spin Crossover in Metal−Organic Frameworks: $[Fe(Pz)_2Pt(CN)_4]$ as a Case Study. *Inorg. Chem.* **2014**, *53*, 11020−11028.
(233) Herchel, R.; Nemec, I.; Machata, M.; Trávníček, Z. Experimental and Theoretical Investigations of Magnetic Exchange Pathways in Structurally Diverse Iron(III) Schiff-Base Complexes. *Inorg. Chem.* **2015**, *54*, 8625−8638.
(234) Impeng, S.; Siwaipram, S.; Bureekaew, S.; Probst, M. Ethane C-H Bond Activate on the Fe(IV)-Oxo Species in a Zn-Based Cluster of Metal-Organic Frameworks: A Density Functional Theory Study. *Phys. Chem. Chem. Phys.* **2017**, *19*, 3782−3791.
(235) Kawamura, A.; Greenwood, A. R.; Filatov, A. S.; Gallagher, A. T.; Galli, G.; Anderson, J. S. Incorporation of Pyrazine and Bipyridine Linkers with High-Spin Fe(II) and Co(II) in a Metal−Organic Framework. *Inorg. Chem.* **2017**, *56*, 3349−3356.
(236) Gándara, F.; Uribe-Romo, F. J.; Britt, D. K.; Furukawa, H.; Lei, L.; Cheng, R.; Duan, X.; O'Keeffe, M.; Yaghi, O. M. Porous, Conductive Metal-Triazolates and Their Structural Elucidation by the Charge-Flipping Method. *Chem. - Eur. J.* **2012**, *18*, 10595−10601.
(237) Zhou, X.-H.; Peng, Y.-H.; Du, X.-D.; Zuo, J.-L.; You, X.-Z. Hydrothermal Syntheses and Structures of Three Novel Coordination Polymers Assembled from 1,2,3-Triazolate Ligands. *CrystEngComm* **2009**, *11*, 1964−1970.
(238) Aubrey, M. L.; Wiers, B. M.; Andrews, S. C.; Sakurai, T.; Reyes-Lillo, S. E.; Hamed, S. M.; Yu, C.-J.; Darago, L. E.; Mason, J. A.; Baeg, J.-O.; Grandjean, F.; Long, G. J.; Seki, S.; Neaton, J. B.; Yang, P.; Long, J. R. Electron Delocalization and Charge Mobility as a Function of Reduction in a Metal−Organic Framework. *Nat. Mater.* **2018**, *17*, 625−632.
(239) McGuirk, C. M.; Siegelman, R. L.; Drisdell, W. S.; Runčevski, T.; Milner, P. J.; Oktawiec, J.; Wan, L. F.; Su, G. M.; Jiang, H. Z. H.; Reed, D. A.; Gonzalez, M. I.; Prendergast, D.; Long, J. R. Cooperative Adsorption of Carbon Disulfide in Diamine-Appended Metal−Organic Frameworks. *Nat. Commun.* **2018**, *9*, 5133.
(240) Reed, D. A.; Xiao, D. J.; Jiang, H. Z. H.; Chakarawet, K.; Oktawiec, J.; Long, J. R. Biomimetic O_2 Adsorption in an Iron Metal−Organic Framework for Air Separation. *Chem. Sci.* **2020**, *11*, 1698−1702.
(241) DeGayner, J. A.; Jeon, I.-R.; Sun, L.; Dincă, M.; Harris, T. D. 2D Conductive Iron-Quinoid Magnets Ordering up to T_c = 105 K via Heterogenous Redox Chemistry. *J. Am. Chem. Soc.* **2017**, *139*, 4175−4184.
(242) Jeon, I.-R.; Negru, B.; Van Duyne, R. P.; Harris, T. D. A 2D Semiquinone Radical-Containing Microporous Magnet with Solvent-Induced Switching from T_c = 26 to 80 K. *J. Am. Chem. Soc.* **2015**, *137*, 15699−15702.
(243) Liu, L.; DeGayner, J. A.; Sun, L.; Zee, D. Z.; Harris, T. D. Reversible Redox Switching of Magnetic Order and Electrical Conductivity in a 2D Manganese Benzoquinoid Framework. *Chem. Sci.* **2019**, *10*, 4652−4661.
(244) Liu, L.; Li, L.; DeGayner, J. A.; Winegar, P. H.; Fang, Y.; Harris, T. D. Harnessing Structural Dynamics in a 2D Manganese−Benzoquinoid Framework To Dramatically Accelerate Metal Transport in Diffusion-Limited Metal Exchange Reactions. *J. Am. Chem. Soc.* **2018**, *140*, 11444−11453.
(245) Thorarinsdottir, A. E.; Harris, T. D. Metal−Organic Framework Magnets. *Chem. Rev.* **2020**, DOI: 10.1021/acs.chemrev.9b00666.
(246) Tiana, D.; Hendon, C. H.; Walsh, A. Ligand Design for Long-Range Magnetic Order in Metal−Organic Frameworks. *Chem. Commun.* **2014**, *50*, 13990−13993.
(247) Greiner, W.; Neise, L.; Stöcker, H. The Models of Ising and Heisenberg. In *Thermodynamics and Statistical Mechanics*; Springer: New York, 1995; pp 436−456.
(248) Heisenberg, W. Zur Theorie des Ferromagnetismus. *Eur. Phys. J. A* **1928**, *49*, 619−636.
(249) Dirac, P. A. M. Quantum Mechanics of Many-Electron Systems. *Proc. Royal. Soc. A* **1929**, *123*, 714−733.
(250) Van Vleck, J. H. A Survey of the Theory of Ferromagnetism. *Rev. Mod. Phys.* **1945**, *17*, 27−47.
(251) Caballol, R.; Castell, O.; Illas, F.; de P R Moreira, I.; Malrieu, J. P. Remarks on the Proper Use of the Broken Symmetry Approach to Magnetic Coupling. *J. Phys. Chem. A* **1997**, *101*, 7860−7866.
(252) Mouesca, J.-M. Density Functional Theory−Broken Symmetry (DFT−BS) Methodology Applied to Electronic and Magnetic Properties of Bioinorganic Prosthetic Groups. In *Metalloproteins*; Fontecilla-Camps, J. C., Nicolet, Y., Eds.; Humana Press: Totowa, NJ, 2014; Vol. *1122*, pp 269−296.
(253) Soda, T.; Kitagawa, Y.; Onishi, T.; Takano, Y.; Shigeta, Y.; Nagao, H.; Yoshioka, Y.; Yamaguchi, K. Ab Initio Computations of Effective Exchange Integrals for H−H, H−He−H and Mn2O2 Complex: Comparison of Broken-Symmetry Approaches. *Chem. Phys. Lett.* **2000**, *319*, 223−230.
(254) Manson, J. L.; Carreiro, K. E.; Lapidus, S. H.; Stephens, P. W.; Goddard, P. A.; Del Sesto, R. E.; Bendix, J.; Ghannadzadeh, S.; Franke, I.; Singleton, J.; Lancaster, T.; Möller, J. S.; Baker, P. J.; Pratt, F. L.; Blundell, S. J.; Kang, J.; Lee, C.; Whangbo, M.-H. Influence of HF_2^- Geometry on Magnetic Interactions Elucidated from Polymorphs of the Metal−Organic Framework $[Ni(HF_2)(Pyz)_2]PF_6$ (Pyz = Pyrazine). *Dalton Trans.* **2012**, *41*, 7235−7243.
(255) Caballol, R.; Castell, O.; Illas, F.; de P R Moreira, I.; Malrieu, J. P. Remarks on the Proper Use of the Broken Symmetry Approach to Magnetic Coupling. *J. Phys. Chem. A* **1997**, *101*, 7860−7866.
(256) Illas, F.; Moreira, I. P. R.; de Graaf, C.; Barone, V. Magnetic Coupling in Biradicals, Binuclear Complexes and Wide-Gap Insulators: A Survey of Ab Initio Wave Function and Density Functional Theory Approaches. *Theor. Chem. Acc.* **2000**, *104*, 265−272.

https://dx.doi.org/10.1021/acs.chemrev.0c00148
Chem. Rev. 2020, 120, 8641−8715

(257) Grant, I. P.; Quiney, H. M. Relativistic Self-Consistent Fields. In *Theoretical and Computational Chemistry*; Elsevier, 2002; Vol. *11*, Chapter 3, pp 107−202.
(258) Skorupskii, G.; Trump, B. A.; Kasel, T. W.; Brown, C. M.; Hendon, C. H.; Dincă, M. Efficient and Tunable One-Dimensional Charge Transport in Layered Lanthanide Metal−Organic Frameworks. *Nat. Chem.* **2020**, *12*, 131−136.
(259) Silveira, O. J.; Chacham, H. Electronic and Spin−Orbit Properties of the Kagome MOF Family M_3(1,2,5,6,9, 10-Triphenylenehexathiol)$_2$ (M = Ni, Pt, Cu and Au). *J. Phys.: Condens. Matter* **2017**, *29*, No. 09LT01.
(260) Wang, A.; Zhang, X.; Feng, Y.; Zhao, M. Chern Insulator and Chern Half-Metal States in the Two-Dimensional Spin-Gapless Semiconductor $Mn_2C_6S_{12}$. *J. Phys. Chem. Lett.* **2017**, *8*, 3770−3775.
(261) Naik, S. R.; Salker, A. V.; Yusuf, S. M.; Meena, S. S. Influence of Co2+ Distribution and Spin−Orbit Coupling on the Resultant Magnetic Properties of Spinel Cobalt Ferrite Nanocrystals. *J. Alloys Compd.* **2013**, *566*, 54−61.
(262) Saines, P. J.; Barton, P. T.; Jura, M.; Knight, K. S.; Cheetham, A. K. Cobalt Adipate, $Co(C_6H_8O_4)$: Antiferromagnetic Structure, Unusual Thermal Expansion and Magnetoelastic Coupling. *Mater. Horiz.* **2014**, *1*, 332−337.
(263) Yang, C.; Dong, R.; Wang, M.; Petkov, P. St.; Zhang, Z.; Wang, M.; Han, P.; Ballabio, M.; Bräuninger, S. A.; Liao, Z.; Zhang, J.; Schwotzer, F.; Zschech, E.; Klauss, H.-H.; Cánovas, E.; Kaskel, S.; Bonn, M.; Zhou, S.; Heine, T.; Feng, X. A Semiconducting Layered Metal-Organic Framework Magnet. *Nat. Commun.* **2019**, *10*, 3260.
(264) Trout, B. L.; Chakraborty, A. K.; Bell, A. T. Local Spin Density Functional Theory Study of Copper Ion-Exchanged ZSM-5. *J. Phys. Chem.* **1996**, *100*, 4173−4179.
(265) Rahm, M.; Hoffmann, R.; Ashcroft, N. W. Atomic and Ionic Radii of Elements 1 -**96**. *Chem. - Eur. J.* **2016**, *22*, 14625−14632.
(266) Ue, M.; Murakami, A.; Nakamura, S. A Convenient Method to Estimate Ion Size for Electrolyte Materials Design. *J. Electrochem. Soc.* **2002**, *149*, A1385.
(267) Yang, L.; Kinoshita, S.; Yamada, T.; Kanda, S.; Kitagawa, H.; Tokunaga, M.; Ishimoto, T.; Ogura, T.; Nagumo, R.; Miyamoto, A.; Koyama, M. A Metal-Organic Framework as an Electrocatalyst for Ethanol Oxidation. *Angew. Chem., Int. Ed.* **2010**, *49*, 5348−5351.
(268) Lee, J.; Farha, O. K.; Roberts, J.; Scheidt, K. A.; Nguyen, S. T.; Hupp, J. T. Metal−Organic Framework Materials as Catalysts. *Chem. Soc. Rev.* **2009**, *38*, 1450−1459.
(269) Mulliken, R. S. Electronic Population Analysis on LCAO−MO Molecular Wave Functions. II. Overlap Populations, Bond Orders, and Covalent Bond Energies. *J. Chem. Phys.* **1955**, *23*, 1841−1846.
(270) Breneman, C. M.; Wiberg, K. B. Determining Atom-Centered Monopoles from Molecular Electrostatic Potentials. The Need for High Sampling Density in Formamide Conformational Analysis. *J. Comput. Chem.* **1990**, *11*, 361−373.
(271) Wang, B.; Lv, X.-L.; Feng, D.; Xie, L.-H.; Zhang, J.; Li, M.; Xie, Y.; Li, J.-R.; Zhou, H.-C. Highly Stable Zr(IV)-Based Metal−Organic Frameworks for the Detection and Removal of Antibiotics and Organic Explosives in Water. *J. Am. Chem. Soc.* **2016**, *138*, 6204−6216.
(272) Li, Z.; Peters, A. W.; Bernales, V.; Ortuño, M. A.; Schweitzer, N. M.; DeStefano, M. R.; Gallington, L. C.; Platero-Prats, A. E.; Chapman, K. W.; Cramer, C. J.; Gagliardi, L.; Hupp, J. T.; Farha, O. K. Metal−Organic Framework Supported Cobalt Catalysts for the Oxidative Dehydrogenation of Propane at Low Temperature. *ACS Cent. Sci.* **2017**, *3*, 31−38.
(273) Li, Z.; Peters, A. W.; Platero-Prats, A. E.; Liu, J.; Kung, C.-W.; Noh, H.; DeStefano, M. R.; Schweitzer, N. M.; Chapman, K. W.; Hupp, J. T.; Farha, O. K. Fine-Tuning the Activity of Metal−Organic Framework-Supported Cobalt Catalysts for the Oxidative Dehydrogenation of Propane. *J. Am. Chem. Soc.* **2017**, *139*, 15251−15258.
(274) Marenich, A. V.; Jerome, S. V.; Cramer, C. J.; Truhlar, D. G. Charge Model 5: An Extension of Hirshfeld Population Analysis for the Accurate Description of Molecular Interactions in Gaseous and Condensed Phases. *J. Chem. Theory Comput.* **2012**, *8*, 527−541.
(275) Hirshfeld, F. L. Bonded-Atom Fragments for Describing Molecular Charge Densities. *Theoret. Chim. Acta* **1977**, *44*, 129−138.
(276) Liu, J.; Ye, J.; Li, Z.; Otake, K.; Liao, Y.; Peters, A. W.; Noh, H.; Truhlar, D. G.; Gagliardi, L.; Cramer, C. J.; Farha, O. K.; Hupp, J. T. Beyond the Active Site: Tuning the Activity and Selectivity of a Metal−Organic Framework-Supported Ni Catalyst for Ethylene Dimerization. *J. Am. Chem. Soc.* **2018**, *140*, 11174−11178.
(277) Vitillo, J. G.; Bhan, A.; Cramer, C. J.; Lu, C. C.; Gagliardi, L. Quantum Chemical Characterization of Structural Single Fe(II) Sites in MIL-Type Metal−Organic Frameworks for the Oxidation of Methane to Methanol and Ethane to Ethanol. *ACS Catal.* **2019**, *9*, 2870−2879.
(278) Bader, R. F. W. Atoms in Molecules. *Acc. Chem. Res.* **1985**, *18*, 9−15.
(279) Bader, R. F. W.; Carroll, M. T.; Cheeseman, J. R.; Chang, C. Properties of Atoms in Molecules: Atomic Volumes. *J. Am. Chem. Soc.* **1987**, *109*, 7968−7979.
(280) Bader, R. F. W. A Quantum Theory of Molecular Structure and Its Applications. *Chem. Rev.* **1991**, *91*, 893−928.
(281) Kumar, P. S. V.; Raghavendra, V.; Subramanian, V. Bader's Theory of Atoms in Molecules (AIM) and Its Applications to Chemical Bonding. *J. Chem. Sci.* **2016**, *128*, 1527−1536.
(282) Sladekova, K.; Campbell, C.; Grant, C.; Fletcher, A. J.; Gomes, J. R. B.; Jorge, M. The Effect of Atomic Point Charges on Adsorption Isotherms of CO_2 and Water in Metal Organic Frameworks. *Adsorption* **2020**, *26*, 663.
(283) Zhang, R.; Liu, J.; Gao, Y.; Hua, M.; Xia, B.; Knecht, P.; Papageorgiou, A. C.; Reichert, J.; Barth, J. V.; Xu, H.; Huang, L.; Lin, N. On-surface Synthesis of a Semiconducting 2D Metal−Organic Framework $Cu_3(C_6O_6)$ Exhibiting Dispersive Electronic Bands. *Angew. Chem.* **2020**, *132*, 2691−2695.
(284) Suksaengrat, P.; Amornkitbamrung, V.; Srepusharawoot, P.; Ahuja, R. Density Functional Theory Study of Hydrogen Adsorption in a Ti-Decorated Mg-Based Metal-Organic Framework-74. *ChemPhysChem* **2016**, *17*, 879−884.
(285) Poulsen, R. D.; Bentien, A.; Graber, T.; Iversen, B. B. Synchrotron Charge-Density Studies in Materials Chemistry: 16 K X-Ray Charge Density of a New Magnetic Metal-Organic Framework Material, $[Mn_2(C_8H_4O_4)_2(C_3H_7NO)_2]$. *Acta Crystallogr., Sect. A: Found. Crystallogr.* **2004**, *60*, 382−389.
(286) Zhang, H.; Liu, J.; Lin, X.; Zhong, Y.; Ren, J.; Wang, Z.; Han, T.; Li, J. A Metal Organic Foam-Derived Zinc Cobalt Sulfide with Improved Binding Energies towards Polysulfides for Lithium−Sulfur Batteries. *Ceram. Int.* **2020**, *46*, 14056−14063.
(287) Tong, Y.; Xue, G.; Wang, H.; Liu, M.; Wang, J.; Hao, C.; Zhang, X.; Wang, D.; Shi, X.; Liu, W.; Li, G.; Tang, Z. Interfacial Coupling between Noble Metal Nanoparticles and Metal−Organic Frameworks for Enhanced Catalytic Activity. *Nanoscale* **2018**, *10*, 16425−16430.
(288) Chen, L.; Huang, W.; Wang, X.; Chen, Z.; Yang, X.; Luque, R.; Li, Y. Catalytically Active Designer Crown-Jewel Pd-Based Nanostructures Encapsulated in Metal−Organic Frameworks. *Chem. Commun.* **2017**, *53*, 1184−1187.
(289) DMello, M. E.; Sundaram, N. G.; Singh, A.; Singh, A. K.; Kalidindi, S. B. An Amine Functionalized Zirconium Metal−Organic Framework as an Effective Chemiresistive Sensor for Acidic Gases. *Chem. Commun.* **2019**, *55*, 349−352.
(290) Li, J.; Huang, H.; Liu, P.; Song, X.; Mei, D.; Tang, Y.; Wang, X.; Zhong, C. Metal-Organic Framework Encapsulated Single-Atom Pt Catalysts for Efficient Photocatalytic Hydrogen Evolution. *J. Catal.* **2019**, *375*, 351−360.
(291) Zuo, Q.; Liu, T.; Chen, C.; Ji, Y.; Gong, X.; Mai, Y.; Zhou, Y. Ultrathin Metal−Organic Framework Nanosheets with Ultrahigh Loading of Single Pt Atoms for Efficient Visible-Light-Driven Photocatalytic H_2 Evolution. *Angew. Chem.* **2019**, *131*, 10304−10309.
(292) Tang, C.; Zhang, C.; Jiang, Z.; Ostrikov, K.; Du, A. Theoretical Discovery of Dirac Half Metal in Experimentally Synthesized Two Dimensional Metal Semiquinoid Frameworks. *J. Mater. Chem. C* **2019**, *7*, 5792−5796.
(293) Mukherjee, S.; Manna, B.; Desai, A. V.; Yin, Y.; Krishna, R.; Babarao, R.; Ghosh, S. K. Harnessing Lewis Acidic Open Metal Sites of

https://dx.doi.org/10.1021/acs.chemrev.0c00148
Chem. Rev. 2020, 120, 8641−8715

Metal−Organic Frameworks: The Foremost Route to Achieve Highly Selective Benzene Sorption over Cyclohexane. *Chem. Commun.* **2016**, *52*, 8215−8218.
(294) Arter, C. A.; Zuluaga, S.; Harrison, D.; Welchman, E.; Thonhauser, T. Fivefold Increase of Hydrogen Uptake in MOF74 through Linker Decorations. *Phys. Rev. B: Condens. Matter Mater. Phys.* **2016**, *94*, 144105.
(295) Ardila-Suárez, C.; Perez-Beltran, S.; Ramírez-Caballero, G. E.; Balbuena, P. B. Enhanced Acidity of Defective MOF-808: Effects of the Activation Process and Missing Linker Defects. *Catal. Sci. Technol.* **2018**, *8*, 847−857.
(296) Song, Z.; Liu, W.; Cheng, N.; Norouzi Banis, M.; Li, X.; Sun, Q.; Xiao, B.; Liu, Y.; Lushington, A.; Li, R.; Liu, L.; Sun, X. Origin of the High Oxygen Reduction Reaction of Nitrogen and Sulfur Co-Doped MOF-Derived Nanocarbon Electrocatalysts. *Mater. Horiz.* **2017**, *4*, 900−907.
(297) Rodríguez, J. I.; Bader, R. F. W.; Ayers, P. W.; Michel, C.; Götz, A. W.; Bo, C. A High Performance Grid-Based Algorithm for Computing QTAIM Properties. *Chem. Phys. Lett.* **2009**, *472*, 149−152.
(298) Yu, M.; Trinkle, D. R. Accurate and Efficient Algorithm for Bader Charge Integration. *J. Chem. Phys.* **2011**, *134*, No. 064111.
(299) Tang, W.; Sanville, E.; Henkelman, G. A Grid-Based Bader Analysis Algorithm without Lattice Bias. *J. Phys.: Condens. Matter* **2009**, *21*, No. 084204.
(300) Sanville, E.; Kenny, S. D.; Smith, R.; Henkelman, G. Improved Grid-Based Algorithm for Bader Charge Allocation. *J. Comput. Chem.* **2007**, *28*, 899−908.
(301) Henkelman, G.; Arnaldsson, A.; Jónsson, H. A Fast and Robust Algorithm for Bader Decomposition of Charge Density. *Comput. Mater. Sci.* **2006**, *36*, 354−360.
(302) Ángyán, J. G.; Jansen, G.; Loss, M.; Hättig, C.; Heß, B. A. Distributed Polarizabilities Using the Topological Theory of Atoms in Molecules. *Chem. Phys. Lett.* **1994**, *219*, 267−273.
(303) Yang, L.-M.; Ravindran, P.; Vajeeston, P.; Svelle, S.; Tilset, M. A Quantum Mechanically Guided View of Cd-MOF-5 from Formation Energy, Chemical Bonding, Electronic Structure, and Optical Properties. *Microporous Mesoporous Mater.* **2013**, *175*, 50−58.
(304) de Oliveira, A.; Alves, J. S.; de Lima, G. F.; De Abreu, H. A. Acidic and Basic Sites of M_2DEBDC (M = Mg or Mn and E = O or S) Acting as Catalysts for Cyanosilylation of Aldehydes. *Polyhedron* **2018**, *154*, 98−107.
(305) Tavares, S. R.; Ramsahye, N.; Maurin, G.; Leitão, A. A. Computational Exploration of the Structure, Stability and Adsorption Properties of the ZIF-9 Metal-Organic Framework. *Microporous Mesoporous Mater.* **2017**, *254*, 170−177.
(306) Yang, L.-M.; Vajeeston, P.; Ravindran, P.; Fjellvåg, H.; Tilset, M. Revisiting Isoreticular MOFs of Alkaline Earth Metals: A Comprehensive Study on Phase Stability, Electronic Structure, Chemical Bonding, and Optical Properties of A−IRMOF-1 (A = Be, Mg, Ca, Sr, Ba). *Phys. Chem. Chem. Phys.* **2011**, *13*, 10191−10203.
(307) Lescouet, T.; Chizallet, C.; Farrusseng, D. The Origin of the Activity of Amine-Functionalized Metal-Organic Frameworks in the Catalytic Synthesis of Cyclic Carbonates from Epoxide and CO_2. *ChemCatChem* **2012**, *4*, 1725−1728.
(308) Rosen, A. S.; Mian, M. R.; Islamoglu, T.; Chen, H.; Farha, O. K.; Notestein, J. M.; Snurr, R. Q. Tuning the Redox Activity of Metal−Organic Frameworks for Enhanced, Selective O_2 Binding: Design Rules and Ambient Temperature O_2 Chemisorption in a Cobalt−Triazolate Framework. *J. Am. Chem. Soc.* **2020**, *142*, 4317−4328.
(309) Reed, A. E.; Weinstock, R. B.; Weinhold, F. Natural Population Analysis. *J. Chem. Phys.* **1985**, *83*, 735−746.
(310) Reed, A. E.; Curtiss, L. A.; Weinhold, F. Intermolecular Interactions from a Natural Bond Orbital, Donor-Acceptor Viewpoint. *Chem. Rev.* **1988**, *88*, 899−926.
(311) Weinhold, F. Natural Bond Orbital Analysis: A Critical Overview of Relationships to Alternative Bonding Perspectives. *J. Comput. Chem.* **2012**, *33*, 2363−2379.
(312) Glendening, E. D.; Landis, C. R.; Weinhold, F. Natural Bond Orbital Methods. *Wiley Interdiscip. Rev.: Comput. Mol. Sci.* **2012**, *2*, 1−42.
(313) Lee, K.; Isley, W. C.; Dzubak, A. L.; Verma, P.; Stoneburner, S. J.; Lin, L.-C.; Howe, J. D.; Bloch, E. D.; Reed, D. A.; Hudson, M. R.; Brown, C. M.; Long, J. R.; Neaton, J. B.; Smit, B.; Cramer, C. J.; Truhlar, D. G.; Gagliardi, L. Design of a Metal−Organic Framework with Enhanced Back Bonding for Separation of N_2 and CH_4. *J. Am. Chem. Soc.* **2014**, *136*, 698−704.
(314) Lochan, R. C.; Head-Gordon, M. Computational Studies of Molecular Hydrogen Binding Affinities: The Role of Dispersion Forces, Electrostatics, and Orbital Interactions. *Phys. Chem. Chem. Phys.* **2006**, *8*, 1357−1370.
(315) Alabugin, I. V.; Gilmore, K. M.; Peterson, P. W. Hyperconjugation. *Wiley Interdiscip. Rev.: Comput. Mol. Sci.* **2011**, *1*, 109−141.
(316) Dunnington, B. D.; Schmidt, J. R. Generalization of Natural Bond Orbital Analysis to Periodic Systems: Applications to Solids and Surfaces via Plane-Wave Density Functional Theory. *J. Chem. Theory Comput.* **2012**, *8*, 1902−1911.
(317) Liu, D.; Zhong, C. Characterization of Lewis Acid Sites in Metal−Organic Frameworks Using Density Functional Theory. *J. Phys. Chem. Lett.* **2010**, *1*, 97−101.
(318) Luz, I.; Llabrés i Xamena, F. X.; Corma, A. Bridging Homogeneous and Heterogeneous Catalysis with MOFs: "Click" Reactions with Cu-MOF Catalysts. *J. Catal.* **2010**, *276*, 134−140.
(319) Odoh, S. O.; Cramer, C. J.; Truhlar, D. G.; Gagliardi, L. Quantum-Chemical Characterization of the Properties and Reactivities of Metal−Organic Frameworks. *Chem. Rev.* **2015**, *115*, 6051−6111.
(320) Nasalevich, M. A.; van der Veen, M.; Kapteijn, F.; Gascon, J. Metal−Organic Frameworks as Heterogeneous Photocatalysts: Advantages and Challenges. *CrystEngComm* **2014**, *16*, 4919−4926.
(321) Gonzalez-Nelson, A.; Coudert, F.-X.; van der Veen, M. Rotational Dynamics of Linkers in Metal−Organic Frameworks. *Nanomaterials* **2019**, *9*, 330.
(322) Feldblyum, J. I.; Liu, M.; Gidley, D. W.; Matzger, A. J. Reconciling the Discrepancies between Crystallographic Porosity and Guest Access As Exemplified by Zn-HKUST-1. *J. Am. Chem. Soc.* **2011**, *133*, 18257−18263.
(323) Wang, L. J.; Deng, H.; Furukawa, H.; Gándara, F.; Cordova, K. E.; Peri, D.; Yaghi, O. M. Synthesis and Characterization of Metal−Organic Framework-74 Containing 2, 4, 6, 8, and 10 Different Metals. *Inorg. Chem.* **2014**, *53*, 5881−5883.
(324) Edgar, M.; Mitchell, R.; Slawin, A. M. Z.; Lightfoot, P.; Wright, P. A. Solid-State Transformations of Zinc 1,4-Benzenedicarboxylates Mediated by Hydrogen-Bond-Forming Molecules. *Chem. - Eur. J.* **2001**, *7*, 5168−5175.
(325) Lee, Y.-G.; Moon, H. R.; Cheon, Y. E.; Suh, M. P. A Comparison of the H_2 Sorption Capacities of Isostructural Metal-Organic Frameworks With and Without Accessible Metal Sites: $[\{Zn_2(Abtc)(Dmf)_2\}_3]$ and $[\{Cu_2(Abtc)(Dmf)_2\}_3]$ versus $[\{Cu_2(Abtc)\}_3]$. *Angew. Chem., Int. Ed.* **2008**, *47*, 7741−7745.
(326) Jensen, J. H. Predicting Accurate Absolute Binding Energies in Aqueous Solution: Thermodynamic Considerations for Electronic Structure Methods. *Phys. Chem. Chem. Phys.* **2015**, *17*, 12441−12451.
(327) Xiao, D. J.; Bloch, E. D.; Mason, J. A.; Queen, W. L.; Hudson, M. R.; Planas, N.; Borycz, J.; Dzubak, A. L.; Verma, P.; Lee, K.; Bonino, F.; Crocellà, V.; Yano, J.; Bordiga, S.; Truhlar, D. G.; Gagliardi, L.; Brown, C. M.; Long, J. R. Oxidation of Ethane to Ethanol by N2O in a Metal−Organic Framework with Coordinatively Unsaturated Iron(II) Sites. *Nat. Chem.* **2014**, *6*, 590−595.
(328) Ortuño, M. A.; Bernales, V.; Gagliardi, L.; Cramer, C. J. Computational Study of First-Row Transition Metals Supported on MOF NU-1000 for Catalytic Acceptorless Alcohol Dehydrogenation. *J. Phys. Chem. C* **2016**, *120*, 24697−24705.
(329) Mondloch, J. E.; Katz, M. J.; Isley, W. C., III; Ghosh, P.; Liao, P.; Bury, W.; Wagner, G. W.; Hall, M. G.; DeCoste, J. B.; Peterson, G. W.; Snurr, R. Q.; Cramer, C. J.; Hupp, J. T.; Farha, O. K. Destruction of Chemical Warfare Agents Using Metal−Organic Frameworks. *Nat. Mater.* **2015**, *14*, 512−516.

https://dx.doi.org/10.1021/acs.chemrev.0c00148
Chem. Rev. 2020, 120, 8641−8715

(330) Kim, I. S.; Borycz, J.; Platero-Prats, A. E.; Tussupbayev, S.; Wang, T. C.; Farha, O. K.; Hupp, J. T.; Gagliardi, L.; Chapman, K. W.; Cramer, C. J.; Martinson, A. B. F. Targeted Single-Site MOF Node Modification: Trivalent Metal Loading via Atomic Layer Deposition. *Chem. Mater.* **2015**, *27*, 4772−4778.
(331) Schreiner, P. R. Relative Energy Computations with Approximate Density Functional Theory—A Caveat! *Angew. Chem., Int. Ed.* **2007**, *46*, 4217−4219.
(332) De Moor, B. A.; Reyniers, M.-F.; Marin, G. B. Physisorption and Chemisorption of Alkanes and Alkenes in H-FAU: A Combined Ab Initio−Statistical Thermodynamics Study. *Phys. Chem. Chem. Phys.* **2009**, *11*, 2939−2958.
(333) Yang, D.; Gaggioli, C. A.; Conley, E.; Babucci, M.; Gagliardi, L.; Gates, B. C. Synthesis and Characterization of Tetrairidium Clusters in the Metal Organic Framework UiO-67: Catalyst for Ethylene Hydrogenation. *J. Catal.* **2020**, *382*, 165−172.
(334) De Santis, E.; Edwards, A. A.; Alexander, B. D.; Holder, S. J.; Biesse-Martin, A.-S.; Nielsen, B. V.; Mistry, D.; Waters, L.; Siligardi, G.; Hussain, R.; Faure, S.; Taillefumier, C. Selective Complexation of Divalent Cations by a Cyclic α,β-Peptoid Hexamer: A Spectroscopic and Computational Study. *Org. Biomol. Chem.* **2016**, *14*, 11371−11380.
(335) Oxford, G. A. E.; Snurr, R. Q.; Broadbelt, L. J. Hybrid Quantum Mechanics/Molecular Mechanics Investigation of (Salen)Mn for Use in Metal−Organic Frameworks. *Ind. Eng. Chem. Res.* **2010**, *49*, 10965−10973.
(336) Bennett, T. D.; Cheetham, A. K.; Fuchs, A. H.; Coudert, F.-X. Interplay between Defects, Disorder and Flexibility in Metal-Organic Frameworks. *Nat. Chem.* **2017**, *9*, 11−16.
(337) Cinar, Z. The Role of Molecular Modeling in TiO2 Photocatalysis. *Molecules* **2017**, *22*, 556.
(338) Liu, L.; Mi, W.; Hao, C.; Qiu, J. Theoretical Studies on How Excited State Hydrogen and Coordination Bonds Affect Luminescent Properties of Metal Organic Framework Cu4(L)4•2EtOH. *Inorg. Chem. Commun.* **2013**, *31*, 69−73.
(339) Wang, B.; Truhlar, D. G. Combined Quantum Mechanical and Molecular Mechanical Methods for Calculating Potential Energy Surfaces: Tuned and Balanced Redistributed-Charge Algorithm. *J. Chem. Theory Comput.* **2010**, *6*, 359−369.
(340) Théry, V.; Rinaldi, D.; Rivail, J.-L.; Maigret, B.; Ferenczy, G. G. Quantum Mechanical Computations on Very Large Molecular Systems: The Local Self-Consistent Field Method: QUANTUM MECHANICAL COMPUTATIONS. *J. Comput. Chem.* **1994**, *15*, 269−282.
(341) Gao, J.; Amara, P.; Alhambra, C.; Field, M. J. A Generalized Hybrid Orbital (GHO) Method for the Treatment of Boundary Atoms in Combined QM/MM Calculations. *J. Phys. Chem. A* **1998**, *102*, 4714−4721.
(342) Yang, D.; Odoh, S. O.; Wang, T. C.; Farha, O. K.; Hupp, J. T.; Cramer, C. J.; Gagliardi, L.; Gates, B. C. Metal−Organic Framework Nodes as Nearly Ideal Supports for Molecular Catalysts: NU-1000- and UiO-66-Supported Iridium Complexes. *J. Am. Chem. Soc.* **2015**, *137*, 7391−7396.
(343) Momeni, M. R.; Pahls, D. R.; Yang, D.; Wang, T. C.; Farha, O. K.; Hupp, J. T.; Cramer, C. J.; Gagliardi, L.; Gates, B. C. Correction to "Metal−Organic Framework Nodes as Nearly Ideal Supports for Molecular Catalysts: NU-1000- and UiO-66-Supported Iridium Complexes. *J. Am. Chem. Soc.* **2017**, *139*, 18406−18406.
(344) Qian, J.; Li, Q.; Liang, L.; Li, T.-T.; Hu, Y.; Huang, S. A Microporous MOF with Open Metal Sites and Lewis Basic Sites for Selective CO_2 Capture. *Dalton Trans.* **2017**, *46*, 14102−14106.
(345) Strauss, I.; Mundstock, A.; Treger, M.; Lange, K.; Hwang, S.; Chmelik, C.; Rusch, P.; Bigall, N. C.; Pichler, T.; Shiozawa, H.; Caro, J. Metal−Organic Framework Co-MOF-74-Based Host−Guest Composites for Resistive Gas Sensing. *ACS Appl. Mater. Interfaces* **2019**, *11*, 14175−14181.
(346) Shustova, N. B.; Ong, T.-C.; Cozzolino, A. F.; Michaelis, V. K.; Griffin, R. G.; Dincă, M. Phenyl Ring Dynamics in a Tetraphenylethylene-Bridged Metal−Organic Framework: Implications for the Mechanism of Aggregation-Induced Emission. *J. Am. Chem. Soc.* **2012**, *134*, 15061−15070.
(347) Vogiatzis, K. D.; Haldoupis, E.; Xiao, D. J.; Long, J. R.; Siepmann, J. I.; Gagliardi, L. Accelerated Computational Analysis of Metal−Organic Frameworks for Oxidation Catalysis. *J. Phys. Chem. C* **2016**, *120*, 18707−18712.
(348) Hajek, J.; Vandichel, M.; Van de Voorde, B.; Bueken, B.; De Vos, D.; Waroquier, M.; Van Speybroeck, V. Mechanistic Studies of Aldol Condensations in UiO-66 and UiO-66-NH_2 Metal Organic Frameworks. *J. Catal.* **2015**, *331*, 1−12.
(349) Caratelli, C.; Hajek, J.; Cirujano, F. G.; Waroquier, M.; Llabres i Xamena, F. X.; Van Speybroeck, V. Nature of Active Sites on UiO-66 and Beneficial Influence of Water in the Catalysis of Fischer Esterification. *J. Catal.* **2017**, *352*, 401−414.
(350) Dolgopolova, E. A.; Moore, T. M.; Ejegbavwo, O. A.; Pellechia, P. J.; Smith, M. D.; Shustova, N. B. A Metal−Organic Framework as a Flask: Photophysics of Confined Chromophores with a Benzylidene Imidazolinone Core. *Chem. Commun.* **2017**, *53*, 7361−7364.
(351) Gu, Z.-G.; Heinke, L.; Wöll, C.; Neumann, T.; Wenzel, W.; Li, Q.; Fink, K.; Gordan, O. D.; Zahn, D. R. T. Experimental and Theoretical Investigations of the Electronic Band Structure of Metal-Organic Frameworks of HKUST-1 Type. *Appl. Phys. Lett.* **2015**, *107*, 183301.
(352) Braglia, L.; Borfecchia, E.; Martini, A.; Bugaev, A. L.; Soldatov, A. V.; Øien-Ødegaard, S.; Lønstad-Bleken, B. T.; Olsbye, U.; Lillerud, K. P.; Lomachenko, K. A.; Agostini, G.; Manzoli, M.; Lamberti, C. The Duality of UiO-67-Pt MOFs: Connecting Treatment Conditions and Encapsulated Pt Species by *Operando* XAS. *Phys. Chem. Chem. Phys.* **2017**, *19*, 27489−27507.
(353) Borfecchia, E.; Øien, S.; Svelle, S.; Mino, L.; Braglia, L.; Agostini, G.; Gallo, E.; Lomachenko, K. A.; Bordiga, S.; Guda, A. A.; Soldatov, M. A.; Soldatov, A. V.; Olsbye, U.; Lillerud, K. P.; Lamberti, C. A XAFS Study of the Local Environment and Reactivity of Pt- Sites in Functionalized UiO-67 MOFs. *J. Phys.: Conf. Ser.* **2016**, *712*, No. 012125.
(354) Øien, S.; Agostini, G.; Svelle, S.; Borfecchia, E.; Lomachenko, K. A.; Mino, L.; Gallo, E.; Bordiga, S.; Olsbye, U.; Lillerud, K. P.; Lamberti, C. Probing Reactive Platinum Sites in UiO-67 Zirconium Metal−Organic Frameworks. *Chem. Mater.* **2015**, *27*, 1042−1056.
(355) Xu, C.; Liu, H.; Li, D.; Su, J.-H.; Jiang, H.-L. Direct Evidence of Charge Separation in a Metal−Organic Framework: Efficient and Selective Photocatalytic Oxidative Coupling of Amines *via* Charge and Energy Transfer. *Chem. Sci.* **2018**, *9*, 3152−3158.
(356) Vermoortele, F.; Vandichel, M.; Van de Voorde, B.; Ameloot, R.; Waroquier, M.; Van Speybroeck, V.; De Vos, D. E. Electronic Effects of Linker Substitution on Lewis Acid Catalysis with Metal-Organic Frameworks. *Angew. Chem., Int. Ed.* **2012**, *51*, 4887−4890.
(357) Ye, J.; Johnson, J. K. Design of Lewis Pair-Functionalized Metal Organic Frameworks for CO_2 Hydrogenation. *ACS Catal.* **2015**, *5*, 2921−2928.
(358) Ye, J.; Johnson, J. K. Catalytic Hydrogenation of CO_2 to Methanol in a Lewis Pair Functionalized MOF. *Catal. Sci. Technol.* **2016**, *6*, 8392−8405.
(359) Dybtsev, D. N.; Nuzhdin, A. L.; Chun, H.; Bryliakov, K. P.; Talsi, E. P.; Fedin, V. P.; Kim, K. A Homochiral Metal−Organic Material with Permanent Porosity, Enantioselective Sorption Properties, and Catalytic Activity. *Angew. Chem.* **2006**, *118*, 930−934.
(360) Seo, J. S.; Whang, D.; Lee, H.; Jun, S. I.; Oh, J.; Jeon, Y. J.; Kim, K. A Homochiral Metal−Organic Porous Material for Enantioselective Separation and Catalysis. *Nature* **2000**, *404*, 982−986.
(361) Horike, S.; Dincă, M.; Tamaki, K.; Long, J. R. Size-Selective Lewis Acid Catalysis in a Microporous Metal-Organic Framework with Exposed Mn^{2+} Coordination Sites. *J. Am. Chem. Soc.* **2008**, *130*, 5854−5855.
(362) Zhang, X.; Huang, Z.; Ferrandon, M.; Yang, D.; Robison, L.; Li, P.; Wang, T. C.; Delferro, M.; Farha, O. K. Catalytic Chemoselective Functionalization of Methane in a Metal−organic Framework. *Nat. Catal.* **2018**, *1*, 356−362.

https://dx.doi.org/10.1021/acs.chemrev.0c00148
Chem. Rev. 2020, 120, 8641−8715

(363) Yang, B.; Wu, X.-P.; Gagliardi, L.; Truhlar, D. G. Methane Functionalization by an Ir(III) Catalyst Supported on a Metal−Organic Framework: An Alternative Explanation of Steric Confinement Effects. *Theor. Chem. Acc.* **2019**, *138*, 107.
(364) Supronowicz, B.; Mavrandonakis, A.; Heine, T. Interaction of Small Gases with the Unsaturated Metal Centers of the HKUST-1 Metal Organic Framework. *J. Phys. Chem. C* **2013**, *117*, 14570−14578.
(365) Maihom, T.; Probst, M.; Limtrakul, J. Computational Study of the Carbonyl−Ene Reaction between Formaldehyde and Propylene Encapsulated in Coordinatively Unsaturated Metal−Organic Frameworks $M_3(btc)_2$ (M = Fe, Co, Ni, Cu and Zn). *Phys. Chem. Chem. Phys.* **2019**, *21*, 2783−2789.
(366) Položij, M.; Rubeš, M.; Čejka, J.; Nachtigall, P. Catalysis by Dynamically Formed Defects in a Metal-Organic Framework Structure: Knoevenagel Reaction Catalyzed by Copper Benzene-1,3,5-Tricarboxylate. *ChemCatChem* **2014**, *6*, 2821−2824.
(367) Liu, Y.; Klet, R. C.; Hupp, J. T.; Farha, O. Probing the Correlations between the Defects in Metal−Organic Frameworks and Their Catalytic Activity by an Epoxide Ring-Opening Reaction. *Chem. Commun.* **2016**, *52*, 7806−7809.
(368) Wu, H.; Chua, Y. S.; Krungleviciute, V.; Tyagi, M.; Chen, P.; Yildirim, T.; Zhou, W. Unusual and Highly Tunable Missing-Linker Defects in Zirconium Metal−Organic Framework UiO-66 and Their Important Effects on Gas Adsorption. *J. Am. Chem. Soc.* **2013**, *135*, 10525−10532.
(369) Svane, K. L.; Bristow, J. K.; Gale, J. D.; Walsh, A. Vacancy Defect Configurations in the Metal−Organic Framework UiO-66: Energetics and Electronic Structure. *J. Mater. Chem. A* **2018**, *6*, 8507−8513.
(370) Canivet, J.; Vandichel, M.; Farrusseng, D. Origin of Highly Active Metal−Organic Framework Catalysts: Defects? Defects! *Dalton Trans.* **2016**, *45*, 4090−4099.
(371) Noh, H.; Cui, Y.; Peters, A. W.; Pahls, D. R.; Ortuño, M. A.; Vermeulen, N. A.; Cramer, C. J.; Gagliardi, L.; Hupp, J. T.; Farha, O. K. An Exceptionally Stable Metal−Organic Framework Supported Molybdenum(VI) Oxide Catalyst for Cyclohexene Epoxidation. *J. Am. Chem. Soc.* **2016**, *138*, 14720−14726.
(372) Platero-Prats, A. E.; League, A. B.; Bernales, V.; Ye, J.; Gallington, L. C.; Vjunov, A.; Schweitzer, N. M.; Li, Z.; Zheng, J.; Mehdi, B. L.; Stevens, A. J.; Dohnalkova, A.; Balasubramanian, M.; Farha, O. K.; Hupp, J. T.; Browning, N. D.; Fulton, J. L.; Camaioni, D. M.; Lercher, J. A.; Truhlar, D. G.; Gagliardi, L.; Cramer, C. J.; Chapman, K. W. Bridging Zirconia Nodes within a Metal−Organic Framework via Catalytic Ni-Hydroxo Clusters to Form Heterobimetallic Nanowires. *J. Am. Chem. Soc.* **2017**, *139*, 10410−10418.
(373) Li, Z.; Schweitzer, N. M.; League, A. B.; Bernales, V.; Peters, A. W.; Getsoian, A. B.; Wang, T. C.; Miller, J. T.; Vjunov, A.; Fulton, J. L.; Lercher, J. A.; Cramer, C. J.; Gagliardi, L.; Hupp, J. T.; Farha, O. K. Sintering-Resistant Single-Site Nickel Catalyst Supported by Metal−Organic Framework. *J. Am. Chem. Soc.* **2016**, *138*, 1977−1982.
(374) Yang, D.; Odoh, S. O.; Borycz, J.; Wang, T. C.; Farha, O. K.; Hupp, J. T.; Cramer, C. J.; Gagliardi, L.; Gates, B. C. Tuning Zr_6 Metal−Organic Framework (MOF) Nodes as Catalyst Supports: Site Densities and Electron-Donor Properties Influence Molecular Iridium Complexes as Ethylene Conversion Catalysts. *ACS Catal.* **2016**, *6*, 235−247.
(375) Canivet, J.; Vandichel, M.; Farrusseng, D. Origin of Highly Active Metal−Organic Framework Catalysts: Defects? Defects! *Dalton Trans.* **2016**, *45*, 4090−4099.
(376) Vermoortele, F.; Bueken, B.; Le Bars, G.; Van de Voorde, B.; Vandichel, M.; Houthoofd, K.; Vimont, A.; Daturi, M.; Waroquier, M.; Van Speybroeck, V.; Kirschhock, C.; De Vos, D. E. Synthesis Modulation as a Tool To Increase the Catalytic Activity of Metal−Organic Frameworks: The Unique Case of UiO-66(Zr). *J. Am. Chem. Soc.* **2013**, *135*, 11465−11468.
(377) Shearer, G. C.; Chavan, S.; Bordiga, S.; Svelle, S.; Olsbye, U.; Lillerud, K. P. Defect Engineering: Tuning the Porosity and Composition of the Metal−Organic Framework UiO-66 via Modulated Synthesis. *Chem. Mater.* **2016**, *28*, 3749−3761.
(378) Ling, S.; Slater, B. Dynamic Acidity in Defective UiO-66. *Chem. Sci.* **2016**, *7*, 4706−4712.
(379) Troya, D. Reaction Mechanism of Nerve-Agent Decomposition with Zr-Based Metal Organic Frameworks. *J. Phys. Chem. C* **2016**, *120*, 29312−29323.
(380) Terranova, Z. L.; Paesani, F. The Effects of Framework Dynamics on the Behavior of Water Adsorbed in the [Zn(l-L)(Cl)] and Co-MOF-74 Metal−Organic Frameworks. *Phys. Chem. Chem. Phys.* **2016**, *18*, 8196−8204.
(381) Islamoglu, T.; Ortuño, M. A.; Proussaloglou, E.; Howarth, A. J.; Vermeulen, N. A.; Atilgan, A.; Asiri, A. M.; Cramer, C. J.; Farha, O. K. Presence versus Proximity: The Role of Pendant Amines in the Catalytic Hydrolysis of a Nerve Agent Simulant. *Angew. Chem., Int. Ed.* **2018**, *57*, 1949−1953.
(382) de Koning, M. C.; van Grol, M.; Breijaert, T. Degradation of Paraoxon and the Chemical Warfare Agents VX, Tabun, and Soman by the Metal−Organic Frameworks UiO-66-NH_2, MOF-808, NU-1000, and PCN-777. *Inorg. Chem.* **2017**, *56*, 11804−11809.
(383) Sadakiyo, M.; Yamada, T.; Honda, K.; Matsui, H.; Kitagawa, H. Control of Crystalline Proton-Conducting Pathways by Water-Induced Transformations of Hydrogen-Bonding Networks in a Metal−Organic Framework. *J. Am. Chem. Soc.* **2014**, *136*, 7701−7707.
(384) Hajek, J.; Vandichel, M.; Van de Voorde, B.; Bueken, B.; De Vos, D.; Waroquier, M.; Van Speybroeck, V. Mechanistic Studies of Aldol Condensations in UiO-66 and UiO-66-NH 2 Metal Organic Frameworks. *J. Catal.* **2015**, *331*, 1−12.
(385) Wang, G.; Sharp, C.; Plonka, A. M.; Wang, Q.; Frenkel, A. I.; Guo, W.; Hill, C.; Smith, C.; Kollar, J.; Troya, D.; Morris, J. R. Mechanism and Kinetics for Reaction of the Chemical Warfare Agent Simulant, DMMP(*g*), with Zirconium(IV) MOFs: An Ultrahigh-Vacuum and DFT Study. *J. Phys. Chem. C* **2017**, *121*, 11261−11272.
(386) Plonka, A. M.; Grissom, T. G.; Musaev, D. G.; Balboa, A.; Gordon, W. O.; Collins-Wildman, D. L.; Ghose, S. K.; Tian, Y.; Ebrahim, A. M.; Mitchell, M. B.; Hill, C. L.; Morris, J. R.; Frenkel, A. I. Effect of Carbon Dioxide on the Degradation of Chemical Warfare Agent Simulant in the Presence of Zr Metal Organic Framework MOF-808. *Chem. Mater.* **2019**, *31*, 9904−9914.
(387) Chung, L. W.; Sameera, W. M. C.; Ramozzi, R.; Page, A. J.; Hatanaka, M.; Petrova, G. P.; Harris, T. V.; Li, X.; Ke, Z.; Liu, F.; Li, H.-B.; Ding, L.; Morokuma, K. The ONIOM Method and Its Applications. *Chem. Rev.* **2015**, *115*, 5678−5796.
(388) Chen, H.; Liao, P.; Mendonca, M. L.; Snurr, R. Q. Insights into Catalytic Hydrolysis of Organophosphate Warfare Agents by Metal−Organic Framework NU-1000. *J. Phys. Chem. C* **2018**, *122*, 12362−12368.
(389) Barea, E.; Maldonado, C. R.; Navarro, J. A. R. MOFs for the Capture and Degradation of Chemical Warfare Agents. In *Metal−Organic Frameworks*; García, H., Navalón, S., Eds.; Wiley-VCH: Weinheim, Germany, 2018; pp 199−221.
(390) Ketrat, S.; Maihom, T.; Wannakao, S.; Probst, M.; Nokbin, S.; Limtrakul, J. Coordinatively Unsaturated Metal−Organic Frameworks $M_3(Btc)_2$ (M = Cr, Fe, Co, Ni, Cu, and Zn) Catalyzing the Oxidation of CO by N_2O: Insight from DFT Calculations. *Inorg. Chem.* **2017**, *56*, 14005−14012.
(391) Ryu, U. J.; Kim, S. J.; Lim, H.-K.; Kim, H.; Choi, K. M.; Kang, J. K. Synergistic Interaction of Re Complex and Amine Functionalized Multiple Ligands in Metal-Organic Frameworks for Conversion of Carbon Dioxide. *Sci. Rep.* **2017**, *7*, 612.
(392) Weitzel, K.-M. On the Distinction between Tight and Loose Transition States in Unimolecular Dissociations. *Chem. Phys. Lett.* **1991**, *186*, 490−494.
(393) Seidl, A.; Gorling, A.; Vogl, P.; Majewski, J. A.; Levy, M. Generalized Kohn-Sham Schemes and the Band-Gap Problem. *Phys. Rev. B: Condens. Matter Mater. Phys.* **1996**, *53*, 3764.
(394) Yu, H. S.; Li, S. L.; Truhlar, D. G. Perspective: Kohn-Sham Density Functional Theory Descending a Staircase. *J. Chem. Phys.* **2016**, *145*, 130901.
(395) Townsend, J.; Kirkland, J. K.; Vogiatzis, K. D. Post-Hartree-Fock Methods: Configuration Interaction, Many-Body Perturbation

https://dx.doi.org/10.1021/acs.chemrev.0c00148
Chem. Rev. 2020, 120, 8641−8715

Theory, Coupled-Cluster Theory. In *Mathematical Physics in Theoretical Chemistry*; Elsevier, 2019; pp 63−117.
(396) Roos, B. O.; Taylor, P. R.; Sigbahn, P. E. M. A complete active space SCF method (CASSCF) using a density matrix formulated super-CI approach. *Chem. Phys.* **1980**, *48*, 157−173.
(397) Siegbahn, P.; Heiberg, A.; Roos, B.; Levy, B. A Comparison of the Super-CI and the Newton-Raphson Scheme in the Complete Active Space SCF Method. *Phys. Scr.* **1980**, *21*, 323−327.
(398) Fales, B. S.; Shu, Y.; Levine, B. G.; Hohenstein, E. G. Complete Active Space Configuration Interaction from State-Averaged Configuration Interaction Singles Natural Orbitals: Analytic First Derivatives and Derivative Coupling Vectors. *J. Chem. Phys.* **2017**, *147*, No. 094104.
(399) Olsen, J.; Jorgensen, P.; Koch, H.; Balkova, A.; Bartlett, R. J. Full Configuration−Interaction and State of the Art Correlation Calculations on Water in a Valence Double-zeta Basis with Polarization Functions. *J. Chem. Phys.* **1996**, *104*, 8007−8015.
(400) Roos, B. A New Method for Large-Scale Cl Calculations. *Chem. Phys. Lett.* **1972**, *15*, 153−159.
(401) Diercksen, G. H. F.; Kraemer, W. P.; Roos, B. O. SCF-CI Studies of Correlation Effects on Hydrogen Bonding and Ion Hydration. *Theoret. Chim. Acta* **1975**, *36*, 249−274.
(402) Keller, S.; Boguslawski, K.; Janowski, T.; Reiher, M.; Pulay, P. Selection of Active Spaces for Multiconfigurational Wavefunctions. *J. Chem. Phys.* **2015**, *142*, 244104.
(403) Liu, C.-M.; Xiong, J.; Zhang, D.-Q.; Wang, B.-W.; Zhu, D.-B. Multiple Thermal Magnetic Relaxation in a Two-Dimensional Ferromagnetic Dysprosium(III) Metal−Organic Framework. *RSC Adv.* **2015**, *5*, 104854−104861.
(404) Nam, W. High-Valent Iron(IV)−Oxo Complexes of Heme and Non-Heme Ligands in Oxygenation Reactions. *Acc. Chem. Res.* **2007**, *40*, 522−531.
(405) Larsen, R. W.; Wojtas, L.; Perman, J.; Musselman, R. L.; Zaworotko, M. J.; Vetromile, C. M. Mimicking Heme Enzymes in the Solid State: Metal−Organic Materials with Selectively Encapsulated Heme. *J. Am. Chem. Soc.* **2011**, *133*, 10356−10359.
(406) Weinberg, D. R.; Gagliardi, C. J.; Hull, J. F.; Murphy, C. F.; Kent, C. A.; Westlake, B. C.; Paul, A.; Ess, D. H.; McCafferty, D. G.; Meyer, T. J. Proton-Coupled Electron Transfer. *Chem. Rev.* **2012**, *112*, 4016−4093.
(407) Bernales, V.; League, A. B.; Li, Z.; Schweitzer, N. M.; Peters, A. W.; Carlson, R. K.; Hupp, J. T.; Cramer, C. J.; Farha, O. K.; Gagliardi, L. Computationally Guided Discovery of a Catalytic Cobalt-Decorated Metal−Organic Framework for Ethylene Dimerization. *J. Phys. Chem. C* **2016**, *120*, 23576−23583.
(408) Ye, J.; Gagliardi, L.; Cramer, C. J.; Truhlar, D. G. Single Ni Atoms and Ni 4 Clusters Have Similar Catalytic Activity for Ethylene Dimerization. *J. Catal.* **2017**, *354*, 278−286.
(409) Otake, K.; Ye, J.; Mandal, M.; Islamoglu, T.; Buru, C. T.; Hupp, J. T.; Delferro, M.; Truhlar, D. G.; Cramer, C. J.; Farha, O. K. Enhanced Activity of Heterogeneous Pd(II) Catalysts on Acid-Functionalized Metal−Organic Frameworks. *ACS Catal.* **2019**, *9*, 5383−5390.
(410) Morris, W.; Volosskiy, B.; Demir, S.; Gándara, F.; McGrier, P. L.; Furukawa, H.; Cascio, D.; Stoddart, J. F.; Yaghi, O. M. Synthesis, Structure, and Metalation of Two New Highly Porous Zirconium Metal−Organic Frameworks. *Inorg. Chem.* **2012**, *51*, 6443−6445.
(411) Cadiau, A.; Xie, L. S.; Kolobov, N.; Shkurenko, A.; Qureshi, M.; Tchalala, M. R.; Park, S. S.; Bavykina, A.; Eddaoudi, M.; Dincă, M.; Hendon, C. H.; Gascon, J. Toward New 2D Zirconium-Based Metal−Organic Frameworks: Synthesis, Structures, and Electronic Properties. *Chem. Mater.* **2020**, *32*, 97−104.
(412) DeCoste, J. B.; Peterson, G. W.; Jasuja, H.; Glover, T. G.; Huang, Y.; Walton, K. S. Stability and Degradation Mechanisms of Metal−Organic Frameworks Containing the $Zr_6O_4(OH)_4$ Secondary Building Unit. *J. Mater. Chem. A* **2013**, *1*, 5642−5650.
(413) George, S. M. Atomic Layer Deposition: An Overview. *Chem. Rev.* **2010**, *110*, 111−131.
(414) Mondloch, J. E.; Katz, M. J.; Planas, N.; Semrouni, D.; Gagliardi, L.; Hupp, J. T.; Farha, O. K. Are Zr_6-Based MOFs Water Stable? Linker Hydrolysis vs. Capillary-Force-Driven Channel Collapse. *Chem. Commun.* **2014**, *50*, 8944−8946.
(415) Nguyen, K. D.; Kutzscher, C.; Ehrling, S.; Senkovska, I.; Bon, V.; de Oliveira, M.; Gutmann, T.; Buntkowsky, G.; Kaskel, S. Insights into the Role of Zirconium in Proline Functionalized Metal-Organic Frameworks Attaining High Enantio- and Diastereoselectivity. *J. Catal.* **2019**, *377*, 41−50.
(416) Yang, D.; Bernales, V.; Islamoglu, T.; Farha, O. K.; Hupp, J. T.; Cramer, C. J.; Gagliardi, L.; Gates, B. C. Tuning the Surface Chemistry of Metal Organic Framework Nodes: Proton Topology of the Metal-Oxide-Like Zr6 Nodes of UiO-66 and NU-1000. *J. Am. Chem. Soc.* **2016**, *138*, 15189−15196.
(417) Planas, N.; Mondloch, J. E.; Tussupbayev, S.; Borycz, J.; Gagliardi, L.; Hupp, J. T.; Farha, O. K.; Cramer, C. J. Defining the Proton Topology of the Zr_6-Based Metal−Organic Framework NU-1000. *J. Phys. Chem. Lett.* **2014**, *5*, 3716−3723.
(418) Korzyński, M. D.; Braglia, L.; Borfecchia, E.; Lomachenko, K. A.; Baldansuren, A.; Hendon, C. H.; Lamberti, C.; Dincă, M. *Quo Vadis Niobium*? Divergent Coordination Behavior of Early-Transition Metals towards MOF-5. *Chem. Sci.* **2019**, *10*, 5906−5910.
(419) Ikuno, T.; Zheng, J.; Vjunov, A.; Sanchez-Sanchez, M.; Ortuño, M. A.; Pahls, D. R.; Fulton, J. L.; Camaioni, D. M.; Li, Z.; Ray, D.; Mehdi, B. L.; Browning, N. D.; Farha, O. K.; Hupp, J. T.; Cramer, C. J.; Gagliardi, L.; Lercher, J. A. Methane Oxidation to Methanol Catalyzed by Cu-Oxo Clusters Stabilized in NU-1000 Metal−Organic Framework. *J. Am. Chem. Soc.* **2017**, *139*, 10294−10301.
(420) Bennett, T. D.; Cheetham, A. K. Amorphous Metal−Organic Frameworks. *Acc. Chem. Res.* **2014**, *47*, 1555−1562.
(421) Bennett, T. D.; Horike, S. Liquid, Glass and Amorphous Solid States of Coordination Polymers and Metal−Organic Frameworks. *Nat. Rev. Mater.* **2018**, *3*, 431−440.
(422) Bennett, T. D.; Yue, Y.; Li, P.; Qiao, A.; Tao, H.; Greaves, N. G.; Richards, T.; Lampronti, G. I.; Redfern, S. A. T.; Blanc, F.; Farha, O. K.; Hupp, J. T.; Cheetham, A. K.; Keen, D. A. Melt-Quenched Glasses of Metal−Organic Frameworks. *J. Am. Chem. Soc.* **2016**, *138*, 3484−3492.
(423) Gaillac, R.; Pullumbi, P.; Beyer, K. A.; Chapman, K. W.; Keen, D. A.; Bennett, T. D.; Coudert, F.-X. Liquid Metal−Organic Frameworks. *Nat. Mater.* **2017**, *16*, 1149−1154.
(424) Umeyama, D.; Horike, S.; Inukai, M.; Itakura, T.; Kitagawa, S. Reversible Solid-to-Liquid Phase Transition of Coordination Polymer Crystals. *J. Am. Chem. Soc.* **2015**, *137*, 864−870.
(425) Bennett, T. D.; Goodwin, A. L.; Dove, M. T.; Keen, D. A.; Tucker, M. G.; Barney, E. R.; Soper, A. K.; Bithell, E. G.; Tan, J.-C.; Cheetham, A. K. Structure and Properties of an Amorphous Metal-Organic Framework. *Phys. Rev. Lett.* **2010**, *104*, 115503.
(426) Bloch, F. Über die Quantenmechanik der Elektronen in Kristallgittern. *Eur. Phys. J. A* **1929**, *52*, 555−600.
(427) Ashcroft, N. W.; Mermin, N. D. *Solid State Physics*; Holt, Rinehart and Winston: New York, 1976.
(428) Zhang, X.-G.; Varga, K.; Pantelides, S. T. Generalized Bloch Theorem for Complex Periodic Potentials: A Powerful Application to Quantum Transport Calculations. *Phys. Rev. B: Condens. Matter Mater. Phys.* **2007**, *76*, No. 035108.
(429) Kratzer, P.; Neugebauer, J. The Basics of Electronic Structure Theory for Periodic Systems. *Front. Chem.* **2019**, *7*, 106.
(430) Biswas, S.; Ahnfeldt, T.; Stock, N. New Functionalized Flexible Al-MIL-53-X (X = -Cl, -Br, $-CH_3$, $-NO_2$, $-(OH)_2$) Solids: Syntheses, Characterization, Sorption, and Breathing Behavior. *Inorg. Chem.* **2011**, *50*, 9518−9526.
(431) Tulchinsky, Y.; Hendon, C. H.; Lomachenko, K. A.; Borfecchia, E.; Melot, B. C.; Hudson, M. R.; Tarver, J. D.; Korzyński, M. D.; Stubbs, A. W.; Kagan, J. J.; Lamberti, C.; Brown, C. M.; Dincă, M. Reversible Capture and Release of Cl_2 and Br_2 with a Redox-Active Metal−Organic Framework. *J. Am. Chem. Soc.* **2017**, *139*, 5992−5997.
(432) Baldereschi, A. Mean-Value Point in the Brillouin Zone. *Phys. Rev. B* **1973**, *7*, 5212−5215.
(433) Aroyo, M. I.; Orobengoa, D.; de la Flor, G.; Tasci, E. S.; Perez-Mato, J. M.; Wondratschek, H. Brillouin-Zone Database on the *Bilbao*

https://dx.doi.org/10.1021/acs.chemrev.0c00148
Chem. Rev. 2020, 120, 8641−8715

Crystallographic Server. *Acta Crystallogr., Sect. A: Found. Adv.* **2014**, *70*, 126−137.
(434) Chadi, D. J. Special Points for Brillouin-Zone Integrations. *Phys. Rev. B* **1977**, *16*, 1746−1747.
(435) Monkhorst, H. J.; Pack, J. D. Special Points for Brillouin-Zone Integrations. *Phys. Rev. B* **1976**, *13*, 5188−5192.
(436) Genova, A.; Pavanello, M. Exploiting the Locality of Periodic Subsystem Density-Functional Theory: Efficient Sampling of the Brillouin Zone. *J. Phys.: Condens. Matter* **2015**, *27*, 495501.
(437) Takahashi, K.; Yoshikawa, A.; Sandhu, A. *Wide Bandgap Semiconductors: Fundamental Properties and Modern Photonic and Electronic Devices*; Springer: Berlin, 2007.
(438) Spoerke, E. D.; Small, L. J.; Foster, M. E.; Wheeler, J.; Ullman, A. M.; Stavila, V.; Rodriguez, M.; Allendorf, M. D. MOF-Sensitized Solar Cells Enabled by a Pillared Porphyrin Framework. *J. Phys. Chem. C* **2017**, *121*, 4816−4824.
(439) Foster, M. E.; Azoulay, J. D.; Wong, B. M.; Allendorf, M. D. Novel Metal−Organic Framework Linkers for Light Harvesting Applications. *Chem. Sci.* **2014**, *5*, 2081−2090.
(440) Stavila, V.; Talin, A. A.; Allendorf, M. D. MOF-Based Electronic and Opto-Electronic Devices. *Chem. Soc. Rev.* **2014**, *43*, 5994−6010.
(441) Butler, K. T.; Hendon, C. H.; Walsh, A. Designing Porous Electronic Thin-Film Devices: Band Offsets and Heteroepitaxy. *Faraday Discuss.* **2017**, *201*, 207−219.
(442) Bredas, J.-L. Mind the Gap! *Mater. Horiz.* **2014**, *1*, 17−19.
(443) Mori-Sánchez, P.; Cohen, A. J. The Derivative Discontinuity of the Exchange−Correlation Functional. *Phys. Chem. Chem. Phys.* **2014**, *16*, 14378−14387.
(444) Mori-Sánchez, P.; Cohen, A. J.; Yang, W. Localization and Delocalization Errors in Density Functional Theory and Implications for Band-Gap Prediction. *Phys. Rev. Lett.* **2008**, *100*, 146401.
(445) Yamada, K. *Electron Correlation in Metals*; Cambridge University Press: Cambridge, UK, New York, 2004.
(446) Matsuda, Y.; Tahir-Kheli, J.; Goddard, W. A. Definitive Band Gaps for Single-Wall Carbon Nanotubes. *J. Phys. Chem. Lett.* **2010**, *1*, 2946−2950.
(447) Godby, R. W.; Schlüter, M.; Sham, L. J. Accurate Exchange-Correlation Potential for Silicon and Its Discontinuity on Addition of an Electron. *Phys. Rev. Lett.* **1986**, *56*, 2415−2418.
(448) Fritsch, D.; Morgan, B. J.; Walsh, A. Self-Consistent Hybrid Functional Calculations: Implications for Structural, Electronic, and Optical Properties of Oxide Semiconductors. *Nanoscale Res. Lett.* **2017**, *12*, 19.
(449) Monserrat, B.; Dreyer, C. E.; Rabe, K. M. Phonon-Assisted Optical Absorption in $BaSnO_3$ from First Principles. *Phys. Rev. B: Condens. Matter Mater. Phys.* **2018**, *97*, 104310.
(450) Morris, A. J.; Monserrat, B. Optical Absorption Driven by Dynamical Symmetry Breaking in Indium Oxide. *Phys. Rev. B: Condens. Matter Mater. Phys.* **2018**, *98*, 161203.
(451) Pathak, A.; Shen, J.-W.; Usman, M.; Wei, L.-F.; Mendiratta, S.; Chang, Y.-S.; Sainbileg, B.; Ngue, C.-M.; Chen, R.-S.; Hayashi, M.; Luo, T.-T.; Chen, F.-R.; Chen, K.-H.; Tseng, T.-W.; Chen, L.-C.; Lu, K.-L. Integration of a (−Cu−S−)n Plane in a Metal−Organic Framework Affords High Electrical Conductivity. *Nat. Commun.* **2019**, *10*, 1721.
(452) Haldar, R.; Batra, K.; Marschner, S. M.; Kuc, A. B.; Zahn, S.; Fischer, R. A.; Bräse, S.; Heine, T.; Wöll, C. Bridging the Green Gap: Metal−Organic Framework Heteromultilayers Assembled from Porphyrinic Linkers Identified by Using Computational Screening. *Chem. - Eur. J.* **2019**, *25*, 7847−7851.
(453) Dhakshinamoorthy, A.; Li, Z.; Garcia, H. Catalysis and Photocatalysis by Metal Organic Frameworks. *Chem. Soc. Rev.* **2018**, *47*, 8134−8172.
(454) Wang, H.; Zhu, Q.-L.; Zou, R.; Xu, Q. Metal-Organic Frameworks for Energy Applications. *Chem.* **2017**, *2*, 52−80.
(455) Liu, W.; Yin, X.-B. Metal−Organic Frameworks for Electrochemical Applications. *TrAC, Trends Anal. Chem.* **2016**, *75*, 86−96.
(456) Zeng, L.; Guo, X.; He, C.; Duan, C. Metal−Organic Frameworks: Versatile Materials for Heterogeneous Photocatalysis. *ACS Catal.* **2016**, *6*, 7935−7947.
(457) Usman, M.; Mendiratta, S.; Lu, K.-L. Semiconductor Metal-Organic Frameworks: Future Low-Bandgap Materials. *Adv. Mater.* **2017**, *29*, 1605071.
(458) Madelung, O. *Introduction to Solid-State Theory*; Solid-State Sciences; Springer, 1978; Vol. *2*.
(459) Rosenberg, H. M. *The Solid State*, 3rd ed.; Oxford Physics; Oxford Science, 1988; Vol. *9*.
(460) Yang, L.-M.; Ravindran, P.; Vajeeston, P.; Tilset, M. Properties of IRMOF-14 and Its Analogues M-IRMOF-14 (M = Cd, Alkaline Earth Metals): Electronic Structure, Structural Stability, Chemical Bonding, and Optical Properties. *Phys. Chem. Chem. Phys.* **2012**, *14*, 4713−4723.
(461) Mancuso, J. L.; Hendon, C. H. Titanium(IV) Inclusion as a Versatile Route to Photoactivity in Metal−Organic Frameworks. *Adv. Theory Simul.* **2019**, *2*, 1900126.
(462) Chong, S.; Kim, J. Rational Modifications of PCN-700 to Induce Electrical Conductivity: A Computational Study. *Dalton Trans.* **2020**, *49*, 102−113.
(463) Choi, J. H.; Choi, Y. J.; Lee, J. W.; Shin, W. H.; Kang, J. K. Tunability of Electronic Band Gaps from Semiconducting to Metallic States via Tailoring Zn Ions in MOFs with Co Ions. *Phys. Chem. Chem. Phys.* **2009**, *11*, 628−631.
(464) Li, Y.; Fu, Y.; Ni, B.; Ding, K.; Chen, W.; Wu, K.; Huang, X.; Zhang, Y. Effects of Ligand Functionalization on the Photocatalytic Properties of Titanium-Based MOF: A Density Functional Theory Study. *AIP Adv.* **2018**, *8*, No. 035012.
(465) Mu, X.; Jiang, J.; Chao, F.; Lou, Y.; Chen, J. Ligand Modification of UiO-66 with an Unusual Visible Light Photocatalytic Behavior for RhB Degradation. *Dalton Trans.* **2018**, *47*, 1895−1902.
(466) Musho, T.; Li, J.; Wu, N. Band Gap Modulation of Functionalized Metal−Organic Frameworks. *Phys. Chem. Chem. Phys.* **2014**, *16*, 23646−23653.
(467) Taddei, M.; Schukraft, G. M.; Warwick, M. E. A.; Tiana, D.; McPherson, M. J.; Jones, D. R.; Petit, C. Band Gap Modulation in Zirconium-Based Metal−Organic Frameworks by Defect Engineering. *J. Mater. Chem. A* **2019**, *7*, 23781−23786.
(468) Zhang, G.; Chan, J. M. W. Reversibly Thermochromic Bismuth-Organic Materials with Tunable Optical Gaps. *J. Mater. Chem. C* **2017**, *5*, 10007−10015.
(469) Grau-Crespo, R.; Aziz, A.; Collins, A. W.; Crespo-Otero, R.; Hernández, N. C.; Rodriguez-Albelo, L. M.; Ruiz-Salvador, A. R.; Calero, S.; Hamad, S. Modeling a Linker Mix-and-Match Approach for Controlling the Optical Excitation Gaps and Band Alignment of Zeolitic Imidazolate Frameworks. *Angew. Chem., Int. Ed.* **2016**, *55*, 16012−16016.
(470) Hendrickx, K.; Vanpoucke, D. E. P.; Leus, K.; Lejaeghere, K.; Van Yperen-De Deyne, A.; Van Speybroeck, V.; Van Der Voort, P.; Hemelsoet, K. Understanding Intrinsic Light Absorption Properties of UiO-66 Frameworks: A Combined Theoretical and Experimental Study. *Inorg. Chem.* **2015**, *54*, 10701−10710.
(471) Taddei, M.; Tiana, D.; Casati, N.; van Bokhoven, J. A.; Smit, B.; Ranocchiari, M. Mixed-Linker UiO-66: Structure−Property Relationships Revealed by a Combination of High-Resolution Powder X-Ray Diffraction and Density Functional Theory Calculations. *Phys. Chem. Chem. Phys.* **2017**, *19*, 1551−1559.
(472) Choi, J. H.; Jeon, H. J.; Choi, K. M.; Kang, J. K. Metal−Organic Frameworks for Visible Light Absorption via Anion Substitution. *J. Mater. Chem.* **2012**, *22*, 10144.
(473) Botas, J. A.; Calleja, G.; Sánchez-Sánchez, M.; Orcajo, M. G. Cobalt Doping of the MOF-5 Framework and Its Effect on Gas-Adsorption Properties. *Langmuir* **2010**, *26*, 5300−5303.
(474) Venkataramanan, N. S.; Sahara, R.; Mizuseki, H.; Kawazoe, Y. Probing the Structure, Stability and Hydrogen Adsorption of Lithium Functionalized Isoreticular MOF-5 (Fe, Cu, Co, Ni and Zn) by Density Functional Theory. *Int. J. Mol. Sci.* **2009**, *10*, 1601−1608.
(475) Pham, H. Q.; Mai, T.; Pham-Tran, N.-N.; Kawazoe, Y.; Mizuseki, H.; Nguyen-Manh, D. Engineering of Band Gap in Metal−Organic Frameworks by Functionalizing Organic Linker: A Systematic

https://dx.doi.org/10.1021/acs.chemrev.0c00148
Chem. Rev. 2020, 120, 8641−8715

Density Functional Theory Investigation. *J. Phys. Chem. C* **2014**, *118*, 4567−4577.
(476) Gascon, J.; Hernández-Alonso, M. D.; Almeida, A. R.; van Klink, G. P. M.; Kapteijn, F.; Mul, G. Isoreticular MOFs as Efficient Photocatalysts with Tunable Band Gap: An Operando FTIR Study of the Photoinduced Oxidation of Propylene. *ChemSusChem* **2008**, *1*, 981−983.
(477) Yang, L.-M.; Ravindran, P.; Vajeeston, P.; Tilset, M. Ab Initio Investigations on the Crystal Structure, Formation Enthalpy, Electronic Structure, Chemical Bonding, and Optical Properties of Experimentally Synthesized Isoreticular Metal−Organic Framework-10 and Its Analogues: M-IRMOF-10 (M = Zn, Cd, Be, Mg, Ca, Sr and Ba). *RSC Adv.* **2012**, *2*, 1618−1631.
(478) Salih, Z. I.; Guo, Y.-J.; Zheng, J.-J.; Zhao, X. Effect of Modified Linkers of MOF-5 on Enhancing Interaction Energies: A Theoretical Study. *Comput. Theor. Chem.* **2015**, *1058*, 28−33.
(479) Yang, L.-M.; Fang, G.-Y.; Ma, J.; Ganz, E.; Han, S. S. Band Gap Engineering of Paradigm MOF-5. *Cryst. Growth Des.* **2014**, *14*, 2532−2541.
(480) Brozek, C. K.; Michaelis, V. K.; Ong, T.-C.; Bellarosa, L.; López, N.; Griffin, R. G.; Dincă, M. Dynamic DMF Binding in MOF-5 Enables the Formation of Metastable Cobalt-Substituted MOF-5 Analogues. *ACS Cent. Sci.* **2015**, *1*, 252−260.
(481) Dodson, R. A.; Wong-Foy, A. G.; Matzger, A. J. The Metal−Organic Framework Collapse Continuum: Insights from Two-Dimensional Powder X-Ray Diffraction. *Chem. Mater.* **2018**, *30*, 6559−6565.
(482) Trousselet, F.; Archereau, A.; Boutin, A.; Coudert, F.-X. Heterometallic Metal−Organic Frameworks of MOF-5 and UiO-66 Families: Insight from Computational Chemistry. *J. Phys. Chem. C* **2016**, *120*, 24885−24894.
(483) Yang, L.-M.; Ganz, E.; Svelle, S.; Tilset, M. Computational Exploration of Newly Synthesized Zirconium Metal−Organic Frameworks UiO-66, −67, −68 and Analogues. *J. Mater. Chem. C* **2014**, *2*, 7111−7125.
(484) Santaclara, J. G.; Olivos-Suarez, A. I.; Gonzalez-Nelson, A.; Osadchii, D.; Nasalevich, M. A.; van der Veen, M. A.; Kapteijn, F.; Sheveleva, A. M.; Veber, S. L.; Fedin, M. V.; Murray, A. T.; Hendon, C. H.; Walsh, A.; Gascon, J. Revisiting the Incorporation of Ti(IV) in UiO-Type Metal−Organic Frameworks: Metal Exchange versus Grafting and Their Implications on Photocatalysis. *Chem. Mater.* **2017**, *29*, 8963−8967.
(485) Lammert, M.; Wharmby, M. T.; Smolders, S.; Bueken, B.; Lieb, A.; Lomachenko, K. A.; Vos, D. D.; Stock, N. Cerium-Based Metal Organic Frameworks with UiO-66 Architecture: Synthesis, Properties and Redox Catalytic Activity. *Chem. Commun.* **2015**, *51*, 12578−12581.
(486) Campanelli, M.; Del Giacco, T.; De Angelis, F.; Mosconi, E.; Taddei, M.; Marmottini, F.; D'Amato, R.; Costantino, F. Solvent-Free Synthetic Route for Cerium(IV) Metal−Organic Frameworks with UiO-66 Architecture and Their Photocatalytic Applications. *ACS Appl. Mater. Interfaces* **2019**, *11*, 45031−45037.
(487) Tu, J.; Zeng, X.; Xu, F.; Wu, X.; Tian, Y.; Hou, X.; Long, Z. Microwave-Induced Fast Incorporation of Titanium into UiO-66 Metal−Organic Frameworks for Enhanced Photocatalytic Properties. *Chem. Commun.* **2017**, *53*, 3361−3364.
(488) Tanabe, K. K.; Cohen, S. M. Engineering a Metal-Organic Framework Catalyst by Using Postsynthetic Modification. *Angew. Chem., Int. Ed.* **2009**, *48*, 7424−7427.
(489) Karagiaridi, O.; Bury, W.; Mondloch, J. E.; Hupp, J. T.; Farha, O. K. Solvent-Assisted Linker Exchange: An Alternative to the De Novo Synthesis of Unattainable Metal-Organic Frameworks. *Angew. Chem., Int. Ed.* **2014**, *53*, 4530−4540.
(490) Ortiz, A. U.; Boutin, A.; Fuchs, A. H.; Coudert, F.-X. Metal−Organic Frameworks with Wine-Rack Motif: What Determines Their Flexibility and Elastic Properties? *J. Chem. Phys.* **2013**, *138*, 174703.
(491) Coudert, F.-X. Responsive Metal−Organic Frameworks and Framework Materials: Under Pressure, Taking the Heat, in the Spotlight, with Friends. *Chem. Mater.* **2015**, *27*, 1905−1916.
(492) Coudert, F.-X.; Boutin, A.; Jeffroy, M.; Mellot-Draznieks, C.; Fuchs, A. H. Thermodynamic Methods and Models to Study Flexible Metal-Organic Frameworks. *ChemPhysChem* **2011**, *12*, 247−258.
(493) Ling, S.; Slater, B. Unusually Large Band Gap Changes in Breathing Metal−Organic Framework Materials. *J. Phys. Chem. C* **2015**, *119*, 16667−16677.
(494) Le, K. N.; Hendon, C. H. Pressure-Induced Metallicity and Piezoreductive Transition of Metal-Centres in Conductive 2-Dimensional Metal−Organic Frameworks. *Phys. Chem. Chem. Phys.* **2019**, *21*, 25773−25778.
(495) Tie, D. Y.; Chen, Z. First Principles Study of the Electronic Properties of a Ni_3 (2,3,6,7,10,11-Hexaaminotriphenylene)$_2$ Monolayer under Biaxial Strain. *RSC Adv.* **2015**, *5*, 55186−55190.
(496) Zhou, Q.; Wang, J.; Chwee, T. S.; Wu, G.; Wang, X.; Ye, Q.; Xu, J.; Yang, S.-W. Topological Insulators Based on 2D Shape-Persistent Organic Ligand Complexes. *Nanoscale* **2015**, *7*, 727−735.
(497) Zhang, X.; Wang, Z.; Zhao, M.; Liu, F. Tunable Topological States in Electron-Doped HTT-Pt. *Phys. Rev. B: Condens. Matter Mater. Phys.* **2016**, *93*, 165401.
(498) Clough, A. J.; Yoo, J. W.; Mecklenburg, M. H.; Marinescu, S. C. Two-Dimensional Metal−Organic Surfaces for Efficient Hydrogen Evolution from Water. *J. Am. Chem. Soc.* **2015**, *137*, 118−121.
(499) Wu, M.; Wang, Z.; Liu, J.; Li, W.; Fu, H.; Sun, L.; Liu, X.; Pan, M.; Weng, H.; Dincă, M.; Fu, L.; Li, J. Conetronics in 2D Metal-Organic Frameworks: Double/Half Dirac Cones and Quantum Anomalous Hall Effect. *2D Mater.* **2017**, *4*, No. 015015.
(500) Adjizian, J.-J.; Briddon, P.; Humbert, B.; Duvail, J.-L.; Wagner, P.; Adda, C.; Ewels, C. Dirac Cones in Two-Dimensional Conjugated Polymer Networks. *Nat. Commun.* **2014**, *5*, 6842.
(501) Huang, X.; Sheng, P.; Tu, Z.; Zhang, F.; Wang, J.; Geng, H.; Zou, Y.; Di, C.; Yi, Y.; Sun, Y.; Xu, W.; Zhu, D. A Two-Dimensional π−d Conjugated Coordination Polymer with Extremely High Electrical Conductivity and Ambipolar Transport Behaviour. *Nat. Commun.* **2015**, *6*, 7408.
(502) Zhao, B.; Zhang, J.; Feng, W.; Yao, Y.; Yang, Z. Quantum Spin Hall and Z 2 Metallic States in an Organic Material. *Phys. Rev. B: Condens. Matter Mater. Phys.* **2014**, *90*, 201403.
(503) Lopez, M. F.; Merino, J. From Quantum Anomalous Hall Phases to Topological Metals in Interacting Decorated Honeycomb Lattices. *Phys. Rev. B: Condens. Matter Mater. Phys.* **2019**, *100*, No. 075154.
(504) Wang, Z. F.; Liu, Z.; Liu, F. Quantum Anomalous Hall Effect in 2D Organic Topological Insulators. *Phys. Rev. Lett.* **2013**, *110*, 196801.
(505) Young, S. M.; Kane, C. L. Dirac Semimetals in Two Dimensions. *Phys. Rev. Lett.* **2015**, *115*, 126803.
(506) Young, S. M.; Zaheer, S.; Teo, J. C. Y.; Kane, C. L.; Mele, E. J.; Rappe, A. M. Dirac Semimetal in Three Dimensions. *Phys. Rev. Lett.* **2012**, *108*, 140405.
(507) *Topological Insulators: Fundamentals and Perspectives*; Ortmann, F., Roche, S., Valenzuela, S. O., Eds.; Wiley-VCH: Weinheim, Germany, 2015.
(508) Foster, M. E.; Sohlberg, K.; Allendorf, M. D.; Talin, A. A. Unraveling the Semiconducting/Metallic Discrepancy in $Ni_3(HITP)_2$. *J. Phys. Chem. Lett.* **2018**, *9*, 481−486.
(509) Foster, M. E.; Sohlberg, K.; Spataru, C. D.; Allendorf, M. D. Proposed Modification of the Graphene Analogue $Ni_3(HITP)_2$ To Yield a Semiconducting Material. *J. Phys. Chem. C* **2016**, *120*, 15001−15008.
(510) Feng, D.; Lei, T.; Lukatskaya, M. R.; Park, J.; Huang, Z.; Lee, M.; Shaw, L.; Chen, S.; Yakovenko, A. A.; Kulkarni, A.; Xiao, J.; Fredrickson, K.; Tok, J. B.; Zou, X.; Cui, Y.; Bao, Z. Robust and Conductive Two-Dimensional Metal−organic Frameworks with Exceptionally High Volumetric and Areal Capacitance. *Nat. Energy* **2018**, *3*, 30−36.
(511) Foster, M. E.; Sohlberg, K.; Allendorf, M. D.; Talin, A. A. Unraveling the Semiconducting/Metallic Discrepancy in $Ni_3(HITP)_2$. *J. Phys. Chem. Lett.* **2018**, *9*, 481−486.
(512) Liu, J.; Lukose, B.; Shekhah, O.; Arslan, H. K.; Weidler, P.; Gliemann, H.; Bräse, S.; Grosjean, S.; Godt, A.; Feng, X.; Müllen, K.;

https://dx.doi.org/10.1021/acs.chemrev.0c00148
Chem. Rev. 2020, 120, 8641−8715

Magdau, I.-B.; Heine, T.; Wöll, C. A Novel Series of Isoreticular Metal Organic Frameworks: Realizing Metastable Structures by Liquid Phase Epitaxy. *Sci. Rep.* **2012**, *2*, No. 921.
(513) Kapustin, E. A.; Lee, S.; Alshammari, A. S.; Yaghi, O. M. Molecular Retrofitting Adapts a Metal−Organic Framework to Extreme Pressure. *ACS Cent. Sci.* **2017**, *3*, 662−667.
(514) Schneider, C.; Bodesheim, D.; Keupp, J.; Schmid, R.; Kieslich, G. Retrofitting Metal-Organic Frameworks. *Nat. Commun.* **2019**, *10*, 4921.
(515) Schneider, C.; Bodesheim, D.; Ehrenreich, M. G.; Crocellà, V.; Mink, J.; Fischer, R. A.; Butler, K. T.; Kieslich, G. Tuning the Negative Thermal Expansion Behavior of the Metal−Organic Framework Cu_3BTC_2 by Retrofitting. *J. Am. Chem. Soc.* **2019**, *141*, 10504−10509.
(516) Dong, L.; Kim, Y.; Er, D.; Rappe, A. M.; Shenoy, V. B. Two-Dimensional π -Conjugated Covalent-Organic Frameworks as Quantum Anomalous Hall Topological Insulators. *Phys. Rev. Lett.* **2016**, *116*, No. 096601.
(517) Kambe, T.; Sakamoto, R.; Kusamoto, T.; Pal, T.; Fukui, N.; Hoshiko, K.; Shimojima, T.; Wang, Z.; Hirahara, T.; Ishizaka, K.; Hasegawa, S.; Liu, F.; Nishihara, H. Redox Control and High Conductivity of Nickel Bis(Dithiolene) Complex π-Nanosheet: A Potential Organic Two-Dimensional Topological Insulator. *J. Am. Chem. Soc.* **2014**, *136*, 14357−14360.
(518) Wang, Z. F.; Su, N.; Liu, F. Prediction of a Two-Dimensional Organic Topological Insulator. *Nano Lett.* **2013**, *13*, 2842−2845.
(519) Liu, Z.; Wang, Z.-F.; Mei, J.-W.; Wu, Y.-S.; Liu, F. Flat Chern Band in a Two-Dimensional Organometallic Framework. *Phys. Rev. Lett.* **2013**, *110*, 106804.
(520) Wang, Z. F.; Liu, Z.; Liu, F. Organic Topological Insulators in Organometallic Lattices. *Nat. Commun.* **2013**, *4*, 1471.
(521) Yang, L.; He, X.; Dinca, M. Triphenylene-Bridged Trinuclear Complexes of Cu: Models for Spin Interactions in Two-Dimensional Electrically Conductive Metal-Organic Frameworks. *J. Am. Chem. Soc.* **2019**, *141*, 10475−10480.
(522) Yilmaz, G.; Peh, S. B.; Zhao, D.; Ho, G. W. Atomic- and Molecular-Level Design of Functional Metal−Organic Frameworks (MOFs) and Derivatives for Energy and Environmental Applications. *Adv. Sci.* **2019**, *6*, 1901129.
(523) Santaclara, J. G.; Kapteijn, F.; Gascon, J.; van der Veen, M. A. Understanding Metal−Organic Frameworks for Photocatalytic Solar Fuel Production. *CrystEngComm* **2017**, *19*, 4118−4125.
(524) Evarestov, R. A.; Smirnov, V. P. Special points of the brillouin zone and their use in the solid state theory. *Phys. Status Solidi B* **1983**, *119*, 9−40.
(525) Chadi, D. J.; Cohen, M. L. Special Points in the Brillouin Zone. *Phys. Rev. B* **1973**, *8*, 5747−5753.
(526) Hoffmann, R. How Chemistry and Physics Meet in the Solid State. *Angew. Chem., Int. Ed. Engl.* **1987**, *26*, 846−878.
(527) Hoffmann, R. Interaction of Orbitals through Space and through Bonds. *Acc. Chem. Res.* **1971**, *4*, 1−9.
(528) Sun, L.; Campbell, M. G.; Dincă, M. Electrically Conductive Porous Metal-Organic Frameworks. *Angew. Chem., Int. Ed.* **2016**, *55*, 3566−3579.
(529) Ivanov, M. V.; Wadumethrige, S. H.; Wang, D.; Rathore, R. Through-Space or Through-Bond? The Important Role of Cofaciality in Orbital Reordering and Its Implications for Hole (De)Stabilization in Polychromophoric Assemblies. *J. Phys. Chem. C* **2017**, *121*, 15639−15643.
(530) Scholes, G. D.; Ghiggino, K. P.; Oliver, A. M.; Paddon-Row, M. N. Through-Space and through-Bond Effects on Exciton Interactions in Rigidly Linked Dinaphthyl Molecules. *J. Am. Chem. Soc.* **1993**, *115*, 4345−4349.
(531) Liu, Z.; Liu, F.; Wu, Y.-S. Exotic Electronic States in the World of Flat Bands: From Theory to Material. *Chin. Phys. B* **2014**, *23*, No. 077308.
(532) Pedersen, F. B. Simple Derivation of the Effective-Mass Equation Using a Multiple-Scale Technique. *Eur. J. Phys.* **1997**, *18*, 43−45.
(533) Dong, R.; Han, P.; Arora, H.; Ballabio, M.; Karakus, M.; Zhang, Z.; Shekhar, C.; Adler, P.; Petkov, P. St.; Erbe, A.; Mannsfeld, S. C. B.; Felser, C.; Heine, T.; Bonn, M.; Feng, X.; Cánovas, E. High-Mobility Band-like Charge Transport in a Semiconducting Two-Dimensional Metal−Organic Framework. *Nat. Mater.* **2018**, *17*, 1027−1032.
(534) Canepa, P.; Tan, K.; Du, Y.; Lu, H.; Chabal, Y. J.; Thonhauser, T. Structural, Elastic, Thermal, and Electronic Responses of Small-Molecule-Loaded Metal−Organic Framework Materials. *J. Mater. Chem. A* **2015**, *3*, 986−995.
(535) Campbell, M. G.; Liu, S. F.; Swager, T. M.; Dincă, M. Chemiresistive Sensor Arrays from Conductive 2D Metal−Organic Frameworks. *J. Am. Chem. Soc.* **2015**, *137*, 13780−13783.
(536) Liu, J.; Zhou, W.; Liu, J.; Howard, I.; Kilibarda, G.; Schlabach, S.; Coupry, D.; Addicoat, M.; Yoneda, S.; Tsutsui, Y.; Sakurai, T.; Seki, S.; Wang, Z.; Lindemann, P.; Redel, E.; Heine, T.; Wöll, C. Photoinduced Charge-Carrier Generation in Epitaxial MOF Thin Films: High Efficiency as a Result of an Indirect Electronic Band Gap? *Angew. Chem., Int. Ed.* **2015**, *54*, 7441−7445.
(537) Li, Y.; Fu, Y.; Ni, B.; Ding, K.; Chen, W.; Wu, K.; Huang, X.; Zhang, Y. Effects of Ligand Functionalization on the Photocatalytic Properties of Titanium-Based MOF: A Density Functional Theory Study. *AIP Adv.* **2018**, *8*, No. 035012.
(538) Yu, S.; Li, S.; Meng, X.; Wan, C.; Ju, X. Tuning the Hydrogen Adsorption Properties of Zn−Based Metal−Organic Frameworks: Combined DFT and GCMC Simulations. *J. Solid State Chem.* **2018**, *266*, 31−36.
(539) Li, J.; Musho, T.; Bright, J.; Wu, N. Functionalization of a Metal-Organic Framework Semiconductor for Tuned Band Structure and Catalytic Activity. *J. Electrochem. Soc.* **2019**, *166*, H3029−H3034.
(540) Erkartal, M.; Durandurdu, M. Pressure-Induced Amorphization of MOF-5: A First Principles Study. *Chem. Sel.* **2018**, *3*, 8056−8063.
(541) Xie, L. S.; Sun, L.; Wan, R.; Park, S. S.; DeGayner, J. A.; Hendon, C. H.; Dincă, M. Tunable Mixed-Valence Doping toward Record Electrical Conductivity in a Three-Dimensional Metal−Organic Framework. *J. Am. Chem. Soc.* **2018**, *140*, 7411−7414.
(542) Zhao, M.; Wang, A.; Zhang, X. Half-Metallicity of a Kagome Spin Lattice: The Case of a Manganese Bis-Dithiolene Monolayer. *Nanoscale* **2013**, *5*, 10404−10408.
(543) Zhang, L.-C.; Zhang, L.; Qin, G.; Zheng, Q.-R.; Hu, M.; Yan, Q.-B.; Su, G. Two-Dimensional Magnetic Metal−Organic Frameworks with the Shastry-Sutherland Lattice. *Chem. Sci.* **2019**, *10*, 10381−10387.
(544) Žutić, I.; Fabian, J.; Das Sarma, S. Spintronics: Fundamentals and Applications. *Rev. Mod. Phys.* **2004**, *76*, 323−410.
(545) Zhang, Y.; Riduan, S. N.; Wang, J. Redox Active Metal- and Covalent Organic Frameworks for Energy Storage: Balancing Porosity and Electrical Conductivity. *Chem. - Eur. J.* **2017**, *23*, 16419−16431.
(546) Wentz, H. C.; Skorupskii, G.; Bonfim, A. B.; Mancuso, J. L.; Hendon, C. H.; Oriel, E. H.; Sazama, G. T.; Campbell, M. G. Switchable Electrical Conductivity in a Three-Dimensional Metal−Organic Framework *via* Reversible Ligand n-Doping. *Chem. Sci.* **2020**, *11*, 1342−1346.
(547) Darago, L. E.; Aubrey, M. L.; Yu, C. J.; Gonzalez, M. I.; Long, J. R. Electronic Conductivity, Ferrimagnetic Ordering, and Reductive Insertion Mediated by Organic Mixed-Valence in a Ferric Semiquinoid Metal−Organic Framework. *J. Am. Chem. Soc.* **2015**, *137*, 15703−15711.
(548) Usov, P. M.; Huffman, B.; Epley, C. C.; Kessinger, M. C.; Zhu, J.; Maza, W. A.; Morris, A. J. Study of Electrocatalytic Properties of Metal−Organic Framework PCN-223 for the Oxygen Reduction Reaction. *ACS Appl. Mater. Interfaces* **2017**, *9*, 33539−33543.
(549) Lin, S.; Usov, P. M.; Morris, A. J. The Role of Redox Hopping in Metal−Organic Framework Electrocatalysis. *Chem. Commun.* **2018**, *54*, 6965−6974.
(550) Sun, L.; Hendon, C. H.; Park, S. S.; Tulchinsky, Y.; Wan, R.; Wang, F.; Walsh, A.; Dinca, M. Is Iron Unique in Promoting Electrical Conductivity in MOFs? *Chem. Sci.* **2017**, *8*, 4450−4457.

https://dx.doi.org/10.1021/acs.chemrev.0c00148
Chem. Rev. 2020, 120, 8641−8715

(551) Hod, I.; Farha, O. K.; Hupp, J. T. Modulating the Rate of Charge Transport in a Metal−Organic Framework Thin Film Using Host:Guest Chemistry. *Chem. Commun.* **2016**, *52*, 1705−1708.
(552) Park, J. G.; Aubrey, M. L.; Oktawiec, J.; Chakarawet, K.; Darago, L. E.; Grandjean, F.; Long, G. J.; Long, J. R. Charge Delocalization and Bulk Electronic Conductivity in the Mixed-Valence Metal−Organic Framework $Fe(1,2,3\text{-Triazolate})_2(BF_4)_x$. *J. Am. Chem. Soc.* **2018**, *140*, 8526−8534.
(553) Darago, L. E.; Aubrey, M. L.; Yu, C. J.; Gonzalez, M. I.; Long, J. R. Electronic Conductivity, Ferrimagnetic Ordering, and Reductive Insertion Mediated by Organic Mixed-Valence in a Ferric Semiquinoid Metal−Organic Framework. *J. Am. Chem. Soc.* **2015**, *137*, 15703−15711.
(554) Sun, L.; Hendon, C. H.; Dincă, M. Coordination-Induced Reversible Electrical Conductivity Variation in the MOF-74 Analogue Fe_2(DSBDC). *Dalton Trans.* **2018**, *47*, 11739−11743.
(555) Sun, L.; Hendon, C. H.; Minier, M. A.; Walsh, A.; Dincă, M. Million-Fold Electrical Conductivity Enhancement in Fe_2(DEBDC) versus Mn_2(DEBDC) (E = S, O). *J. Am. Chem. Soc.* **2015**, *137*, 6164−6167.
(556) Sun, L.; Hendon, C. H.; Park, S. S.; Tulchinsky, Y.; Wan, R.; Wang, F.; Walsh, A.; Dincă, M. Is Iron Unique in Promoting Electrical Conductivity in MOFs? *Chem. Sci.* **2017**, *8*, 4450−4457.
(557) Aubrey, M. L.; Wiers, B. M.; Andrews, S. C.; Sakurai, T.; Reyes-Lillo, S. E.; Hamed, S. M.; Yu, C.-J.; Darago, L. E.; Mason, J. A.; Baeg, J.-O.; Grandjean, F.; Long, G. J.; Seki, S.; Neaton, J. B.; Yang, P.; Long, J. R. Electron Delocalization and Charge Mobility as a Function of Reduction in a Metal−Organic Framework. *Nat. Mater.* **2018**, *17*, 625−632.
(558) Creutz, C. Mixed Valence Complexes of d^5−d^6 Metal Centers. In *Progress in Inorganic Chemistry*; Lippard, S. J., Ed.; John Wiley & Sons: Hoboken, NJ, 2007; pp 1−73.
(559) Narayan, T. C.; Miyakai, T.; Seki, S.; Dincă, M. High Charge Mobility in a Tetrathiafulvalene-Based Microporous Metal−Organic Framework. *J. Am. Chem. Soc.* **2012**, *134*, 12932−12935.
(560) Park, S. S.; Hontz, E. R.; Sun, L.; Hendon, C. H.; Walsh, A.; Van Voorhis, T.; Dinca, M. Cation-Dependent Intrinsic Electrical Conductivity in Isostructural Tetrathiafulvalene-Based Microporous Metal−Organic Frameworks. *J. Am. Chem. Soc.* **2015**, *137*, 1774−1777.
(561) Dey, P.; Paul, J.; Wang, Z.; Stevens, C. E.; Liu, C.; Romero, A. H.; Shan, J.; Hilton, D. J.; Karaiskaj, D. Optical Coherence in Atomic-Monolayer Transition-Metal Dichalcogenides Limited by Electron-Phonon Interactions. *Phys. Rev. Lett.* **2016**, *116*, 127402.
(562) Segall, B.; Mahan, G. D. Phonon-Assisted Recombination of Free Excitons in Compound Semiconductors. *Phys. Rev.* **1968**, *171*, 935−948.
(563) Shang, H.; Carbogno, C.; Rinke, P.; Scheffler, M. Lattice Dynamics Calculations Based on Density-Functional Perturbation Theory in Real Space. *Comput. Phys. Commun.* **2017**, *215*, 26−46.
(564) *Ab Initio Calculation of Phonon Spectra*; Devreese, J. T., Van Doren, V. E., Van Camp, P. E., Eds.; Springer: Boston, 1983.
(565) Kresse, G.; Furthmüller, J.; Hafner, J. Ab Initio Force Constant Approach to Phonon Dispersion Relations of Diamond and Graphite. *Europhys. Lett.* **1995**, *32*, 729−734.
(566) Wang, Y.; Shang, S.-L.; Fang, H.; Liu, Z.-K.; Chen, L.-Q. First-Principles Calculations of Lattice Dynamics and Thermal Properties of Polar Solids. *npj Comp. Mater.* **2016**, *2*, 16006.
(567) Giannozzi, P.; de Gironcoli, S.; Pavone, P.; Baroni, S. Ab Initio Calculation of Phonon Dispersions in Semiconductors. *Phys. Rev. B: Condens. Matter Mater. Phys.* **1991**, *43*, 7231.
(568) Kamencek, T.; Bedoya-Martínez, N.; Zojer, E. Understanding Phonon Properties in Isoreticular Metal-Organic Frameworks from First Principles. *Phys. Rev. Mater.* **2019**, *3*, 116003.
(569) Wang, X.; Guo, R.; Xu, D.; Chung, J.; Kaviany, M.; Huang, B. Anisotropic Lattice Thermal Conductivity and Suppressed Acoustic Phonons in MOF-74 from First Principles. *J. Phys. Chem. C* **2015**, *119*, 26000−26008.
(570) Yin, M. T.; Cohen, M. L. Microscopic Theory of the Phase Transformation and Lattice Dynamics of Si. *Phys. Rev. Lett.* **1980**, *45*, 1004−1007.
(571) *Emergent Phenomena in Correlated Matter: Lecture Notes of the Autumn School Correlated Electrons 2013 at Forschungszentrum Jülich, 23−27 September 2013*; Pavarini, E., Institute for Advanced Simulation, Ed.; Schriften des Forschungszentrums Jülich Reihe Modeling and Simulation, Forschungszentrum Jülich: Jülich, 2013.
(572) Hohenberg, P.; Kohn, W. Inhomogeneous Electron Gas. *Phys. Rev.* **1964**, *136*, B864−B871.
(573) Togo, A.; Tanaka, I. First Principles Phonon Calculations in Materials Science. *Scr. Mater.* **2015**, *108*, 1−5.
(574) Wang, L.; Wang, C.; Sun, Y.; Shi, K.; Deng, S.; Lu, H. Large Negative Thermal Expansion Provided by Metal-Organic Framework MOF-5: A First-Principles Study. *Mater. Chem. Phys.* **2016**, *175*, 138−145.
(575) Zhou, W.; Yildirim, T. Lattice Dynamics of Metal-Organic Frameworks: Neutron Inelastic Scattering and First-Principles Calculations. *Phys. Rev. B: Condens. Matter Mater. Phys.* **2006**, *74*, 180301.
(576) Zhou, W.; Wu, H.; Yildirim, T.; Simpson, J. R.; Walker, A. R. H. Origin of the Exceptional Negative Thermal Expansion in Metal-Organic Framework-5 $Zn_4O(1,4\text{-benzenedicarboxylate})_3$. *Phys. Rev. B: Condens. Matter Mater. Phys.* **2008**, *78*, No. 054114.
(577) Iacomi, P.; Formalik, F.; Marreiros, J.; Shang, J.; Rogacka, J.; Mohmeyer, A.; Behrens, P.; Ameloot, R.; Kuchta, B.; Llewellyn, P. L. Role of Structural Defects in the Adsorption and Separation of C3 Hydrocarbons in Zr-Fumarate-MOF (MOF-801). *Chem. Mater.* **2019**, *31*, 8413−8423.
(578) Jha, P. K.; Gupta, S. D.; Gupta, S. K. Puzzling Phonon Dispersion Curves and Vibrational Mode Instability in Superconducting $MgCNi_3$. *AIP Adv.* **2012**, *2*, No. 022120.
(579) Rimmer, L. H. N.; Dove, M. T.; Goodwin, A. L.; Palmer, D. C. Acoustic Phonons and Negative Thermal Expansion in MOF-5. *Phys. Chem. Chem. Phys.* **2014**, *16*, 21144−21152.
(580) Lock, N.; Christensen, M.; Wu, Y.; Peterson, V. K.; Thomsen, M. K.; Piltz, R. O.; Ramirez-Cuesta, A. J.; McIntyre, G. J.; Norén, K.; Kutteh, R.; Kepert, C. J.; Kearley, G. J.; Iversen, B. B. Scrutinizing Negative Thermal Expansion in MOF-5 by Scattering Techniques and Ab Initio Calculations. *Dalton Trans.* **2013**, *42*, 1996−2007.
(581) Tan, K.; Zuluaga, S.; Gong, Q.; Canepa, P.; Wang, H.; Li, J.; Chabal, Y. J.; Thonhauser, T. Water Reaction Mechanism in Metal Organic Frameworks with Coordinatively Unsaturated Metal Ions: MOF-74. *Chem. Mater.* **2014**, *26*, 6886−6895.
(582) Grev, R. S.; Janssen, C. L.; Schaefer, H. F. Concerning Zero-point Vibrational Energy Corrections to Electronic Energies. *J. Chem. Phys.* **1991**, *95*, 5128−5132.
(583) Vanpoucke, D. E. P.; Lejaeghere, K.; Van Speybroeck, V.; Waroquier, M.; Ghysels, A. Mechanical Properties from Periodic Plane Wave Quantum Mechanical Codes: The Challenge of the Flexible Nanoporous MIL-47(V) Framework. *J. Phys. Chem. C* **2015**, *119*, 23752−23766.
(584) Peressutti, G.; Skagerstam, B.-S. Finite Temperature Effects in Quantum Field Theory. *Phys. Lett. B* **1982**, *110*, 406−410.
(585) McQuarrie, D. A. *Statistical Thermodynamics*; Harper and Row: New York, 1973.
(586) Merrick, J. P.; Moran, D.; Radom, L. An Evaluation of Harmonic Vibrational Frequency Scale Factors. *J. Phys. Chem. A* **2007**, *111*, 11683−11700.
(587) Pople, J. A.; Scott, A. P.; Wong, M. W.; Radom, L. Scaling Factors for Obtaining Fundamental Vibrational Frequencies and Zero-Point Energies from HF/6-31G* and MP2/6-31G* Harmonic Frequencies. *Isr. J. Chem.* **1993**, *33*, 345−350.
(588) Rauhut, G.; Pulay, P. Transferable Scaling Factors for Density Functional Derived Vibrational Force Fields. *J. Phys. Chem.* **1995**, *99*, 3093−3100.
(589) Andrade, S. G.; Gonçalves, L. C. S.; Jorge, F. E. Scaling Factors for Fundamental Vibrational Frequencies and Zero-Point Energies

https://dx.doi.org/10.1021/acs.chemrev.0c00148
Chem. Rev. 2020, 120, 8641−8715

Obtained from HF, MP2, and DFT/DZP and TZP Harmonic Frequencies. *J. Mol. Struct.: THEOCHEM* **2008**, *864*, 20−25.
(590) Kesharwani, M. K.; Brauer, B.; Martin, J. M. L. Frequency and Zero-Point Vibrational Energy Scale Factors for Double-Hybrid Density Functionals (and Other Selected Methods): Can Anharmonic Force Fields Be Avoided? *J. Phys. Chem. A* **2015**, *119*, 1701−1714.
(591) Tantirungrotechai, Y.; Phanasant, K.; Roddecha, S.; Surawatanawong, P.; Sutthikhum, V.; Limtrakul, J. Scaling Factors for Vibrational Frequencies and Zero-Point Vibrational Energies of Some Recently Developed Exchange-Correlation Functionals. *J. Mol. Struct.: THEOCHEM* **2006**, *760*, 189−192.
(592) Tully, J. C. Molecular Dynamics with Electronic Transitions. *J. Chem. Phys.* **1990**, *93*, 1061−1071.
(593) Craig, C. F.; Duncan, W. R.; Prezhdo, O. V. Trajectory Surface Hopping in the Time-Dependent Kohn-Sham Approach for Electron-Nuclear Dynamics. *Phys. Rev. Lett.* **2005**, *95*, 163001.
(594) Syzgantseva, M. A.; Stepanov, N. F.; Syzgantseva, O. A. Carrier Lifetimes and Recombination Pathways in Metal−Organic Frameworks. *J. Phys. Chem. Lett.* **2019**, *10*, 5041−5046.
(595) Musho, T.; Wu, N. Ab Initio Calculation of Electronic Charge Mobility in Metal−Organic Frameworks. *Phys. Chem. Chem. Phys.* **2015**, *17*, 26160−26165.
(596) Bardeen, J.; Shockley, W. Deformation Potentials and Mobilities in Non-Polar Crystals. *Phys. Rev.* **1950**, *80*, 72−80.
(597) McDougall, J.; Stoner, E. C. The Computation of Fermi−Dirac Functions. *Philos. Trans. Royal Soc. Lon. A* **1938**, *237*, 67−104.
(598) Musho, T. D.; Yasin, A. S. Ab-Initio Study of the Electron Mobility in a Functionalized UiO-66 Metal Organic Framework. *J. Electron. Mater.* **2018**, *47*, 3692−3700.
(599) Walton, K. S.; Snurr, R. Q. Applicability of the BET Method for Determining Surface Areas of Microporous Metal−Organic Frameworks. *J. Am. Chem. Soc.* **2007**, *129*, 8552−8556.
(600) Marshall, C. R.; Staudhammer, S. A.; Brozek, C. K. Size Control over Metal-Organic Framework Porous Nanocrystals. *Chem. Sci.* **2019**, *10*, 9396−9408.
(601) McCluskey, M. D.; Haller, E. E. *Dopands and Defects in Semiconductors*, 2nd ed.; CRC Press, 2018.
(602) Müller, K.; Fink, K.; Schöttner, L.; Koenig, M.; Heinke, L.; Wöll, C. Defects as Color Centers: The Apparent Color of Metal−Organic Frameworks Containing Cu^{2+} -Based Paddle-Wheel Units. *ACS Appl. Mater. Interfaces* **2017**, *9*, 37463−37467.
(603) Sholl, D. S.; Lively, R. P. Defects in Metal−Organic Frameworks: Challenge or Opportunity? *J. Phys. Chem. Lett.* **2015**, *6*, 3437−3444.
(604) Fang, Z.; Bueken, B.; De Vos, D. E.; Fischer, R. A. Defect-Engineered Metal-Organic Frameworks. *Angew. Chem., Int. Ed.* **2015**, *54*, 7234−7254.
(605) Smyth, D. M. *The Defect Chemistry of Metal Oxides*, 1st ed.; Monographs on the Physics and Chemistry of Materials; Oxford University Press, 2000.
(606) McCluskey, M. D.; Haller, E. E. *Dopants and Defects in Semiconductors*, 2nd ed.; CRC Press.
(607) Shearer, G. C.; Chavan, S.; Ethiraj, J.; Vitillo, J. G.; Svelle, S.; Olsbye, U.; Lamberti, C.; Bordiga, S.; Lillerud, K. P. Tuned to Perfection: Ironing Out the Defects in Metal−Organic Framework UiO-66. *Chem. Mater.* **2014**, *26*, 4068−4071.
(608) Gutov, O. V.; Hevia, M. G.; Escudero-Adán, E. C.; Shafir, A. Metal−Organic Framework (MOF) Defects under Control: Insights into the Missing Linker Sites and Their Implication in the Reactivity of Zirconium-Based Frameworks. *Inorg. Chem.* **2015**, *54*, 8396−8400.
(609) Jiang, Z.-R.; Wang, H.; Hu, Y.; Lu, J.; Jiang, H.-L. Polar Group and Defect Engineering in a Metal-Organic Framework: Synergistic Promotion of Carbon Dioxide Sorption and Conversion. *ChemSusChem* **2015**, *8*, 878−885.
(610) Queisser, H. J. Defects in Semiconductors: Some Fatal, Some Vital. *Science* **1998**, *281*, 945−950.
(611) Lee, S. J.; Doussot, C.; Baux, A.; Liu, L.; Jameson, G. B.; Richardson, C.; Pak, J. J.; Trousselet, F.; Coudert, F.-X.; Telfer, S. G. Multicomponent Metal−Organic Frameworks as Defect-Tolerant Materials. *Chem. Mater.* **2016**, *28*, 368−375.
(612) Sun, L.; Liao, B.; Sheberla, D.; Kraemer, D.; Zhou, J.; Stach, E. A.; Zakharov, D.; Stavila, V.; Talin, A. A.; Ge, Y.; Allendorf, M. D.; Chen, G.; Léonard, F.; Dincă, M. A Microporous and Naturally Nanostructured Thermoelectric Metal-Organic Framework with Ultralow Thermal Conductivity. *Joule* **2017**, *1*, 168−177.
(613) Walsh, A.; Catlow, C. R. A. Photostimulated Reduction Processes in a Titania Hybrid Metal-Organic Framework. *ChemPhysChem* **2010**, *11*, 2341−2344.
(614) Dissegna, S.; Epp, K.; Heinz, W. R.; Kieslich, G.; Fischer, R. A. Defective Metal-Organic Frameworks. *Adv. Mater.* **2018**, *30*, 1704501.
(615) Kozachuk, O.; Luz, I.; Llabrés i Xamena, F. X.; Noei, H.; Kauer, M.; Albada, H. B.; Bloch, E. D.; Marler, B.; Wang, Y.; Muhler, M.; Fischer, R. A. Multifunctional, Defect-Engineered Metal-Organic Frameworks with Ruthenium Centers: Sorption and Catalytic Properties. *Angew. Chem., Int. Ed.* **2014**, *53*, 7058−7062.
(616) Wu, X.; Luo, Y.; Sun, M.; Qian, J.; Cao, Y.; Ai, X.; Yang, H. Low-Defect Prussian Blue Nanocubes as High Capacity and Long Life Cathodes for Aqueous Na-Ion Batteries. *Nano Energy* **2015**, *13*, 117−123.
(617) Goodwin, A. L. Opportunities and Challenges in Understanding Complex Functional Materials. *Nat. Commun.* **2019**, *10*, 4461.
(618) Ruankaew, N.; Yoshida, N.; Phongphanphanee, S. Solvated Lithium Ions in Defective Prussian Blue. *IOP Conf. Ser.: Mater. Sci. Eng.* **2019**, *526*, No. 012032.
(619) Kumar, A.; Yusuf, S. M.; Yakhmi, J. V.; Aswal, D. K.; Debnath, A. K. Study Of Nature Of Structural Defects In A Prussian Blue Type $Cu_{0.73}Mn_{0.77}Fe(CN)_6{\cdot}zH_2O$ Molecular Magnet. *AIP Conf. Proc.* **2010**, *1313*, 218−220.
(620) Yang, D.; Ortuno, M. A.; Bernales, V.; Cramer, C. J.; Gagliardi, L.; Gates, B. C. Structure and Dynamics of Zr_6O_8 Metal-Organic Framework Node Surfaces Probed with Ethanol Dehydration as a Catalytic Test Reaction. *J. Am. Chem. Soc.* **2018**, *140*, 3751−3759.
(621) Cliffe, M. J.; Wan, W.; Zou, X.; Chater, P. A.; Kleppe, A. K.; Tucker, M. G.; Wilhelm, H.; Funnell, N. P.; Coudert, F.-X.; Goodwin, A. L. Correlated Defect Nanoregions in a Metal−Organic Framework. *Nat. Commun.* **2014**, *5*, 4176.
(622) Liu, L.; Chen, Z.; Wang, J.; Zhang, D.; Zhu, Y.; Ling, S.; Huang, K.-W.; Belmabkhout, Y.; Adil, K.; Zhang, Y.; Slater, B.; Eddaoudi, M.; Han, Y. Imaging Defects and Their Evolution in a Metal−Organic Framework at Sub-Unit-Cell Resolution. *Nat. Chem.* **2019**, *11*, 622−628.
(623) Zhang, C.; Han, C.; Sholl, D. S.; Schmidt, J. R. Computational Characterization of Defects in Metal−Organic Frameworks: Spontaneous and Water-Induced Point Defects in ZIF-8. *J. Phys. Chem. Lett.* **2016**, *7*, 459−464.
(624) He, H.; Hashemi, L.; Hu, M.-L.; Morsali, A. The Role of the Counter-Ion in Metal-Organic Frameworks' Chemistry and Applications. *Coord. Chem. Rev.* **2018**, *376*, 319−347.
(625) Svane, K. L.; Bristow, J. K.; Gale, J. D.; Walsh, A. Vacancy Defect Configurations in the Metal−Organic Framework UiO-66: Energetics and Electronic Structure. *J. Mater. Chem. A* **2018**, *6*, 8507−8513.
(626) Bristow, J. K.; Svane, K. L.; Tiana, D.; Skelton, J. M.; Gale, J. D.; Walsh, A. Free Energy of Ligand Removal in the Metal−Organic Framework UiO-66. *J. Phys. Chem. C* **2016**, *120*, 9276−9281.
(627) Marreiros, J.; Caratelli, C.; Hajek, J.; Krajnc, A.; Fleury, G.; Bueken, B.; De Vos, D. E.; Mali, G.; Roeffaers, M. B. J.; Van Speybroeck, V.; Ameloot, R. Active Role of Methanol in Post-Synthetic Linker Exchange in the Metal−Organic Framework UiO-66. *Chem. Mater.* **2019**, *31*, 1359−1369.
(628) Cai, G.; Jiang, H.-L. A Modulator-Induced Defect-Formation Strategy to Hierarchically Porous Metal-Organic Frameworks with High Stability. *Angew. Chem., Int. Ed.* **2017**, *56*, 563−567.
(629) Wu, H.; Chua, Y. S.; Krungleviciute, V.; Tyagi, M.; Chen, P.; Yildirim, T.; Zhou, W. Unusual and Highly Tunable Missing-Linker Defects in Zirconium Metal−Organic Framework UiO-66 and Their Important Effects on Gas Adsorption. *J. Am. Chem. Soc.* **2013**, *135*, 10525−10532.

https://dx.doi.org/10.1021/acs.chemrev.0c00148
Chem. Rev. 2020, 120, 8641−8715

(630) Jiao, Y.; Liu, Y.; Zhu, G.; Hungerford, J. T.; Bhattacharyya, S.; Lively, R. P.; Sholl, D. S.; Walton, K. S. Heat-Treatment of Defective UiO-66 from Modulated Synthesis: Adsorption and Stability Studies. *J. Phys. Chem. C* **2017**, *121*, 23471−23479.
(631) Vandichel, M.; Hajek, J.; Vermoortele, F.; Waroquier, M.; De Vos, D. E.; Van Speybroeck, V. Active Site Engineering in UiO-66 Type Metal−Organic Frameworks by Intentional Creation of Defects: A Theoretical Rationalization. *CrystEngComm* **2015**, *17*, 395−406.
(632) Vandichel, M.; Hajek, J.; Ghysels, A.; De Vos, A.; Waroquier, M.; Van Speybroeck, V. Water Coordination and Dehydration Processes in Defective UiO-66 Type Metal Organic Frameworks. *CrystEngComm* **2016**, *18*, 7056−7069.
(633) Musho, T.; Li, J.; Wu, N. Band Gap Modulation of Functionalized Metal−Organic Frameworks. *Phys. Chem. Chem. Phys.* **2014**, *16*, 23646−23653.
(634) Yasin, A. S.; Li, J.; Wu, N.; Musho, T. Study of the Inorganic Substitution in a Functionalized UiO-66 Metal−Organic Framework. *Phys. Chem. Chem. Phys.* **2016**, *18*, 12748−12754.
(635) Li, J.; Liu, Y.; Ai, Y.; Alsaedi, A.; Hayat, T.; Wang, X. Combined Experimental and Theoretical Investigation on Selective Removal of Mercury Ions by Metal Organic Frameworks Modified with Thiol Groups. *Chem. Eng. J.* **2018**, *354*, 790−801.
(636) You, W.; Liu, Y.; Howe, J. D.; Tang, D.; Sholl, D. S. Tuning Binding Tendencies of Small Molecules in Metal−Organic Frameworks with Open Metal Sites by Metal Substitution and Linker Functionalization. *J. Phys. Chem. C* **2018**, *122*, 27486−27494.
(637) Maihom, T.; Wannakao, S.; Boekfa, B.; Limtrakul, J. Production of Formic Acid via Hydrogenation of CO2 over a Copper-Alkoxide-Functionalized MOF: A Mechanistic Study. *J. Phys. Chem. C* **2013**, *117*, 17650−17658.
(638) Braglia, L.; Borfecchia, E.; Lomachenko, K. A.; Bugaev, A. L.; Guda, A. A.; Soldatov, A. V.; Bleken, B. T. L.; Øien-Ødegaard, S.; Olsbye, U.; Lillerud, K. P.; Bordiga, S.; Agostini, G.; Manzoli, M.; Lamberti, C. Tuning Pt and Cu Sites Population inside Functionalized UiO-67 MOF by Controlling Activation Conditions. *Faraday Discuss.* **2017**, *201*, 265−286.
(639) de Oliveira, A.; de Lima, G. F.; De Abreu, H. A. Structural and Electronic Properties of M-MOF-74 (M = Mg, Co or Mn). *Chem. Phys. Lett.* **2018**, *691*, 283−290.
(640) Sun, Y.; Zhuo, Z.; Wu, X. Ferroelectricity and Magnetism in Metal-Formate Frameworks of $[NH_4][M(HCOO)_3]$ (M = Sc to Zn): A First-Principles Study. *RSC Adv.* **2016**, *6*, 113234−113239.
(641) Howe, J. D.; Morelock, C. R.; Jiao, Y.; Chapman, K. W.; Walton, K. S.; Sholl, D. S. Understanding Structure, Metal Distribution, and Water Adsorption in Mixed-Metal MOF-74. *J. Phys. Chem. C* **2017**, *121*, 627−635.
(642) Wu, Y.; Chen, H.; Xiao, J.; Liu, D.; Liu, Z.; Qian, Y.; Xi, H. Adsorptive Separation of Methanol−Acetone on Isostructural Series of Metal−Organic Frameworks M-BTC (M = Ti, Fe, Cu, Co, Ru, Mo): A Computational Study of Adsorption Mechanisms and Metal-Substitution Impacts. *ACS Appl. Mater. Interfaces* **2015**, *7*, 26930−26940.
(643) Trousselet, F.; Archereau, A.; Boutin, A.; Coudert, F.-X. Heterometallic Metal−Organic Frameworks of MOF-5 and UiO-66 Families: Insight from Computational Chemistry. *J. Phys. Chem. C* **2016**, *120*, 24885−24894.
(644) Heinz, W. R.; Kratky, T.; Drees, M.; Wimmer, A.; Tomanec, O.; Günther, S.; Schuster, M.; Fischer, R. A. Mixed Precious-Group Metal−Organic Frameworks: A Case Study of the HKUST-1 Analogue $[Rux Rh_3-x(BTC)_2]$. *Dalton Trans.* **2019**, *48*, 12031−12039.
(645) Hendrickx, K.; Joos, J. J.; De Vos, A.; Poelman, D.; Smet, P. F.; Van Speybroeck, V.; Van Der Voort, P.; Lejaeghere, K. Exploring Lanthanide Doping in UiO-66: A Combined Experimental and Computational Study of the Electronic Structure. *Inorg. Chem.* **2018**, *57*, 5463−5474.
(646) Sava Gallis, D. F.; Parkes, M. V.; Greathouse, J. A.; Zhang, X.; Nenoff, T. M. Enhanced O2 Selectivity versus N2 by Partial Metal Substitution in Cu-BTC. *Chem. Mater.* **2015**, *27*, 2018−2025.
(647) Lee, S.; Choe, W. Postsynthetic Linker Exchange in Metal-Organic Frameworks. In *Series on Chemistry, Energy and the Environment*; World Scientific, 2018; Vol. *02*, pp 143−182.
(648) Kassie, A. A.; Duan, P.; McClure, E. T.; Schmidt-Rohr, K.; Woodward, P. M.; Wade, C. R. Postsynthetic Metal Exchange in a Metal−Organic Framework Assembled from Co(III) Diphosphine Pincer Complexes. *Inorg. Chem.* **2019**, *58*, 3227−3236.
(649) Yin, Z.; Wan, S.; Yang, J.; Kurmoo, M.; Zeng, M.-H. Recent Advances in Post-Synthetic Modification of Metal−Organic Frameworks: New Types and Tandem Reactions. *Coord. Chem. Rev.* **2019**, *378*, 500−512.
(650) Botas, J. A.; Calleja, G.; Sánchez-Sánchez, M.; Orcajo, M. G. Effect of Zn/Co Ratio in MOF-74 Type Materials Containing Exposed Metal Sites on Their Hydrogen Adsorption Behaviour and on Their Band Gap Energy. *Int. J. Hydrogen Energy* **2011**, *36*, 10834−10844.
(651) Villajos, J. A.; Orcajo, G.; Martos, C.; Botas, J. Á.; Villacañas, J.; Calleja, G. Co/Ni Mixed-Metal Sited MOF-74 Material as Hydrogen Adsorbent. *Int. J. Hydrogen Energy* **2015**, *40*, 5346−5352.
(652) Kahr, J.; Morris, R. E.; Wright, P. A. Post-Synthetic Incorporation of Nickel into CPO-27(Mg) to Give Materials with Enhanced Permanent Porosity. *CrystEngComm* **2013**, *15*, 9779−9786.
(653) DeCoste, J. B.; Browe, M. A.; Wagner, G. W.; Rossin, J. A.; Peterson, G. W. Removal of Chlorine Gas by an Amine Functionalized Metal−Organic Framework via Electrophilic Aromatic Substitution. *Chem. Commun.* **2015**, *51*, 12474−12477.
(654) Tovar, T. M.; Iordanov, I.; Sava Gallis, D. F. S.; Decoste, J. B. Enhancing Van Der Waals Interactions of Functionalized UiO-66 with Non-polar Adsorbates: The Unique Effect of Para Hydroxyl Groups. *Chem. - Eur. J.* **2018**, *24*, 1931−1937.
(655) De Vos, A.; Hendrickx, K.; Van Der Voort, P.; Van Speybroeck, V.; Lejaeghere, K. Missing Linkers: An Alternative Pathway to UiO-66 Electronic Structure Engineering. *Chem. Mater.* **2017**, *29*, 3006−3019.
(656) Talin, A. A.; Centrone, A.; Ford, A. C.; Foster, M. E.; Stavila, V.; Haney, P.; Kinney, R. A.; Szalai, V.; El Gabaly, F.; Yoon, H. P.; Léonard, F.; Allendorf, M. D. Tunable Electrical Conductivity in Metal-Organic Framework Thin-Film Devices. *Science* **2014**, *343*, 66−69.
(657) Hendon, C. H.; Walsh, A. Chemical Principles Underpinning the Performance of the Metal−Organic Framework HKUST-1. *Chem. Sci.* **2015**, *6*, 3674−3683.
(658) Schneider, C.; Ukaj, D.; Koerver, R.; Talin, A. A.; Kieslich, G.; Pujari, S. P.; Zuilhof, H.; Janek, J.; Allendorf, M. D.; Fischer, R. A. High Electrical Conductivity and High Porosity in a Guest@MOF Material: Evidence of TCNQ Ordering within Cu_3BTC_2 Micropores. *Chem. Sci.* **2018**, *9*, 7405−7412.
(659) Foster, M. E.; Sohlberg, K.; Spataru, C. D.; Allendorf, M. D. Proposed Modification of the Graphene Analogue $Ni_3(HITP)_2$ To Yield a Semiconducting Material. *J. Phys. Chem. C* **2016**, *120*, 15001−15008.
(660) Saouma, C. T.; Richard, S.; Smolders, S.; Delley, M. F.; Ameloot, R.; Vermoortele, F.; De Vos, D. E.; Mayer, J. M. Bulk-to-Surface Proton-Coupled Electron Transfer Reactivity of the Metal−Organic Framework MIL-125. *J. Am. Chem. Soc.* **2018**, *140*, 16184−16189.
(661) Momeni, M. R.; Cramer, C. J. Structural Characterization of Pristine and Defective $[Zr_{12}(\mu_3\text{-}O)_8(\mu_3\text{-}OH)_8(\mu_2\text{-}OH)_6]^{18+}$ Double-Node Metal−Organic Framework and Predicted Applications for Single-Site Catalytic Hydrolysis of Sarin. *Chem. Mater.* **2018**, *30*, 4432−4439.
(662) Thornton, A. W.; Babarao, R.; Jain, A.; Trousselet, F.; Coudert, F.-X. Defects in Metal−Organic Frameworks: A Compromise between Adsorption and Stability? *Dalton Trans* **2016**, *45*, 4352−4359.
(663) Wei, R.; Gaggioli, C. A.; Li, G.; Islamoglu, T.; Zhang, Z.; Yu, P.; Farha, O. K.; Cramer, C. J.; Gagliardi, L.; Yang, D.; Gates, B. C. Tuning the Properties of Zr6O8 Nodes in the Metal Organic Framework UiO-66 by Selection of Node-Bound Ligands and Linkers. *Chem. Mater.* **2019**, *31*, 1655−1663.
(664) Bueken, B.; Van Velthoven, N.; Krajnc, A.; Smolders, S.; Taulelle, F.; Mellot-Draznieks, C.; Mali, G.; Bennett, T. D.; De Vos, D. Tackling the Defect Conundrum in UiO-66: A Mixed-Linker Approach

to Engineering Missing Linker Defects. *Chem. Mater.* **2017**, *29*, 10478−10486.
(665) Momeni, M. R.; Cramer, C. J. Computational Screening of Roles of Defects and Metal Substitution on Reactivity of Different Single- vs Double-Node Metal−Organic Frameworks for Sarin Decomposition. *J. Phys. Chem. C* **2019**, *123*, 15157−15165.
(666) Harvey, J. A.; Greathouse, J. A.; Sava Gallis, D. F. Defect and Linker Effects on the Binding of Organophosphorous Compounds in UiO-66 and Rare-Earth MOFs. *J. Phys. Chem. C* **2018**, *122*, 26889−26896.
(667) Lin, S.; Bediako, J. K.; Song, M.-H.; Kim, J.-A.; Cho, C.-W.; Zhao, Y.; Choi, J.-W.; Yun, Y.-S. Effective Recovery of Pt(IV) from Acidic Solution by a Defective Metal−Organic Frameworks Using Central Composite Design for Synthesis. *ACS Sustainable Chem. Eng.* **2019**, *7*, 7510−7518.
(668) Cliffe, M. J.; Castillo-Martínez, E.; Wu, Y.; Lee, J.; Forse, A. C.; Firth, F. C. N.; Moghadam, P. Z.; Fairen-Jimenez, D.; Gaultois, M. W.; Hill, J. A.; Magdysyuk, O. V.; Slater, B.; Goodwin, A. L.; Grey, C. P. Metal−Organic Nanosheets Formed via Defect-Mediated Transformation of a Hafnium Metal−Organic Framework. *J. Am. Chem. Soc.* **2017**, *139*, 5397−5404.
(669) Rodríguez-Albelo, L. M.; López-Maya, E.; Hamad, S.; Ruiz-Salvador, A. R.; Calero, S.; Navarro, J. A. R. Selective Sulfur Dioxide Adsorption on Crystal Defect Sites on an Isoreticular Metal Organic Framework Series. *Nat. Commun.* **2017**, *8*, 14457.
(670) Choi, J.; Lin, L.-C.; Grossman, J. C. Role of Structural Defects in the Water Adsorption Properties of MOF-801. *J. Phys. Chem. C* **2018**, *122*, 5545−5552.
(671) Qi, K.; Hou, R.; Zaman, S.; Qiu, Y.; Xia, B. Y.; Duan, H. Construction of Metal−Organic Framework/Conductive Polymer Hybrid for All-Solid-State Fabric Supercapacitor. *ACS Appl. Mater. Interfaces* **2018**, *10*, 18021−18028.
(672) Yan, Y.; Gu, P.; Zheng, S.; Zheng, M.; Pang, H.; Xue, H. Facile Synthesis of an Accordion-like Ni-MOF Superstructure for High-Performance Flexible Supercapacitors. *J. Mater. Chem. A* **2016**, *4*, 19078−19085.
(673) Miner, E. M.; Gul, S.; Ricke, N. D.; Pastor, E.; Yano, J.; Yachandra, V. K.; Van Voorhis, T.; Dincă, M. Mechanistic Evidence for Ligand-Centered Electrocatalytic Oxygen Reduction with the Conductive MOF Ni_3(Hexaiminotriphenylene)$_2$. *ACS Catal.* **2017**, *7*, 7726−7731.
(674) Sheberla, D.; Bachman, J. C.; Elias, J. S.; Sun, C.-J.; Shao-Horn, Y.; Dincă, M. Conductive MOF Electrodes for Stable Supercapacitors with High Areal Capacitance. *Nat. Mater.* **2017**, *16*, 220−224.
(675) Lu, X. F.; Xia, B. Y.; Zang, S.-Q.; Lou, X. W. D. Metal-Organic Frameworks Based Electrocatalysts for the Oxygen Reduction Reaction. *Angew. Chem., Int. Ed.* **2020**, *59*, 4634−4650.
(676) Aiyappa, H. B.; Masa, J.; Andronescu, C.; Muhler, M.; Fischer, R. A.; Schuhmann, W. MOFs for Electrocatalysis: From Serendipity to Design Strategies. *Small Methods* **2019**, *3*, 1800415.
(677) Drake, T.; Ji, P.; Lin, W. Site Isolation in Metal−Organic Frameworks Enables Novel Transition Metal Catalysis. *Acc. Chem. Res.* **2018**, *51*, 2129−2138.
(678) Hu, Z.; Zhao, D. Metal−Organic Frameworks with Lewis Acidity: Synthesis, Characterization, and Catalytic Applications. *CrystEngComm* **2017**, *19*, 4066−4081.
(679) Li, P.-Z.; Wang, X.-J.; Liu, J.; Lim, J. S.; Zou, R.; Zhao, Y. A Triazole-Containing Metal−Organic Framework as a Highly Effective and Substrate Size-Dependent Catalyst for CO_2 Conversion. *J. Am. Chem. Soc.* **2016**, *138*, 2142−2145.
(680) Oxford, G. A. E.; Snurr, R. Q.; Broadbelt, L. J. Hybrid Quantum Mechanics/Molecular Mechanics Investigation of (Salen)Mn for Use in Metal−Organic Frameworks. *Ind. Eng. Chem. Res.* **2010**, *49*, 10965−10973.
(681) García-García, P.; Müller, M.; Corma, A. MOF Catalysis in Relation to Their Homogeneous Counterparts and Conventional Solid Catalysts. *Chem. Sci.* **2014**, *5*, 2979−3007.
(682) Zheng, S.; Yang, P.; Zhang, F.; Chen, D.-L.; Zhu, W. Pd Nanoparticles Encaged within Amine-Functionalized Metal-Organic Frameworks: Catalytic Activity and Reaction Mechanism in the Hydrogenation of 2,3,5-Trimethylbenzoquinone. *Chem. Eng. J.* **2017**, *328*, 977−987.
(683) Jiang, D.; Fang, G.; Tong, Y.; Wu, X.; Wang, Y.; Hong, D.; Leng, W.; Liang, Z.; Tu, P.; Liu, L.; Xu, K.; Ni, J.; Li, X. Multifunctional Pd@UiO-66 Catalysts for Continuous Catalytic Upgrading of Ethanol to *n*-Butanol. *ACS Catal.* **2018**, *8*, 11973−11978.
(684) Zou, L.; Feng, D.; Liu, T.-F.; Chen, Y.-P.; Yuan, S.; Wang, K.; Wang, X.; Fordham, S.; Zhou, H.-C. A Versatile Synthetic Route for the Preparation of Titanium Metal−Organic Frameworks. *Chem. Sci.* **2016**, *7*, 1063−1069.
(685) Genna, D. T.; Wong-Foy, A. G.; Matzger, A. J.; Sanford, M. S. Heterogenization of Homogeneous Catalysts in Metal−Organic Frameworks via Cation Exchange. *J. Am. Chem. Soc.* **2013**, *135*, 10586−10589.
(686) Bury, W.; Fairen-Jimenez, D.; Lalonde, M. B.; Snurr, R. Q.; Farha, O. K.; Hupp, J. T. Control over Catenation in Pillared Paddlewheel Metal−Organic Framework Materials via Solvent-Assisted Linker Exchange. *Chem. Mater.* **2013**, *25*, 739−744.
(687) Takaishi, S.; DeMarco, E. J.; Pellin, M. J.; Farha, O. K.; Hupp, J. T. Solvent-Assisted Linker Exchange (SALE) and Post-Assembly Metallation in Porphyrinic Metal−Organic Framework Materials. *Chem. Sci.* **2013**, *4*, 1509−1513.
(688) Beloqui Redondo, A.; Morel, F. L.; Ranocchiari, M.; van Bokhoven, J. A. Functionalized Ruthenium−Phosphine Metal−Organic Framework for Continuous Vapor-Phase Dehydrogenation of Formic Acid. *ACS Catal.* **2015**, *5*, 7099−7103.
(689) Wang, Z.; Cohen, S. M. Tandem Modification of Metal−Organic Frameworks by a Postsynthetic Approach. *Angew. Chem.* **2008**, *120*, 4777−4780.
(690) Goesten, M. G.; Juan-Alcañiz, J.; Ramos-Fernandez, E. V.; Sai Sankar Gupta, K. B.; Stavitski, E.; van Bekkum, H.; Gascon, J.; Kapteijn, F. Sulfation of Metal−Organic Frameworks: Opportunities for Acid Catalysis and Proton Conductivity. *J. Catal.* **2011**, *281*, 177−187.
(691) Mondloch, J. E.; Bury, W.; Fairen-Jimenez, D.; Kwon, S.; DeMarco, E. J.; Weston, M. H.; Sarjeant, A. A.; Nguyen, S. T.; Stair, P. C.; Snurr, R. Q.; Farha, O. K.; Hupp, J. T. Vapor-Phase Metalation by Atomic Layer Deposition in a Metal−Organic Framework. *J. Am. Chem. Soc.* **2013**, *135*, 10294−10297.
(692) Manna, K.; Zhang, T.; Lin, W. Postsynthetic Metalation of Bipyridyl-Containing Metal−Organic Frameworks for Highly Efficient Catalytic Organic Transformations. *J. Am. Chem. Soc.* **2014**, *136*, 6566−6569.
(693) Guan, Q.; Wang, B.; Chai, X.; Liu, J.; Gu, J.; Ning, P. Comparison of Pd-UiO-66 and Pd-UiO-66-NH_2 Catalysts Performance for Phenol Hydrogenation in Aqueous Medium. *Fuel* **2017**, *205*, 130−141.
(694) Shen, L.; Wu, W.; Liang, R.; Lin, R.; Wu, L. Highly Dispersed Palladium Nanoparticles Anchored on UiO-66(NH_2) Metal-Organic Framework as a Reusable and Dual Functional Visible-Light-Driven Photocatalyst. *Nanoscale* **2013**, *5*, 9374−9382.
(695) Eyring, H. The Activated Complex in Chemical Reactions. *J. Chem. Phys.* **1935**, *3*, 107.
(696) Bernales, V.; Ortuño, M. A.; Truhlar, D. G.; Cramer, C. J.; Gagliardi, L. Computational Design of Functionalized Metal−Organic Framework Nodes for Catalysis. *ACS Cent. Sci.* **2018**, *4*, 5−19.
(697) Jensen, F. *Introduction to Computational Chemistry*, 2nd ed.; John Wiley & Sons: Chichester, UK, Hoboken, NJ, 2007.
(698) Cruz-Olvera, D.; de la Trinidad Vasquez, A.; Geudtner, G.; Vásquez-Pérez, J. M.; Calaminici, P.; Köster, A. M. Transition-State Searches in Metal Clusters by First-Principle Methods. *J. Phys. Chem. A* **2015**, *119*, 1494−1501.
(699) Wales, D. J. *Energy Landscapes*; Cambridge Molecular Science; Cambridge University Press: Cambridge, UK, New York, 2003.
(700) E, W.; Ren, W.; Vanden-Eijnden, E. String Method for the Study of Rare Events. *Phys. Rev. B: Condens. Matter Mater. Phys.* **2002**, *66*, No. 052301.

https://dx.doi.org/10.1021/acs.chemrev.0c00148
Chem. Rev. 2020, 120, 8641−8715

(701) E, W.; Ren, W.; Vanden-Eijnden, E. Simplified and Improved String Method for Computing the Minimum Energy Paths in Barrier-Crossing Events. *J. Chem. Phys.* **2007**, *126*, 164103.
(702) Peters, B.; Heyden, A.; Bell, A. T.; Chakraborty, A. A Growing String Method for Determining Transition States: Comparison to the Nudged Elastic Band and String Methods. *J. Chem. Phys.* **2004**, *120*, 7877−7886.
(703) Henkelman, G.; Jónsson, H. Improved Tangent Estimate in the Nudged Elastic Band Method for Finding Minimum Energy Paths and Saddle Points. *J. Chem. Phys.* **2000**, *113*, 9978−9985.
(704) Henkelman, G.; Uberuaga, B. P.; Jónsson, H. A Climbing Image Nudged Elastic Band Method for Finding Saddle Points and Minimum Energy Paths. *J. Chem. Phys.* **2000**, *113*, 9901−9904.
(705) Trygubenko, S. A.; Wales, D. J. A Doubly Nudged Elastic Band Method for Finding Transition States. *J. Chem. Phys.* **2004**, *120*, 2082−2094.
(706) Jonsson, H.; Mills, G.; Jacobsen, K. W. Classical and Quantum Dynamics in Condensed Phase Simulations. In *Classical and Quantum Dynamics in Condensed Phase Simulations*; World Scientific: Singapore, 1998; pp 385−404.
(707) Ulissi, Z. W.; Medford, A. J.; Bligaard, T.; Nørskov, J. K. To Address Surface Reaction Network Complexity Using Scaling Relations Machine Learning and DFT Calculations. *Nat. Commun.* **2017**, *8*, 14621.
(708) Ji, Z.; Li, J.-Q. Density Functional Study of CO Oxidation on Pt and PtMo. *Chem. Phys. Lett.* **2006**, *424*, 111−114.
(709) Lee, D. H.; Xu, J.; Meng, Y. S. An Advanced Cathode for Na-Ion Batteries with High Rate and Excellent Structural Stability. *Phys. Chem. Chem. Phys.* **2013**, *15*, 3304−3312.
(710) Rong, Z.; Malik, R.; Canepa, P.; Sai Gautam, G.; Liu, M.; Jain, A.; Persson, K.; Ceder, G. Materials Design Rules for Multivalent Ion Mobility in Intercalation Structures. *Chem. Mater.* **2015**, *27*, 6016−6021.
(711) Eames, C.; Frost, J. M.; Barnes, P. R. F.; O'Regan, B. C.; Walsh, A.; Islam, M. S. Ionic Transport in Hybrid Lead Iodide Perovskite Solar Cells. *Nat. Commun.* **2015**, *6*, 7497.
(712) Vilhelmsen, L. B.; Walton, K. S.; Sholl, D. S. Structure and Mobility of Metal Clusters in MOFs: Au, Pd, and AuPd Clusters in MOF-74. *J. Am. Chem. Soc.* **2012**, *134*, 12807−12816.
(713) Ming, Y.; Kumar, N.; Siegel, D. J. Water Adsorption and Insertion in MOF-5. *ACS Omega* **2017**, *2*, 4921−4928.
(714) Li, Y.; Wang, X.; Xu, D.; Chung, J. D.; Kaviany, M.; Huang, B. H_2O Adsorption/Desorption in MOF-74: *Ab Initio* Molecular Dynamics and Experiments. *J. Phys. Chem. C* **2015**, *119*, 13021−13031.
(715) Ren, W.; Vanden-Eijnden, E. A Climbing String Method for Saddle Point Search. *J. Chem. Phys.* **2013**, *138*, 134105.
(716) Tian, Y.; Xu, X.; Wu, J. Thermodynamic Route to Efficient Prediction of Gas Diffusivity in Nanoporous Materials. *Langmuir* **2017**, *33*, 11797−11803.
(717) Zhou, M.; Tian, Y.; Fei, W.; Wu, J. Fractionation of Isotopic Methanes with Metal−Organic Frameworks. *J. Phys. Chem. C* **2019**, *123*, 7397−7407.
(718) Zhou, M.; Vassallo, A.; Wu, J. Toward the Inverse Design of MOF Membranes for Efficient D_2/H_2 Separation by Combination of Physics-Based and Data-Driven Modeling. *J. Membr. Sci.* **2020**, *598*, 117675.
(719) Smidstrup, S.; Pedersen, A.; Stokbro, K.; Jónsson, H. Improved Initial Guess for Minimum Energy Path Calculations. *J. Chem. Phys.* **2014**, *140*, 214106.
(720) Maragakis, P.; Andreev, S. A.; Brumer, Y.; Reichman, D. R.; Kaxiras, E. Adaptive Nudged Elastic Band Approach for Transition State Calculation. *J. Chem. Phys.* **2002**, *117*, 4651−4658.
(721) Sheppard, D.; Terrell, R.; Henkelman, G. Optimization Methods for Finding Minimum Energy Paths. *J. Chem. Phys.* **2008**, *128*, 134106.
(722) Torrisi, A.; Mellot-Draznieks, C.; Bell, R. G. Impact of Ligands on CO_2 Adsorption in Metal-Organic Frameworks: First Principles Study of the Interaction of CO_2 with Functionalized Benzenes. I. Inductive Effects on the Aromatic Ring. *J. Chem. Phys.* **2009**, *130*, 194703.
(723) Lee, K.; Kim, Y.-H.; Sun, Y. Y.; West, D.; Zhao, Y.; Chen, Z.; Zhang, S. B. Hole-Mediated Hydrogen Spillover Mechanism in Metal-Organic Frameworks. *Phys. Rev. Lett.* **2010**, *104*, 236101.
(724) Perdew, J. P.; Burke, K.; Ernzerhof, M. Generalized Gradient Approximation Made Simple. *Phys. Rev. Lett.* **1996**, *77*, 3865−3868.
(725) Grimme, S. Semiempirical GGA-Type Density Functional Constructed with a Long-Range Dispersion Correction. *J. Comput. Chem.* **2006**, *27*, 1787−1799.
(726) Simons, J.; Nichols, J. Strategies for Walking on Potential Energy Surfaces Using Local Quadratic Approximations. *Int. J. Quantum Chem.* **1990**, *38*, 263−276.
(727) Nichols, J.; Taylor, H.; Schmidt, P.; Simons, J. Walking on Potential Energy Surfaces. *J. Chem. Phys.* **1990**, *92*, 340.
(728) Baker, J. An Algorithm for the Location of Transition States. *J. Comput. Chem.* **1986**, *7*, 385−395.
(729) Wales, D. J. Finding Saddle Points for Clusters. *J. Chem. Phys.* **1989**, *91*, 7002−7010.
(730) Banerjee, A.; Adams, N.; Simons, J.; Shepard, R. Search for Stationary Points on Surfaces. *J. Phys. Chem.* **1985**, *89*, 52−57.
(731) Cramer, C. J. *Essentials of Computational Chemistry: Theories and Models*, 2nd ed..; Wiley: West Sussex, UK, 2004.
(732) Cerjan, C. J.; Miller, W. H. On Finding Transition States. *J. Chem. Phys.* **1981**, *75*, 2800−2806.
(733) Henkelman, G.; Jónsson, H. A Dimer Method for Finding Saddle Points on High Dimensional Potential Surfaces Using Only First Derivatives. *J. Chem. Phys.* **1999**, *111*, 7010−7022.
(734) Henkelman, G.; Jónsson, H. A Dimer Method for Finding Saddle Points on High Dimensional Potential Surfaces Using Only First Derivatives. *J. Chem. Phys.* **1999**, *111*, 7010−7022.
(735) Sun, D.; Liu, W.; Fu, Y.; Fang, Z.; Sun, F.; Fu, X.; Zhang, Y.; Li, Z. Noble Metals Can Have Different Effects on Photocatalysis Over Metal-Organic Frameworks (MOFs): A Case Study on M/NH_2-MIL-125(Ti) (M = Pt and Au). *Chem. - Eur. J.* **2014**, *20*, 4780−4788.
(736) Heyden, A.; Bell, A. T.; Keil, F. J. Efficient Methods for Finding Transition States in Chemical Reactions: Comparison of Improved Dimer Method and Partitioned Rational Function Optimization Method. *J. Chem. Phys.* **2005**, *123*, 224101.
(737) Frisch, M. J.; Trucks, G. W.; Schlegel, H. B.; Scuseria, G. E.; Robb, M. A.; Cheeseman, J. R.; Scalmani, G.; Barone, V.; Petersson, G. A.; Nakatsuji, H.; Li, X.; Caricato, M.; Marenich, A.; Bloino, J.; Janesko, B. G.; Gomperts, R.; Mennucci, B.; Hratchian, H. P.; Ortiz, J. V.; Izmaylov, A. F.; Sonnenberg, J. L.; Williams-Young, D., Ding, F.; Lipparini, F.; Egidi, F.; Goings, J.; Peng, B.; Petrone, A.; Henderson, T.; Ranasinghe, D.; Zakrzewski, V. G.; Gao, J.; Rega, N.; Zheng, G.; Liang, W.; Hada, M.; Ehara, M.; Toyota, K.; Fukuda, R.; Hasegawa, J.; Ishida, M.; Nakajima, T.; Honda, Y.; Kitao, O.; Nakai, H.; Vreven, T.; Throssell, K.; Montgomery, J. A., Jr.; Peralta, J. E.; Ogliaro, F.; Bearpark, M.; Heyd, J. J.; Brothers, E.; Kudin, K. N.; Staroverov, V. N.; Keith, T.; Kobayashi, R.; Normand, J.; Raghavachari, K.; Rendell, A.; Burant, J. C.; Iyengar, S. S.; Tomasi, J.; Cossi, M.; Millam, J. M.; Klene, M.; Adamo, C.; Cammi, R.; Ochterski, J. W.; Martin, R. L.; Morokuma, K.; Farkas, O.; Foresman, J. B.; Fox, D. J., *Gaussian 09*, revision A.02; Gaussian, Inc.: Wallingford CT, 2016.
(738) Peng, C.; Bernhard Schlegel, H. Combining Synchronous Transit and Quasi-Newton Methods to Find Transition States. *Isr. J. Chem.* **1993**, *33*, 449−454.
(739) Schlegel, H. B. Optimization of Equilibrium Geometries and Transition Structures. *J. Comput. Chem.* **1982**, *3*, 214−218.
(740) Halgren, T. A.; Lipscomb, W. N. The Synchronous-Transit Method for Determining Reaction Pathways and Locating Molecular Transition States. *Chem. Phys. Lett.* **1977**, *49*, 225−232.
(741) Baker, J.; Hehre, W. J. Geometry Optimization in Cartesian Coordinates: The End of TheZ-Matrix? *J. Comput. Chem.* **1991**, *12*, 606−610.
(742) Foresman, J. B.; Frisch, A. *Exploring Chemistry with Electronic Structure Methods*, 3rd ed.; Gaussian, Inc: Wallingford, CT, 2015.

https://dx.doi.org/10.1021/acs.chemrev.0c00148
Chem. Rev. 2020, 120, 8641−8715

(743) Li, X.; Cheetham, A. K.; Jiang, J. CO2 Cycloaddition with Propylene Oxide to Form Propylene Carbonate on a Copper Metal-Organic Framework: A Density Functional Theory Study. *Mol. Catal.* **2019**, *463*, 37−44.
(744) Barona, M.; Ahn, S.; Morris, W.; Hoover, W.; Notestein, J. M.; Farha, O. K.; Snurr, R. Q. Computational Predictions and Experimental Validation of Alkane Oxidative Dehydrogenation by Fe_2M MOF Nodes. *ACS Catal.* **2020**, *10*, 1460−1469.
(745) Rosen, A. S.; Notestein, J. M.; Snurr, R. Q. Identifying Promising Metal−Organic Frameworks for Heterogeneous Catalysis via High-throughput Periodic Density Functional Theory. *J. Comput. Chem.* **2019**, *40*, 1305−1318.
(746) Zong, S.; Zhang, Y.; Lu, N.; Ma, P.; Wang, J.; Shi, X.-R. A DFT Screening of M-HKUST-1 MOFs for Nitrogen-Containing Compounds Adsorption. *Nanomaterials* **2018**, *8*, 958.
(747) Latimer, A. A.; Kulkarni, A. R.; Aljama, H.; Montoya, J. H.; Yoo, J. S.; Tsai, C.; Abild-Pedersen, F.; Studt, F.; Nørskov, J. K. Understanding Trends in C−H Bond Activation in Heterogeneous Catalysis. *Nat. Mater.* **2017**, *16*, 225−229.
(748) Maihom, T.; Choomwattana, S.; Khongpracha, P.; Probst, M.; Limtrakul, J. Formaldehyde Encapsulated in Lithium-Decorated Metal-Organic Frameworks: A Density Functional Theory Study. *ChemPhysChem* **2012**, *13*, 245−249.
(749) Yoshizawa, K.; Shiota, Y.; Yamabe, T. Intrinsic Reaction Coordinate Analysis of the Conversion of Methane to Methanol by an Iron−Oxo Species: A Study of Crossing Seams of Potential Energy Surfaces. *J. Chem. Phys.* **1999**, *111*, 538−545.
(750) Fukui, K. Formulation of the Reaction Coordinate. *J. Phys. Chem.* **1970**, *74*, 4161−4163.
(751) Pechukas, P. On Simple Saddle Points of a Potential Surface, the Conservation of Nuclear Symmetry along Paths of Steepest Descent, and the Symmetry of Transition States. *J. Chem. Phys.* **1976**, *64*, 1516−1521.
(752) Taketsugu, T.; Gordon, M. S. Dynamic Reaction Path Analysis Based on an Intrinsic Reaction Coordinate. *J. Chem. Phys.* **1995**, *103*, 10042−10049.
(753) Kozuch, S.; Shaik, S. How to Conceptualize Catalytic Cycles? The Energetic Span Model. *Acc. Chem. Res.* **2011**, *44*, 101−110.
(754) Kozuch, S.; Martin, J. M. L. The Rate-Determining Step Is Dead. Long Live the Rate-Determining State! *ChemPhysChem* **2011**, *12*, 1413−1418.
(755) Murdoch, J. R. What Is the Rate-Limiting Step of a Multistep Reaction? *J. Chem. Educ.* **1981**, *58*, 32.
(756) Amatore, C.; Jutand, A. Mechanistic and Kinetic Studies of Palladium Catalytic Systems. *J. Organomet. Chem.* **1999**, *576*, 254−278.
(757) Kozuch, S. A Refinement of Everyday Thinking: The Energetic Span Model for Kinetic Assessment of Catalytic Cycles: Energetic Span, a Refinement of Everyday Thinking. *WIREs Comp. Mol. Sci.* **2012**, *2*, 795−815.
(758) Dumesic, J. A., Huber, G. W.; Boudart, M. Principles of Heterogeneous Catalysis. In *Handbook of Heterogeneous Catalysis*; Ertl, G., Knözinger, H., Schüth, F.. Weitkamp, J., Eds.; Wiley, 2008.
(759) Keil, F. J. Complexities in Modeling of Heterogeneous Catalytic Reactions. *Comp. Math. Appl.* **2013**, *65*, 1674−1697.
(760) Pollak, E.; Child, M. S.; Pechukas, P. Classical Transition State Theory: A Lower Bound to the Reaction Probability. *J. Chem. Phys.* **1980**, *72*, 1669−1678.
(761) Truhlar, D. G.; Garrett, B. C. Variational Transition-State Theory. *Acc. Chem. Res.* **1980**, *13*, 440−448.
(762) Piletic, I. R.; Edney, E. O.; Bartolotti, L. J. Barrierless Reactions with Loose Transition States Govern the Yields and Lifetimes of Organic Nitrates Derived from Isoprene. *J. Phys. Chem. A* **2017**, *121*, 8306−8321.
(763) Bao, J. L.; Truhlar, D. G. Variational Transition State Theory: Theoretical Framework and Recent Developments. *Chem. Soc. Rev.* **2017**, *46*, 7548−7596.
(764) Nørskov, J. K.; Bligaard, T.; Rossmeisl, J.; Christensen, C. H. Towards the Computational Design of Solid Catalysts. *Nat. Chem.* **2009**, *1*, 37−46.
(765) Studt, F.; Abild-Pedersen, F.; Bligaard, T.; Sorensen, R. Z.; Christensen, C. H.; Norskov, J. K. Identification of Non-Precious Metal Alloy Catalysts for Selective Hydrogenation of Acetylene. *Science* **2008**, *320*, 1320−1322.
(766) Norskov, J. K.; Abild-Pedersen, F.; Studt, F.; Bligaard, T. Density Functional Theory in Surface Chemistry and Catalysis. *Proc. Natl. Acad. Sci. U. S. A.* **2011**, *108*, 937−943.
(767) Nilsson, A.; Pettersson, L. G. M.; Hammer, B.; Bligaard, T.; Christensen, C. H.; Nørskov, J. K. The Electronic Structure Effect in Heterogeneous Catalysis. *Catal. Lett.* **2005**, *100*, 111−114.
(768) Gajdo, M.; Eichler, A.; Hafner, J. CO Adsorption on Close-Packed Transition and Noble Metal Surfaces: Trends from *Ab Initio* Calculations. *J. Phys.: Condens. Matter* **2004**, *16*, 1141−1164.
(769) Nanba, Y.; Koyama, M. NO Adsorption on 4d and 5d Transition-Metal (Rh, Pd, Ag, Ir, and Pt) Nanoparticles: Density Functional Theory Study and Supervised Learning. *J. Phys. Chem. C* **2019**, *123*, 28114−28122.
(770) Nørskov, J. K.; Studt, F.; Abild-Pedersen, F.; Bligaard, T. *Fundamental Concepts in Heterogeneous Catalysis*; Wiley: Hoboken, NJ, 2015.
(771) Mao, X.; Ling, C.; Tang, C.; Yan, C.; Zhu, Z.; Du, A. Predicting a New Class of Metal-Organic Frameworks as Efficient Catalyst for Bi-Functional Oxygen Evolution/Reduction Reactions. *J. Catal.* **2018**, *367*, 206−211.
(772) Abild-Pedersen, F.; Greeley, J.; Studt, F.; Rossmeisl, J.; Munter, T. R.; Moses, P. G.; Skúlason, E.; Bligaard, T.; Nørskov, J. K. Scaling Properties of Adsorption Energies for Hydrogen-Containing Molecules on Transition-Metal Surfaces. *Phys. Rev. Lett.* **2007**, *99*, No. 016105.
(773) Rosen, A. S.; Notestein, J. M.; Snurr, R. Q. Structure−Activity Relationships That Identify Metal−Organic Framework Catalysts for Methane Activation. *ACS Catal.* **2019**, *9*, 3576−3587.
(774) Dhakshinamoorthy, A.; Opanasenko, M.; Čejka, J.; Garcia, H. Metal Organic Frameworks as Heterogeneous Catalysts for the Production of Fine Chemicals. *Catal. Sci. Technol.* **2013**, *3*, 2509−2540.
(775) Liu, M.; Wu, J.; Hou, H. Metal−Organic Framework (MOF)-Based Materials as Heterogeneous Catalysts for C−H Bond Activation. *Chem. - Eur. J.* **2018**, *25*, 2935−2948.
(776) Doonan, C. J.; Sumby, C. J. Metal−Organic Framework Catalysis. *CrystEngComm* **2017**, *19*, 4044−4048.
(777) Borboudakis, G.; Stergiannakos, T.; Frysali, M.; Klontzas, E.; Tsamardinos, I.; Froudakis, G. E. Chemically Intuited, Large-Scale Screening of MOFs by Machine Learning Techniques. *npj Comp. Mater.* **2017**, *3*, 40.
(778) Butler, K. T.; Davies, D. W.; Cartwright, H.; Isayev, O.; Walsh, A. Machine Learning for Molecular and Materials Science. *Nature* **2018**, *559*, 547−555.
(779) Schütt, K. T.; Gastegger, M.; Tkatchenko, A.; Müller, K.-R.; Maurer, R. J. Unifying Machine Learning and Quantum Chemistry with a Deep Neural Network for Molecular Wavefunctions. *Nat. Commun.* **2019**, *10*, 5024.
(780) Sanchez-Lengeling, B.; Wei, J. N.; Lee, B. K.; Gerkin, R. C.; Aspuru-Guzik, A.; Wiltschko, A. B. Machine Learning for Scent: Learning Generalizable Perceptual Representations of Small Molecules. *arXiv:1910.10685 [physics, stat]*, **2019**.
(781) Noh, J.; Kim, J.; Stein, H. S.; Sanchez-Lengeling, B.; Gregoire, J. M.; Aspuru-Guzik, A.; Jung, Y. Inverse Design of Solid-State Materials via a Continuous Representation. *Matter* **2019**, *1*, 1370−1384.
(782) Bucior, B. J.; Rosen, A. S.; Haranczyk, M.; Yao, Z.; Ziebel, M. E.; Farha, O. K.; Hupp, J. T.; Siepmann, J. I.; Aspuru-Guzik, A.; Snurr, R. Q. Identification Schemes for Metal−Organic Frameworks To Enable Rapid Search and Cheminformatics Analysis. *Cryst. Growth Des.* **2019**, *19*, 6682−6697.
(783) Jha, D.; Ward, L.; Paul, A.; Liao, W.; Choudhary, A.; Wolverton, C.; Agrawal, A. ElemNet: Deep Learning the Chem. Mater. From Only Elemental Composition. *Sci. Rep.* **2018**, *8*, 17593.
(784) Cova, T. F. G. G.; Pais, A. A. C. C. Deep Learning for Deep Chemistry: Optimizing the Prediction of Chemical Patterns. *Front. Chem.* **2019**, *7*, 809.

https://dx.doi.org/10.1021/acs.chemrev.0c00148
Chem. Rev. 2020, 120, 8641−8715

(785) Duvenaud, D.; Maclaurin, D.; Aguilera-Iparraguirre, J.; Gómez-Bombarelli, R.; Hirzel, T.; Aspuru-Guzik, A.; Adams, R. P. Convolutional Networks on Graphs for Learning Molecular Fingerprints. *arXiv:1509.09292 [cs, stat]*, **2015**.
(786) Jinich, A.; Sanchez-Lengeling, B.; Ren, H.; Harman, R.; Aspuru-Guzik, A. A Mixed Quantum Chemistry/Machine Learning Approach for the Fast and Accurate Prediction of Biochemical Redox Potentials and Its Large-Scale Application to 315 000 Redox Reactions. *ACS Cent. Sci.* **2019**, *5*, 1199−1210.
(787) Elton, D. C.; Boukouvalas, Z.; Fuge, M. D.; Chung, P. W. Deep Learning for Molecular Design—a Review of the State of the Art. *Mol. Sys. Des. Eng.* **2019**, *4*, 828−849.
(788) de Almeida, A. F.; Moreira, R.; Rodrigues, T. Synthetic Organic Chemistry Driven by Artificial Intelligence. *Nat. Rev. Chem.* **2019**, *3*, 589−604.
(789) Mater, A. C.; Coote, M. L. Deep Learning in Chemistry. *J. Chem. Inf. Model.* **2019**, *59*, 2545−2559.
(790) Moghadam, P. Z.; Rogge, S. M. J.; Li, A.; Chow, C.-M.; Wieme, J.; Moharrami, N.; Aragones-Anglada, M.; Conduit, G.; Gomez-Gualdron, D. A.; Van Speybroeck, V.; Fairen-Jimenez, D. Structure-Mechanical Stability Relations of Metal-Organic Frameworks via Machine Learning. *Matter* **2019**, *1*, 219−234.
(791) Anderson, R.; Rodgers, J.; Argueta, E.; Biong, A.; Gómez-Gualdrón, D. A. Role of Pore Chemistry and Topology in the CO_2 Capture Capabilities of MOFs: From Molecular Simulation to Machine Learning. *Chem. Mater.* **2018**, *30*, 6325−6337.
(792) Aghaji, M. Z.; Fernandez, M.; Boyd, P. G.; Daff, T. D.; Woo, T. K. Quantitative Structure-Property Relationship Models for Recognizing Metal Organic Frameworks (MOFs) with High CO_2 Working Capacity and CO_2 /CH_4 Selectivity for Methane Purification. *Eur. J. Inorg. Chem.* **2016**, *2016*, 4505−4511.
(793) Winter, R.; Montanari, F.; Noé, F.; Clevert, D.-A. Learning Continuous and Data-Driven Molecular Descriptors by Translating Equivalent Chemical Representations. *Chem. Sci.* **2019**, *10*, 1692−1701.
(794) Pardakhti, M.; Moharreri, E.; Wanik, D.; Suib, S. L.; Srivastava, R. Machine Learning Using Combined Structural and Chemical Descriptors for Prediction of Methane Adsorption Performance of Metal Organic Frameworks (MOFs). *ACS Comb. Sci.* **2017**, *19*, 640−645.
(795) Glavatskikh, M.; Leguy, J.; Hunault, G.; Cauchy, T.; Da Mota, B. Dataset's Chemical Diversity Limits the Generalizability of Machine Learning Predictions. *J. Cheminf.* **2019**, *11*, 69.
(796) Zhang, Y.; Ling, C. A Strategy to Apply Machine Learning to Small Datasets in Materials Science. *npj Comp. Mater.* **2018**, *4*, 25.
(797) Venkatraman, V.; Evjen, S.; Lethesh, K. C.; Raj, J. J.; Knuutila, H. K.; Fiksdahl, A. Rapid, Comprehensive Screening of Ionic Liquids towards Sustainable Applications. *Sus. Energy Fuels* **2019**, *3* (10), 2798−2808.
(798) Afzal, M. A. F.; Cheng, C.; Hachmann, J. Combining First-Principles and Data Modeling for the Accurate Prediction of the Refractive Index of Organic Polymers. *J. Chem. Phys.* **2018**, *148*, 241712.
(799) Gaillac, R.; Pullumbi, P.; Beyer, K. A.; Chapman, K. W.; Keen, D. A.; Bennett, T. D.; Coudert, F.-X. Liquid Metal−Organic Frameworks. *Nat. Mater.* **2017**, *16*, 1149−1154.
(800) Park, H.; Mall, R.; Alharbi, F. H.; Sanvito, S.; Tabet, N.; Bensmail, H.; El-Mellouhi, F. Learn-and-Match Molecular Cations for Perovskites. *J. Phys. Chem. A* **2019**, *123*, 7323−7334.
(801) Anderson, R.; Rodgers, J.; Argueta, E.; Biong, A.; Gómez-Gualdrón, D. A. Role of Pore Chemistry and Topology in the CO_2 Capture Capabilities of MOFs: From Molecular Simulation to Machine Learning. *Chem. Mater.* **2018**, *30*, 6325−6337.
(802) Zhang, X.; Zhang, K.; Lee, Y. Machine Learning Enabled Tailor-Made Design of Application-Specific Metal−Organic Frameworks. *ACS Appl. Mater. Interfaces* **2020**, *12*, 734−743.
(803) Eckhoff, M.; Behler, J. From Molecular Fragments to the Bulk: Development of a Neural Network Potential for MOF-5. *J. Chem. Theory Comput.* **2019**, *15*, 3793−3809.
(804) Janet, J. P.; Liu, F.; Nandy, A.; Duan, C.; Yang, T.; Lin, S.; Kulik, H. J. Designing in the Face of Uncertainty: Exploiting Electronic Structure and Machine Learning Models for Discovery in Inorganic Chemistry. *Inorg. Chem.* **2019**, *58*, 10592−10606.
(805) Jha, D.; Choudhary, K.; Tavazza, F.; Liao, W.; Choudhary, A.; Campbell, C.; Agrawal, A. Enhancing Materials Property Prediction by Leveraging Computational and Experimental Data Using Deep Transfer Learning. *Nat. Commun.* **2019**, *10*, 5316.
(806) Bard, A. J. Thermodynamic Potential for the Anodic Dissolution of N-Type Semiconductors. *J. Electrochem. Soc.* **1977**, *124*, 1706.
(807) Hao, J.; Xu, X.; Fei, H.; Li, L.; Yan, B. Functionalization of Metal-Organic Frameworks for Photoactive Materials. *Adv. Mater.* **2018**, *30*, 1705634.
(808) Wang, S.; Wang, X. Multifunctional Metal-Organic Frameworks for Photocatalysis. *Small* **2015**, *11*, 3097−3112.
(809) Kong, X.-J.; Lin, Z.; Zhang, Z.-M.; Zhang, T.; Lin, W. Hierarchical Integration of Photosensitizing Metal-Organic Frameworks and Nickel-Containing Polyoxometalates for Efficient Visible-Light-Driven Hydrogen Evolution. *Angew. Chem., Int. Ed.* **2016**, *55*, 6411−6416.
(810) Gu, X.; Lu, Z.-H.; Jiang, H.-L.; Akita, T.; Xu, Q. Synergistic Catalysis of Metal−Organic Framework-Immobilized Au−Pd Nanoparticles in Dehydrogenation of Formic Acid for Chemical Hydrogen Storage. *J. Am. Chem. Soc.* **2011**, *133*, 11822−11825.
(811) Dhakshinamoorthy, A.; Asiri, A. M.; García, H. Metal-Organic Framework (MOF) Compounds: Photocatalysts for Redox Reactions and Solar Fuel Production. *Angew. Chem., Int. Ed.* **2016**, *55*, 5414−5445.
(812) Sham, L. J.; Schluter, M. Density-Functional Theory of the Energy Gap. *Phys. Rev. Lett.* **1983**, *51*, 1888−1891.
(813) Runge, E.; Gross, E. K. U. Density-Functional Theory for Time-Dependent Systems. *Phys. Rev. Lett.* **1984**, *52*, 997−1000.
(814) Rüger, R.; Niehaus, T.; van Lenthe, E.; Heine, T.; Visscher, L. Vibrationally Resolved UV/Vis Spectroscopy with Time-Dependent Density Functional Based Tight Binding. *J. Chem. Phys.* **2016**, *145*, 184102.
(815) Peterson, G. W.; DeCoste, J. B.; Glover, T. G.; Huang, Y.; Jasuja, H.; Walton, K. S. Effects of Pelletization Pressure on the Physical and Chemical Properties of the Metal−Organic Frameworks $Cu_3(BTC)_2$ and UiO-66. *Microporous Mesoporous Mater.* **2013**, *179*, 48−53.
(816) Flage-Larsen, E.; Røyset, A.; Cavka, J. H.; Thorshaug, K. Band Gap Modulations in UiO Metal−Organic Frameworks. *J. Phys. Chem. C* **2013**, *117*, 20610−20616.
(817) Musho, T.; Li, J.; Wu, N. Band Gap Modulation of Functionalized Metal−Organic Frameworks. *Phys. Chem. Chem. Phys.* **2014**, *16*, 23646−23653.
(818) Yan, D.; Lloyd, G. O.; Delori, A.; Jones, W.; Duan, X. Tuning Fluorescent Molecules by Inclusion in a Metal-Organic Framework: An Experimental and Computational Study. *ChemPlusChem* **2012**, *77*, 1112−1118.
(819) Wei, Z.; Gu, Z.-Y.; Arvapally, R. K.; Chen, Y.-P.; McDougald, R. N.; Ivy, J. F.; Yakovenko, A. A.; Feng, D.; Omary, M. A.; Zhou, H.-C. Rigidifying Fluorescent Linkers by Metal−Organic Framework Formation for Fluorescence Blue Shift and Quantum Yield Enhancement. *J. Am. Chem. Soc.* **2014**, *136*, 8269−8276.
(820) Brozek, C. K.; Dincă, M. Ti^{3+}-, $V^{2+/3+}$-, $Cr^{2+/3+}$-, Mn^{2+}-, and Fe^{2+}-Substituted MOF-5 and Redox Reactivity in Cr- and Fe-MOF-5. *J. Am. Chem. Soc.* **2013**, *135*, 12886−12891.
(821) Van Wyk, A.; Smith, T.; Park, J.; Deria, P. Charge-Transfer within Zr-Based Metal−Organic Framework: The Role of Polar Node. *J. Am. Chem. Soc.* **2018**, *140*, 2756−2760.
(822) Cozzolino, A. F.; Brozek, C. K.; Palmer, R. D.; Yano, J.; Li, M.; Dincă, M. Ligand Redox Non-Innocence in the Stoichiometric Oxidation of Mn_2(2,5-Dioxidoterephthalate) (Mn-MOF-74). *J. Am. Chem. Soc.* **2014**, *136*, 3334−3337.
(823) Saouma, C. T.; Tsou, C.-C.; Richard, S.; Ameloot, R.; Vermoortele, F.; Smolders, S.; Bueken, B.; DiPasquale, A. G.; Kaminsky, W.; Valdez, C. N.; De Vos, D. E.; Mayer, J. M. Sodium-

https://dx.doi.org/10.1021/acs.chemrev.0c00148
Chem. Rev. 2020, 120, 8641−8715

Coupled Electron Transfer Reactivity of Metal−Organic Frameworks Containing Titanium Clusters: The Importance of Cations in Redox Chemistry. *Chem. Sci.* **2019**, *10*, 1322−1331.
(824) Gaggioli, C. A.; Stoneburner, S. J.; Cramer, C. J.; Gagliardi, L. Beyond Density Functional Theory: The Multiconfigurational Approach To Model Heterogeneous Catalysis. *ACS Catal.* **2019**, *9*, 8481−8502.
(825) Gagliardi, L.; Truhlar, D. G.; Li Manni, G.; Carlson, R. K.; Hoyer, C. E.; Bao, J. L. Multiconfiguration Pair-Density Functional Theory: A New Way To Treat Strongly Correlated Systems. *Acc. Chem. Res.* **2017**, *50*, 66−73.
(826) Lyakh, D. I.; Musiał, M.; Lotrich, V. F.; Bartlett, R. J. Multireference Nature of Chemistry: The Coupled-Cluster View. *Chem. Rev.* **2012**, *112*, 182−243.
(827) Gong, Y.-N.; Ouyang, T.; He, C.-T.; Lu, T.-B. Photoinduced Water Oxidation by an Organic Ligand Incorporated into the Framework of a Stable Metal−Organic Framework. *Chem. Sci.* **2016**, *7*, 1070−1075.
(828) Scholes, G. D.; Rumbles, G. Excitons in Nanoscale Systems. *Nat. Mater.* **2006**, *5*, 683−696.
(829) Izquierdo, M. A.; Broer, R.; Havenith, R. W. A. Theoretical Study of the Charge Transfer Exciton Binding Energy in Semiconductor Materials for Polymer: Fullerene-Based Bulk Heterojunction Solar Cells. *J. Phys. Chem. A* **2019**, *123*, 1233−1242.
(830) Koch, S. W.; Kira, M.; Khitrova, G.; Gibbs, H. M. Semiconductor Excitons in New Light. *Nat. Mater.* **2006**, *5*, 523−531.
(831) Civalleri, B.; Napoli, F.; Noël, Y.; Roetti, C.; Dovesi, R. Ab-Initio Prediction of Materials Properties with CRYSTAL: MOF-5 as a Case Study. *CrystEngComm* **2006**, *8*, 364−371.
(832) Wang, G.; Sun, Q.; Liu, Y.; Huang, B.; Dai, Y.; Zhang, X.; Qin, X. A Bismuth-Based Metal-Organic Framework as an Efficient Visible-Light-Driven Photocatalyst. *Chem. - Eur. J.* **2015**, *21*, 2364−2367.
(833) Fischer, R. A.; Wöll, C. Layer-by-Layer Liquid-Phase Epitaxy of Crystalline Coordination Polymers at Surfaces. *Angew. Chem., Int. Ed.* **2009**, *48*, 6205−6208.
(834) Zhou, E.-H.; Li, B.-H.; Chen, W.-X.; Luo, Z.; Liu, J.; Singh, A.; Kumar, A.; Jin, J.-C. Photocatalytic Degradation of Organic Dyes by a Stable and Biocompatible Zn(II) MOF Having Ferulic Acid: Experimental Findings and Theoretical Correlation. *J. Mol. Struct.* **2017**, *1149*, 352−356.
(835) Williams, D. E.; Dolgopolova, E. A.; Pellechia, P. J.; Palukoshka, A.; Wilson, T. J.; Tan, R.; Maier, J. M.; Greytak, A. B.; Smith, M. D.; Krause, J. A.; Shustova, N. B. Mimic of the Green Fluorescent Protein Beta-Barrel: Photophysics and Dynamics of Confined Chromophores Defined by a Rigid Porous Scaffold. *J. Am. Chem. Soc.* **2015**, *137*, 2223−2226.
(836) Chambers, M. B.; Wang, X.; Elgrishi, N.; Hendon, C. H.; Walsh, A.; Bonnefoy, J.; Canivet, J.; Quadrelli, E. A.; Farrusseng, D.; Mellot-Draznieks, C.; Fontecave, M. Photocatalytic Carbon Dioxide Reduction with Rhodium-Based Catalysts in Solution and Heterogenized within Metal-Organic Frameworks. *ChemSusChem* **2015**, *8*, 603−608.
(837) Jin, J.-C.; Wu, J.; Liu, W.-C.; Ma, A.-Q.; Liu, J.-Q.; Singh, A.; Kumar, A. A New Zn(II) Metal−Organic Framework Having 3D $CdSO_4$ Topology as Luminescent Sensor and Photocatalyst for Degradation of Organic Dyes. *New J. Chem.* **2018**, *42*, 2767−2775.
(838) Bordiga, S.; Lamberti, C.; Ricchiardi, G.; Regli, L.; Bonino, F.; Damin, A.; Lillerud, K.-P.; Bjorgen, M.; Zecchina, A. Electronic and Vibrational Properties of a MOF-5 Metal−Organic Framework: ZnO Quantum Dot Behaviour. *Chem. Commun.* **2004**, 2300−2301.
(839) Tachikawa, T.; Choi, J. R.; Fujitsuka, M.; Majima, T. Photoinduced Charge-Transfer Processes on MOF-5 Nanoparticles: Elucidating Differences between Metal-Organic Frameworks and Semiconductor Metal Oxides. *J. Phys. Chem. C* **2008**, *112*, 14090−14101.
(840) Yang, L.-M.; Vajeeston, P.; Ravindran, P.; Fjellvåg, H.; Tilset, M. Theoretical Investigations on the Chemical Bonding, Electronic Structure, And Optical Properties of the Metal−Organic Framework MOF-5. *Inorg. Chem.* **2010**, *49*, 10283−10290.
(841) Ji, M.; Lan, X.; Han, Z.; Hao, C.; Qiu, J. Luminescent Properties of Metal−Organic Framework MOF-5: Relativistic Time-Dependent Density Functional Theory Investigations. *Inorg. Chem.* **2012**, *51*, 12389−12394.
(842) De Vos, A.; Hendrickx, K.; Van Der Voort, P.; Van Speybroeck, V.; Lejaeghere, K. Missing Linkers: An Alternative Pathway to UiO-66 Electronic Structure Engineering. *Chem. Mater.* **2017**, *29*, 3006−3019.
(843) Komatsu, T.; Taylor, J. M.; Kitagawa, H. Design of a Conducting Metal−Organic Framework: Orbital-Level Matching in MIL-140A Derivatives. *Inorg. Chem.* **2016**, *55*, 546−548.
(844) Wang, S.; Kitao, T.; Guillou, N.; Wahiduzzaman, M.; Martineau-Corcos, C.; Nouar, F.; Tissot, A.; Binet, L.; Ramsahye, N.; Devautour-Vinot, S.; Kitagawa, S.; Seki, S.; Tsutsui, Y.; Briois, V.; Steunou, N.; Maurin, G.; Uemura, T.; Serre, C. A Phase Transformable Ultrastable Titanium-Carboxylate Framework for Photoconduction. *Nat. Commun.* **2018**, *9*, 1660.
(845) Gao, J.; Miao, J.; Li, P.-Z.; Teng, W. Y.; Yang, L.; Zhao, Y.; Liu, B.; Zhang, Q. A P-Type Ti(IV)-Based Metal−Organic Framework with Visible-Light Photo-Response. *Chem. Commun.* **2014**, *50*, 3786−3788.
(846) Santaclara, J. G.; Olivos-Suarez, A. I.; Gonzalez-Nelson, A.; Osadchii, D.; Nasalevich, M. A.; van der Veen, M. A.; Kapteijn, F.; Sheveleva, A. M.; Veber, S. L.; Fedin, M. V.; Murray, A. T.; Hendon, C. H.; Walsh, A.; Gascon, J. Revisiting the Incorporation of Ti(IV) in UiO-Type Metal−Organic Frameworks: Metal Exchange versus Grafting and Their Implications on Photocatalysis. *Chem. Mater.* **2017**, *29*, 8963−8967.
(847) Fu, Y.; Sun, D.; Chen, Y.; Huang, R.; Ding, Z.; Fu, X.; Li, Z. An Amine-Functionalized Titanium Metal-Organic Framework Photocatalyst with Visible-Light-Induced Activity for CO_2 Reduction. *Angew. Chem., Int. Ed.* **2012**, *51*, 3364−3367.
(848) Shi, L.; Wang, T.; Zhang, H.; Chang, K.; Meng, X.; Liu, H.; Ye, J. An Amine-Functionalized Iron(III) Metal-Organic Framework as Efficient Visible-Light Photocatalyst for Cr(VI) Reduction. *Adv. Sci.* **2015**, *2*, 1500006.
(849) Sun, M.; Yan, S.; Sun, Y.; Yang, X.; Guo, Z.; Du, J.; Chen, D.; Chen, P.; Xing, H. Enhancement of Visible-Light-Driven CO_2 Reduction Performance Using an Amine-Functionalized Zirconium Metal−Organic Framework. *Dalton Trans.* **2018**, *47*, 909−915.
(850) Shen, L.; Liang, S.; Wu, W.; Liang, R.; Wu, L. Multifunctional NH_2-Mediated Zirconium Metal−Organic Framework as an Efficient Visible-Light-Driven Photocatalyst for Selective Oxidation of Alcohols and Reduction of Aqueous Cr(VI). *Dalton Trans.* **2013**, *42*, 13649−13657.
(851) Liang, R.; Shen, L.; Jing, F.; Wu, W.; Qin, N.; Lin, R.; Wu, L. NH 2 -Mediated Indium Metal−Organic Framework as a Novel Visible-Light-Driven Photocatalyst for Reduction of the Aqueous Cr(VI). *Appl. Catal., B* **2015**, *162*, 245−251.
(852) Chambers, M. B.; Wang, X.; Ellezam, L.; Ersen, O.; Fontecave, M.; Sanchez, C.; Rozes, L.; Mellot-Draznieks, C. Maximizing the Photocatalytic Activity of Metal−Organic Frameworks with Aminated-Functionalized Linkers: Substoichiometric Effects in MIL-125-NH_2. *J. Am. Chem. Soc.* **2017**, *139*, 8222−8228.
(853) Doitomi, K.; Hirao, H. Hybrid Computational Approaches for Deriving Quantum Mechanical Insights into Metal−Organic Frameworks. *Tetrahedron Lett.* **2017**, *58*, 2309−2317.
(854) Llabresixamena, F.; Abad, A.; Corma, A.; Garcia, H. MOFs as Catalysts: Activity, Reusability and Shape-Selectivity of a Pd-Containing MOF. *J. Catal.* **2007**, *250*, 294−298.
(855) Boldog, I.; Xing, L.; Schulz, A.; Janiak, C. Influence of Sterically Non-Hindering Methyl Groups on Adsorption Properties of Two Classical Zinc and Copper MOF Types. *C. R. Chim.* **2012**, *15*, 866−877.
(856) Brown, J. W.; Henderson, B. L.; Kiesz, M. D.; Whalley, A. C.; Morris, W.; Grunder, S.; Deng, H.; Furukawa, H.; Zink, J. I.; Stoddart, J. F.; Yaghi, O. M. Photophysical Pore Control in an Azobenzene-Containing Metal−Organic Framework. *Chem. Sci.* **2013**, *4*, 2858−2864.
(857) *Multiscale Simulation Methods in Molecular Sciences: Winter School, 2−6 March 2009, Forschungszentrum Jülich, Germany; Lecture*

https://dx.doi.org/10.1021/acs.chemrev.0c00148
Chem. Rev. 2020, 120, 8641−8715

Notes; Grotendorst, J., Attig, N., Eds.; NIC Series; John von Neumann Institute for Computing; Supercomputing CentreInstitute for Advanced Simulation, Forschungszentrum Jülich: Jülich, 2009.
(858) Cameron, M. I.; Morisco, D.; Hofstetter, D.; Uman, E.; Wilkinson, J.; Kennedy, Z. C.; Fontenot, S. A.; Lee, W. T.; Hendon, C. H.; Foster, J. M. Systematically Improving Espresso: Insights from Mathematical Modeling and Experiment. *Matter* **2020**, *2*, 631−648.
(859) Lee, K.; Moorthy, S.; Ghosh, S. Multiple Scale Computational Model for Damage in Composite Materials. *Comp. Meth. Appl. Mech. Eng.* **1999**, *172*, 175−201.
(860) Jackson, R. L.; Streator, J. L. A Multi-Scale Model for Contact between Rough Surfaces. *Wear* **2006**, *261*, 1337−1347.
(861) Wu, X. B.; Smeins, F. E. Multiple-Scale Habitat Modeling Approach for Rare Plant Conservation. *Land. Urban Plan.* **2000**, *51*, 11−28.
(862) Biello, J. A.; Majda, A. J. A New Multiscale Model for the Madden−Julian Oscillation. *J. Atmos. Sci.* **2005**, *62*, 1694−1721.
(863) Merchant, T. P.; Gobbert, M. K.; Cale, T. S.; Borucki, L. J. Multiple Scale Integrated Modeling of Deposition Processes. *Thin Solid Films* **2000**, *365*, 368−375.
(864) Buckley, A. K.; Lee, M.; Cheng, T.; Kazantsev, R. V.; Larson, D. M.; Goddard, W. A., III; Toste, F. D.; Toma, F. M. Electrocatalysis at Organic−Metal Interfaces: Identification of Structure−Reactivity Relationships for CO_2 Reduction at Modified Cu Surfaces. *J. Am. Chem. Soc.* **2019**, *141*, 7355−7364.
(865) Chen, Y.; Huang, Y.; Cheng, T.; Goddard, W. A. Identifying Active Sites for CO_2 Reduction on Dealloyed Gold Surfaces by Combining Machine Learning with Multiscale Simulations. *J. Am. Chem. Soc.* **2019**, *141*, 11651−11657.
(866) Stamatakis, M.; Christiansen, M. A.; Vlachos, D. G.; Mpourmpakis, G. Multiscale Modeling Reveals Poisoning Mechanisms of MgO-Supported Au Clusters in CO Oxidation. *Nano Lett.* **2012**, *12*, 3621−3626.
(867) Chung, L. W.; Sameera, W. M. C.; Ramozzi, R.; Page, A. J.; Hatanaka, M.; Petrova, G. P.; Harris, T. V.; Li, X.; Ke, Z.; Liu, F.; Li, H.-B.; Ding, L.; Morokuma, K. The ONIOM Method and Its Applications. *Chem. Rev.* **2015**, *115*, 5678−5796.
(868) Vreven, T.; Morokuma, K. Hybrid Methods: ONIOM-(QM:MM) and QM/MM. In *Annual Reports in Computational Chemistry*; Elsevier, 2006; Vol. *2*, Chapter 3, pp 35−51.
(869) Dapprich, S.; Komáromi, I.; Byun, K. S.; Morokuma, K.; Frisch, M. J. A New ONIOM Implementation in Gaussian98. Part I. The Calculation of Energies, Gradients, Vibrational Frequencies and Electric Field Derivatives. *J. Mol. Struct.: THEOCHEM* **1999**, *461*−*462*, 1−21.
(870) Groenhof, G. Introduction to QM/MM Simulations. In *Biomolecular Simulations*; Monticelli, L., Salonen, E., Eds.; Humana Press: Totowa, NJ, 2013; Vol. *924*, pp 43−66.
(871) Vreven, T.; Morokuma, K.; Farkas, Ö.; Schlegel, H. B.; Frisch, M. J. Geometry Optimization with QM/MM, ONIOM, and Other Combined Methods. I. Microiterations and Constraints. *J. Comput. Chem.* **2003**, *24*, 760−769.
(872) Bjornsson, R.; Bühl, M. Modeling Molecular Crystals by QM/MM: Self-Consistent Electrostatic Embedding for Geometry Optimizations and Molecular Property Calculations in the Solid. *J. Chem. Theory Comput.* **2012**, *8*, 498−508.
(873) Madarász, Á.; Berta, D.; Paton, R. S. Development of a True Transition State Force Field from Quantum Mechanical Calculations. *J. Chem. Theory Comput.* **2016**, *12*, 1833−1844.
(874) Yang, Y.; Shin, Y. K.; Li, S.; Bennett, T. D.; van Duin, A. C. T.; Mauro, J. C. Enabling Computational Design of ZIFs Using ReaxFF. *J. Phys. Chem. B* **2018**, *122*, 9616−9624.
(875) Coupry, D. E.; Addicoat, M. A.; Heine, T. Extension of the Universal Force Field for Metal−Organic Frameworks. *J. Chem. Theory Comput.* **2016**, *12*, 5215−5225.
(876) Heinen, J.; Burtch, N. C.; Walton, K. S.; Dubbeldam, D. Flexible Force Field Parameterization through Fitting on the Ab Initio-Derived Elastic Tensor. *J. Chem. Theory Comput.* **2017**, *13*, 3722−3730.
(877) Spellmeyer, D. C.; Houk, K. N. Force-Field Model for Intramolecular Radical Additions. *J. Org. Chem.* **1987**, *52*, 959−974.
(878) Boyd, P. G.; Moosavi, S. M.; Witman, M.; Smit, B. Force-Field Prediction of Materials Properties in Metal-Organic Frameworks. *J. Phys. Chem. Lett.* **2017**, *8*, 357−363.
(879) Wagner, J. P.; Schreiner, P. R. London Dispersion in Molecular Chemistry - Reconsidering Steric Effects. *Angew. Chem., Int. Ed.* **2015**, *54*, 12274−12296.
(880) Rappe, A. K.; Casewit, C. J.; Colwell, K. S.; Goddard, W. A.; Skiff, W. M. UFF, a Full Periodic Table Force Field for Molecular Mechanics and Molecular Dynamics Simulations. *J. Am. Chem. Soc.* **1992**, *114*, 10024−10035.
(881) Cornell, W. D.; Cieplak, P.; Bayly, C. I.; Gould, I. R.; Merz, K. M.; Ferguson, D. M.; Spellmeyer, D. C.; Fox, T.; Caldwell, J. W.; Kollman, P. A. A Second Generation Force Field for the Simulation of Proteins, Nucleic Acids, and Organic Molecules. *J. Am. Chem. Soc.* **1995**, *117*, 5179−5197.
(882) Dewar, M. J. S.; Zoebisch, E. G.; Healy, E. F.; Stewart, J. J. P. Development and Use of Quantum Mechanical Molecular Models. 76. AM1: A New General Purpose Quantum Mechanical Molecular Model. *J. Am. Chem. Soc.* **1985**, *107*, 3902−3909.
(883) Mayo, S. L.; Olafson, B. D.; Goddard, W. A. DREIDING: A Generic Force Field for Molecular Simulations. *J. Phys. Chem.* **1990**, *94*, 8897−8909.
(884) Bougeard, D.; Brémard, C.; De Jaeger, R.; Lemmouchi, Y. Conformational Stability and Force Field of Chloromonophosphazenes: MNDO Calculations, Vibrational Spectra and Normal Coordinate Analyses of $Cl_3PNP(X)Cl_2$ (X = O, S) and $[Cl_3PNPCl_3]$-[Y] (Y = Cl, PCl_6). *Spectrochim. Acta, Part A* **1993**, *49*, 199−208.
(885) Bristow, J. K.; Tiana, D.; Walsh, A. Transferable Force Field for Metal-Organic Frameworks from First-Principles: BTW-FF. *J. Chem. Theory Comput.* **2014**, *10*, 4644−4652.
(886) Bureekaew, S.; Amirjalayer, S.; Tafipolsky, M.; Spickermann, C.; Roy, T. K.; Schmid, R. MOF-FF - A Flexible First-Principles Derived Force Field for Metal-Organic Frameworks. *Phys. Status Solidi B* **2013**, *250*, 1128−1141.
(887) Bo, C.; Maseras, F. QM/MM Methods in Inorganic Chemistry. *Dalton Trans.* **2008**, 2911−2919.
(888) Cao, L.; Ryde, U. On the Difference Between Additive and Subtractive QM/MM Calculations. *Front. Chem.* **2018**, *6*, 89.
(889) Roßbach, S.; Ochsenfeld, C. Influence of Coupling and Embedding Schemes on QM Size Convergence in QM/MM Approaches for the Example of a Proton Transfer in DNA. *J. Chem. Theory Comput.* **2017**, *13*, 1102−1107.
(890) Ho, J.; Shao, Y.; Kato, J. Do Better Quality Embedding Potentials Accelerate the Convergence of QM/MM Models? The Case of Solvated Acid Clusters. *Molecules* **2018**, *23*, 2466.
(891) Vreven, T.; Morokuma, K. On the Application of the IMOMO (Integrated Molecular Orbital + Molecular Orbital) Method. *J. Comput. Chem.* **2000**, *21*, 1419−1432.
(892) Vreven, T.; Morokuma, K. Prediction of the Dissociation Energy of Hexaphenylethane Using the ONIOM(MO:MO:MO) Method. *J. Phys. Chem. A* **2002**, *106*, 6167−6170.
(893) Vreven, T.; Byun, K. S.; Komáromi, I.; Dapprich, S.; Montgomery, J. A.; Morokuma, K.; Frisch, M. J. Combining Quantum Mechanics Methods with Molecular Mechanics Methods in ONIOM. *J. Chem. Theory Comput.* **2006**, *2*, 815−826.
(894) Svensson, M.; Humbel, S.; Froese, R. D. J.; Matsubara, T.; Sieber, S.; Morokuma, K. ONIOM: A Multilayered Integrated MO + MM Method for Geometry Optimizations and Single Point Energy Predictions. A Test for Diels−Alder Reactions and $Pt(P(t\text{-}Bu)_3)_2 + H_2$ Oxidative Addition. *J. Phys. Chem.* **1996**, *100*, 19357−19363.
(895) Woo, T. K.; Cavallo, L.; Ziegler, T. Implementation of the IMOMM Methodology for Performing Combined QM/MM Molecular Dynamics Simulations and Frequency Calculations. *Theor. Chem. Acc.* **1998**, *100* (5−6), 307−313.
(896) Maseras, F.; Morokuma, K. IMOMM: A New Integratedab Initio + Molecular Mechanics Geometry Optimization Scheme of

https://dx.doi.org/10.1021/acs.chemrev.0c00148
Chem. Rev. 2020, 120, 8641−8715

Equilibrium Structures and Transition States. *J. Comput. Chem.* **1995**, *16*, 1170−1179.
(897) Matsubara, T.; Maseras, F.; Koga, N.; Morokuma, K. Application of the New "Integrated MO + MM" (IMOMM) Method to the Organometallic Reaction $Pt(PR_3)_2 + H_2$ (R = H, Me, *t* -Bu, and Ph). *J. Phys. Chem.* **1996**, *100*, 2573−2580.
(898) Humbel, S.; Sieber, S.; Morokuma, K. The IMOMO Method: Integration of Different Levels of Molecular Orbital Approximations for Geometry Optimization of Large Systems: Test for *n* -butane Conformation and S_N2 Reaction: RCl+Cl $^-$. *J. Chem. Phys.* **1996**, *105*, 1959−1967.
(899) Svensson, M.; Humbel, S.; Morokuma, K. Energetics Using the Single Point IMOMO (Integrated Molecular Orbital+molecular Orbital) Calculations: Choices of Computational Levels and Model System. *J. Chem. Phys.* **1996**, *105*, 3654−3661.
(900) Maseras, F. The IMOMM Method Opens the Way for the Accurate Calculation of "Real" Transition Metal Complexes. *Chem. Commun.* **2000**, 1821−1827.
(901) Calderón, J.; Añez, R.; Alejos, P. Effect of Cavity Size on the Adsorption of Small Molecules on Two Isoreticular Cobalt-Based MOF: An ONIOM Approach. *Comput. Theor. Chem.* **2019**, *1156*, 1−10.
(902) Maihom, T.; Boekfa, B.; Sirijaraensre, J.; Nanok, T.; Probst, M.; Limtrakul, J. Reaction Mechanisms of the Methylation of Ethene with Methanol and Dimethyl Ether over H-ZSM-5: An ONIOM Study. *J. Phys. Chem. C* **2009**, *113*, 6654−6662.
(903) Pianwanit, A.; Kritayakornupong, C.; Vongachariya, A.; Selphusit, N.; Ploymeerusmee, T.; Remsungnen, T.; Nuntasri, D.; Fritzsche, S.; Hannongbua, S. The Optimal Binding Sites of CH_4 and CO_2 Molecules on the Metal-Organic Framework MOF-5: ONIOM Calculations. *Chem. Phys.* **2008**, *349*, 77−82.
(904) Moeljadi, A. M. P.; Schmid, R.; Hirao, H. Dioxygen Binding to Fe-MOF-74: Microscopic Insights from Periodic QM/MM Calculations. *Can. J. Chem.* **2016**, *94*, 1144−1150.
(905) Hirao, H.; Ng, W. K. H.; Moeljadi, A. M. P.; Bureekaew, S. Multiscale Model for a Metal−Organic Framework: High-Spin Rebound Mechanism in the Reaction of the Oxoiron(IV) Species of Fe-MOF-74. *ACS Catal.* **2015**, *5*, 3287−3291.
(906) Cui, Q.; Guo, H.; Karplus, M. Combining *Ab Initio* and Density Functional Theories with Semiempirical Methods. *J. Chem. Phys.* **2002**, *117*, 5617−5631.
(907) Banik, S. D.; Nandi, N. Influence of the Conserved Active Site Residues of Histidyl TRNA Synthetase on the Mechanism of Aminoacylation Reaction. *Biophys. Chem.* **2011**, *158*, 61−72.
(908) Braga, C. F.; Longo, R. L. Conformational Analysis of Protonated Cyclo-[(S)-Phenylalanyl-(S)-Histidyl] and Its Complex with Benzaldehyde within Metal-Organic Frameworks (MOFs). *J. Braz. Chem. Soc.* **2008**, *19*, 321−328.
(909) Daniel, C. R. A.; Rodrigues, N. M.; da Costa, N. B., Jr.; Freire, R. O. Are Quantum Chemistry Semiempirical Methods Effective to Predict Solid State Structure and Adsorption in Metal-Organic Frameworks. *J. Phys. Chem. C* **2015**, *119*, 23398−23406.
(910) Vaughan, O. Porous by Design: Porous Artificial Crystals. *Nature* **2014**, *511*, 19.
(911) de M Seabra, G.; Walker, R. C.; Roitberg, A. E. Are Current Semiempirical Methods Better Than Force Fields? A Study from the Thermodynamics Perspective. *J. Phys. Chem. A* **2009**, *113*, 11938−11948.
(912) Zheng, M.; Liu, Y.; Wang, C.; Liu, S.; Lin, W. Cavity-Induced Enantioselectivity Reversal in a Chiral Metal−Organic Framework Brønsted Acid Catalyst. *Chem. Sci.* **2012**, *3*, 2623−2627.
(913) Barone, V.; Cossi, M. Quantum Calculation of Molecular Energies and Energy Gradients in Solution by a Conductor Solvent Model. *J. Phys. Chem. A* **1998**, *102*, 1995−2001.
(914) Cortese, R.; Duca, D. A DFT Study of IRMOF-3 Catalysed Knoevenagel Condensation. *Phys. Chem. Chem. Phys.* **2011**, *13*, 15995−16004.
(915) Kulik, H. J.; Zhang, J.; Klinman, J. P.; Martínez, T. J. How Large Should the QM Region Be in QM/MM Calculations? The Case of Catechol *O* -Methyltransferase. *J. Phys. Chem. B* **2016**, *120*, 11381−11394.
(916) Amara, P.; Field, M. J.; Alhambra, C.; Gao, J. The Generalized Hybrid Orbital Method for Combined Quantum Mechanical/Molecular Mechanical Calculations: Formulation and Tests of the Analytical Derivatives. *Theor. Chem. Acc.* **2000**, *104*, 336−343.
(917) Pu, J.; Gao, J.; Truhlar, D. G. Combining Self-Consistent-Charge Density-Functional Tight-Binding (SCC-DFTB) with Molecular Mechanics by the Generalized Hybrid Orbital (GHO) Method. *J. Phys. Chem. A* **2004**, *108*, 5454−5463.
(918) Pu, J.; Gao, J.; Truhlar, D. G. Generalized Hybrid-Orbital Method for Combining Density Functional Theory with Molecular Mechanicals. *ChemPhysChem* **2005**, *6*, 1853−1865.
(919) Garcia-Viloca, M.; Gao, J. Generalized Hybrid Orbital for the Treatment of Boundary Atoms in Combined Quantum Mechanical and Molecular Mechanical Calculations Using the Semiempirical Parameterized Model 3 Method. *Theor. Chem. Acc.* **2004**, *111*, 280−286.
(920) Ohnishi, Y.; Nakao, Y.; Sato, H.; Sakaki, S. Frontier Orbital Consistent Quantum Capping Potential (FOC-QCP) for Bulky Ligand of Transition Metal Complexes. *J. Phys. Chem. A* **2008**, *112*, 1946−1955.
(921) Alary, F.; Poteau, R.; Heully, J.-L.; Barthelat, J.-C.; Daudey, J.-P. A New Method for Modeling Spectator Chemical Groups in Ab Initio Calculations: Effective Group Potentials. *Theor. Chem. Acc.* **2000**, *104*, 174−178.
(922) Zhang, Y.; Lee, T.-S.; Yang, W. A Pseudobond Approach to Combining Quantum Mechanical and Molecular Mechanical Methods. *J. Chem. Phys.* **1999**, *110*, 46−54.
(923) Lewin, J. L.; Cramer, C. J. Modified Carbon Pseudopotential for Use in ONIOM Calculations of Alkyl-Substituted Metallocenes. *J. Phys. Chem. A* **2008**, *112*, 12754−12760.
(924) Dumont, E.; Chaquin, P. The H* Method: Hydrogen Atoms with a Fictitious Nuclear Charge. A Versatile Theoretical Tool for Study of Atom and Group Properties as Substituents: Electronegativity and Partition of σ and π Contributions. *J. Mol. Struct.: THEOCHEM* **2004**, *680*, 99−106.
(925) Koga, N.; Morokuma, K. A Simple Scheme of Estimating Substitution or Substituent Effects in the Ab Initio MO Method Based on the Shift Operator. *Chem. Phys. Lett.* **1990**, *172*, 243−248.
(926) Rivail, J.-L.; Monari, A.; Assfeld, X. The Non Empirical Local Self Consistent Field Method: Application to Quantum Mechanics/Molecular Mechanics (QM/MM) Modeling of Large Biomolecular Systems. In *Quantum Modeling of Complex Molecular Systems*; Rivail, J.-L., Ruiz-Lopez, M., Assfeld, X., Eds.; Springer International Publishing: Cham, 2015; Vol. *21*, pp 343−365.
(927) Wu, X.-P.; Gagliardi, L.; Truhlar, D. G. Combined Quantum Mechanical and Molecular Mechanical Method for Metal−Organic Frameworks: Proton Topologies of NU-1000. *Phys. Chem. Chem. Phys.* **2018**, *20*, 1778−1786.
(928) Wu, X.-P.; Gagliardi, L.; Truhlar, D. G. Parameterization of Combined Quantum Mechanical and Molecular Mechanical Methods: Bond-Tuned Link Atoms. *Molecules* **2018**, *23*, 1309.
(929) Lin, H.; Truhlar, D. G. QM/MM: What Have We Learned, Where Are We, Where Do We Go from Here? *Theor. Chem. Acc.* **2007**, *117*, 185−199.
(930) Lin, H.; Truhlar, D. G. Redistributed Charge and Dipole Schemes for Combined Quantum Mechanical and Molecular Mechanical Calculations. *J. Phys. Chem. A* **2005**, *109*, 3991−4004.
(931) Cho, S.-H.; Ma, B.; Nguyen, S. T.; Hupp, J. T.; Albrecht-Schmitt, T. E. A Metal−Organic Framework Material That Functions as an Enantioselective Catalyst for Olefin Epoxidation. *Chem. Commun.* **2006**, 2563−2565.
(932) Cavallo, L.; Jacobsen, H. Electronic Effects in (Salen)Mn-Based Epoxidation Catalysts. *J. Org. Chem.* **2003**, *68*, 6202−6207.
(933) Wu, X.-P.; Gagliardi, L.; Truhlar, D. Parametrization of Combined Quantum Mechanical and Molecular Mechanical Methods: Bond-Tuned Link Atoms. *Molecules* **2018**, *23*, 1309.
(934) Wu, X.-P.; Gagliardi, L.; Truhlar, D. G. Multilink F* Method for Combined Quantum Mechanical and Molecular Mechanical Calcu-

https://dx.doi.org/10.1021/acs.chemrev.0c00148
Chem. Rev. 2020, 120, 8641−8715

lations of Complex Systems. *J. Chem. Theory Comput.* **2019**, *15*, 4208−4217.
(935) Tamura, H.; Gordon, M. S. Ab Initio Study of Nucleation on the Diamond (100) Surface during Chemical Vapor Deposition with Methyl and H Radicals. *Chem. Phys. Lett.* **2005**, *406*, 197−201.
(936) Yu, D.; Yazaydin, A. O.; Lane, J. R.; Dietzel, P. D. C.; Snurr, R. Q. A Combined Experimental and Quantum Chemical Study of CO_2 Adsorption in the Metal−Organic Framework CPO-27 with Different Metals. *Chem. Sci.* **2013**, *4*, 3544−3556.
(937) Catlow, C. R. A.; Bromley, S. T.; Hamad, S.; Mora-Fonz, M.; Sokol, A. A.; Woodley, S. M. Modeling Nano-Clusters and Nucleation. *Phys. Chem. Chem. Phys.* **2010**, *12*, 786−811.
(938) Choomwattana, S.; Maihom, T.; Khongpracha, P.; Probst, M.; Limtrakul, J. Structures and Mechanisms of the Carbonyl-Ene Reaction between MOF-11 Encapsulated Formaldehyde and Propylene: An ONIOM Study. *J. Phys. Chem. C* **2008**, *112*, 10855−10861.
(939) Gomez-Gualdron, D. A.; Dix, S. T.; Getman, R. B.; Snurr, R. Q. A Modeling Approach for MOF-Encapsulated Metal Catalysts and Application to n-Butane Oxidation. *Phys. Chem. Chem. Phys.* **2015**, *17*, 27596−27608.
(940) Gamage, N.-D. H.; McDonald, K. A.; Matzger, A. J. MOF-5-Polystyrene: Direct Production from Monomer, Improved Hydrolytic Stability, and Unique Guest Adsorption. *Angew. Chem., Int. Ed.* **2016**, *55*, 12099−12103.

https://dx.doi.org/10.1021/acs.chemrev.0c00148
Chem. Rev. 2020, 120, 8641−8715